CRANFIELD UNIVERSITY

KLEMENTINA GEROVA

THERMO-FLUID EFFECTS ASSOCIATED WITH MODELLING SUBSCALE AUTOMOTIVE HEAT EXCHANGERS

SCHOOL OF AEROSPACE, TRANSPORT AND MANUFACTURING

PhD THESIS

This page intentionally left blank.

CRANFIELD UNIVERSITY

SCHOOL OF OF AEROSPACE, TRANSPORT AND MANUFACTURING

Ph.D. THESIS

Academic Year: 2015

KLEMENTINA GEROVA

Thermo-Fluid Effects Associated with Modelling Subscale Automotive Heat Exchangers

Supervisors: Prof. A.M. Savill and Dr. N.J. Lawson

December 2015

This thesis is submitted in partial fulfilment of the requirements for the degree of Doctor of Philosophy.

This page intentionally left blank.

Abstract

Automotive components are tested extensively in wind tunnels by automotive manufacturers and race teams. This is usually achieved using an accurate scale model representation of the component within the wind tunnel.

Automotive heat exchangers, however, are comprised of numerous intricate geometries and are therefore impractical to produce at model scale. Instead they are simply modelled as pressure drops, achieved using a thin mesh or honeycomb of known porosity. Most commercial computational fluid dynamics solvers ignore the geometry of the heat exchanger and instead model it as a discontinuity with a known pressure drop and heat transfer.

The pressure drop across an automotive heat exchanger, however, was found to vary with both the coolant temperature and the angle of inclination of the heat exchanger. This thesis initially presents a relationship between the pressure drop coefficient and the inclination angle for varying media porosities. Mathematical relationships for inclination angles of 0°, 15°, 30° and 45° were derived relating this pressure drop coefficient to the porosity of the media. Weighted least squares is proposed over ordinary least squares when obtaining the Forchheimer equation coefficients from experimental measurements.

Investigation extends into the thermo-fluid effects on a full scale automotive heat exchanger when inclined at 0°, 15°, 30° and 45°. It was found, depending on the angle, that there was a difference in the pressure drop of up to 10% between the unheated and heated (100 °C) heat exchanger. Based on the proposed mathematical relationship, this correlated to a 4% decrease in porosity in order to accurately model the automotive heat exchanger at subscale.

The thesis concludes with experimental and numerical investigation into the heat transfer on a hydrodynamically and thermally developing flow within a radiator channel. Laser doppler anemometry measurements recorded a 1.5% increase in the centreline velocity compared to 0.8% obtained from numerical simulation.

Keywords: automotive heat transfer, wind tunnel radiator modelling, subscale radiators, developing radiator matrix channel flow, thermally developing flow.

This page intentionally left blank.

Acknowledgements

I am very thankful to a great number of people who have helped me throughout my time at Cranfield University. Firstly, I wish to thank my supervisors Professor Mark Savill and Dr. Nicholas Lawson for their guidance and input from the start and throughout the project. I would also like to thank Dr. Mark Finnis and Dr. Ian Barden for their useful comments on the thesis structure. In addition, Dr. Ben Thornber and Dr. Evgeniy Shapiro for their computational advice. I am also thankful to Barry Walker at Cranfield University who provided technical guidance on the experimental configurations. I am also greatly appreciative of the staff at Young Calibration for their technical input regarding industrial testing.

In addition, this thesis would not be possible without the people who have helped me outside of academia, notably Roy Chamberlain and Craig Wilde from the Cranfield University Fitness Centre and Richard Rogers from National Flying Laboratory. Dr. Stefan Velikov, Dr. Quintain Mcenteggart, Dr. Max Star, Dr. Matyas Benke, Dr. Jeremy Appleyard, Dr. Cinzia Taccoli, Dr. Natalia Di Matteo, Dr. Uyi Igie, Luca Camosi, Remi Lansiaux, Fran Mena and Olivier Bouzigues who have helped me enormously throughout my time at Cranfield University. Snezhi Kovacheva, Mariyana Boyanova, Stela Yordanova-Yancheva and Vihra Kostova, my lifelong friends.

This thesis would not be possible without the recommendation from my undergraduate supervisor, Professor Eben Cobb from WPI. In addition, it would not have been possible without Dr. Pierre Gauthier from Concordia University for teaching my first aerodynamics course.

Lastly, I wish to thank my family for their love and financial support, without whom none of this would have been possible and in particular my husband Dr. Jason Barden for his continued motivation to get me to complete the writing of this thesis.

Finally, I wish to dedicate this thesis to my father Dr. Orlin Angelov Gerov who sadly passed away on the 19th December 2010 and isn't here to see me hand in.

This page intentionally left blank.

Contents

List of Figures

List of Tables

This page intentionally left blank.

Nomenclature

Latin Symbols

A, B, C	Polynomial coefficients
A, $B_{weighted}$	Weighted polynomial coefficients
b	Estimate of $\hat{\beta}$
c	Empirical coefficient for porous materials
c_p	Specific heat capacity
$c_{p(a)}$	Specific heat capacity of air
$c_{p(c)}$	Specific heat capacity of liquid coolant
$C_{1,2}$	Pressure jump coefficients for porous materials
C_{2f}	Pressure jump coefficients for ANSYS® FLUENT® 15.0
C_c	Specific heat capacity of cold fluid
C_h	Specific heat capacity of hot fluid
$C_{\min}$	Minimum capacity rate
C_r	Heat capacity ratio
D_ω	Cross diffusion term
$E_{\gamma 1,2}$	Transition source term
f_i	External force vector
$F_{1,2}$	Blending Functions
F_{length}	Length of transition region
F_{onset}	Onset of transition
g	Gravitational force
G_k	Turbulent kinetic energy production
G_ω	Generation of specific dissipation
h	Heat transfer coefficient
I	Turbulence intensity
k	Turbulent kinetic energy
K	Permeability
K_θ	Pressure loss coefficient

L	Characteristic length
$\dot{m}_a$	Mass flux of air
$\dot{m}_c$	Mass flux of liquid coolant
$\dot{m_{c,h}}$	Mass flux of fluid
M_w	Gas molecular weight
Nu	Nusselt number
Nu_x	Local Nusselt number based on x
p	Local pressure
$P_{\gamma 1,2}$	Transition source term
$P_{\theta t}$	Transition momentum thickness Reynolds number source term
Pr	Prandtl number
q	Dynamic pressure
$\overrightarrow{q}$	Heat flux
Q, $\dot{Q}$	Heat exchanger transfer rate
$\overrightarrow{r}$	Displacement vector
r_i	Residual of i$^{\text{th}}$ data point
R	Gas constant
$Rad._{Cc}$	Radiator with cold coolant
$Rad._{Hc}$	Radiator with hot coolant
Re	Reynolds number
$R\tilde{e}_{\theta t}$	Transition momentum thickness Reynolds number
R^2	Coefficient of determination
Re_x	Local Reynolds number based on distance (x)
S	Effective temperature or sum of squared errors or strain rate tensor
S_k	User defined turbulence constant
S_ω	User define turbulence constant
T	Static temperature
T_0	Reference temperature
T_{ai}	Ambient temperature
$T_{\mathrm{a(in)}}$	Ambient fluid inlet
$T_{\mathrm{a(out)}}$	Ambient fluid outlet
T_{Air}	Temperature of freestream fluid
T_{BP}	Coolant boiling temperature
$T_{c,ci}$	Coolant radiator inlet temperature
$T_{\mathrm{c(in)}}$	Coolant radiator inlet temperature
$T_{\mathrm{c(out)}}$	Coolant radiator outlet temperature
$T_{\text{cold (in)}}$	Cold fluid inlet temperature
T_{h}	Hot fluid inlet temperature
$T_{\text{hot (in)}}$	Hot fluid inlet temperature
T_{Plate}	Temperature of heated plate

u	Fluid velocity
u_*	Friction velocity
u_{rms}	Root mean squared velocity
U	Overall heat transfer coefficient or fluid velocity
$\overline{U}$	Average velocity
$U_{0,\infty}$	Freestream fluid velocity
v	Fluid velocity
v_∞	Freestream fluid velocity
w_i	Regression weight
y/δ	Shape profile
x/L	Normalised horizontal displacement
Y	Inertial factor
y^+	Dimensionless wall distance
y_i	Observed response value
$\hat{y}_i$	Fitted response value
Y_k	Dissipation of k
Y_ω	Dissipation of ω
y/H	Normalised vertical displacement
z/W	Normalised horizontal traverse

Greek Symbols

α	Angle of incidence with respect to the vertical (y) plane
α_p	Thermal diffusion rate
α_f	Permeability of the medium used in ANSYS® FLUENT® 15.0
β	Porosity
$\hat{\beta}$	Coefficient estimates
$\beta_{eff.}$	Effective porosity
γ	Intermittency
Γ_k	Effective diffusivity of k
Γ_ω	Effective diffusivity of ω
δ	Velocity boundary layer thickness
δ_t	Thermal boundary layer thickness
δ_x	Porous media thickness
$\delta\theta$	Increment in temperature
$\delta\theta_{lmtd}$	Logarithmic Mean Temperature Difference
$\delta\theta_m$	Mean temperature difference between fluids
Δm	Media thickness
ΔP	Pressure drop

ΔT	Temperature difference
ΔU_x	Percentage velocity change
ε	Heat transfer effectiveness or turbulent dissipation
ε-NTU	NTU effectiveness
μ	Dynamic viscosity or mean
μ_0	Reference fluid viscosity
μ_t	Turbulent viscosity
ν	Kinematic viscosity
ρ	Fluid density
σ	Standard deviation
$\sigma_{k,m}$	Porous constants
σ^2	Variance
τ_w	Wall shear stress
ϕ	Cell centroid
Φ	Convected quantity within flow field
ω	Specific dissipation
Ω	Vorticity magnitude

Acronyms

ATB	Air-to-Boil
$CFMCHE$	Conjugate Counter Flow Microchannel Heat-Exchanger
CFD	Computational Fluid Dynamics
CFT	Curve Fitting Toolbox
DAQ	Data Acquisition
FFT	Fast Fourier Transform
HC	Honeycomb
HCE	Heteroscedastic-Consitent Errors
HXC	Heat Exchanger
ICE	Internal Combustion Engine
LDA	Laser Doppler Anemometry
LDV	Laser Doppler Velocimetry
$LMTD$	Log-Mean Temperature Difference
$MIRA$	Motor Industry Research Association
NTU	Number of Heat Transfer Units
OEM	Original Equipment Manufacturer
OLS	Ordinary Least Squares

PIV	Particle Image velocimetry
PSI	Pounds per Square Inch
$RANS$	Reynolds-Averaged Navier-Stokes
$RMIT$	Royal Melbourne Institute of Technology
RMS	Root Mean Squared
SAE	Society of Automotive Engineers
SD	Specific Dissipation
$SIMPLE$	Semi-Implicit Method for Pressure-Linked Equations
SST	Shear Stress Transport
SUV	Sports Utility Vehicle
UDF	User Defined Function
WLS	Weighted Least Squares

Definitions

Nu — Nusselt number, based on heat transfer coefficient (h), thermal conductivity (k) and characteristic length (L), $\text{Nu} = \frac{hL}{k}$
and appears on page 78.

Pr — Prandtl number, based on viscous diffusion rate (ν) and thermal diffusion rate (α_p), $\text{Pr} = \frac{\nu}{\alpha_p} = \frac{c_p \mu}{k}$
and appears on page 78.

Re — Reynolds number, based on free stream velocity (V_∞) and characteristic length (L), $\text{Re} = \frac{\rho V_\infty L}{\mu}$
and appears on page 78.

St — Stanton number, based on Nusselt number (Nu), Reynolds number (Re) and Prandtl number (Pr), $\text{St} = \frac{\text{Nu}}{\text{Re} \cdot \text{Pr}}$
and appears on page 95.

This page intentionally left blank.

Chapter 1

Introduction

1.1 Types of Heat Exchangers

Heat transfer between two fluids or a fluid and solid is one of the most common physical phenomenon. It can be easily seen in our daily lives with examples such as the heating system or refrigerator within our homes. The devices that use heat transfer are broadly termed heat exchangers. They come in various shapes and sizes and are commonly classified by the flow arrangement or the type of construction.

The simplest heat exchanger is one with a two fluid circular tube bundle as shown in Fig. 1.1a. A key disadvantage of this construction is that the only way surface area density can be increased is to decrease the diameter of the tubes. This poses severe limitations on what can be constructed since fabrication and cost usually limit the minimum tube diameter to no less than a quarter of an inch (approximately 6 mm) [1].

An effective way to increase the surface area density is therefore through the use of channel fins as an additional, secondary surface. Figure 1.1b shows an example of finned circular tubes where circular fins have been attached to the outside of the circular tubes [1]. The fins can be placed on either side of a gas-to-liquid heat exchanger or even used in a liquid-to-liquid one. If placed on the liquid side an important consideration must be taken into account. Due to the relatively high thermal conductivity of liquids, high convection heat transfer rates must be conducted along the fins and thus the conduction resistance may destroy the advantage of the extra surface area gained. Another variation of the finned-tube arrangement is shown in Fig. 1.1c. The tubes can be either flat or circular.

A large area density on both fluid sides can be achieved in a similar manner as shown in Figs. 1.1d and 1.1e. This fin and plate arrangement is assembled as a sandwich of flat plates bonded by interconnecting fins. The two fluids are carried between alternate pairs of plates and can be arranged in either counterflow or

crossflow which provides an additional degree of flexibility.

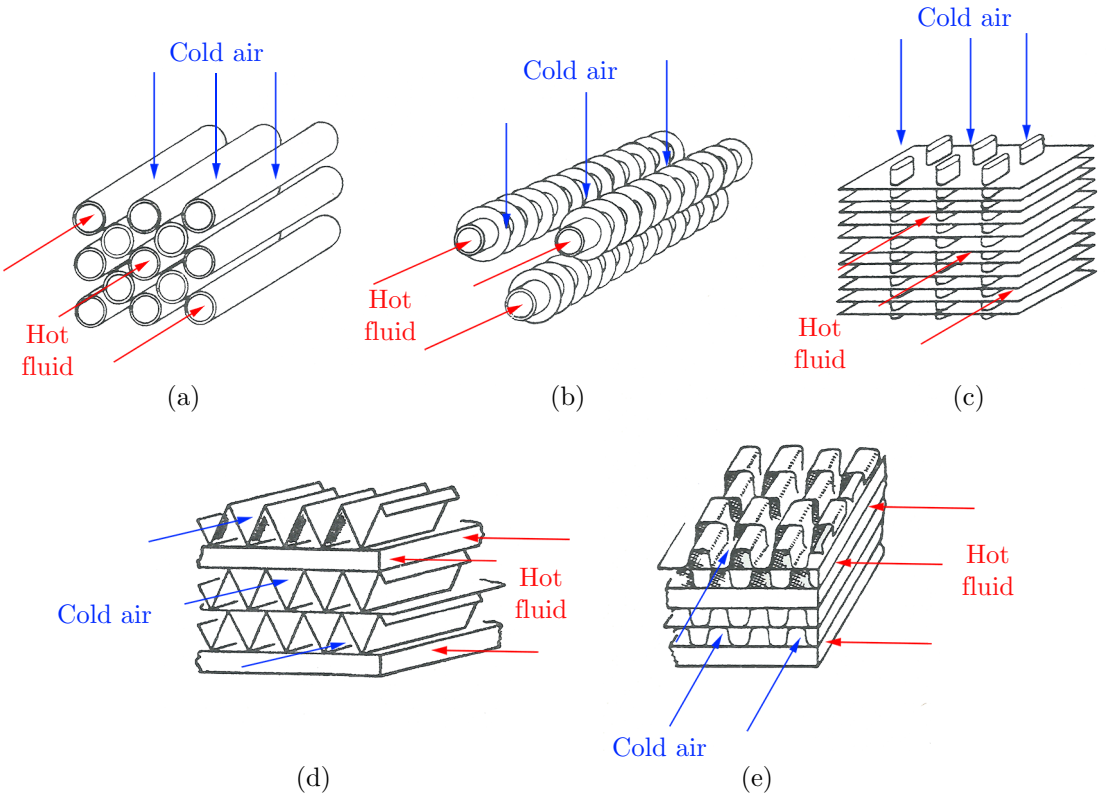

Figure 1.1 Geometries of typical heat exchangers [1].

As mentioned earlier, heat exchangers can be classified in a variety of ways. A further classification can occur based on their flow arrangement. In the parallel flow arrangement, the hot and cold fluids enter at the same end, flow in the same direction and exit at the same end. In the counter flow arrangement, however, the fluids enter at opposite ends, travel in opposing directions and leave at opposite ends. Alternatively a third arrangement is possible. Known as a cross-flow arrangement, the two fluids enter nominally perpendicular to each other. Heat exchanger classification can be extended further to take into account the number of passes the fluid makes. Automobile radiators, which are the main topic of this research, have historically had a cross-flow single-pass arrangement. This was primarily due to the location of the heat exchanger between the front grill and engine block.

Recent concern over climate change has forced automotive and race car manufacturers to focus on improved fuel efficiency in an effort to reduce the overall emissions from their vehicles. This has resulted in renewed interest in the drag characteristics of automotive cooling systems. This has prompted investigation into the optimum

location and geometry of the heat exchanger(s). The use of decorative grills and modern active vane systems have made it necessary to investigate heat exchanger behaviour when the air is not perpendicular to the coolant flow. In addition, race car manufacturers are restricted on the geometry and size of the overall vehicle, these restrictions often change between racing seasons, resulting in changes of both the location and geometry of the heat exchanger. An example of a race car radiator from a 2004 Ferrari Formula 1 car is shown in Fig. 1.2. There has therefore been an increase focus in correctly assessing the cooling capabilities of inclined radiators.

Figure 1.2 A 2004 Ferrari Formula 1 side panel with radiator [2].

Current heat exchanger performance is measured using either wind tunnel testing, numerical simulation or a combination of both. For both scaled wind tunnel testing and computational simulation, it is impractical to use a detailed radiator geometry. For scaled wind tunnel testing, laminations of porous sheets and honeycombs are used to mimic the flow through the core of a heat exchanger. For computational simulations, heat exchangers are usually represented as a discontinuity with a known pressure drop and heat transfer coefficient.

1.2 Engine Cooling Systems

Though highly optimised, modern internal combustion engines (ICE) generally only have a thermal efficiency of around 35-45% [3]. Thermal efficiency is defined as the ratio between useful mechanical power and the resultant unwanted heat generated. As a result, typically between 55-65% of the energy from the fuel is converted into heat and it is the job of the cooling system to dissipate this unwanted heat. Temperatures in the combustion chamber of an engine can reach up to 2500 °C, therefore if the engine goes without cooling even for a short period, the metal components can exceed their melting point [4]. This would result in serious consequences for the engine. Two approaches have been adopted to address this problem: liquid-cooled and air-cooled systems.

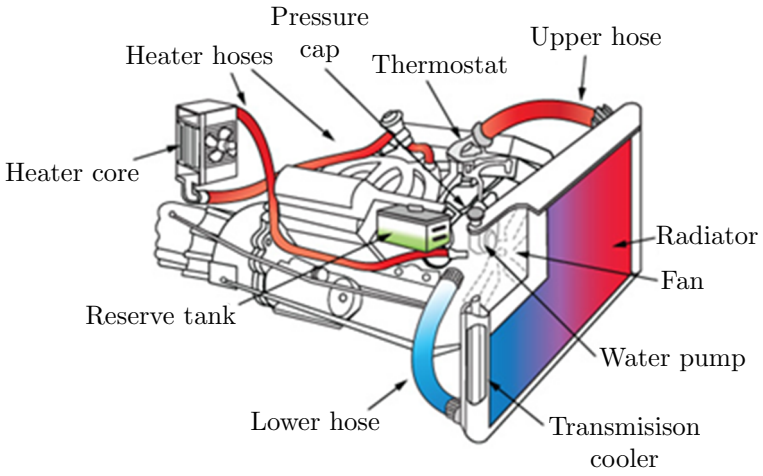

Figure 1.3 A typical liquid cooled internal combustion engine arrangement [5].

The air-cooled system can typically be found on older cars, with only a few modern motorcycles still using it. The engine is typically covered with fins to conduct the heat away from the cylinder. In addition, a powerful fan forces air over these fins, cooling the engine by transferal of heat to the air (forced conduction). Since most modern cars are liquid-cooled, this type of cooling system will be the main focus within this thesis. In a liquid-cooled system, the cooling fluid circulates through pipes and passageways in the engine as shown in Fig. 1.3. As this liquid passes through the engine it absorbs and removes the extra heat, thus cooling the engine. After the fluid leaves the engine, it passes through the radiator (the heat exchanger) which transfers the heat from the fluid to the ambient air.

Vehicles powered by internal combustion engines are designed to operate in a wide variety of conditions including extreme ambient temperatures. These tem-

peratures can vary from well below freezing to well over 38 °C. This leads to the need for a cooling fluid that has a very low freezing and a very high boiling point. Furthermore, the liquid needs to possess optimal thermal capacitance.

One such fluid is water, it is one of the most effective heat transfer fluids, however, its freezing point is too high for it to be used in ICE engines. For this reason the fluid used in most practical applications is a mixture of water and ethylene glycol ($C_2H_6O_2$), popularly termed as antifreeze. By adding ethylene glycol to water, the boiling and freezing points are changed significantly, as shown in Table 1.1.

Table 1.1 Boiling and freezing points of antifreeze at 1 atm (101.325 kPa) [6].

		$C_2H_6O_2/H_2O$			
	Pure Water	40/60	50/50	60/40	70/30
Freezing Point	0 °C	−24 °C	−37 °C	−52 °C	−64 °C
Boiling Point	100 °C	106 °C	108 °C	111 °C	114 °C

Even though addition of ethylene glycol can significantly increase the performance of the cooling fluid, the peak system temperature can still be between 121 °C and 135 °C and thus cause the fluid to boil. In order to raise the boiling point the cooling system can be pressurized. Most modern ICE cooling systems have a pressure limit of 14-15 pounds per square inch (psi) (96.5–103.4 kPa, respectively) which raises the boiling point by approximately another 25 °C [4].

1.3 Automotive Radiators

Radiators are the heat exchangers most often used for cooling internal combustion engines but they can also be used for cooling auxiliary systems. It is sometimes necessary for a car to be equipped with a second radiator to increase the cooling capacity when the size of the original radiator cannot be increased. Additionally, some engines have an oil cooler (a separate, smaller radiator) to cool the engine oil.

Cars with an automatic transmission often connect with additional pipework to the main radiator. This allows the transmission fluid to transfer its heat to the coolant in the radiator whilst preventing the mixing of the transmission and radiator fluids. Less commonly, power steering fluid, brake fluid, and other hydraulic fluids may be cooled by auxiliary radiators on the vehicle. Turbocharged or supercharged engines have an intercooler, which is an air-to-air or air-to-water radiator used to cool the incoming air charge, not to cool the engine.

The invention of the first automotive radiator is attributed to Karl Benz (the patent is shown in Fig. 1.4), while Wilhelm Maybach [7] is credited for designing the first honeycomb radiator for the Mercedes 35 hp. Early construction methods for the honeycomb radiators used round tubes swaged (typically through extrusion by force into a confining die) into hexagons at their ends, then stacked together and soldered [1]. As they only touched at their ends, this formed what became in effect a solid water tank with many air tubes through it.

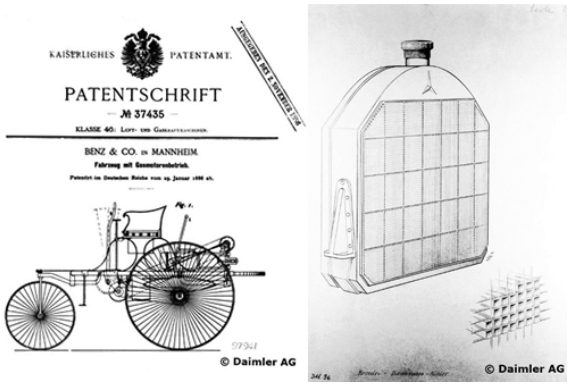

Figure 1.4 Karl Benz patent application for an automotive heat exchanger [7].

Modern radiators save money and weight by using either plastic or aluminium headers in conjunction with an aluminium core. They are constructed of a pair of header tanks, linked by a core with many narrow passageways (shown in Fig. 1.5), giving a high surface area relative to volume.

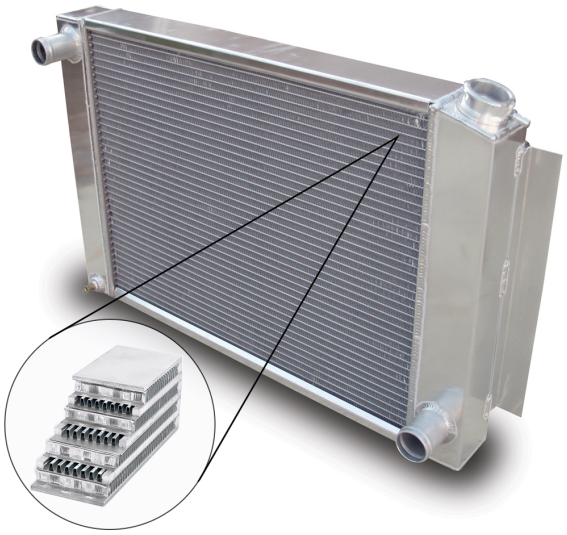

Figure 1.5 A typical aluminium automotive radiator [8].

This core is usually made of stacked layers of metal sheet, pressed to form channels and soldered or brazed together. The radiator transfers the heat from the fluid inside to the air outside, thereby cooling the fluid, which in turn cools the engine.

Radiators are typically mounted in a position where they receive airflow from the forward movement of the vehicle, such as behind a front grill. Where engines are mid or rear-mounted, it is common to mount the radiator behind a front grill to achieve sufficient airflow, even though this requires long coolant pipes. Alternatively, the radiator may draw air from the flow over the top of the vehicle or inside specifically designed air ducts.

1.4 Wind Tunnel Testing of Automotive Radiators

The primary function of the automotive radiator is to dissipate the heat produced by the vehicle's engine. This has to be achieved under a wide range of operating conditions in order to maintain the engine temperature within its optimal operating range. Failure to do so would lead to overheating problems and thus vehicle manufacturers carry out extensive testing prior to final production. Their evaluation methods are usually a combination of on-road and wind tunnel testing.

On-road testing offers direct assessment of the cooling performance under real road conditions. The repeatability of such tests, however, is often hard to achieve due to the constantly changing atmospheric conditions (wind velocity and air temperature) as well as variations in the terrain. On the other hand, wind tunnel testing of automotive radiators can be conducted in a predictable and controlled environment that provides a reasonable approximation to on-road conditions. In such cases, the primary requirement is to accurately reproduce the required pressure drop and flow deviation due to the heat exchanger element.

Perforated plates have been used to simulate the blockage effects of heat exchangers in wind tunnels, however, their characteristics have been found to be significantly different to those of full scale radiators [9]. Currently, the most common method of modelling a sub-scale radiator core is by use of a wire grid and honeycomb 'sandwich' [10]. The honeycomb core is important because it forces the flow to pass through the block in a purely axial direction as it would in an actual radiator core.

For a more detailed modelling of the radiator core flow it would be necessary to account for the difference in pressure drop arising due to thermal effects. This would require radiator testing with ambient and heated coolant. The addition of heat to the test models has been shown to play a significant role in the accurate replication of the full scale automotive radiator [11].

1.5 Project Aims and Objectives

The aim of this thesis is to investigate the thermo-fluid effects associated with modelling a subscale heat exchanger. This aim is divided into the two main areas of interest. Firstly, the use of porous materials to represent the pressure drop (ΔP) associated with a heat exchanger and secondly, the effect of heat transfer on this pressure drop.

The associated objectives derived from the aims of the project were separated into experimental and numerical objectives as follows:

Experimental

- To determine the relationship between the pressure drop (ΔP) and porosity (β) for porous media as a function of the angle of inclination (α).
- To investigate the relationship between pressure drop (ΔP) and inclination angle (α) for a full scale radiator and the effect of heat transfer on this relationship.
- To determine the effective porosity ($\beta_{\text{eff.}}$) required to account for the change in the pressure drop (ΔP) due to heat transfer.
- To investigate the heat rejection performance of the radiator as a function of the inclination angle (α).
- To calculate the pressure drops (ΔP) and heat transfer coefficients (h) required for numerical simulation.
- To investigate the mechanisms behind the increase in pressure drop (ΔP) due to heat addition.

Computational Fluid Dynamics

- To use the relationship between pressure drop (ΔP) and porosity (β) obtained from the experimental data to simulate porous media.
- To investigate the numerical methodology of simulating inclined porous media.
- To accurately simulate the aerodynamic and thermal properties of a full scale radiator.
- To simulate the effects of inclination on the numerical model.
- To simulate simultaneously developing hydrodynamic and thermal channel flow associated with a matrix channel within an automotive radiator.

1.6 Thesis Structure

The thesis is divided into six chapters and they are organised as follows:

Chapter 1 presents an introduction into the various types of heat exchangers and the methods used to wind tunnel test them.

Chapter 2 presents an overview of current published literature on automotive heat exchangers.

Chapter 3 investigates the effects of porosity and inclination on the pressure drop across gauzes and honeycombs.

Chapter 4 investigates the pressure drop and heat transfer properties of a full scale generic automotive heat exchanger.

Chapter 5 investigates the effect of heat transfer within a simplified channel from the matrix of an automotive heat exchanger.

Chapter 6 draws the overall conclusions of the thesis and provides scope for possible future work.

The references are located at the end of Chapter 6, with the appendices located at the end of the thesis. The appendices and are organised as follows:

Appendix A covers the governing heat exchanger equations used within the thesis.

Appendix B contains information on the experimental measurement techniques presented within the thesis.

Appendix C provides the mathematical background on the turbulence models used in the numerical simulations.

Appendix D contains additional material relating to the porous media used within Chapter 3.

Appendix E holds additional data on the full scale radiator used within Chapter 4.

Appendix F contains additional material relating to the radiator matrix channel flow experiment used within Chapter 5.

1.7 Publications

1.7.1 Journal Publications

K. Gerova, S. Velikov and K. Garry. The effects of porosity and inclination on the pressure drop across porous screens and honeycombs used for heat exchanger simulations in wind tunnel studies, *SAE International Journal of Passenger Cars - Mechanical Systems, 6(2):483-494, 2013*, doi:10.4271/2012-01-2340.

K. Gerova and A. Savill. On optimum choice of Forchheimer equation coefficients for Computational Fluid Dynamics simulation of heat exchangers, *SAE International Journal of Passenger Cars - Mechanical Systems, 8(2):779-785, 2015*, doi:10.4271/2015-01-9110.

1.7.2 Pending Journal Publications

K. Gerova and M. Savill. The heat transfer effects and pressure drop characteristics on an inclined generic automotive heat exchanger, *SAE International Journal of Passenger Cars - Mechanical Systems.*

K. Gerova, N.J. Lawson, J. Barden, M. Finnis and A. Savill. A wind tunnel and numerical study of the heat transfer effects for a scaled automotive heat exchanger, *International Journal of Heat and Fluid Flow.*

Chapter 2

Literature Review

2.1 Analytical Methods

There are a limited number of publications [12–16] that use analytical approaches to determine the performance of automotive heat exchangers. This is mainly due to the fact that these methods assume a uniform velocity distribution through the face of the radiator when, in fact, the distribution is rather complex and importantly, non-uniform.

There are two main approaches available for determining the performance of a heat exchanger:

- Log-Mean Temperature Difference (LMTD)
- Effectiveness-NTU method (ε-NTU)

A detailed explanation of these methods is given in Sections 2.1.1 and 2.1.2, respectively.

2.1.1 Log Mean Temperature Difference (LMTD)

The Log Mean Temperature Difference (LMTD) method is used to determine the temperature of the driving fluids within an internal combustion engine (ICE) vehicle radiator, assuming a constant flow rate and fluid thermal properties. It is a logarithmic average of the temperature difference between the hot and cold fluids at each end of the exchanger. The larger the LMTD, the more heat is transferred, the equation for LMTD is shown in Eq. (2.1), further details of this method have been presented in Section A.1 of Appendix A.

$$\Delta\theta_{\text{lmtd}} = US\frac{\Delta\theta_2 - \Delta\theta_1}{\ln\frac{\Delta\theta_2}{\Delta\theta_1}}. \tag{2.1}$$

After a series of publications on temperature differences within multipass heat exchangers [17, 18], Bowman et al. [12] published an overview paper. They attempted to present a simplified method for determining the true mean temperature difference from the log mean temperature difference for various flow and surface arrangements encountered in heat exchangers. They achieved this by means of correction factor plots.

Beard et al. [13] applied LMTD to the calculation of heat dissipation performance of different types of radiator core designs. The radiators were presented as cross-flow heat exchangers as suggested by Bowman et al. [12]. The authors compared their calculated values with those obtained from experiments. The results showed a maximum error of approximately 10% between experimental and calculated results.

2.1.2 Effectiveness-NTU (ε-NTU)

The LMTD method for heat exchanger analysis is applicable when the fluid inlet and outlet temperatures are both known. If this is not the case, then the LMTD method becomes iterative. In order to avoid this, the effectiveness-NTU (ε-NTU) approach can be used. This method involves the calculation of the Number of Heat transfer Units (NTU), effectiveness (ε) and the heat capacity ratio (C_r). Further details of this method have been presented in Section A.2 of Appendix A.

Emmenthal et al. [14] used the effectiveness (ε) operating characteristic in their method for designing liquid cooling systems. Furthermore, they deduced a criterion for rating different radiator matrix designs. Chiou [15] presented the effect of two-dimensional nonuniformity of the inlet temperature of the cooling air flow. The effectiveness of the engine radiator was calculated for a variety of designs and operating conditions. Relations between the correction factor for heat transfer effectiveness and NTU of the engine radiator were presented.

Eichlseder et al. [16] used the ε-NTU approach to investigate the influence of the size and type of radiator for their cooling system evaluation program. Fellague et al. [19] instead applied the NTU method for a subdivided heat exchanger where the radiator was divided into smaller cells which are effectively micro heat exchangers and the NTU method was applied to each cell.

2.2 Performance Assessment Methods

2.2.1 Air-to-Boil (ATB)

The Air-to-Boil parameter (ATB) has been widely used by automotive manufacturers as an indicator of the temperature limitations of the fluid in a cooling system

at a given operating condition. It is benchmarked by the Society of Automotive Engineers' (SAE) standards J819 [20] and J814 [21]; further details of this method are presented in Section A.3 of Appendix A.

The earliest work using the ATB parameter was in the Chevrolet Research Department. They developed a computer program for predicting engine cooling performance for a chosen radiator [22, 23]. The system's ATB temperature was used as the primary dependent variable for the mathematical model. Mosier et al. [24] applied a similar approach to multi-component systems consisting of: a radiator, oil cooler and condenser. Costelli [25] plotted ATB levels for each transmission gear, thus plotting a diagram known as an ATB gird.

Williams [26] studied the grille open area as a design parameter. By correlating it to the ATB he showed the grille area to be a poor predictor of ram airflow and cooling drag. Chapman et al. [27] measured the effect of the ram air velocity variation on the ATB values of a cooling system. The measurements showed an increase in the ATB values with an increase of ram air velocity.

Emmelmann et al. [28] outlines the relationship between an increase in frontal area opening and the ATB temperature. A very specific optimum front opening area was found, where no further improvements on the ATB could be made by simply increasing the openness of the frontal area. Ecer et al. [29] presented a methodology for predicting ATB temperatures. The velocity distribution over the radiator was found to be crucial in determining ATB. Additionally, the assumption of constant inlet air temperature appears not to produce significant errors in predicting ATB temperatures.

2.2.2 Specific Dissipation (SD)

The specific dissipation parameter (SD) initially appeared in publications by Stratton et al. [30] and later by Paish et al. [31]. In both publications the authors use it to express the heat transfer ability of a radiator matrix. No further publications became available until the late 80's and early 90's when the parameter was reinvented by independent research at the Royal Melbourne Institute of Technology (RMIT). Several studies carried out by Hird et al. [32] were aimed at investigating the effectiveness of the parameter for engine cooling system evaluation. Further details on the specific dissipation parameter are presented in Section A.4 of Appendix A.

Lin et al. [33] carried out a series of experiments in order to compare the performance parameters ATB and SD. The tests were performed at three different wind tunnel facilities: RMIT's closed-circuit wind tunnel, Monash University's full-scale (shown in Fig. 2.1) wind tunnel and Ford Australia Environmental Wind Tunnel. They found the SD to be insensitive to the variation of the air and coolant temperatures, thus enabling the SD to be used in both stable and slightly varying test

conditions.

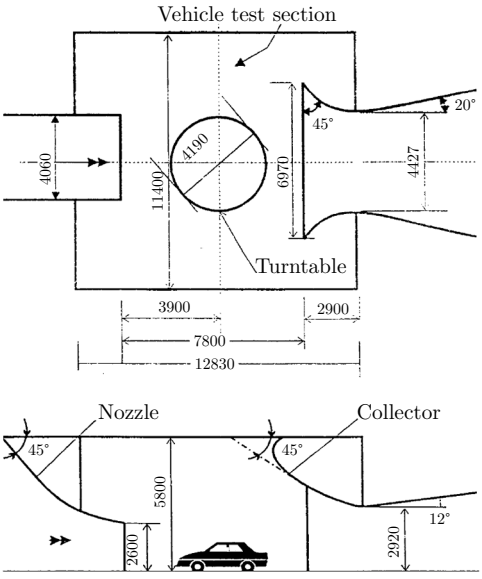

Vehicle test section

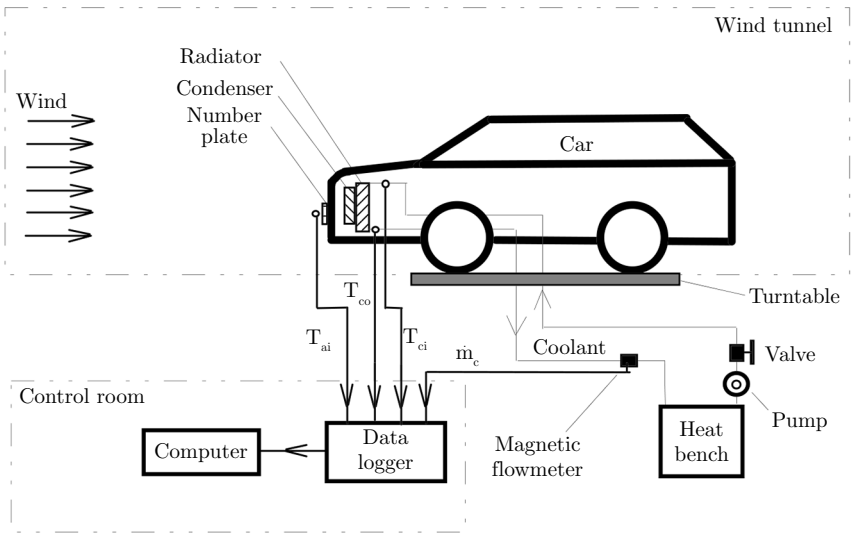

Car engine cooling system test layout

Figure 2.1 Monash University's vehicle test section and cooling system layout [33].

In other publications Lin et al. [34, 35] used SD to indicate the effect of cross wind, changes in ambient air temperature, coolant radiator inlet temperatures and coolant flow rates on the engine cooling of a full scale vehicle. As a result a theoretical model for the calculation of specific dissipation was developed.

Ng et al. [36] carried out series of on-road and wind tunnel tests to validate the process of evaluating vehicle cooling system performance. Comparisons were drawn between the SD measures on the road with those measured in the wind tunnel at high blockage (30%). Additionally, Ng et al. [37] also studied the influence of airflow distribution and different average core velocities on the Specific Dissipation.

2.3 Experimental Methods

Since there is a wide variety of experimental techniques available, for ease they have been split into velocity and pressure measurement approaches. Techniques that do not fit into these two classifications have also been included. Detailed description of the used experimental equipment is presented in Appendix B.

In terms of industry standards [38] it is useful to note that most North American manufacturers favour the use of propeller anemometers. Siemens NA, General Motors and Ford all use a variety of four, six or eight bladed anemometers with the exception of Chrysler-Jeep who use hot film probes.

European manufacturers on the other hand primarily use pressure measurement techniques. Mercedes-Benz uses a combined pitot-static pressure probe. The Motor Industry Research Association (MIRA) uses a technique based on a fixed array pitot and reverse-pitot tubes embedded inside the radiator core. Volvo uses micro-orifices to measure pressure differences.

2.3.1 Pressure Based Techniques

Oler et al. [39] investigated the factors affecting the cooling opening mechanical energy losses. In order to isolate this effect the design of the wind tunnel models used represented only the front portion of a car. A loss coefficient based on the change in total pressure between freestream conditions and the front face of the heat exchanger was established. Additionally, they found a relationship between the front end losses, cooling air flow rate, vehicle speed and the size and location of the openings.

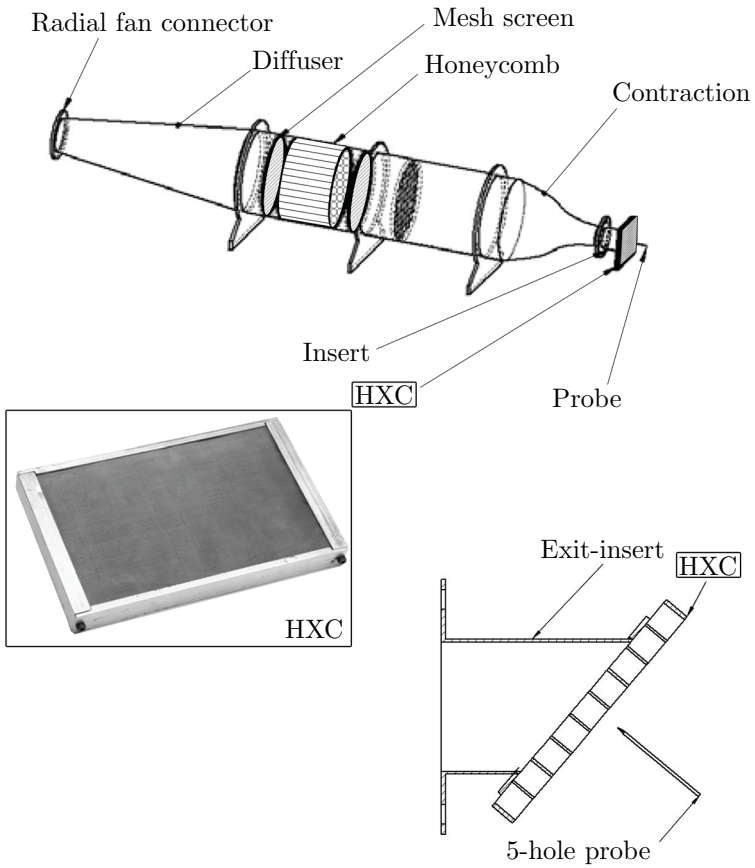

Figure 2.2 Experimental arrangement for the testing of a scale model heat exchanger [40].

Ruijsink [41] developed a microprobe system consisting of 48 pitot-static probes mounted inside the radiator matrix. The key advantage of the system was that it didn't protrude the front face of the radiator and thus had no influence on the inflow towards the radiator. He found that the gap between the radiator matrix and the tanks that exists in most radiators can account for up to 10% of air spill.

Using a 5-hole pitot tube Lyu et al. [42] investigated the flow rate and nonuniformity of the axial flow velocity entering a radiator. They found that the incoming flow splits into two around the upper and lower bumper. The flow interacting with the radiator is primarily from the lower opening under the bumper. Furthermore, Christoffersen et al. [40], using the same probe type (shown in Fig. 2.2), conducted flow angularity measurements. They found that the flow behind a heat exchanger consisted of multiple shear layers and wakes from the fins.

Both Schaub et al. [43] and Takahashi [44] used total pressure probes to measure

the total pressure on the exit face of a radiator. They demonstrated that the solid blockage created in wind tunnel testing differs significantly from the data obtained in free air experiments.

Browand et al. [45] experimentally determined the air flow through a cooling module consisting of: an air-conditioning condenser and engine radiator. They measured the stagnation pressure by means of small kiel probes located at a total of 32 points. They found a unique relationship between pressure drop and local flow velocity expressed as an exponential function.

2.3.2 Velocity Based Techniques

Olson [46] was the first to developed a testing technique using a rake of multiple vane anemometers for the purpose of determining the total airflow and airflow distribution through a cooling system heat exchanger. The test resulted in providing an objective measurement capability of airflow and allowed for the quantification of the airflow distribution as a function of various components (e.g. bumper, grille, fan and shroud).

Schaub [43] measured the flow velocities through a radiator with a 2 inch (50.8 mm) diameter vertical bank of six propeller anemometers. This was traversed horizontally to 8 positions across the exit face of the radiator core, giving an array of 48 sampling stations. They found that the indicated velocities were 6% larger than the average velocities and hence needed compensation.

Berneburg [47] used eleven air vanes capable of detecting reverse flow. He went on to note the importance of being able to detect the flow direction. According to his research, if the car was in a stop-and-go or hot-idle traffic there would be no ram airflow and thus the fans would be sucking back in hot air from the region around the engine.

In order to measure the air velocity across a radiator, Ap [48] employed five micro-propellers of 10 mm diameter fixed on an aluminium bar. Using this set-up, he scanned the radiator's surface and revealed that the air velocity distribution is rather nonuniform. Williams et al. [49] measured the radiator airflows using a radiator instrumentation package consisting of twelves vane anemometers (shown in Fig. 2.3), 4.5 inch (114 mm) in diameter. The obtained data was used to construct ram curves.

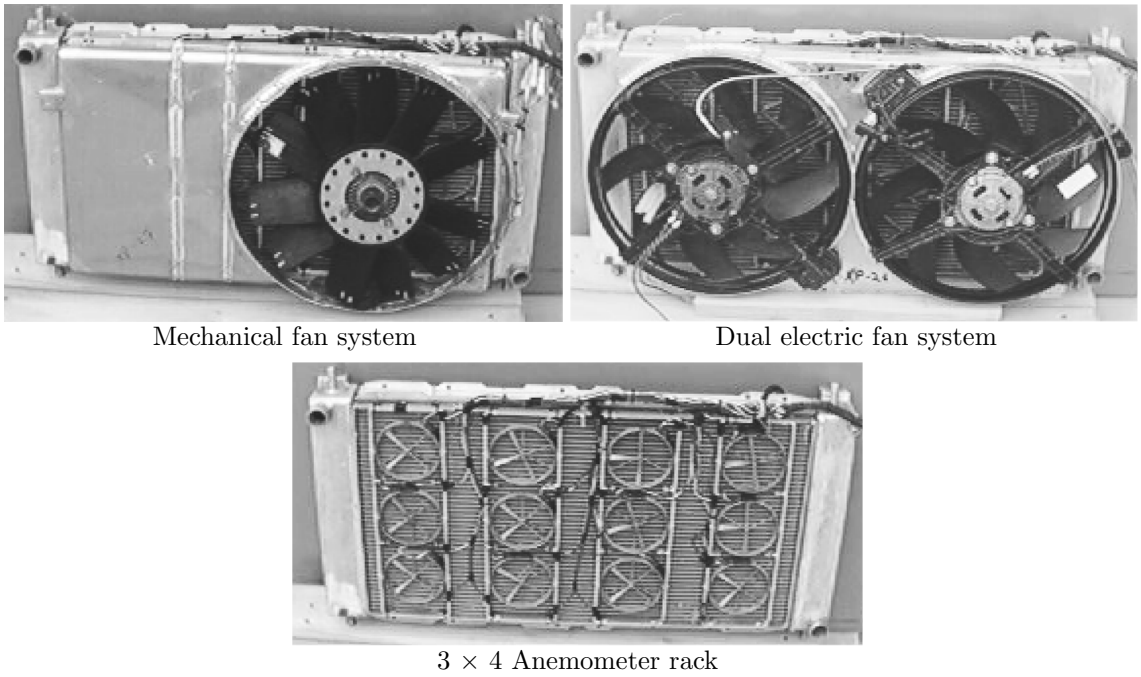

Figure 2.3 Vane anemometer mountings on mechanical and electrically cooled radiators [49].

Shimonosono [50] used a hot-wire probe to obtain an accurate picture of the flow state behind the cooling fan. They observed a slightly spiraling flow immediately behind the cooling fans. In this region the flow velocity is approximately $10\,\mathrm{m\,s^{-1}}$ compared to a $3\,\mathrm{m\,s^{-1}}$ flow velocity through the radiator. It was concluded that the fan rotation accelerates the flow velocity behind the radiator quite significantly.

Baxendale [51] obtained three-dimensional velocity measurements using a 2D cross-wire hot-wire probe. This was achieved by taking two readings at each measuring point with the probe rotated at 90° about its axis between readings. It was, however, noted that the validity of hot-wire measurements are subject to certain limitations. Since only the cooling effect of the airflow upon the hot wire is measured, the sensors could not distinguish between forward and reversed flows .

Chrysler [38] uses a variation of the hot-wire anemometer called a hot film probe. Using a fixed array of 15 hot film probes, they investigated the effect of distance between a condenser and the anemometer measuring plane. They found upstream blockage to have very little consequence with respect to accuracy of the measurements.

The Technical Development Centre of GM Europe [52] carried out an experimental test program using a two-component fibre-link laser velocimeter. They measured local velocities behind the radiator and the rear-fan shroud. They noted the diffi-

cultly of accessing the measuring point through the compacted engine compartment and the repeatability concerns of positioning the probe by hand.

Pharoah [53] used a two component Laser Doppler Velocimetry (LDV) system to study aerodynamic performance of a heat exchanger and shrouded fan and to provide validation data for Computational Fluid Dynamics (CFD) simulations. To allow for optical access of the LDV system, the fan's shroud was replaced with one made from plexi-glass. They managed to capture the highly three-dimensional flow through the cooling module.

2.3.3 Other Techniques

Fujikake et al. [54] developed a sensor to measure the air velocity distribution at the front of a radiator. Its main feature is that the output of the thermocouple is insensitive to the air temperature. This was achieved through the use of an anemometer and thermocouple, the thermocouples directly measured the temperatures of electrically heated wires cooled by the airflow velocity measured by the anemometer. As the cold junction of the thermocouple is at the same temperature as the airflow, the output of the thermocouple is insensitive to variations in the air temperature.

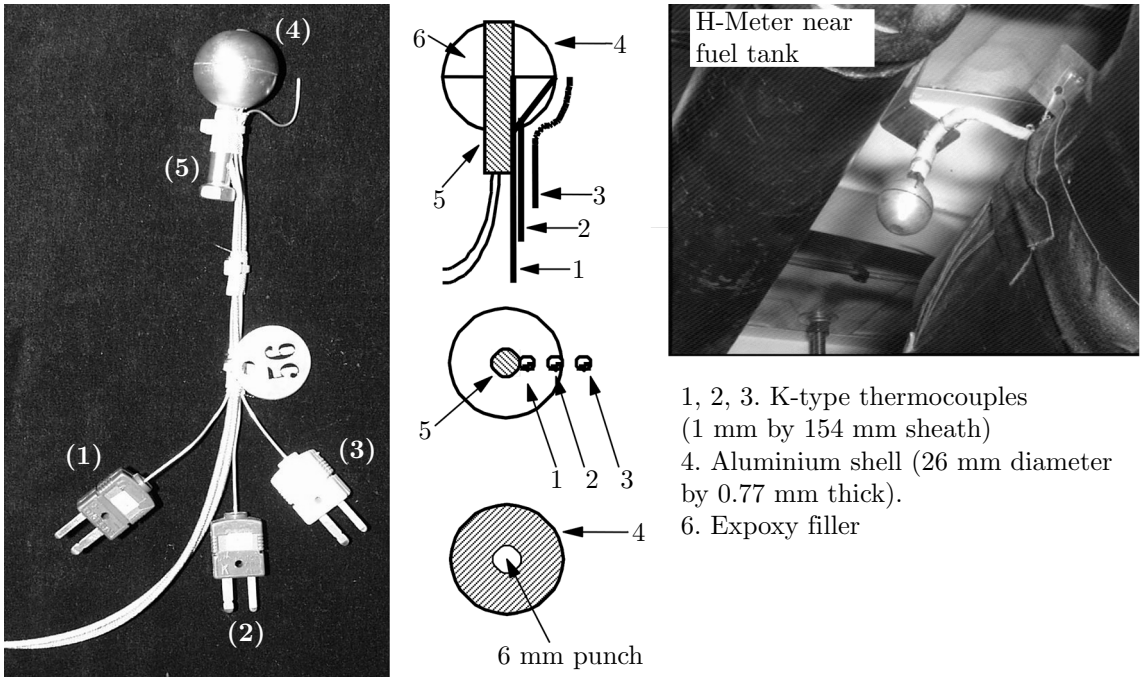

Figure 2.4 H-Meter design and example installation [55].

Dudley et al. [55] developed a 26 mm spherical transducer (H-meter, shown in

Fig. 2.4) to measures directly the local heat transfer coefficient in vehicle underhoods. The transducer contained three thermocouples and a battery powered heater. The spherical shape was chosen in order to be less sensitive to the flow direction.

Hoshino et al. [56] used a 3D smoke tunnel to improve the engine cooling performance qualitatively. They studied the airflow pattern approaching the radiator by visual observation of kerosene vapor injected 4 m ahead of the vehicle.

2.4 CFD Modelling

With the ever-increasing computational resources available to engineers, Computational Fluid Dynamics (CFD) has proven to be an integral tool in the study of cooling flows. Most commercial CFD solvers use Reynolds-Averaged Navier-Stokes (RANS) in conjunction with turbulence models. This is mainly due to the extensively available validation literature on turbulence models. A detailed description of RANS modelling is presented in Appendix C.

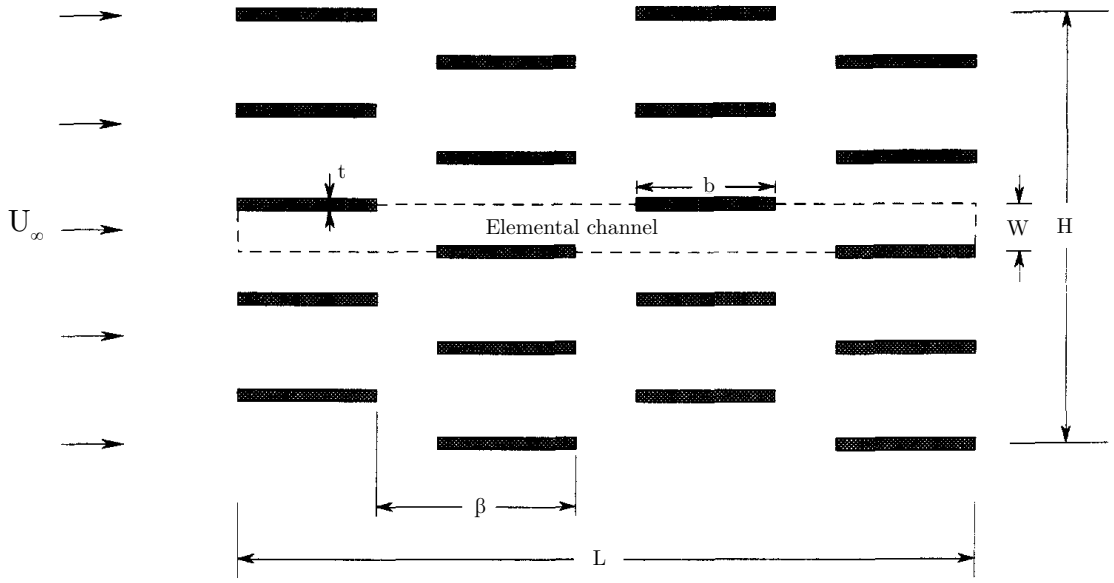

Figure 2.5 Numerical simulation of staggered parallel plates subject to forced convection [57].

Early research into heat exchangers was conducted by Fowler et al. [57], who used simplified representations of heat exchanger geometries in order to model the heat transfer numerically. They used an arrangement of staggered parallel plates in a fixed volume with forced convection heat transfer. The geometric arrangement

was varied by changing the plate spacing, number of plates and the degree to which the plates were staggered. They demonstrated that there exists an optimal spacing between two adjacent row of plates. An example of a simplified parallel plate heat exchanger geometry is shown in Fig. 2.5.

Notable early numerical work was also conducted by Bejan et al. [58–60], who investigated the optimum design and spacing of simple plate heat exchangers. With the increase in computation power over time, however, the ability to model more complicated geometry became feasible.

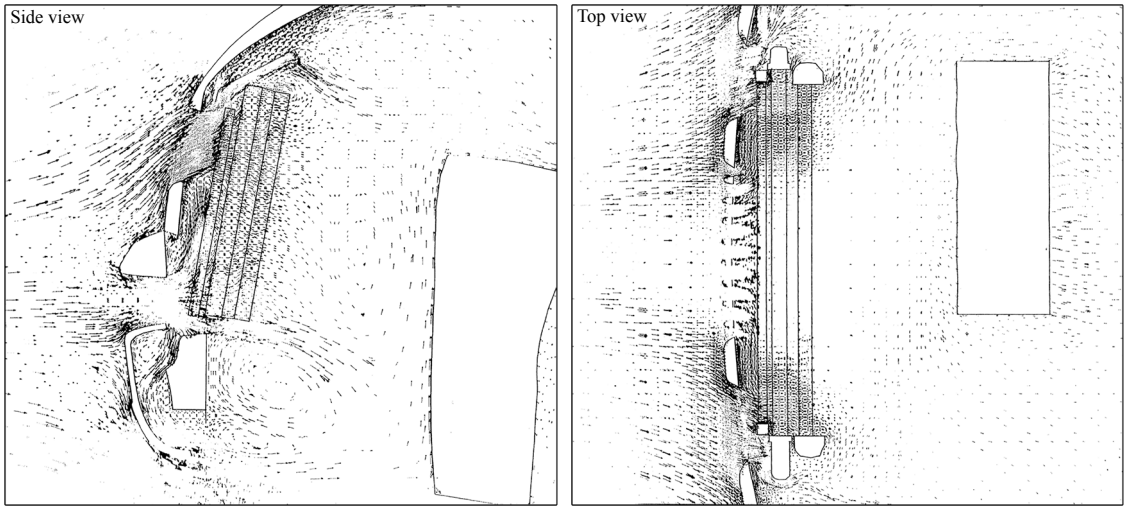

Figure 2.6 Velocity field within a radiator of a Daewoo van [61].

Yasuki et al. [62] used RANS simulations to predict the airflow through a radiator and condenser. They noted the reduced development cost and time by providing approximate results through use of CFD. Fellague et al. [19] developed a CFD algorithm for calculating the velocities and temperature distribution on the face of a radiator. Additionally, the program was developed to predict performance of new radiators based on experimental data from existing components.

Ecer et al. [29] used CFD software to calculate the air-velocity distribution and resulting Air-to-Boil (ATB) temperatures. Their objective was to show how CFD can be used in practical engineering tool to enhance the design process. They concluded that the velocity distribution over the radiator was found to be crucial in determining the ATB temperature. The assumption of constant inlet air temperature appeared not to produce significant errors.

Pervaiz et al. [63] used the commercial code STAR-CD® to model refrigerant in a condenser. Both fluids were numerically solved using the $k - \varepsilon$ turbulence model while accounting for the phase change the refrigerant goes through.

Haidar et al. [61] used CFD to investigate the modelling of under-bonnet flows (shown in Fig. 2.6) and more specifically the volume flow rate entering the cooling pack. This was achieved using the $k - \varepsilon$ turbulence model with integrated wall functions. They found that the inclusion of an engine bay under-tray reduces the volume flow rate through the cooling pack by approximately 30-40%.

Williams et al. [64] studied 23 vehicle front-end configurations at 4 non-idle operating conditions. Both numerical simulations and experimental wind tunnel testing was carried out to validate and quantify the accuracy of the in-house CFD code (UH3D) used by Ford.

Beamer et al. [65] investigated flow characteristics of automotive heat exchangers with multilouver fins, shown in Fig. 2.7. The primary goal of this project was to confirm the flow and heat transfer enhancement mechanisms due to the use of multilouver fins. Steady state 2D laminar analysis was conducted alongside experimental validation. They concluded that the flow mechanism responsible for the heat transfer and flow efficiency was the boundary layer growth along the louvers.

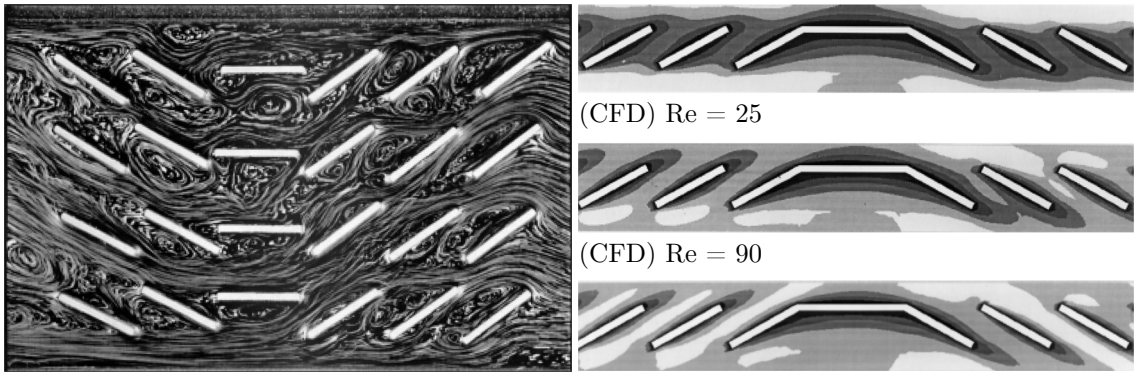

Figure 2.7 Experimental and numerical simulation of multilouver fins [65].

Andra et al. [66] compared two underhood models (shown in Fig. 2.8) in an attempt to study the effect of boundary and geometry specifications on the numerical simulation of a front-end cooling system. The simplified model was to be used in the early design stages when most of the component locations would still be unknown. A box like engine was used so that it provided the necessary blockage at the exit of the cooling fans. The simulation were run using the commercial code ANSYS® FLUENT®. The RANS $k - \varepsilon$ turbulence model was used with a uniform velocity profile. The results showed that the difference in flow rates between the two cases remains practically constant at all speeds.

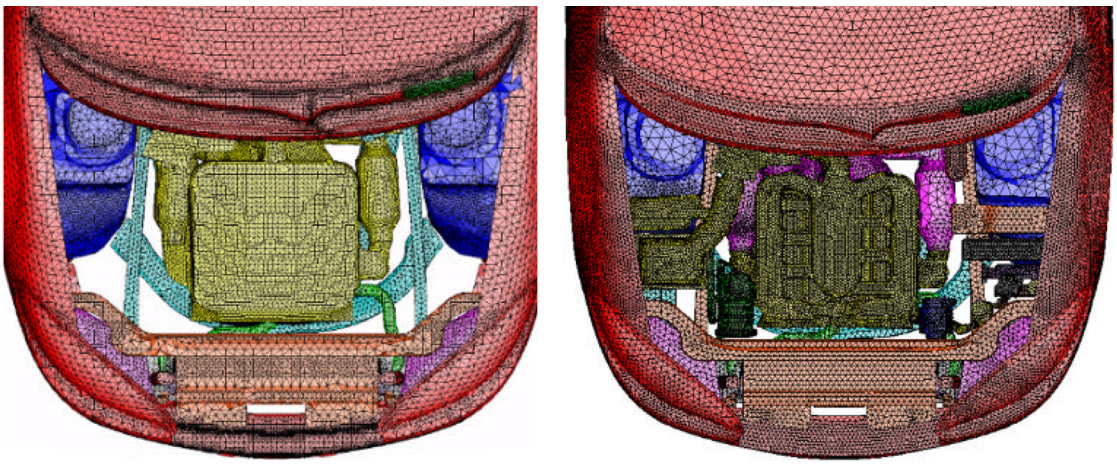

Simple model Complete model

Figure 2.8 Numerical simulation of front-end cooling [66].

Lee et al. [67] developed a 3D radiator model for computational purposes that accounts for the non-uniformity effects of air velocity distribution across it. The heat exchanger was modeled as a porous medium, while a rotating reference frame was used for the cooling fans. They concluded that the non-uniformity increases with vehicle speed. Furthermore, the non-uniformity decreases the heat transfer of the radiator, increasing the coolant temperature. They demonstrated the importance of including non-uniformity effects for more accurate CFD predictions.

Due to the complex geometry of louvered fins, it was not possible for Uhl et al. [68] to model the air-side of a heat exchanger in detail. A porous medium was therefore used for the core of the heat exchanger to simulate the pressure drop. The measurements of the porous media coefficients for the calculations were obtained experimentally.

Shome et al. [69] used CFD to predict the air-to-boil (ATB) temperature of a Sport Utility Vehicle (SUV) radiator. The predicted ATB values were compared with experimental data obtained from outdoor cooling trials. A detailed CFD model was used that included the under-hood engine compartment components, the front end cooling modules, the front grill and bumper. The CFD predicted values and the experimental data agreed to within 3–5 °C for the operating conditions tested.

Christoffersen et al. [40] used CFD to compare a simplified heat exchanger model to a full scale unit. It was shown that despite the two heat exchangers being the same dimension, the lack of modelling of the fin geometry on the simplified model lead to a lack of accuracy in capturing the flow physics through the heat exchanger.

2.5 Chapter Conclusions

Due to the high cost of full scale wind tunnel testing during the developmental stages of both road vehicles and race cars, subscale model testing is often used. It is therefore of vital importance that the scale models accurately capture the flow characteristics of the full scale components. As the cooling package is one of the largest contributors to the overall vehicle drag, it is essential that the heat exchanger is accurately represented in model form. Due to limitations in manufacturing techniques, however, it is impractical to make a scaled heat exchanger and instead, a simplified representation of the heat exchangers is often used.

Scaled heat exchangers are frequently represented by combination of laminations of porous sheets and honeycombs. The porous screens provide the needed pressure drop across the heat exchangers while the honeycombs act as flow guides. One element that is often neglected when scaling down a heat exchanger is the fin geometry, this is omitted due to their small size (at full scale) and fragile nature. The fins, however, play an integral part in the heat transfer and therefore their effect must be accounted for when scaling.

In order to maintain maximum similarity between the full and sub scale heat exchangers, one must account for the variation in the flow field due to the geometry simplification. In addition, road vehicles and race cars often incline the heat exchanger adding further complexity in the requirements of modelling at subscale.

Previously published literature deals mostly with the flow characteristics on the face and through full scale heat exchangers. There are detailed studies of the effect of both front end vehicle configurations and fan geometries. Little research, however, has been conducted into the flow through scaled heat exchangers and more specifically, their representation at subscale by porous screens.

The purpose of this research is therefore to investigate, in detail, the pressure drop properties of porous screens and the effects of inclination. Additionally a study of the thermal effect of a full scale radiator and the resulting choice of subscale representation is investigated.

Chapter 3

Subscale Heat Exchangers

The modelling of heat exchanger air flow characteristics in a wind tunnel at sub-scale (smaller than full-scale), as well as for numerical simulation, requires an accurate representation of the full-scale pressure drop (ΔP) and flow physics across the heat exchanger. Sub-scale heat exchangers in wind tunnels are normally represented using a combination of laminations of various porous materials and honeycombs [10].

In view of this, a series of experimental and computational measurements of the pressure drop (ΔP) across screens with porosities (β) in the range $0.41 \leq \beta \leq 0.76$ were investigated. The aim was to establish a relationship between the porosity and the pressure drop characteristics of a given material at various angles of inclination (α) to the free-stream flow.

Additionally, the present chapter investigates the use of weighted least squares regression to correct the obtained Forchheimer equation coefficients. It was found that the residual errors associated with the data were a function of the underlying experimental measurements.

3.1 Introduction

The flow of fluid through porous screens is of engineering interest due to the wide range of applications including membrane permeability in the biomedical industry [70], insect entry into greenhouses [71], and flow control in wind tunnels [72].

The specific application of interest in this chapter is the use of laminations of porous sheets and honeycombs to facilitate a sub-scale simulation of the complex geometry of a heat exchanger in wind tunnel studies. In such cases, the primary requirement is to accurately reproduce the required pressure drop and flow deviation due to the heat exchanger element.

It is normal practice, particularly in race car applications and occasionally in conventional passenger cars, for the heat exchanger element to be inclined relative

to the flow within an internal duct. This has the effect of increasing radiator size without impacting on vehicle frontal area. There is clearly a compromise between heat exchanger size and the reduced aerothermal performance in terms of both effective local velocity component and the increased free stream pressure change (resulting in aerodynamic drag).

Previous investigations of the flow through porous materials have been performed by experiments in wind tunnels as well as by numerical simulation. These have mainly involved the measurement of the pressure distribution and flow visualization around porous screens and gauzes. The first of such was carried out by Taylor [73] with the study of the theoretical relationship between gauze porosity and drag. Subsequently, Taylor et al. [74] extended their study to the air resistance of perforated sheets, gauze and fabrics. Schubauer et al. [72] conducted a series of experiments dealing with the pressure drop and streamline deflection of damping screens for angles of inclination up to 45°. They showed that the pressure drop is only a function of the solidity of the screen and the velocity component normal to it. They also found that the deflection of the streamlines depended solely on the resistance coefficient of the screen.

Baines et al. [75] conducted analytical and experimental studies on the relative pressure drop as a function of screen form and porosity, the capacity of screens to modify the velocity distribution around itself and the resulting characteristics of turbulence produced. Carrothers et al. [76] summarized all the available correlations for the pressure drop coefficients through wire mesh screens and textile nettings.

Further studies of flow in the wakes of perforated plates and gauze screens were carried out by Reynolds [77], who set up a mathematical model to predict the deflection of the flow passing through gauzes. Koo et al. [78] proposed a mathematical model which replaces a screen with a distribution of velocity sources. Their experimental and numerical data showed good agreement for the velocity profiles downstream of the gauze. O'Hern et al. [79] numerically studied flow downstream of fine-mesh screens. They found that the recirculating region behind the screen is found to grow almost linearly with Reynolds number.

Brundrett [80] formulated a new general correlation equation for pressure drop through woven wire and cloth screens for incompressible flows. He furthermore quantified the errors produced by screen porosity variation due to manufacturing tolerances, local screen damage or variable tension created during installation.

Miguel [81] investigated airflow characteristics of a number of screening materials. Based on the obtained results he concluded that the shape of the yard and mesh geometry have a negligible influence on the airflow characteristics of screening materials. Ito et al. [82] carried out a series of open-jet wind tunnel tests to obtain the static pressure near a 2D plane gauze for a range of angles of inclination. Additionally they visualized the flow pattern through the gauze using a smoke wind

tunnel.

More recently, O'Neil [83], used a source panel method, investigated the different singularity flow models available to describe the time-mean flow field through and around finite screens. Dong et al. [84, 85] used scaled wind tunnel simulations to study the mean flow regimes behind fences with varying porosities at different wind velocities. They further extended their investigation to the turbulent fields behind upright porous fences.

Valera et al. [86] evaluated the geometrical characteristics and airflow resistance of upright insect-proof screens. Based on obtained pressure drop coefficients, they proposed an overall governing equation for the relationship between the porosity of the screen and Reynolds number of the airflow. Teitel et al. [71] investigated the effect of screen inclination on the flow parameters behind porous screens. They found that at 90°, the air velocity profile was constant with height, while upon inclination of the screen to 45°, the velocity increased with height. Conversely for 135°, the velocity decreased with height.

Teitel et al. [71, 87, 88] also investigated the effect of screen inclination on the flow parameters behind porous screens using Computational Fluid Dynamics (CFD). Furthermore, they compared the simulation of the flow through a realistic woven screen and that through the porous media approach.

In the present chapter, porous materials are investigated specifically in relation to their applicability to model heat exchanger elements in sub-scale wind tunnel and in computational simulations. The aim being to establish a relationship between the porosity (β) and the pressure drop (ΔP) characteristics of a given material at various angles of inclination to the free-stream flow (α).

3.2 Mechanics of the Fluid Flow through Porous Media

The first investigation into flow though porous media was carries out by French scientist Henry Darcy in his study of hydrological systems for water supply in the city of Dijon [89]. He performed steady-state unidirectional flow experiments for a uniform sand column. Based on his experimental observations he proposed what we know today as Darcy's Law given by

$$u = \frac{K}{\mu}\frac{\partial P}{\partial x}, \tag{3.1}$$

where μ is the dynamic viscosity and K is the permeability, P the static pressure and x the direction of flow. It is valid for creeping isothermal laminar fluid flow with Reynolds number less than 1.

For Reynolds numbers larger than 10, however, a breakdown in linearity is observed [90]. Austrian scientist Phillip Forchheimer investigated fluid flow through porous media in this higher velocity regime. During his study, he observed that as the flow velocity increases, the inertial effects started dominating the flow [91]. In order to account for these higher velocity effects, he suggested the inclusion of an inertial term representing the kinetic energy to Darcy's Law. Forchheimer's equation was obtained experimentally and is given by

$$\frac{\partial P}{\partial x} = \frac{\mu}{K}u + \rho\left(\frac{Y}{K^{1/2}}\right)u^2, \tag{3.2}$$

where ρ is the fluid density, μ is the dynamic viscosity, K is the permeability, Y the inertial factor and u is the velocity normal to the porous face.

The permeability (K) of a porous medium represents the ability of fluids to flow through the material and is an intrinsic property of the material. It should not be confused with porosity (β) which is measure of the open space in a material, and is a fraction of the volume of open area over the total area [92]. Permeability is measured in (m^2), while porosity is nondimentional.

The permeability and inertial factor can be obtained by equating a second order polynomial to Forchheimer's equation [71, 81, 86, 93, 94], given by

$$\Delta P = Au^2 + Bu, \tag{3.3}$$

where the permeability (K) and inertial factors (Y) are given by

$$K = \frac{\mu\Delta x}{B} \qquad \text{and} \qquad Y = \frac{A\sqrt{K}}{\Delta x\rho}. \tag{3.4}$$

Brundrett [80] formulated a new general correlation equation for pressure drop through woven wire and cloth screens for incompressible flows using a pressure loss coefficient (K_θ), given by

$$\Delta P = 0.5K_\theta\rho u^2, \tag{3.5}$$

where,

$$K_\theta = \cos^2\theta\left(\frac{1-\beta^2}{\beta^2}\right)\left[\frac{\sigma_m}{\sigma_k}\frac{7.125}{\mathrm{Re}\cos\theta} + \frac{0.88}{\log(\mathrm{Re}\cos\theta + 1.25)}\right] + 0.055\log(Re\cos\theta). \tag{3.6}$$

Miguel [81] investigated the airflow characteristics of a number of screening materials. Based on the obtained results he concluded that the shape of the yard and mesh geometry have a negligible influence on the airflow characteristics of screening

materials. Additionally, he proposed equations that relate the screen permeability (K) and inertial factor (Y) to the screen porosity (β)

$$K = 3.44 \times 10^{-9}\beta^{1.6} \qquad \text{and} \qquad Y = 4.3 \times 10^{-2}\beta^{-2.13}. \tag{3.7}$$

Valera et al. [86] evaluated the geometrical characteristics and airflow resistance of upright insect-proof screens. Based on obtained pressure drop coefficients, they proposed an overall governing equation for the relationship between the porosity of the screen and Reynolds number of the airflow. Different correlations were suggested for the screen permeability and inertial factors as a function of the porosity

$$K = 5.68 \times 10^{-8}\beta^{3.68} \qquad \text{and} \qquad Y = 5.67 \times 10^{-2}\beta^{-1.1604}. \tag{3.8}$$

Flores-Velazquez et al. [95] suggested yet another relationship between Y and K, based on previously published data

$$K = 2.0 \times 10^{-7}\beta^{3.3531} \qquad \text{and} \qquad Y = 0.342 \times 10^{-2}\beta^{-2.5917}. \tag{3.9}$$

3.3 Experimental Methodology

The purpose of this study is to obtain pressure drop (ΔP) data across screens of various porosities (β) at varying angles of inclination (α). This was achieved using a blower wind tunnel with the porous screen fixed to the working section so as to cover its entire cross section. A render of the fore-mentioned wind tunnel set-up is presented in Fig. 3.1. Sections 1 and 2 are fixed while 3 and 4 are varied depending on the angle the mesh is positioned at. A schematic of the wind tunnel along with the variations used within the experiment are shown in Sections D.3 and D.4 of Appendix D.

The reference pressure is measured far upstream of the mesh through a ring of static pressure tappings. Static pressure measurements are carried out at the centreline of the working section both upstream and downstream of mesh, in effect measuring a 2D flow. For 0° inclination the readings are pneumatically averaged values of the wind tunnel floor and ceiling tappings, while at all other angles they are taken as individual measurements closer to the mesh and as pneumatic averages further out. Furthermore, two pneumatically averaged side tappings were used on each side of the mesh to obtain readings immediately across the mesh.

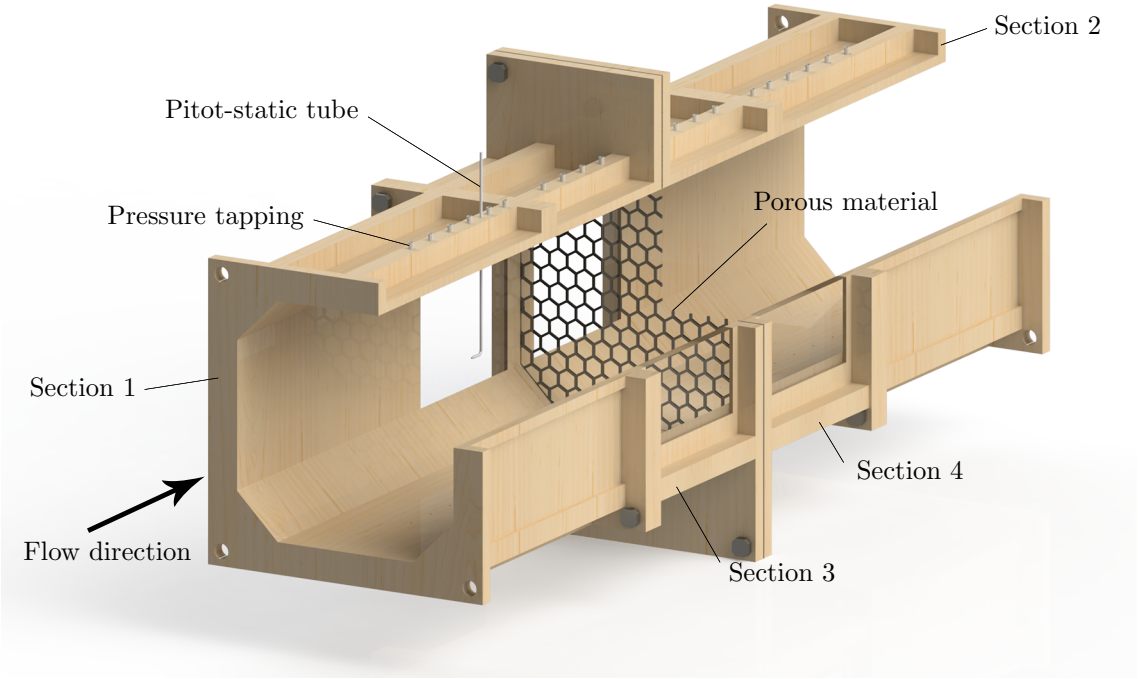

Figure 3.1 Render of Cranfield University's blower wind tunnel working section.

The pressure tubes from the static, pitot-static and reference ring pressure tapping were connected to OMEGA® PX 139 pressure transducers. The relative error of the pressure transducers specified by the manufacturer is ±0.3% of the pressure measurement. A detailed error analysis can be found in Section D.7 of Appendix D.

The transducers were also connected to the input channels of the National Instruments™ data acquisition (DAQ) hardware. The PC used for the data acquisition uses a National Instruments™ DAQ card with LabVIEW™ software. A custom DAQ program was written for the tests.

The wind tunnel measurements were conducted at 0°, 15°, 30° and 45° angles of inclination. The wind tunnel velocity was measured with a centre line pitot-static tube at 113.5 mm from the working section floor. The wind tunnel speed varied between 3 m/s and 35 m/s. The velocity profile in the empty working section was measured at the lateral centreline and was found to be uniform (within ± 1% of the mean value) for more than 90% of the working section height (see Section D.5 of Appendix D).

For this experiment materials with porosity (β) between 0.76 and 0.10 were tested. Most of the materials used had manufacturer data for their porosity. For ones without, the porosity was calculated by first capturing images of the samples with a microscope, then they were converted from true colour to black and white

using Pixcavator IA 4.2. The program measured the porosity as the ratio of black and white pixels. Porosity (in percentage) was defined as

$$\text{Porosity}(\beta) = \left[\frac{(\text{open screen area})}{(\text{complete screen area})}\right](\%). \tag{3.10}$$

Thus, values can be vary between 100% (theoretically) and 0% (solid flat plate) with a measurement tolerance of approximately ± 0.03%.

Several runs were performed with materials of porosity between 35% and 10%. For these porous screens severe blockage effects occurred as the fan speed was increased and the flow stagnated causing a pressure to build up extending backwards to the fan. Due to this effect measurement speeds with these materials could not exceed 7 m/s and further tests with these materials were abandoned.

To evaluate the global pressure drop variation with porosity and angle of incidence, the value of ΔP was taken between both ends of the wind tunnel to exclude the previously described effects of inclining the screen on the pressure distribution at the top and bottom of the wind tunnel. For the purpose of non-dimensionalising the data obtained, a pressure drop coefficient was introduced as follows

$$\frac{\Delta P}{q} = \frac{(\text{ pressure drop across screen})}{(\text{dynamic pressure in working section})}. \tag{3.11}$$

Assuming an average thickness of 1 mm for the tested meshes in the current experiments, the Reynolds number range is between approximately 400 (7 m/s) and 2000 (35 m/s).

Several runs have been performed to verify the repeatability of the obtained data. Additionally, repeatability tests were run in order to identify whether the side pressure tapping readings are affected by the positioning of the meshes. The results are presented in Section D.6 of Appendix D. The results show good repeatability. Furthermore, error analysis was performed (see Section D.7 of Appendix D) for a sample porosity (β) value of 50%.

3.4 Numerical Simulation Methodology

The porous jump media approach is widely used in simulating screens in Computational Fluid Dynamics (CFD). When the Navier-Stokes equations are solved numerically the source term in the momentum equation is replaced by Forchheimer's equation, shown in Eq. (3.12).

Porous jump conditions in ANSYS® FLUENT® 15.0 are used to model thin membranes with known velocity vs. pressure-drop characteristics. It is a 1D simplification of a porous media model and is used for modelling pressure drops through

screens and filters when not concerned with heat transfer. The porous-jump zone must be modelled as the interface between cells, a type of internal face zone.

The thin porous medium has a finite thickness over which the pressure change is defined as a combination of Darcy's Law and an additional inertial loss term [96].

$$\Delta P = -\left(\frac{\mu}{\alpha_f} v + C_{2f} \frac{1}{2} \rho v^2\right) \Delta m, \tag{3.12}$$

where μ is the laminar fluid viscosity, α_f is the permeability of the medium, C_{2f} is the pressure-jump coefficient, v is the velocity normal to the porous face and Δm is the thickness of the medium.

In order to determine the inputs for the porous jump, Eq. (3.12) needs to be fitted through the pressure drop vs. velocity graph, given by

$$\Delta P = Av^2 + Bv. \tag{3.13}$$

Once this is plotted the values of C_2 and α can be found through Eqs. (3.14) and (3.15)

$$A = C_{2f} \frac{1}{2} \rho \qquad \text{and} \qquad B = \frac{\mu}{\alpha_f}, \tag{3.14}$$

$$C_{2f} = \frac{2A}{\rho \Delta m} \qquad \text{and} \qquad \alpha_f = \frac{\mu \Delta m}{B}. \tag{3.15}$$

Further information about the numerical simulation methodology is presented in Section D.12 in Appendix D.

3.5 Porous Material Results

3.5.1 Effect of Screen Porosity and Inclination on Pressure Drop

Idelchik [97] describes the pressure drop coefficient ($\Delta P/q$) of barriers distributed uniformly over tube or duct cross-sections to be dependent on their porosity (β), shape (holes arrangement) and flow Reynolds number (Re). Data included in Hou et al. [98] for screens of various shape and porosity suggests that $\Delta P/q$ becomes independent of Reynolds number (based on free-stream velocity and screen thickness) for Re > 500.

The variation of $\Delta P/q$ with velocity for 0–45° screen inclination is shown in Fig. 3.2. It is evident that for materials with a porosity (β) greater than 0.50,

$\Delta P/q$ becomes virtually independent of Reynolds number for Re $\geq$ 500 ($v \sim 8$ m/s) regardless of the mesh inclination (α), which is in good agreement with Idelchik [97].

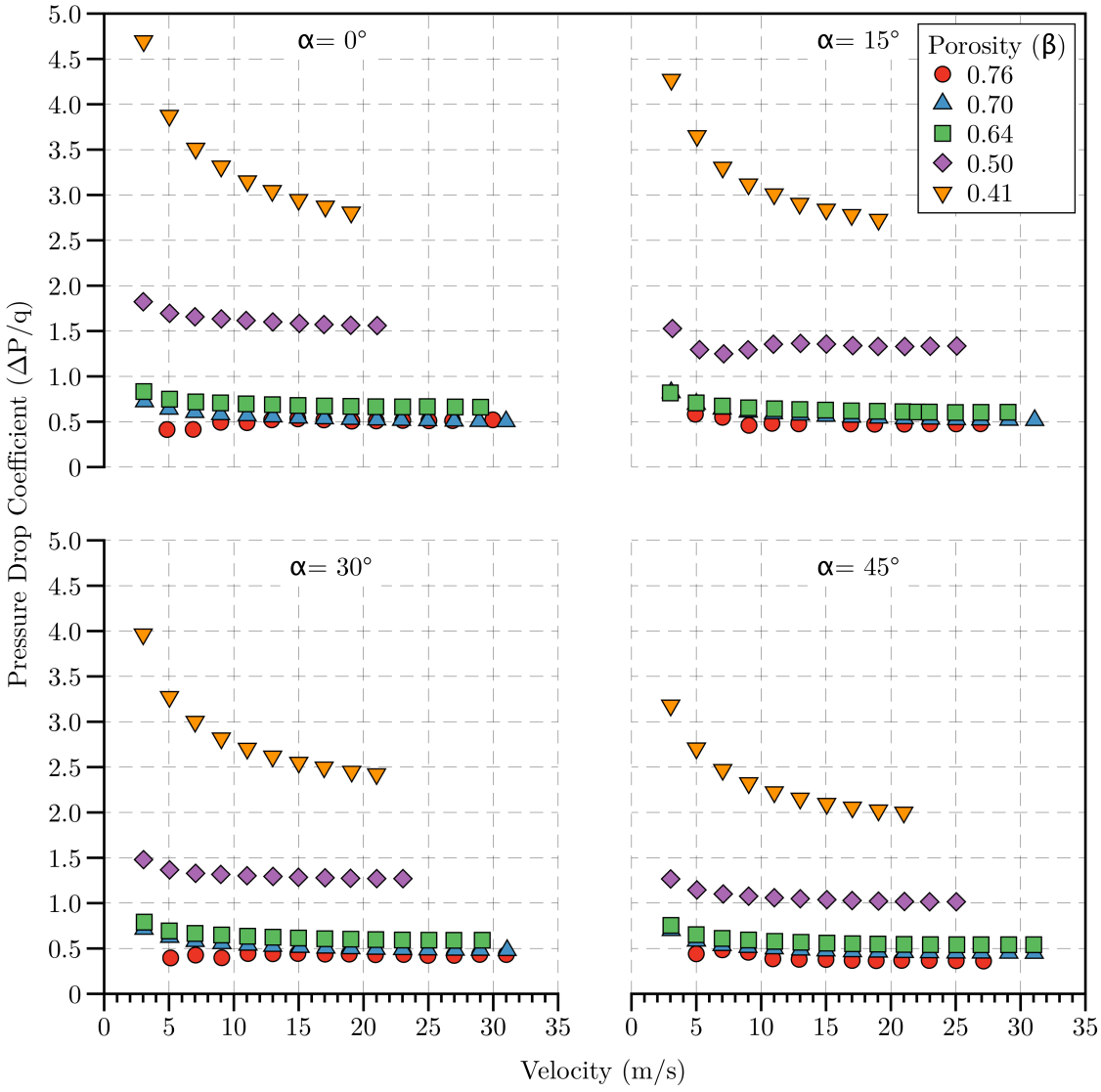

Figure 3.2 Pressure drop coefficient ($\Delta P/q$) variation with velocity (v) and angle of inclination (α).

The pressure drop coefficient ($\Delta P/q$) variation for $\beta = 0.41$ shows a tendency to become constant at higher speeds outside the tested range. For a given porosity, $\Delta P/q$ reduces with angle of inclination, thus inclining the screen would reduce its aerodynamic loading. As evident from Fig. 3.2, this effect increases with increased

angle of inclination. For example, at Re $\sim$ 1280 (v = 19 m/s) the pressure drop coefficient for $\beta = 0.41$ is reduced only by 1.6% between 0° and 15°, whereas between 0° and 45° the reduction is 39%.

Comparing the screens of high porosity ($\beta > 0.60$), only small differences in their pressure drop coefficient ($\Delta P/q$) variation with free-stream velocity and mesh inclination (α) are evident. Changes in the inclination have a considerably smaller effect on $\Delta P/q$ compared to materials of 0.50 and 0.41 porosity.

The measured variation of pressure drop coefficient with porosity for each screen inclination is shown in Fig. 3.3. For Re > 450 and porosity range of $0.40 < \beta < 0.80$, the pressure drop coefficient was found to vary with the power of the screen porosity as follows

$$\frac{\Delta P}{q} = C_1 \beta^{(C_2)}, \tag{3.16}$$

where the proportionality constant C_1 and the exponent C_2 vary with screen inclination.

These were obtained using exponential curve fitting of the form in Eq. (3.3) on page 28 and are given in Table 3.1 for each inclination angle (α) tested. The complete equations and their corresponding coefficients of determination R^2 are shown in Fig. 3.3.

Table 3.1 Proportionality and exponential coefficients ($\Delta P/q$) for the variation of pressure drop coefficient with porosity (β).

α (°)	α (rad)	C_1	C_2
0	0	0.192	-3.048
15	0.262	0.193	-2.902
30	0.524	0.182	-2.912
45	0.785	0.177	-2.699

Between 0° and 45°, the coefficients C_1 and C_2 show the following 3$^{\text{rd}}$ order polynomial relationships with the angle of inclination

$$C_1 = 0.167\alpha^3 - 0.219\alpha^2 + 0.050\alpha + 0.192, \tag{3.17}$$

$$C_2 = 3.520\alpha^3 - 3.903\alpha^2 + 1.338\alpha - 3.048, \tag{3.18}$$

where α is in radians. It should be noted that at the lower end of the screen porosity range ($\beta \approx 0.40$), the pressure drop coefficient does not become completely independent of Reynolds number (Re) within the range tested. Consequently, the accuracy of the empirical relationships, shown in Eqs. (3.16)-(3.18), decreases for screens of such porosity. Additionally, it is evident that the mathematical relationships identified are not representative towards the low ($\beta = 0$) and high ($\beta = 1$) ends of the porosity range. In the latter case, where no screen material is present, the pressure drop should be theoretically zero, yet they yield a small positive value for $\Delta P/q$, equal to C_1.

References [98] and [97] show two different empirical relationships for describing the variation of $\Delta P/q$, denoted as a resistance coefficient, with porosity for screens placed normal to the flow within a duct. Comparing experimental and numerical data on a perforated plate, Hou et al. [98] used the following equation

$$\frac{\Delta P}{q} = \frac{1}{c^2\beta^2} - 1, \tag{3.19}$$

where the coefficient c varies with the porous material's open area arrangement shape (holes distribution). For a circular holes arrangement, Hou et al. [98] used a value of $c = 0.85$.

Although showing a qualitatively similar variation, Eq. (3.19) overestimates the current experimental data at $\alpha = 0^\circ$ (shown in Fig. 3.3) mainly due to the choice of c. For $c = 1.17$, Eq. (3.19) shows very good agreement with the current experimental data when $\alpha = 0^\circ$.

Idelchik [97] suggested the following empirical equation based on data obtained for circular metal wire screens with square-shaped holes

$$\frac{\Delta P}{q} = k(1-\beta) + \left(\frac{1}{\beta} - 1\right)^2, \tag{3.20}$$

where $k = 1.3$ for Reynolds numbers Re ≥ 500 based on free-stream velocity and wire thickness. This is the case for the current experimental data when the velocity is greater than 8 m/s (Re ~ 550). Equation (3.20) is in excellent agreement with the experimental data at $\alpha = 0^\circ$ (shown in Fig. 3.3). Furthermore, by reducing the value of k appropriately (shown in Fig. 3.3), Eq. (3.20) also shows similar agreement to the experimental data for the inclined screens at $\alpha = 15^\circ$, 30° and 45°.

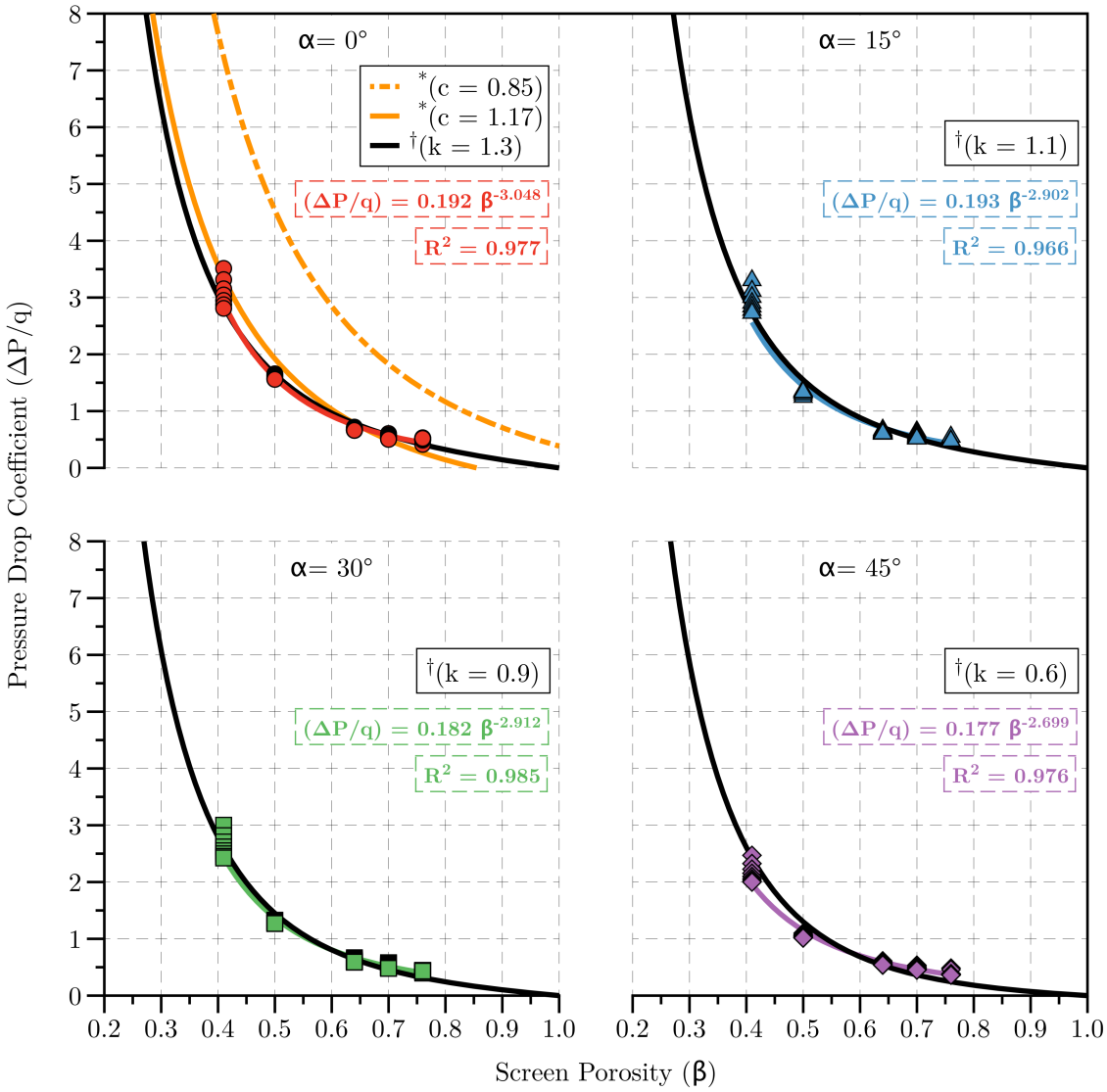

Figure 3.3 Pressure drop coefficient ($\Delta P/q$) variation with porosity (β) and angle of inclination (α). *Data reproduced from Hou et al. [98], †data reproduced from Idelchik [97].

3.5.2 Effect of Screen Porosity and Inclination on Permeability

In this study, the pressure drop (ΔP) across each screen and honeycomb tested is presented as a function of the upstream velocity and a second order polynomial

fitted through the data points.

The permeability (K) and inertial factor (Y) coefficient were calculated from the coefficients of the polynomial and are presented in Table 3.2. Identifiable trends are as expected with the permeability increasing with an increase in mesh porosity (β) for a given inclination angle (α). Furthermore, the permeability increases with increase in angle up to 45° for a given porosity, thus creating a higher mass flow rate.

The equations obtained using exponential curve fitting, relating the permeability and porosity of meshes at different angles and the respective coefficients of determination are given in Table 3.3. These are in good agreement with the trends obtained by both Miguel [81] and Valera et al. [86].

Table 3.2 Summary of the calculated permeability (K) and inertial factors (Y) for the tested screens between 0° and 45° angle of inclination (α).

	β	A	B	R^2	K (m^2)	Y
$\alpha = 0°$	0.76	0.37	1.52	0.99	2.36E-08	2.30E-02
	0.70	0.27	1.07	1.00	1.69E-08	2.90E-02
	0.64	0.38	0.23	1.00	1.59E-08	1.98E-01
	0.50	0.81	1.23	1.00	7.38E-09	1.15E-01
	0.41	1.30	7.13	1.00	1.52E-09	6.99E-02
$\alpha = 15°$	0.76	0.30	0.43	1.00	8.46E-08	3.59E-02
	0.70	0.29	0.97	1.00	2.23E-08	2.94E-02
	0.64	0.35	0.30	1.00	1.23E-08	1.61E-01
	0.50	0.78	1.24	0.99	7.30E-09	1.11E-01
	0.41	1.39	5.68	1.00	1.91E-09	8.42E-02
$\alpha = 30°$	0.76	0.26	0.19	1.00	1.93E-07	4.64E-02
	0.70	0.27	0.61	1.00	3.57E-08	3.54E-02
	0.64	0.34	0.42	1.00	8.58E-09	1.31E-01
	0.50	0.75	0.40	1.00	2.26E-08	1.87E-01
	0.41	1.26	4.42	1.00	2.48E-09	8.66E-02
$\alpha = 45°$	0.76	0.22	0.04	1.00	8.41E-07	8.14E-02
	0.70	0.26	0.36	1.00	5.94E-08	4.36E-02
	0.64	0.32	0.17	1.00	2.09E-08	1.91E-01
	0.50	0.59	0.48	1.00	1.86E-08	1.34E-01
	0.41	1.05	3.48	1.00	3.10E-09	8.05E-02

Table 3.3 Summary of the obtained equations relating permeability (K) and porosity (β) for the tested screens between 0° and 45° angle of inclination (α).

α (°)	K (m^2)	R^2
0	$8.52 \times 10^{-8}\beta^{4.15}$	0.92
15	$2.03 \times 10^{-7}\beta^{5.22}$	0.90
30	$6.57 \times 10^{-7}\beta^{6.12}$	0.90
45	$1.71 \times 10^{-6}\beta^{7.47}$	0.80

3.5.3 Use of Weighted Least Squares for Coefficient Generation

The standard linear regression model used to obtain the A and B coefficients makes strong assumptions about the behavior of the errors, more specifically, that the errors are normally and independently distributed with zero mean (μ) and constant variance (σ^2). Experimental measurements, however, have inherently non constant variance in the error term. Examination of the residuals using the Breusch-Pagan test [99] found that it was significant at a level of 5% and therefore the residuals were found to be heteroscedastic.

The Curve Fitting Toolbox™ in MATLAB® was used to obtain the original A and B coefficients by Gerova et al. [100]. MATLAB® implements the method of least fitted squares. To obtain the coefficient estimates, the least-squares method minimizes the summed square of the residuals. The residual for the i$^{\text{th}}$ data point (r_i) is defined as the difference between the observed response value (y_i) and the fitted response value ($\hat{y}_i$)

$$r_i = y_i - \hat{y}_i. \tag{3.21}$$

The summed square of residuals is given by

$$S = \sum_{i=1}^{n} r_i^2 = \sum_{i=1}^{n} (y_i - \hat{y}_i)^2, \tag{3.22}$$

where n is the number of data points included in the fit and S is the sum of the squared error estimates.

To remove the heteroscedasticity present within the residuals, weighted least squares regression was used. This is achieved through the addition of scale factor or

weight (w_i) to the fitting process. The weighs define how much each value influences the final parameter estimates.

$$S = \sum_{i=1}^{n} w_i (y_i - \hat{y}_i)^2, \tag{3.23}$$

where

$$w_i = \frac{1}{\sigma_i^2}. \tag{3.24}$$

The weighting matrix used was White's heteroscedasticity-consistent estimator [101]. A summary of the unweighted and weighted A and B coefficients is presented in Table 3.4.

Table 3.4 Summary of calculated weighted and unweighted A and B coefficients for the tested screens between 0° and 45° angle of inclination (α).

	β	A	B	A_{weighted}	B_{weighted}
$\alpha = 0°$	0.76	0.37	1.52	0.31	0.26
	0.70	0.27	1.07	0.35	0.88
	0.64	0.38	0.23	0.38	0.20
	0.50	0.81	1.23	0.83	0.82
	0.41	1.30	7.13	1.41	4.95
$\alpha = 15°$	0.76	0.30	0.43	0.27	1.11
	0.70	0.29	0.97	0.30	0.76
	0.64	0.35	0.30	0.35	0.47
	0.50	0.78	1.24	0.79	0.17
	0.41	1.39	5.68	1.37	3.90
$\alpha = 30°$	0.76	0.26	0.19	0.26	0.15
	0.70	0.27	0.61	0.27	0.56
	0.64	0.34	0.42	0.33	0.52
	0.50	0.75	0.40	0.75	0.40
	0.41	1.26	4.42	1.27	3.96
$\alpha = 45°$	0.76	0.22	0.04	0.21	0.24
	0.70	0.26	0.36	0.25	0.49
	0.64	0.32	0.17	0.31	0.41
	0.50	0.59	0.48	0.59	0.58
	0.41	1.05	3.48	1.06	3.13

Few studies exist that relate screen porosity (β), its permeability (K) and its inertial factor (Y). Nonetheless, the studies predict vastly varying values for the A and B coefficients. One study that investigates the discrepancies in published literature was conducted by Teitel et al. [87] for Re < 60. Due to the limited range of Re numbers investigated by Teitel et al., a secondary study was needed for flow regimes applicable to the simulation of heat exchangers (Re > 500, $v \approx 8$ m/s).

Teitel at al. [87] investigated the accuracy of the proposed global relationship between permeability and inertial factor to porosity by Miguel [81]. They concluded that the proposed relations given in Eq. (3.2) lead to a large overestimation of the pressure drop values. They predicted approximately five times higher K and 1.5 times higher Y values. Similar discrepancy were observed when comparing pressure drops obtained by Miguel for higher Reynolds numbers (see Figs. 3.4 and 3.5).

Valera et al. [86] published a different set of equations that relate screen permeability (K) and inertial factor (Y) to screen porosity (β). In order to obtain these equations they used a $\Delta P = Au^2 + Bu + C$, second order polynomial fit through their data. This type of fit is an inappropriate choice, as it poses a non-zero value of the pressure drop for zero velocity. This leads to incorrect K and Y equations. The individual A, B and C coefficients are presented in the paper and when the data is reproduced, can be fitted without the use of the constant term. The modified coefficients agree with the trends, but the K and Y equations proposed by Miguel [81] should not be used due to the inaccuracy of this more generalised form.

Flores-Velazquez et al. [95] proposed equations for K and Y based on the work of both Valera et al [86] and Miguel [81], however, due to the afore-mentioned inaccuracies in the underlying equations, the new equations proposed by Flores-Velazquez et al. are inherently erroneous.

Teitel et al. [87] investigated the flow through realistic woven screens and porous model conditions using CFD; validating their findings with wind tunnel data. They found that the results from the simulation of flow through porous media slabs had a velocity 20-25 times faster than that obtained from physical woven screens. Teitel et al. found that the values of the Forchheimer coefficients varied with Reynolds number but that the changes in these values can be assumed to be relatively small for Re $= 130 \sim 160$.

The obtained pressure drop values, both through the use of Eq. (3.6) on page 28 for the porous media approach and the simulation of realistic screens using CFD, show good correlation with the high Reynolds number wind tunnel data by Gerova et al. [100].

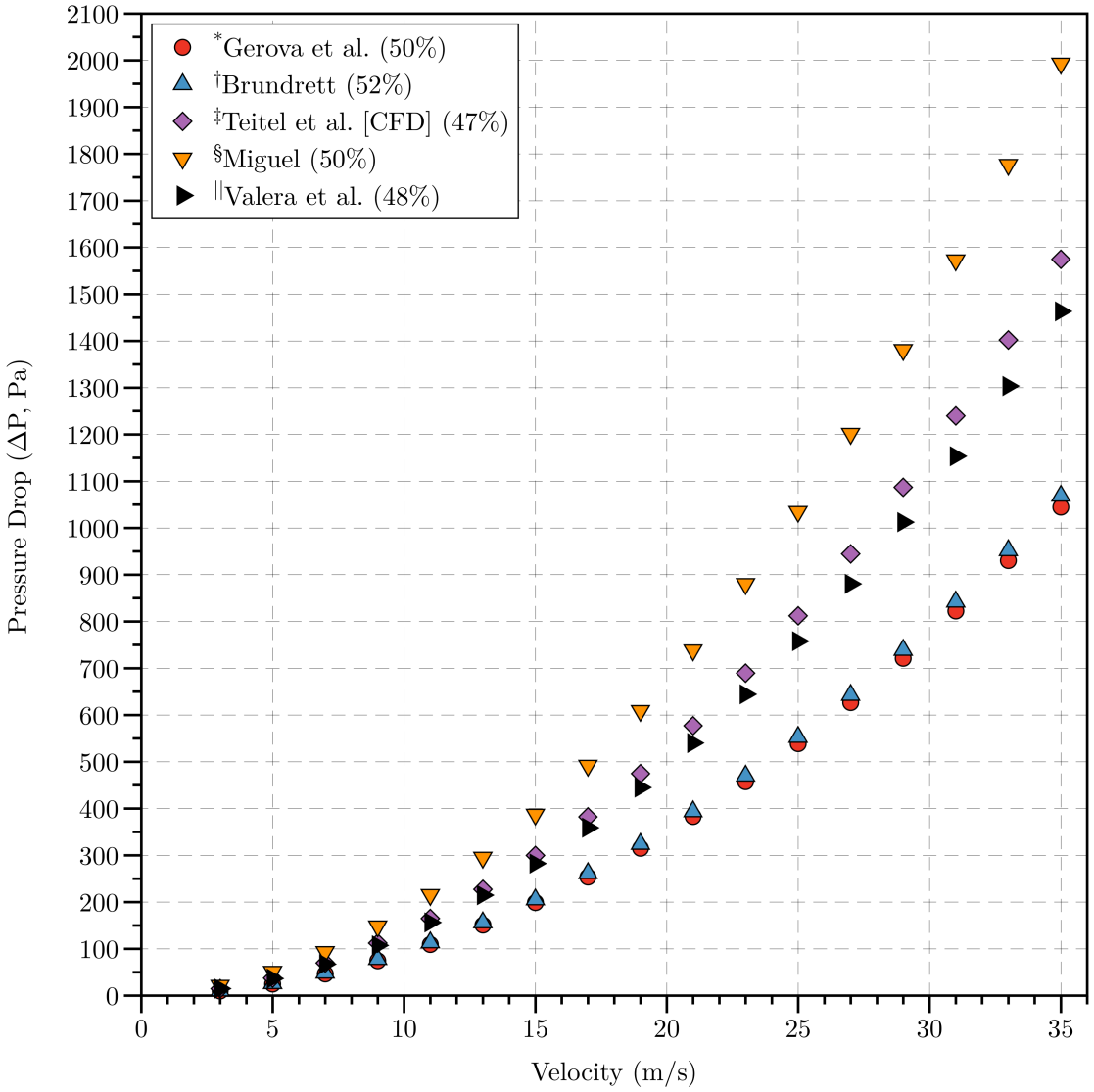

Figure 3.4 Comparison between various published pressure drops (ΔP) for porosities (β) of around 50%. *Data reproduced from Gerova et al. [100], †data reproduced from Brundrett [80], ‡data reproduced from Teitel et al. [87], §data reproduced from Miguel [81], ||data reproduced from Valera et al. [86].

Teitel et al. [87] proposed a relationship for the A and B coefficients as a function of porosity

$$A = 0.1641\beta^{(-2.593)} \qquad B = 0.1909\beta^{(-2.610)}. \tag{3.25}$$

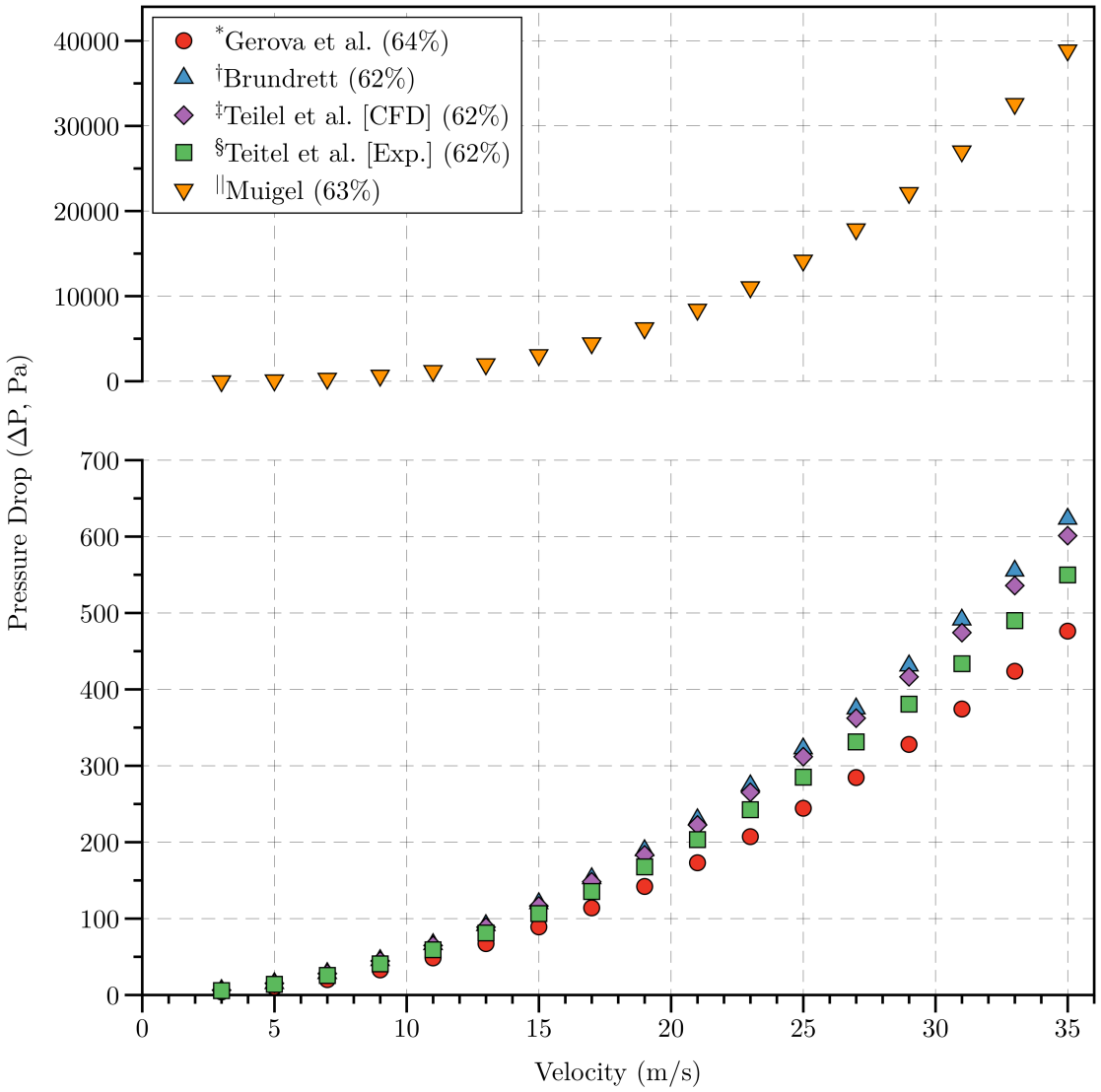

Figure 3.5 Comparison between various published pressure drops (ΔP) for porosities (β) of around 62%. *Data reproduced from Gerova et al. [100], †data reproduced from Brundrett [80], ‡data reproduced from Teitel et al. [87], §data reproduced from Teitel [71], ||data reproduced from Miguel. [81].

The R^2 for the power law fit of their function A was 0.894 and for high Reynolds number flows gives an overestimate of the pressure drop on average of 40%.

From the overview of the available relations for pressure drop through woven screens it can be concluded that the best method to use in obtaining the A and B coefficient is that proposed by Brundrett [80]. Equation (3.6) treats each screen

individually rather than using a general correlation that relates K and Y to the porosity of the screen.

3.5.4 Simulation of Porous Media in CFD

Two-dimensional CFD simulations were carried out using the same material properties of the porous meshes from the experimental set-up. The commercial code ANSYS® FLUENT® 15.0 was used, in conjunction with the $k-\varepsilon$ turbulence model with standard wall functions [96] and the porous jump boundary condition for the screen. The calculated face permeability (α_f) and pressure jump coefficient (C_{2f}) needed for inputs into ANSYS® FLUENT® 15.0 can be found in Table 3.5.

Table 3.5 Summary of calculated C_{2f} and α_f coefficients for the tested screens of various porosities (β) between 0 and 45 angle of inclination (α).

	Inclination Angle (α, °)	C_{2f}	α_f
$\beta = 76\%$	0	514	6.94E-08
	15	443	1.62E-08
	30	426	1.22E-07
	45	351	7.49E-08
$\beta = 70\%$	0	580	2.05E-08
	15	505	2.39E-08
	30	452	3.27E-08
	45	422	3.66E-08
$\beta = 64\%$	0	630	8.92E-08
	15	575	3.87E-08
	30	559	3.53E-08
	45	516	4.39E-08
$\beta = 50\%$	0	1370	2.21E-08
	15	1316	1.06E-07
	30	1240	4.49E-08
	45	975	3.11E-08
$\beta = 41\%$	0	2327	3.65E-09
	15	2279	4.67E-09
	30	2110	4.60E-09
	45	1754	5.74E-09

The convergence criteria for the residuals was set to 10^{-6}. A grid independence study was carried out with the 0° case, with meshes containing 9,200, 36,800 and

147,200 grid cells. Further information on the CFD methodology is given in Section D.12 of Appendix D. Comparison between experimental and CFD results is shown in Fig. 3.6. The figure shows a variation of less than 1% in the pressure drop values for the angles tested.

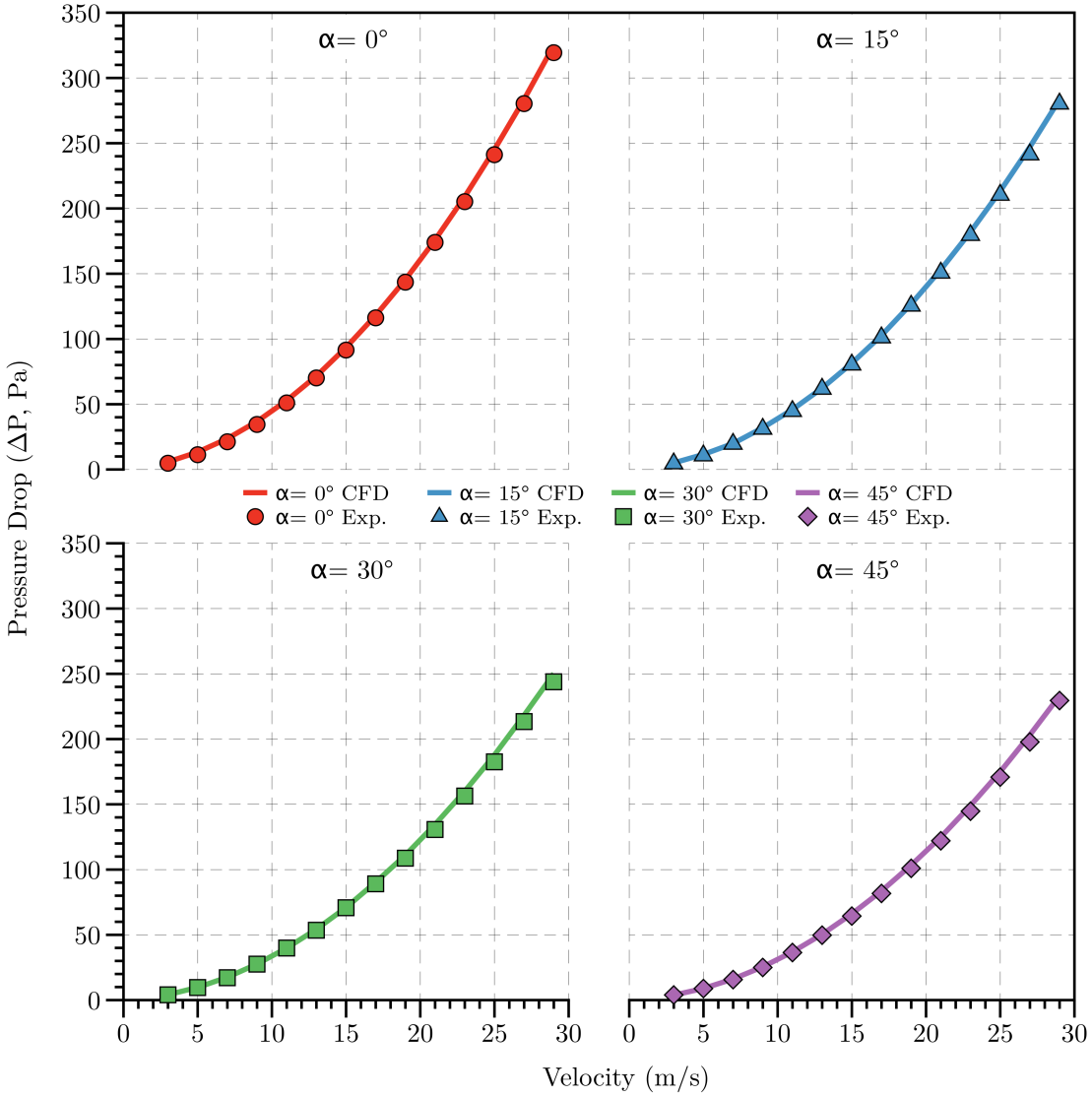

Figure 3.6 Numerical and experimental pressure drops (ΔP) with weighted Forchheimer equation coefficients for a porosity (β) of 0.70.

It must be noted that care should be taken when defining the face permeability and pressure jump coefficient for meshes at an inclination. Using the values for a

perpendicular case and just physically adjusting the mesh geometry to an angle of incidence will not give the same result as using the correct input values for the desired angle of incidence. Additionally, as the porous media is seen as a discontinuity, the velocity streamlines are unaffected by the inclination of the geometry as shown in Fig. 3.7.

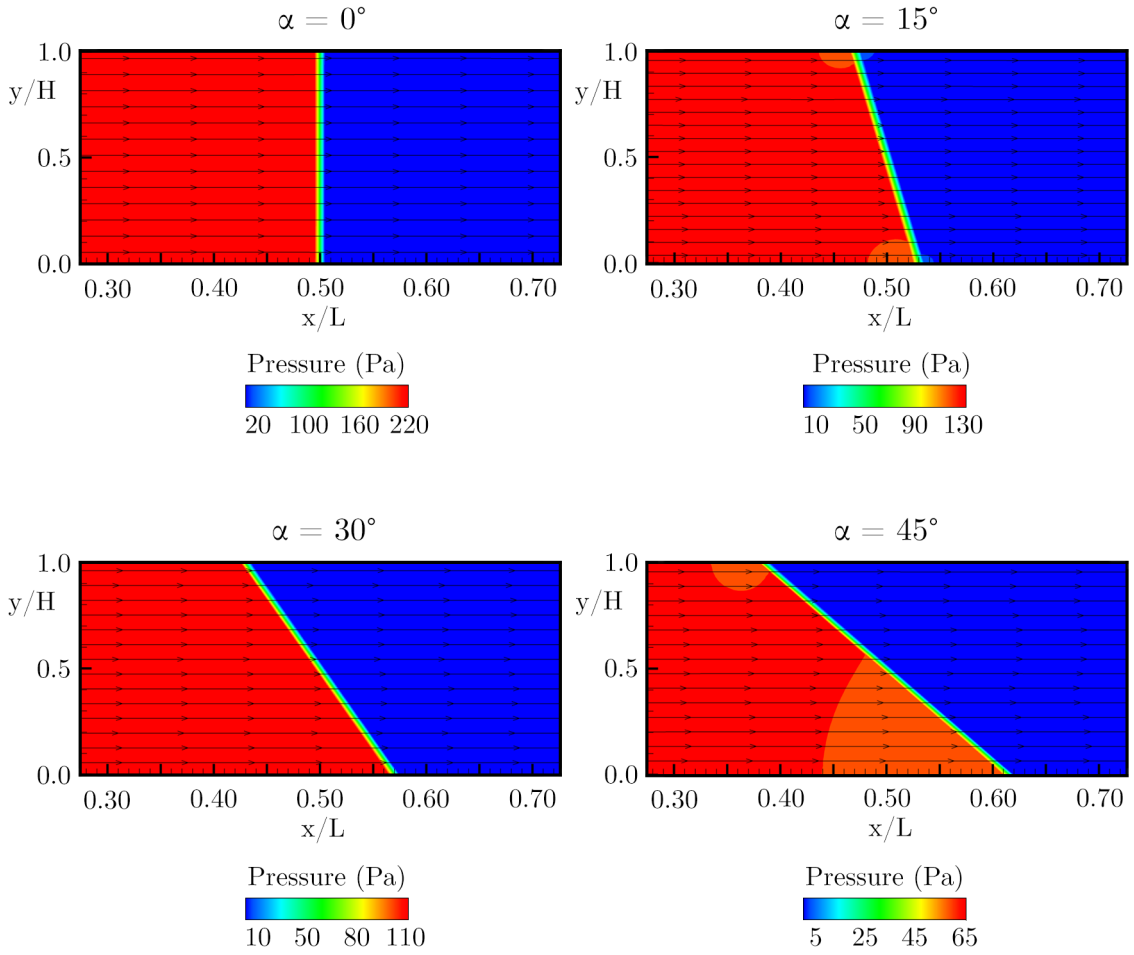

Figure 3.7 Streamlines for various material inclination angles (α) at a velocity (v) of 15 m/s and material porosity (β) of 0.50.

3.5.5 Effect of Screen Depth

Recognizing the degree to which a conventional heat exchanger matrix may influence the local flow direction, having a finite thickness and being made up of a series of narrow channels, it is common to use honeycomb to replicate this characteristic in many sub-scale simulations.

Three different hexagonal honeycombs (HC) with an identical matrix structure, channel height of 0.005 m and channel depths of 0.005 m, 0.01 m and 0.02 m respectively, were studied to assess the effect of the material depth on flow characteristics. Experimental measurements were made over a range of Reynolds numbers ($2500 < \mathrm{Re} < 45000$) based on channel depth. They were measured to have a porosity of approximately 95%.

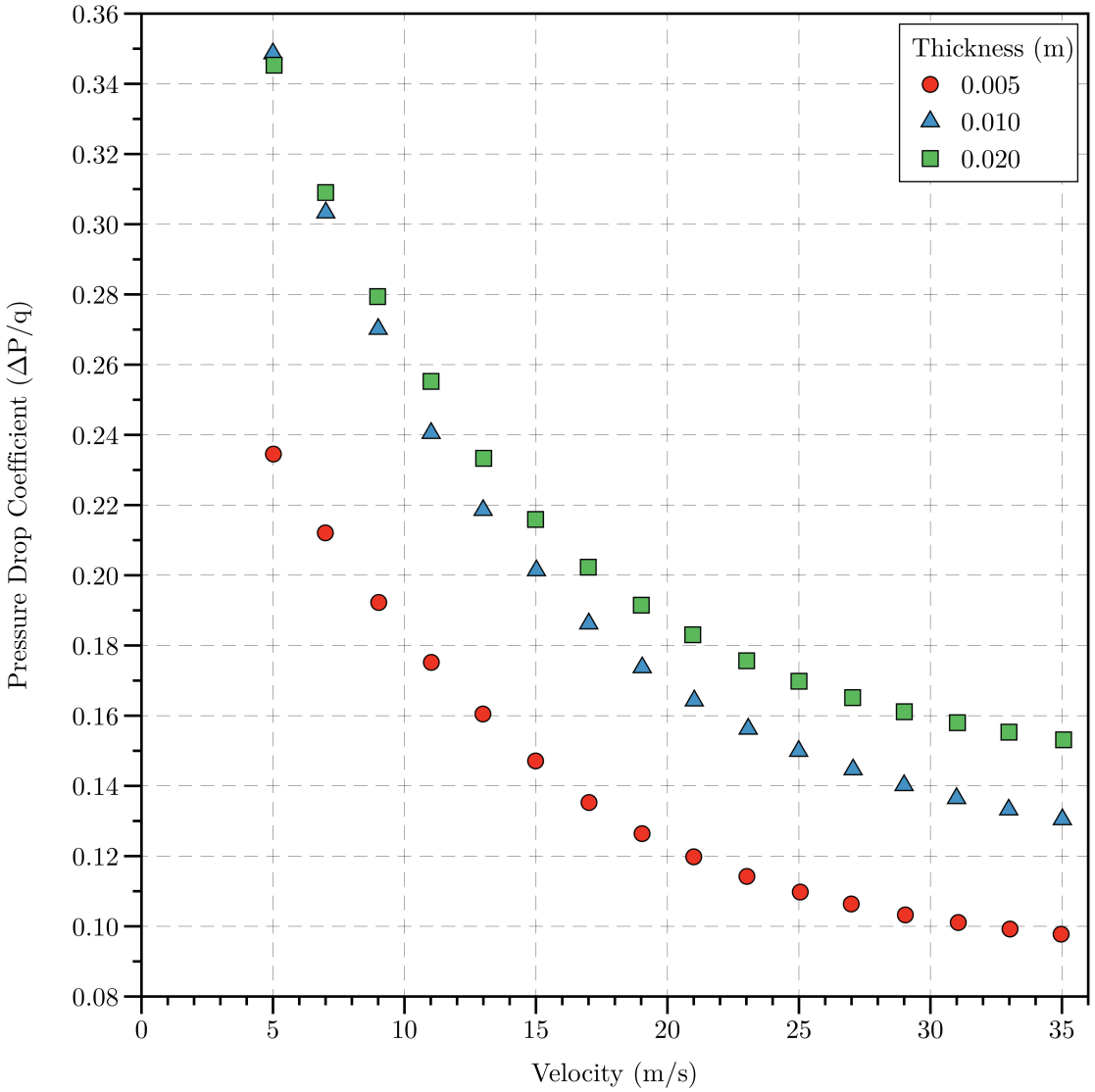

Figure 3.8 Variation of pressure drop coefficient ($\Delta P/q$) with velocity (v) for honeycomb screens of varying thickness at 0° inclination (α).

As with the thin porous materials the pressure drop coefficient of the honeycombs

(regardless of their depth) shows a tendency to become constant with increasing Reynolds number, as shown in Fig. 3.8.

The permeability (K) and inertial factor (Y) for the honeycombs were calculated in the same way as for the porous meshes by use of Eq. (3.4) on page 28. The permeability of the honeycombs was seen to increase with depth (see Table 3.6). Furthermore, the coefficient of the leading quadratic term (A) of the polynomial (from Eq. (3.14) on page 32) increases with the channel length, thus accounting for the greater pressure drop with increase in length.

Table 3.6 Summary of the permeability (K) and inertial factor (Y) for the honeycombs at 0° angle of inclination (α).

Length (m)	A	B	R^2	K (m^2)	Y
0.005	0.04	0.73	1.00	1.25E-07	2.33E-03
0.010	0.05	1.19	1.00	1.52E-07	1.51E-03
0.020	0.07	0.92	1.00	3.94E-07	1.81E-03

Since inclining the honeycombs reduces their effective porosity, with the increase of incidence angle the pressure drop coefficient values converge at 45° incline. This leads to the conclusion that there is an angle for which the pressure drop coefficient values become independent of material thickness.

The method outlined in Section 3.5.3 to obtain the weighted A and B coefficients was applied to the honeycombs. In addition, the weighted method was also applied in the calculation of the C_{2f} and α_f inputs used for the CFD simulation.

Table 3.7 Summary of calculated C_{2f} and α_f coefficients for the tested honeycombs at 0° angle of inclination (α).

Δm (m)	A	B	A_{weighted}	B_{weighted}	C_{2f}	α_f
0.005	0.04	0.73	0.036	0.76	11.87	1.19E-07
0.010	0.05	1.19	0.047	1.09	7.76	1.67E-07
0.020	0.07	0.92	0.063	1.01	5.19	3.59E-07

In ANSYS® FLUENT® 15.0 the thickness of the medium is the actual thickness of the porous region in the model. Thus, if the thicknesses used in the model differs

from the actual thicknesses, one must make the appropriate adjustments to the coefficients.

Figure 3.9 shows that the simulation results varied from the experimental data when only the material thickness (Δm) value was modified and not the corresponding porous jump coefficients.

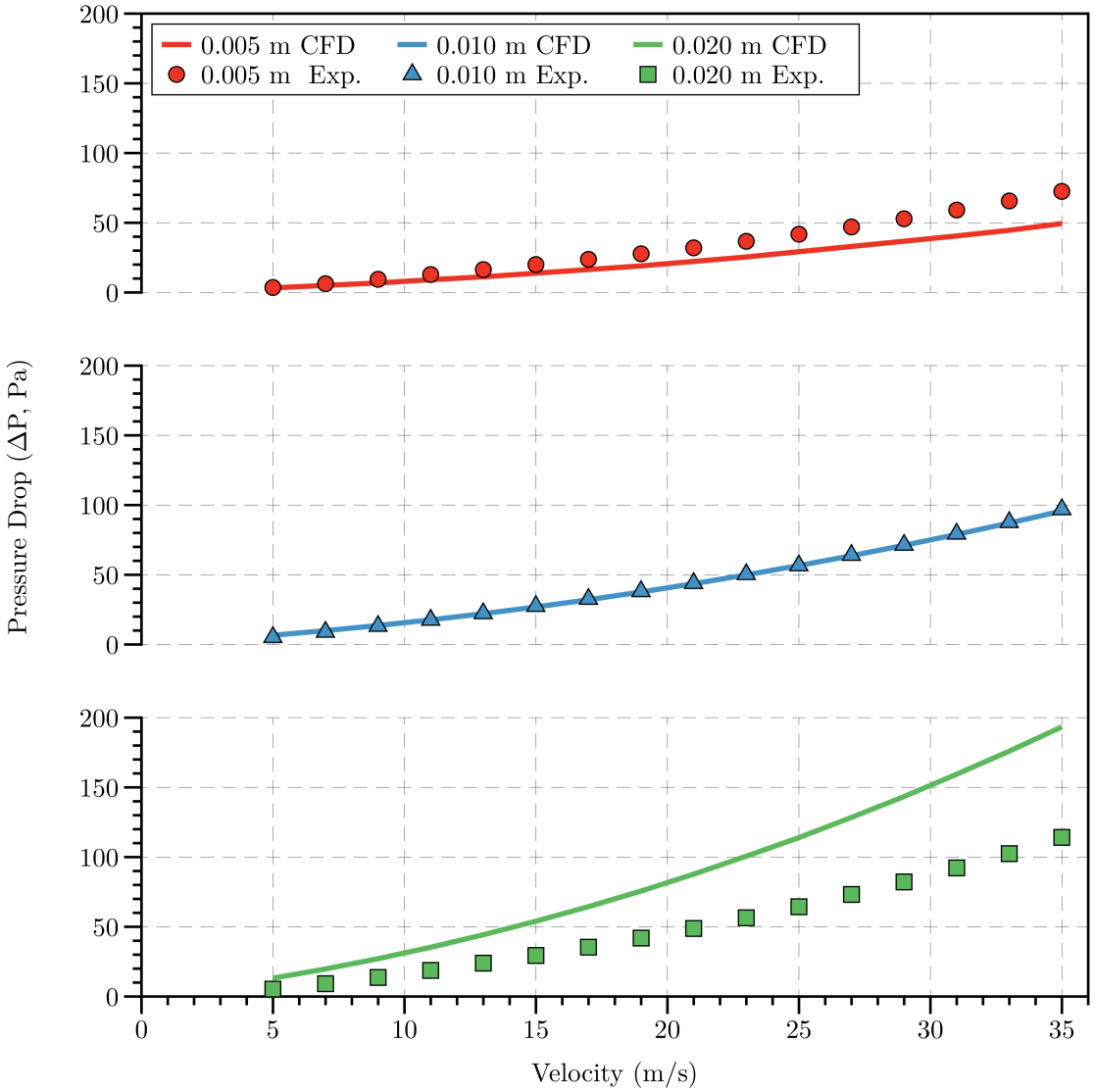

Figure 3.9 Numerical and experimental pressure drops (ΔP) for $C_{2f} = 7.76$ and $\alpha_f = 1.67\text{E-}07$.

3.6 Chapter Conclusion

The local static pressure variation in the near and far field of screens of variable porosity (β) in the range $0.41 \leq \beta \leq 0.76$ was investigated in a duct blower wind tunnel for free-stream Reynolds numbers (based on screen thickness) in the range $200 < \mathrm{Re} < 2100$ and screen angles of inclination to the free stream (α) of between 0 and 45°.

Based on the results obtained in this study the following conclusions can be drawn:

- For screen porosities of $\beta \geq 0.5$ the pressure drop coefficient ($\Delta P/q$) was found to be independent of Reynolds number above $\mathrm{Re} = 500$.
- The measured pressure drop coefficient decreases exponentially with increasing screen porosity. This trend held for all angles of inclination (α) tested.
- The measured pressure drop coefficient reduces with inclination of the screen for a given porosity. The magnitude of this effect becomes smaller for higher porosity values and for porosities of $\beta \geq 0.6$ the pressure drop coefficient was observed to be independent of angle of inclination.
- The screen permeability (K) was found to increase with increasing screen porosity and angle of inclination. When a honeycomb screen was used to investigate the influence of screen thickness, the permeability was found to increase with screen depth.
- Mathematical relationships were calculated for both the screen pressure drop coefficient and the permeability based on the experimental data obtained at a 0° angle of inclination, which compare well with available data in the literature. These expressions were extended to incorporate the effect of screen inclination.
- The standard linear regression model used to obtain the Forchheimer equation coefficients makes strong assumptions about the behavior of the errors, more specifically, that the errors have constant variance (σ^2). If the coefficients are obtained from experimental measurements, a check for heteroscedasticity must be performed. If the variance of the error term is found to be a function of the underlying measurement, it is recommended to use weighted least squares in favour of ordinary least squares.
- From the overview of the available relations for pressure drop through woven screens it can be concluded that the best method to use in obtaining the A and B coefficient is that proposed by Brundrett [80]. Equation (3.6) on page 28

treats each screen individually rather than using a general correlation that relates K and Y to the porosity of the screen.

- The porous jump boundary conditions in ANSYS® FLUENT® 15.0 can be used to model thin membranes with known velocity vs. pressure-drop characteristics. The CFD results matched closely with the experimental data, with only slight variation due to the fact they were modelled using coefficients obtained through data fitting. In contrast, the simulation results varied from the experimental data when only the material thickness (Δm) value was modified and not the corresponding porous jump coefficients.

Chapter 4

Full Scale Radiator Flow

The modelling of heat exchanger air flow characteristics for both wind tunnel testing and numerical simulation requires an in-depth understanding of the heat transfer properties of the full scale heat exchanger and how they impact the pressure drop (ΔP) across the radiator.

The previous chapter dealt with a series of iso-thermal experimental measurements and computational estimates of the pressure drop across screens of varying porosity (β). This data can be used for modelling sub-scale heat exchangers, where the full scale radiator matrix core is represented as a combination of lamination of various porous materials and honeycombs.

The main aim of this chapter is to establish a relationship between the pressure drop and heat transfer properties of a generic full scale automotive heat exchanger at various angles of inclination (α). Additionally, the present chapter investigates the use of Computational Fluid Dynamics (CFD) for modelling the experimentally tested heat exchanger.

4.1 Introduction

With both wind tunnel testing and numerical simulation playing an integral part of a vehicle development program, it is of vital importance to accurately capture the thermal and fluid properties of full scale automotive radiators. This requires knowledge of the experimental pressure drop and heat transfer across the element concerned. Previous investigations of the flow through automotive heat exchangers have mainly involved the measurement of the pressure distribution and flow visualisation.

Many authors have dealt with the cooling system and its components. The earliest work was carried out by Kays and London [1]. Despite their comprehensive data on matrix cores, work in this area cannot be considered complete.

Paish and Stapleford [11] demonstrated the feasibility of the cooling system design to be reduced to a calculation from the engine and radiator matrix data. They noted a 10% difference, recorded experimentally between the air pressure drop coefficients ($\Delta P/q$) of a cold vs. hot radiator matrix. Emmenthal et al. [14] used a novel method to design the cooling system on an automobile. Firstly, they used experimental data to characterize each individual component of the cooling system. They then considered the interaction of all the components together using computational techniques.

Fujikake et al. [54] developed a sensor to measure the airflow rate and air velocity distribution at an automotive radiator front.

Stafford [9] studied the blockage effect and the estimated heat rejection of simulated heat exchangers for wind tunnel models. This set up included inclining the core at various angles to the flow direction and simulating the exit ducting and turning vanes. The results of this investigation showed that perforated plates were adequate for heat exchanger simulations in wind tunnel models.

Haidar et el. [61] demonstrated the benefits of employing CFD for modelling the underbonnet flow characteristics of a passenger car. They tested three radiator thicknesses at variable velocities and concluded that for a given radiator size, as the vehicle speed increases, both the pressure drop and volume flow rate through the radiator increase. Ruijsink [41] developed a microprobe system in order to obtain input data and validate CFD simulations of cooling airflow.

Ng et al. [37] developed a pressure-based technique for the purpose of radiator cooling airflow measurement. The technique was used to quantify the local time-averaged air velocity through radiator cores in a wind tunnel. The pressure difference indicated by the technique was found to be a function of the normal component of the air velocity. Additionally, they found a considerable lack of uniformity across the radiator front face of a typical passenger vehicle. Williams [26] examines the aerodynamic drag and external interference of the cooling airflow on the engine. An analytical expression for cooling drag is introduced to understand and interpret the cooling drag measurements and particularly the interference at the inlet and exit. Empirical coefficients of the interferences are introduced as a representation of the exterior pressure distribution.

Jama et al. [102] varied the area of the cooling air intakes to permit the minimum amount of cooling air required for an adequate engine cooling. A full-size modern 'family' saloon was tested at the Monash University Aero-acoustic Wind Tunnel. The cooling air intakes of the vehicle were shielded progressively until fully blocked. Results from these tests found the optimum method for shielding the cooling intakes which minimised the drag coefficient was vertical strips.

Christofersen et al. [103] developed a scaled model heat exchanger for use in wind tunnel testing. In their work, a CFD numerical solver was used to show that in

simplifying the heat exchanger model, the flow physics through the heat exchanger were no longer accurate. Based on the findings from their CFD simulations, a physical model of a heat exchanger was developed and presented in the article. The heat exchanger was then modelled as a porous medium and treated numerically as a momentum sink.

Gerova et al. [100, 104] measured experimentally the pressure drop (ΔP) through screens with porosity (β) in the range 0.41-0.76. They established a relationship between the porosity and the pressure drop characteristics of a given material at various angles of inclination (α) to the free-stream flow. Furthermore, the numerical simulation of porous materials was investigated. The aim was to establish the most appropriate choice of Forchheimer coefficients for when simulating heat exchangers using CFD.

Henriksson et al. [105] investigated the pressure drops and heat transfer rates for three compact heat exchangers, where the heat exchangers were angled at 10°, 30°, 60° and 90° relative to the incoming airflow. Their investigation showed that for a specific mass airflow rate, a more inclined heat exchanger resulted in a lower static pressure drop and at the same time a higher heat transfer rate. Inexplicably, for the 60° cases the pressure drop both increased and decreased compared to the 90° cases, depending on the heat exchanger design. Additionally, they investigated a downflow and crossflow orientation of the heat exchangers but found the pressure drop and heat transfer-rate variation to be negligible between the downflow and crossflow orientation of the heat exchanger.

4.2 Experimental Methodology

The purpose of the experiment is to obtain pressure drop and heat transfer data across a typical automotive heat exchanger at various inclination angles relative to the free stream. The experiments were run by Young Calibration, a dedicated automotive heat exchanger test facility. The tests were performed using a test matrix with measurements made at locations specified by the author. The tests were performed using a blower wind tunnel such that the radiator core matrix could be mounted in the blown duct covering its entire cross section area. A custom working section was therefore fabricated to maintain a constant cross section area for the radiator core for the various angles of inclination. As the inclination angle (α) increased past 0°, a cover was added to the upper section of the tunnel to maintain this constant cross section working area within the tunnel. This produced a ducting effect prior to the entrance of the radiator similar to the ducting effect experienced in an automotive sidepod. No outlet ducting was installed and the radiator vented directly to ambient air. A schematic of the blower wind tunnel

arrangement and working section is presented in Section E.3 and Section E.4 of Appendix E, respectively.

Temperature controlled coolant was pumped into the radiator through insulated coolant pipework. The measurements of the temperature and pressure were taken within 150 mm both upstream and downstream of the radiator inlet and outlet spigots. The temperature was measured using PT100 $1/10^{\text{th}}$ DIN temperature probe, while the flow rate used a Siemens MAGFLOW MAG5000 electromagnetic flow meter. The estimated uncertainty of the temperature measurement does not exceed $\pm 0.5\,°\text{C}$. The coolant temperature was set to 60 °C, 70 °C, 80 °C, 90 °C and 100 °C. The coolant used was a 50:50 volume mix between Texaco XLC and water, the resulting heat capacity C_p specified by the manufacturer was $3.64\,\text{kJ}\,\text{kg}^{-1}\,\text{K}^{-1}$ at 100 °C. The flow rates for the tests were maintained at $120\,\text{l}\,\text{min}^{-1}$ (approximately $1.7 \times 10^{-5}\,\text{m}^3\,\text{s}^{-1}$).

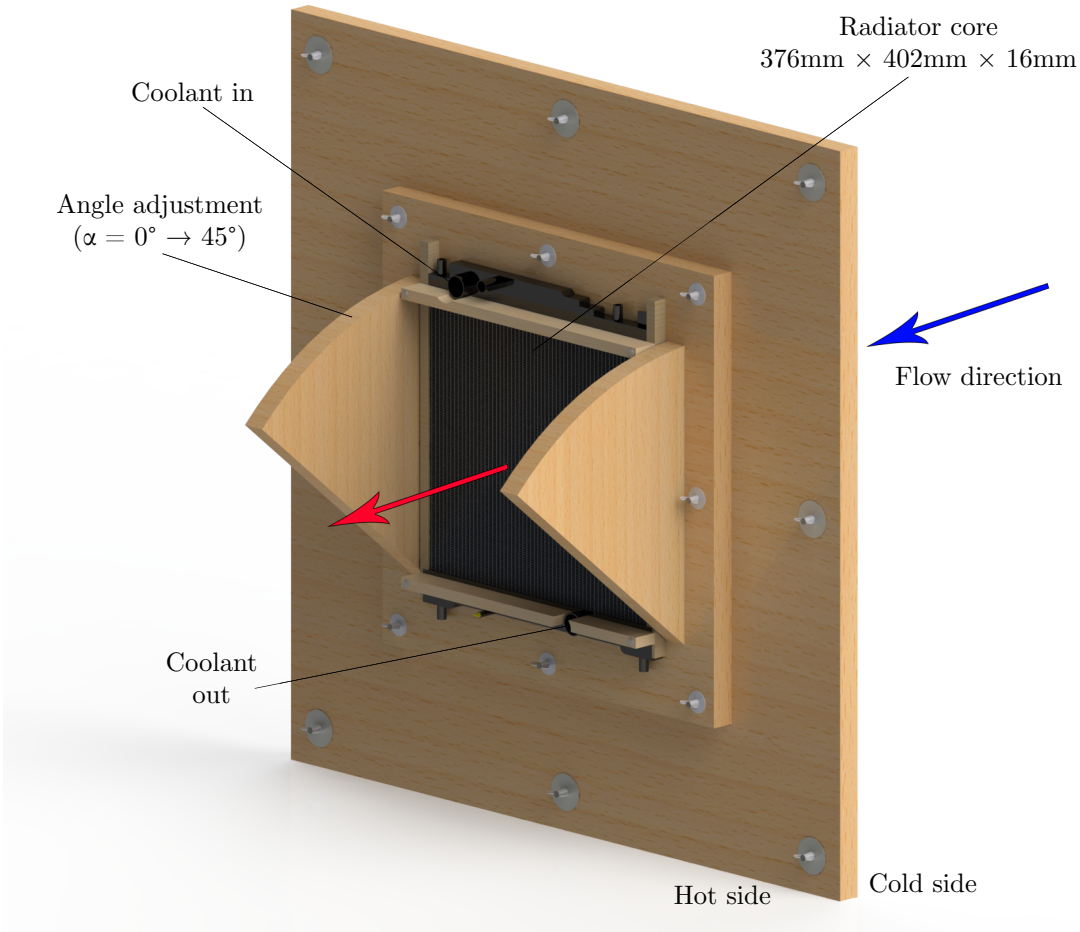

Figure 4.1 Render of Young Calibration's blower wind tunnel working section.

The wind tunnel speed was varied between 5 and 15 m/s and the freestream air had a temperature of 25 °C. The automotive radiator used was a DENSO DRM50056 radiator. This radiator is an OEM (Original Equipment Manufacturer) for Toyota and the radiator is commonly found in small displacement (1.0–1.4 l) engines fitted to vehicles such as the Toyota IQ. The radiator matrix dimensions were 376 × 402 × 16 mm with 62 tubes, 1 row and had an average fin density 81 fin/dm. The radiator was set up in a downflow arrangement shown in Fig. 4.1.

The reference pressure is measured just upstream of the contraction, using the pneumatic average taken from a ring of static pressure tappings. The pressure tubes from the static, pitot-static and reference ring pressure tappings were connected to GE Druck PTX511 pressure transducers. The relative measurement error specified by the manufacturer is ±0.5% of the measured pressure. A detailed error analysis is presented in Section E.7 of Appendix E. The transducers were also connected to the input channels of a data acquisition (DAQ) hardware.

The PC used for the data acquisition uses a National Instruments™ DAQ card with National Instruments™ LabVIEW™ software. A custom DAQ program was written for the tests. The wind tunnel measurements were conducted with screens inclined at 0°, 15°, 30° and 45° away from the free stream. Additionally, thermal images where taken using an Optris P1450 thermal imaging camera.

4.3 Numerical Simulation Methodology

ANSYS® FLUENT® 15.0 offers three radiator models in order to simulate heat transfer. The models are: Radiator Boundary, Macro Heat Exchanger and Dual Cell Model. The later Macro Heat Exchanger and Dual Cell Model are primarily used in the design and optimisation of multi-pass heat exchangers. Most automotive radiators feature single pass tube and fin design and as a result, the radiator boundary model is the most appropriate for simulating the heat transfer.

The computational domain used was 376 × 402 × 2016 mm (x, y, z), in order to match (in x and y) the matrix core size of the radiator. The radiator depth is not required in Fluent's Radiator Boundary model and therefore is modelled in a similar manner to a porous jump. The turbulence model used was the $k - \varepsilon$ model with standard wall functions. The air density (ρ) and inlet velocity (v) were obtained from the experimental data. Further information on the CFD methodology is available in Section E.8 of Appendix E.

The Radiator Boundary model requires the pressure drop coefficient ($\Delta P / \frac{1}{2}\rho v^2$) as a function of the tunnel velocity (v) in order to model the pressure drop across the radiator. To model heat transfer, the model also requires the heat transfer coefficient (h) as a function of the tunnel velocity (v).

4.4 Experimental Results

4.4.1 Effect of Temperature on the Pressure Drop across an Automotive Heat Exchanger

Figure 4.2 shows the thermal images of the tested radiator at 100 °C at 11 m/s for angles in the range: 0–45°. It can be seen that overall, the temperature of the hot side of the radiator is independent of its angle of inclination (α). This implies that the ducting used to incline the radiator produces a uniform velocity distribution through the face (cold side) of the radiator.

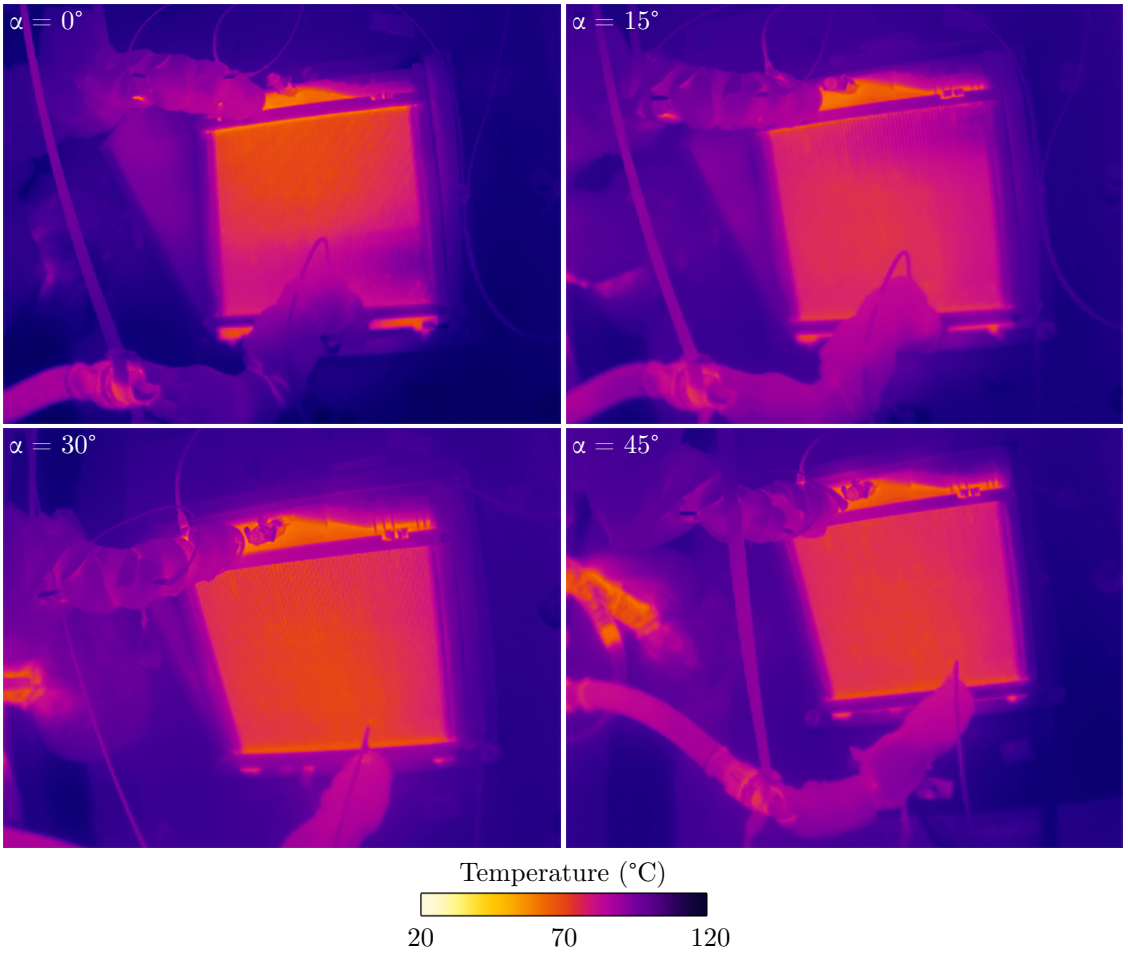

Figure 4.2 Thermal images for various radiator inclination angles (α), coolant inlet temperature ($T_{c(in)} = 100\,°C$) and velocity ($v = 11$ m/s).

It can also be seen in Fig. 4.2 that at 0° there is a hot spot (of approximately 95 °C) near the bottom of the radiator, while at 15° this is observed towards the top of the radiator. At 30° and 45° the radiator temperature appears to be more uniformly distributed. There is no inherent reason for this hot spot other than internal fowling of the coolant at these angles.

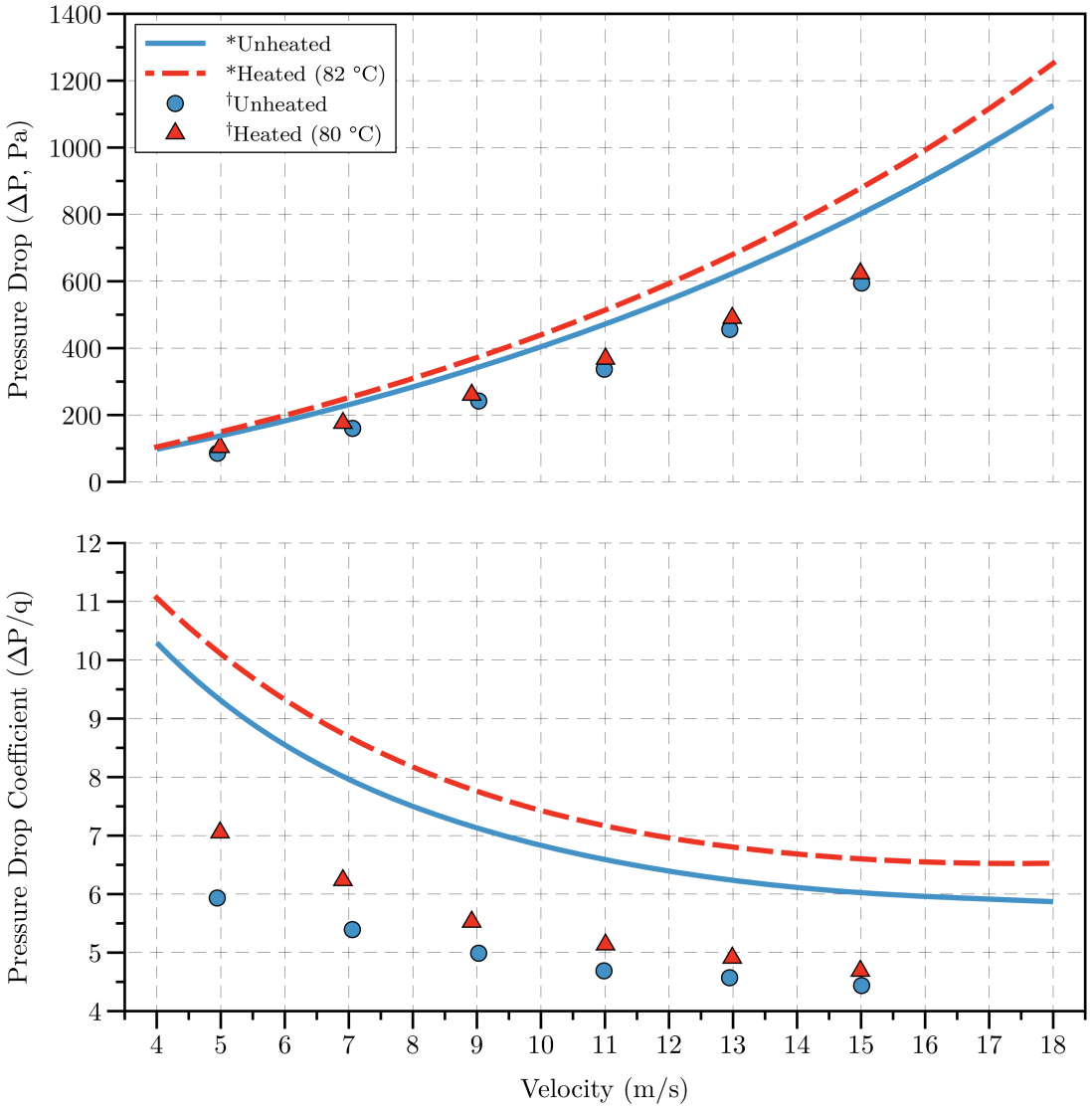

Figure 4.3 Pressure drop (ΔP) and pressure drop coefficient ($\Delta P/q$) variation with velocity (v) for an unheated and heated (∼80 °C) radiator at 0° inclination (α). *Data reproduced from Paish et al. [11], †data reproduced from Table E.1 on page 186 in Appendix E.

Initial comparison of the obtained data was made against Paish et al. [11] and is shown in Fig. 4.3. The variables used by Paish et al. [11] and the current study are shown in Table 4.1.

From Fig. 4.3 it is apparent that the baseline test by Paish et al. [11] produces a larger pressure drop throughout the velocity range tested. Due to advances in manufacturing processes the DENSO radiator (manufactured in 2015) used for the current study is more than twice as thin (16 mm) as the Audi radiator (manufactured in 1967, 34 mm thickness) used by Paish et al. [11]. This results in a much lower pressure drop for all velocities tested, this in agreement with the results obtained on page 46 in Section 3.5.5 of Chapter 3. At approximately 13 m/s this equates to a pressure drop of 456 Pa for the DENSO radiator compared to the Audi's value of 666 Pa.

Figure 4.3 also shows good agreement between Paish et al. [11] and the current study for the pressure drop (ΔP) difference between the unheated and heated cases. Paish et al. [11] reported a pressure difference of 61.0 Pa (9.2 %) over the unheated case (at 13.5 m/s) compared to 34.5 Pa (7.6%) for the current study (at 13 m/s).

A comparison of the total heat rejection measured by Paish et al. [11] and the current study is shown in Table 4.1.

Table 4.1 Heat rejection and pressure drop (ΔP) comparison with Paish et al. [11].

Item	Paish et al. [11]	Current Study
Radiator Make	Audi	DENSO
Radiator (fins/dm)	59	81
Radiator Area (m^2)	0.0906	0.1511
Radiator Material	Steel and Brass	Plastic and Aluminium
Coolant	Pure Water	50:50 Ethylene Glycol and Water
Coolant Temperature (°C)	82.2	80.0
Coolant Flow Rate (L/min)	114	120
Air Velocity (m/s)	13.5	13.0
Heat Rejection (kW)	32.2	42.0
Pressure Drop (Unheated)	666.1	455.9
Pressure Drop (Heated)	727.1	490.4
ΔP (Pa)	61.0	34.5
ΔP (%)	9.2	7.6

It was expected, due to the copper material used in the construction of the Audi radiator and the pure water used for coolant, that the radiator used by Paish et

al. [11] would have a higher heat rejection than the current study.

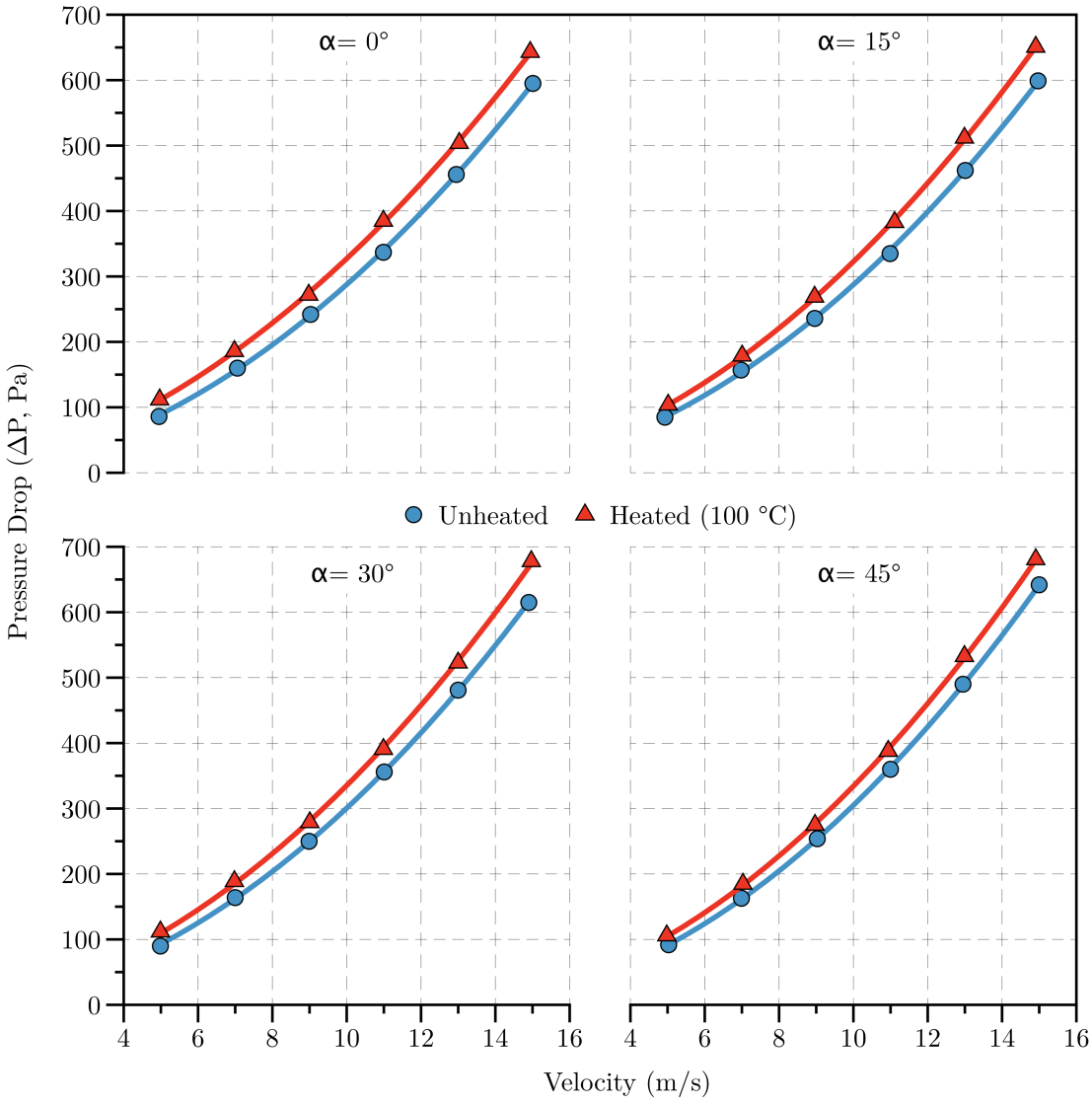

Figure 4.4 Pressure drop (ΔP) vs. velocity (v) for an unheated and heated (100 °C) radiator.

The thermal conductivity of copper is 385 $\mathrm{W\,m^{-1}\,K^{-1}}$ compared to aluminium's value of 205 $\mathrm{W\,m^{-1}\,K^{-1}}$, in addition the heat capacity of water is 4.18 $\mathrm{kJ\,kg^{-1}\,K^{-1}}$ compared to the 3.58 $\mathrm{kJ\,kg^{-1}\,K^{-1}}$ (at 80°) of the Texaco XLC and water mix used in the current study. Table 4.1, however, shows that the current study has a higher heat rejection of 42.0 kW compared to the Audi designed radiator which has a heat

rejection of 32.3 kW. The higher heat rejection from the DENSO radiator most likely occurs due to higher fin density offering a larger surface area for heat transfer in conjunction with a slightly larger overall radiator geometry.

Figure 4.4 shows the air pressure drop (ΔP) vs. velocity (v) for the remaining test angles of inclination for the unheated and heated radiator cases. From the figure it is evident that for all inclination angles (α) tested the pressure drop of the unheated case is lower than that of the heated case.

Table 4.2 Pressure drop (ΔP) and percentage increase of pressure drop (over unheated) for an unheated and heated radiator.

	Velocity (m/s)	ΔP (Unheated) (25 °C, Pa)	ΔP (Heated) (100 °C, Pa)	$\Delta(\Delta P)$ (Pa)	Percentage Difference (%)
$\alpha = 0°$	5.0	86.4	112.3	25.9	30.0
	7.0	159.8	186.1	26.3	16.5
	9.0	242.0	272.1	30.1	12.4
	11.0	336.7	384.6	47.9	14.2
	13.0	456.0	504.3	48.4	10.6
	15.0	594.8	643.3	48.5	8.1
$\alpha = 15°$	5.0	85.4	103.6	18.3	21.4
	7.0	157.0	178.6	21.6	13.7
	9.0	236.3	269.0	32.7	13.8
	11.0	334.7	382.5	47.9	14.3
	13.0	462.5	511.9	49.5	10.7
	15.0	599.5	651.0	51.5	8.6
$\alpha = 30°$	5.0	90.4	111.9	21.4	23.7
	7.0	163.7	188.5	24.9	15.2
	9.0	249.9	278.8	28.8	11.5
	11.0	356.2	391.1	34.9	9.8
	13.0	480.7	523.1	42.4	8.8
	15.0	615.2	678.0	62.8	10.2
$\alpha = 45°$	5.0	92.2	106.2	14.0	15.2
	7.0	162.7	184.7	22.0	13.5
	9.0	253.7	275.4	21.8	8.6
	11.0	359.9	388.2	28.3	7.9
	13.0	490.2	532.5	42.3	8.6
	15.0	641.6	680.7	39.1	6.1

The corresponding tabular data is shown in Table 4.2. The maximum air pressure drop (ΔP) of the heated and unheated radiator is 48.5 Pa, 51.5 Pa, 62.8 Pa and

39.1 Pa for 0°, 15°, 30° and 45°, respectively. This corresponds to a percentage difference (over the unheated radiator) of 8.1%, 8.6%, 10.2% and 6.0% for 0°, 15°, 30° and 45°, respectively. The general trend is for the percentage difference to decrease, whilst the magnitude of the difference increases as the velocity increases for each inclination angle (α).

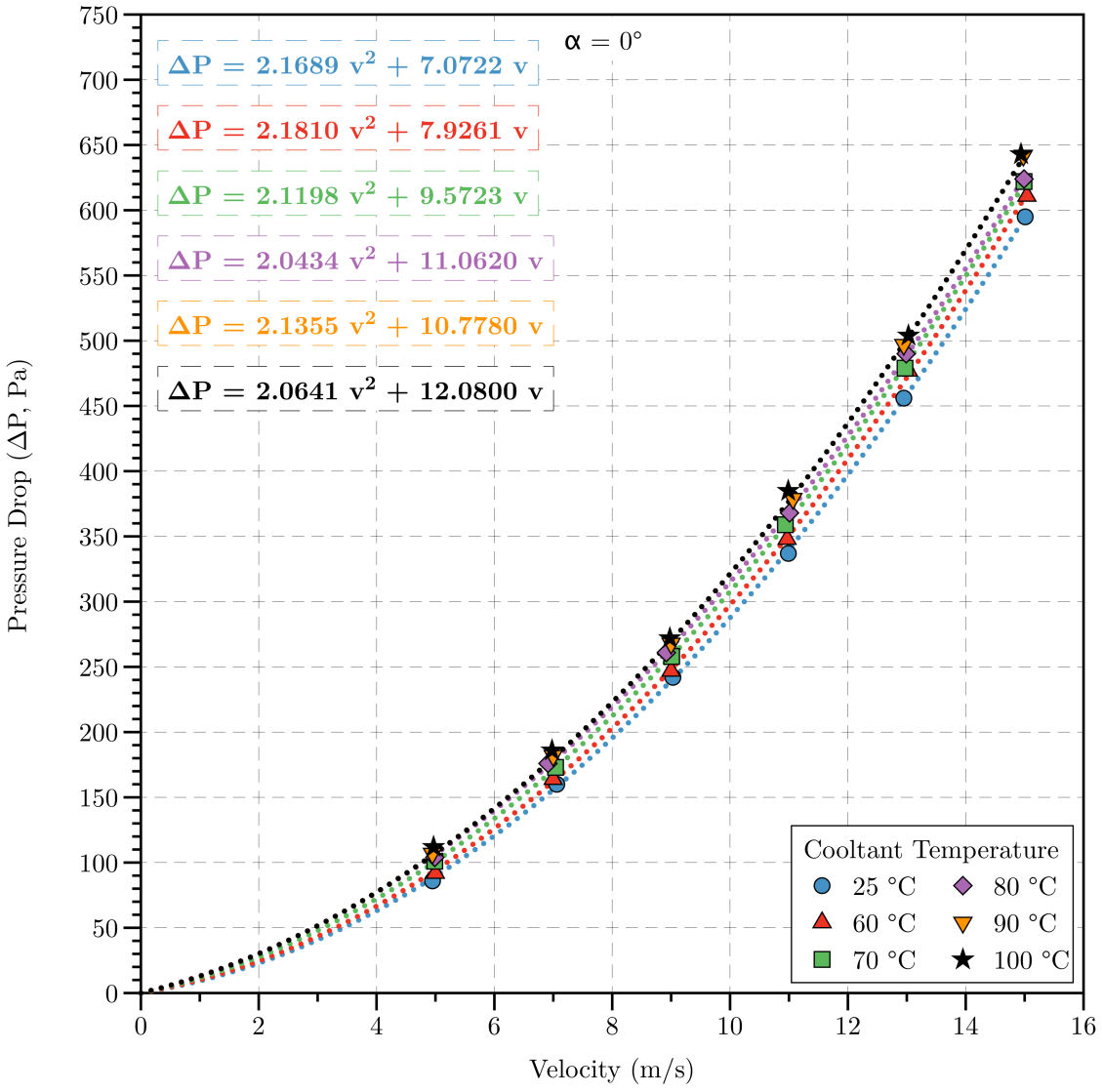

Figure 4.5 Pressure drop (ΔP) vs. velocity (v) at an inclination (α) of 0°.

The reason for the increase in pressure drop (ΔP) due to the addition of heat is that for an increase in temperature, the kinematic viscosity of air (ν) increases. This

causes the local Reynolds number (Re_x) to be lower than the corresponding local Reynolds number for the unheated case. This results in a thicker boundary layer within each channel in the radiator matrix and as a result of the no-slip condition, an increase in the centreline velocity. This increase in the centreline velocity results in a larger static pressure drop (ΔP) across the radiator core. This effect is investigated in more detail in Chapter 5.

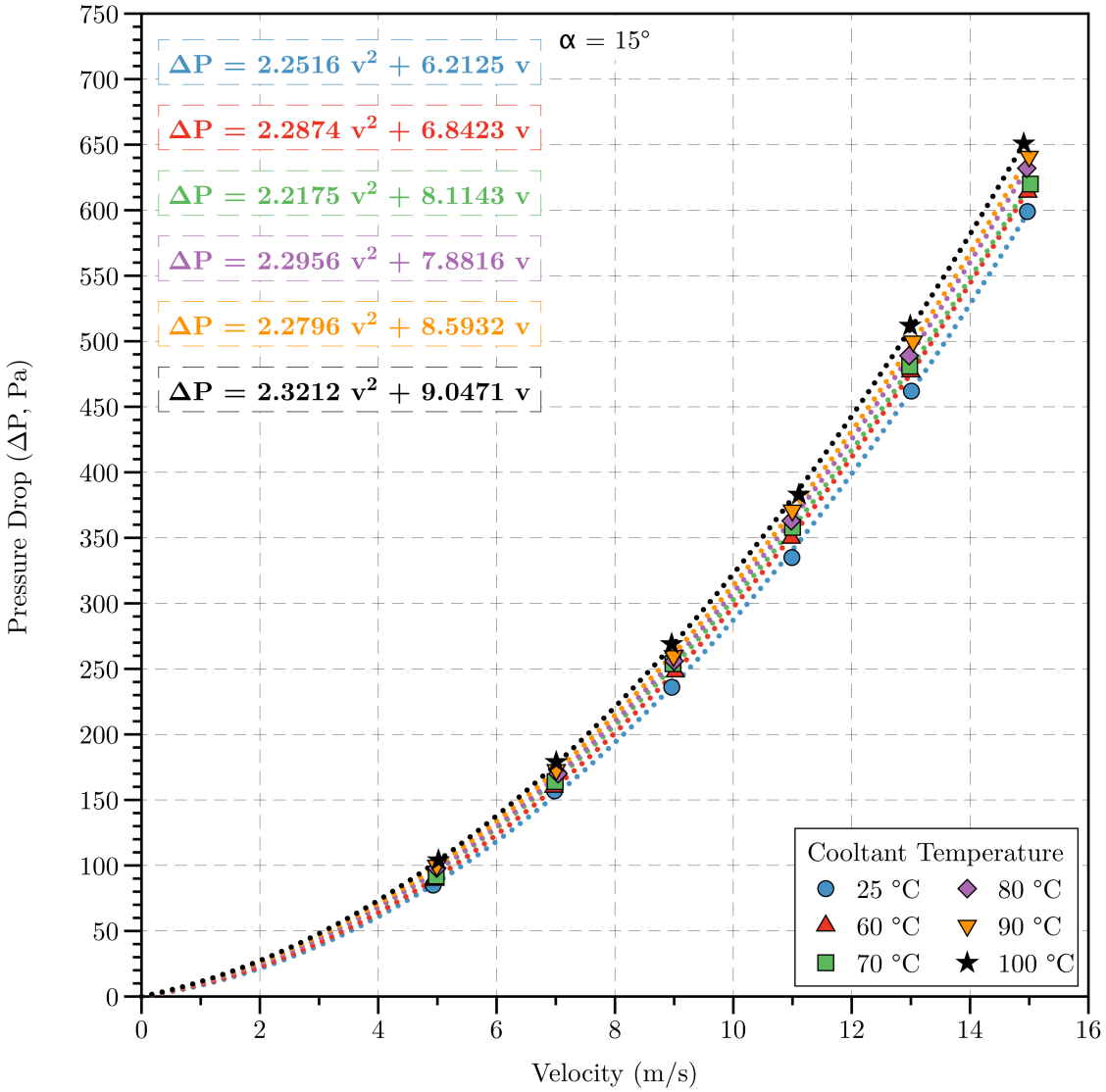

Figure 4.6 Pressure drop (ΔP) vs. velocity (v) at an inclination (α) of 15°.

Based on the results from Paish et al. [11], with an increase in velocity there is a point at which the pressure drop (ΔP) becomes independent of velocity. This

is in agreement with the results obtained in Chapter 3 for the porous media, the percentage difference for the radiators will therefore converge to a fixed value close to the 15 m/s value.

The 8.1% difference at 0° agrees with Paish et al. [11] who stated a 10% difference (at 18.2 m/s) for an automotive radiator that was tested. Additionally, it can be seen that with an increase in angle of inclination, the maximum pressure drop increases up to 30° and then decreases for 45°.

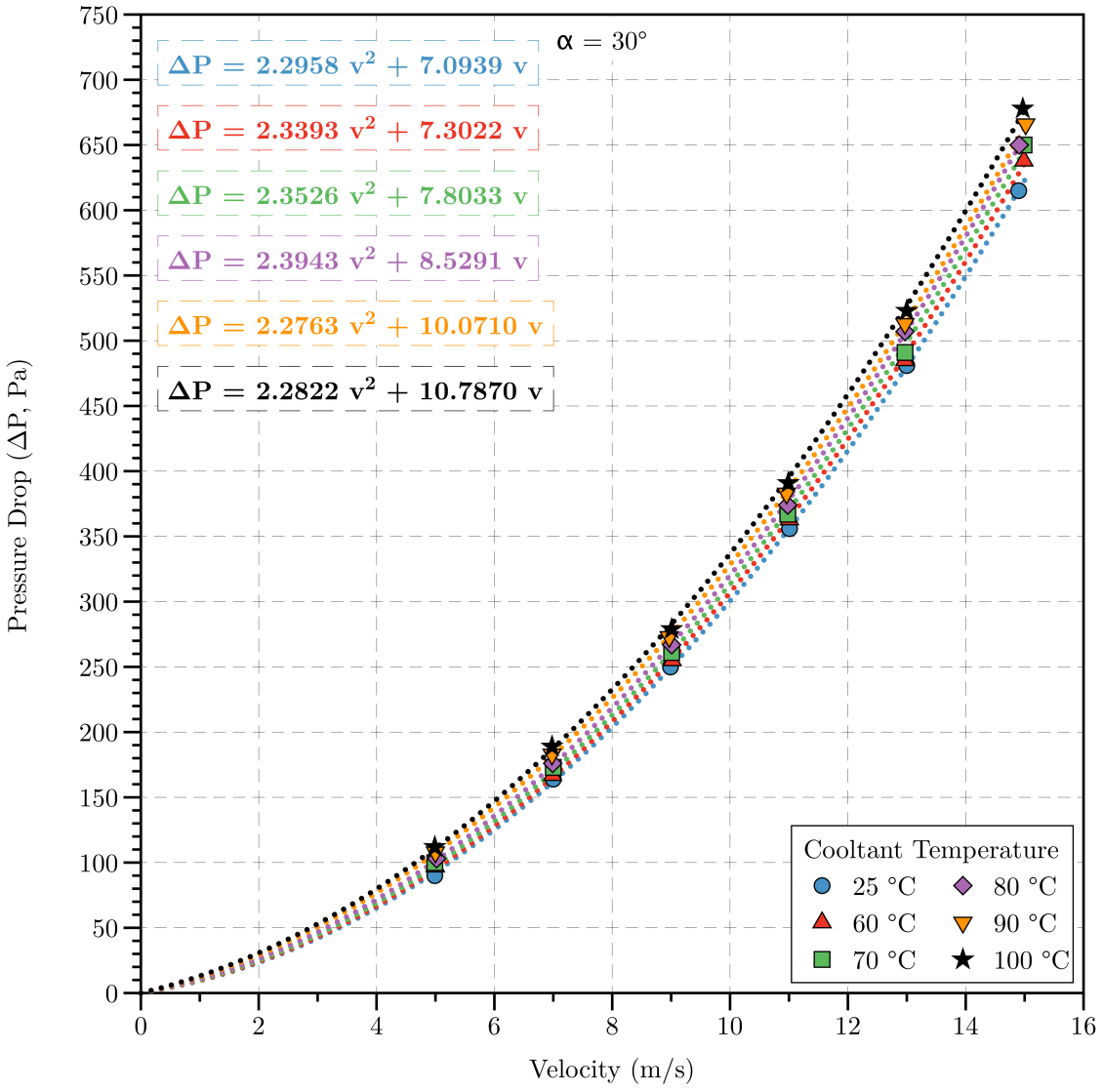

Figure 4.7 Pressure drop (ΔP) vs. velocity (v) at an inclination (α) of 30°.

A more detailed effect of the coolant temperature on the air side pressure drop,

including the pressure drop equation fits are shown in Figs. 4.5 - 4.8. For a specific coolant temperature, an increase in the air velocity results in an increase in the pressure drop, this trend is observable for all the angles tested. An increase in the temperature of the coolant results in a corresponding pressure drop increase for all angles of inclination.

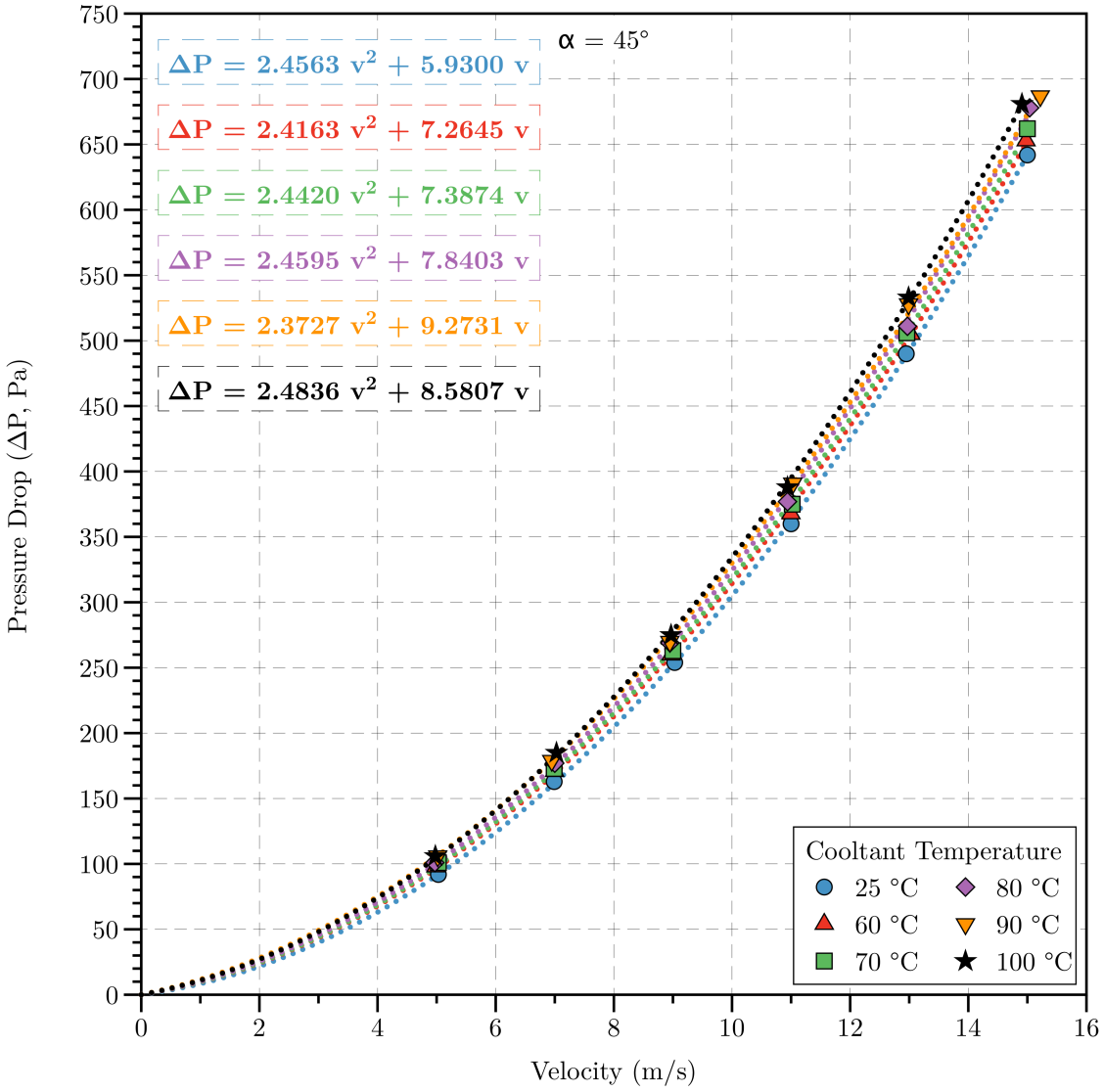

Figure 4.8 Pressure drop (ΔP) vs. velocity (v) at an inclination (α) of 45°.

For each coolant temperature, an increase in the angle of inclination results in an increase in the pressure drop of approximately 5%. Similar results have been

reported by Henriksson et al. [105] and Kim et al [106]. The remaining test data for alternate coolant temperatures can be found in Section E.6 of Appendix E.

4.4.2 Effect of Coolant Temperature on the Heat Rejection from an Automotive Radiator

Figure 4.9 presents the heat rejection vs. velocity for the coolant temperatures tested for each angle of inclination. It can be seen from the figure that an increase in the coolant temperature results in an increase in the heat rejection. The gradient of the heat rejection curve also increases for an increase in temperature, resulting in a larger heat rejection difference between coolant temperatures as the velocity increases. This trend is observed independent of angle of inclination.

The heat rejection from the coolant is therefore dependent of the angle of inclination of the radiator. Table 4.3 contains the data for a coolant temperature of 100 °C as a function of velocity (v) and angle of inclination (α). Table 4.3 shows that for velocities up to approximately 9 m/s the 0° inclination has a higher heat rejection. As the velocity increases, however, the inclined radiators begin to have a higher heat rejection compared to the 0° case.

For the final measured velocity of 15 m/s the 30° inclined radiator has the highest heat rejection followed by 45°, 15° and 0°. This is in good agreement with the corresponding pressure drops of 678 Pa, 681 Pa, 651 Pa and 643 Pa for $\alpha = 30°$, 45°, 15° and 0°, respectively. The 45° had a larger pressure drop compared to the 30° case due to the geometry of the radiator as opposed to purely cooling drag.

Table 4.3 Heat rejection as a function of velocity (v) and angle of inclination (α).

Velocity	Heat Rejection (kW)			
(m/s)	$\alpha = 0°$	$\alpha = 15°$	$\alpha = 30°$	$\alpha = 45°$
5.0	32.62	32.37	32.44	32.55
7.0	40.64	40.19	40.82	40.23
9.0	46.54	46.78	46.80	46.50
11.0	52.92	53.07	52.72	52.95
13.0	57.55	58.14	57.97	58.41
15.0	62.38	62.83	63.56	63.55

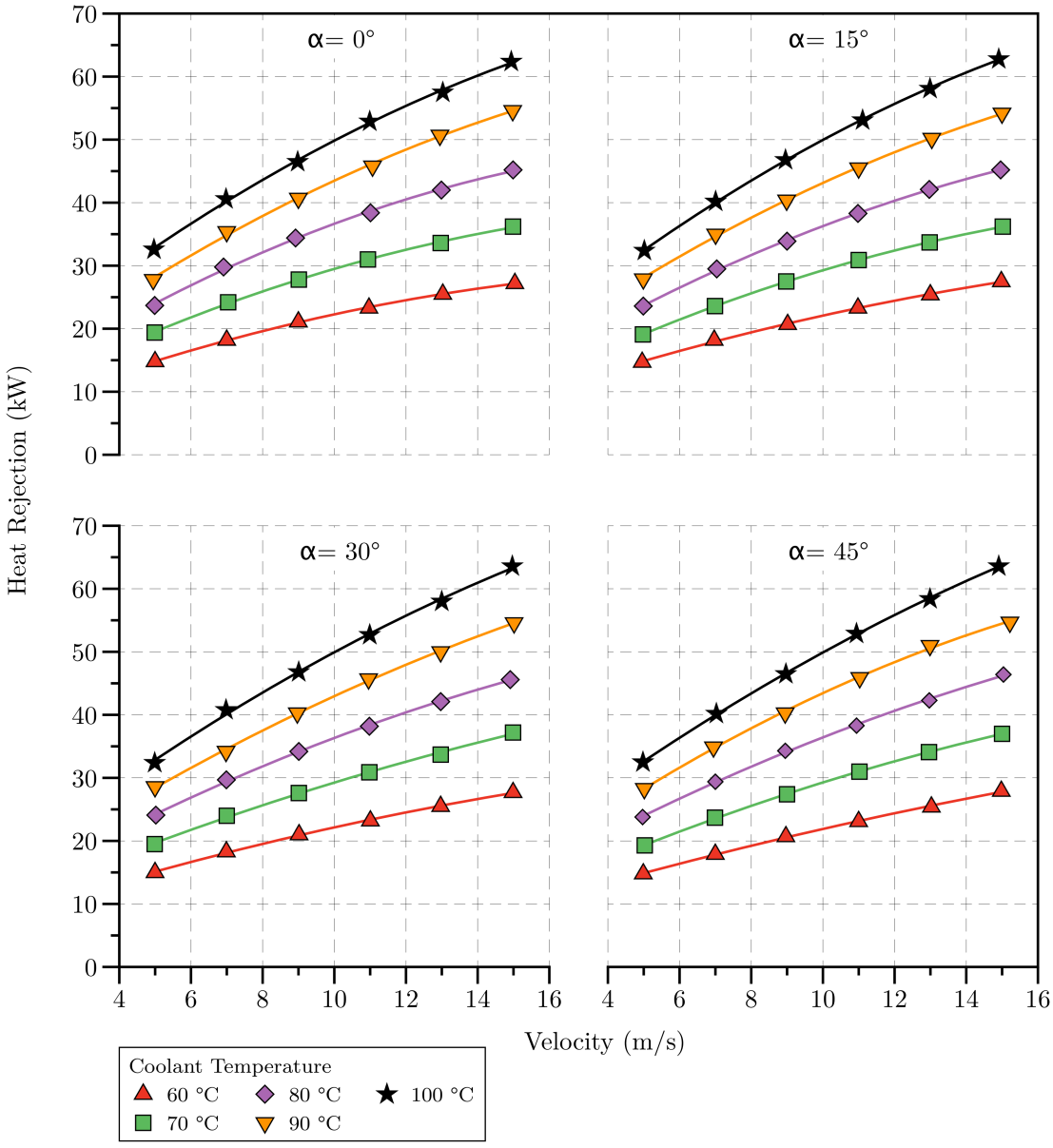

Figure 4.9 Heat rejection vs. velocity (v) for various coolant temperatures at various inclinations (α).

Combining the data in Table 4.3 with the data from Table 4.2 for 15 m/s gives the effective performance of the radiator as a function of the inclination angle, shown in Table 4.4. Table 4.4 shows that the most efficient radiator is the 0° inclined radiator, with the largest ratio of heat transfer : pressure drop of 0.0970. The least efficient radiator was the 45° inclined radiator producing the lowest ratio of heat transfer :

pressure drop of 0.0934. Whilst the overall heat transfer increases compared to the 0° radiator, the efficiency of the radiator from an aerodynamic perspective, decreases.

Table 4.4 Pressure drop (ΔP) and heat rejection data for 15 m/s and 100 °C coolant temperature.

Item	Inclination Angle (°)			
	$\alpha = 0°$	$\alpha = 15°$	$\alpha = 30°$	$\alpha = 45°$
Heat Rejection (kW)	62.38	62.83	63.56	63.55
Pressure Drop (ΔP, Pa)	643.3	651.0	678.0	680.7
(kW/ Pa)	0.0970	0.0965	0.0937	0.0934

4.4.3 Choice of Mesh Porosity for Modelling a Subscale Heat Exchanger

An important conclusion can be drawn from the results presented earlier, the pressure drop coefficient ($\Delta P/q$) of a given heat exchanger increases with the addition of heat. From Eq. (3.16) on page 34 in Chapter 3, this pressure drop coefficient was correlated to the porosity (β) and as a result, in order to account for the thermal properties of the heat exchanger at subscale, a porosity based on the heated pressure drop value must be chosen.

Table 4.5 Effective porosity ($\beta_{\text{eff.}}$) for an unheated and heated radiator at a velocity (v) of 15 m/s.

Inclination Angle (α, °)	Unheated $\beta_{\text{eff.}}$ (%)	Heated $\beta_{\text{eff.}}$ (%)	Δ (*Unheated - Heated*, %)
0	35.7	34.3	3.9
15	33.8	32.4	4.2
30	32.9	31.5	4.1
45	29.5	28.3	3.9

Figure 4.10 shows the pressure drop coefficient[1] ($\Delta P/q$) for the porous media

[1]The air density (ρ) used to calculate the dynamic pressure (q) was based on an average of the

and the heat exchanger with and without heated coolant.

Using Eq. (3.16) - (3.18) from page 34 in Chapter 3, it is possible to equate the pressure drop coefficient of an automotive radiator to a mesh of given porosity (β). Table 4.5 shows there is an approximate 4% decrease in the porosity requirement needed to accurately model a heated heat exchanger in subscale.

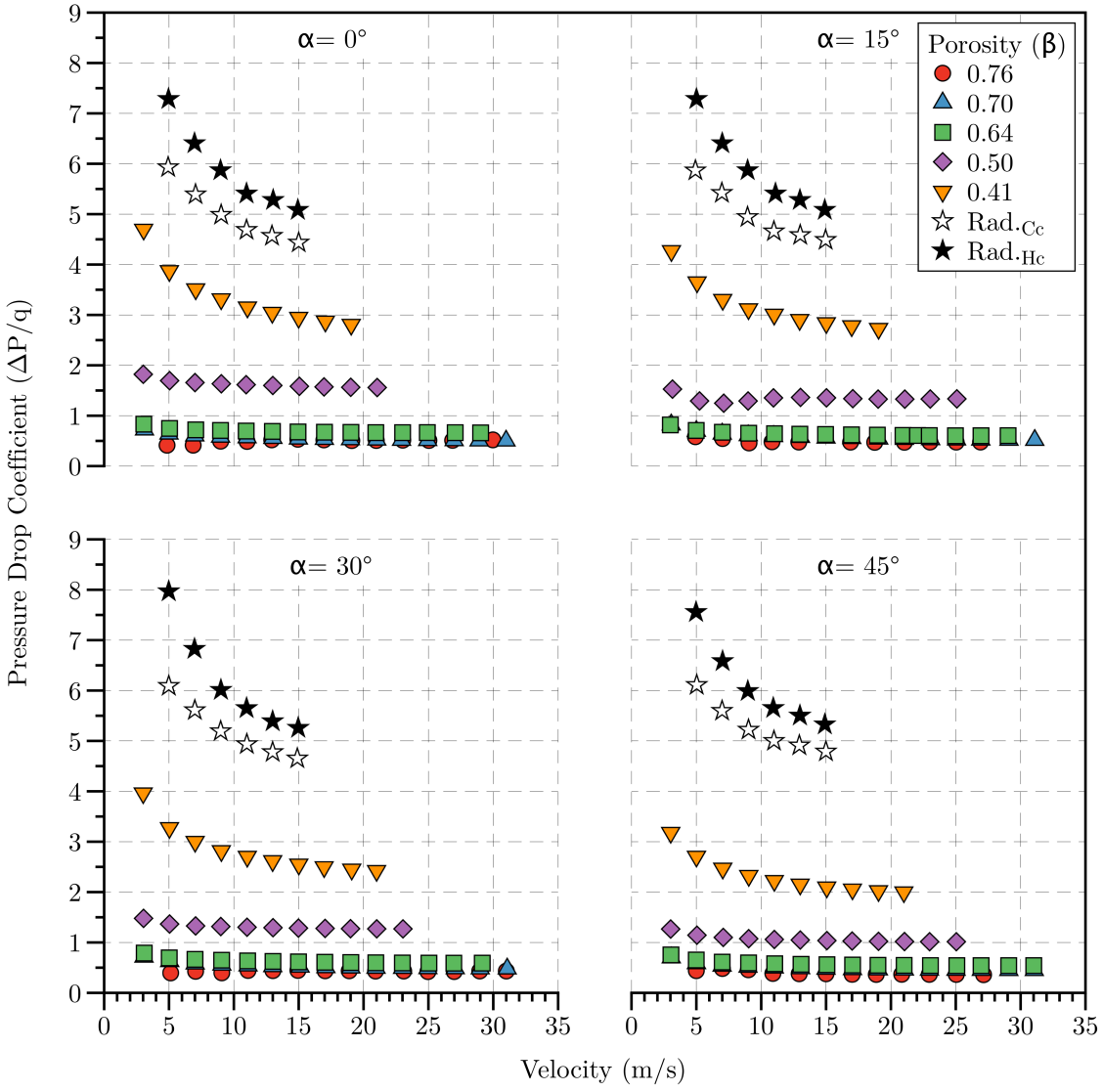

Figure 4.10 Pressure drop coefficient ($\Delta P/q$) vs. velocity (v) for meshes of varying porosity (β) and an automotive radiator with cold coolant ($Rad._{Cc}$) and hot (100 °C) coolant ($Rad._{Hc}$).

inlet and outlet air temperatures of the radiator.

4.5 Numerical Results

ANSYS® FLUENT® 15.0 models an automotive heat exchanger as a discontinuity, the model requires the pressure drop coefficient ($\Delta P/q = \Delta P/\frac{1}{2}\rho v^2$) and the heat transfer coefficient (h), both as functions of the tunnel velocity (v). The methodology for calculation and implementation of the pressure drop within ANSYS® FLUENT® 15.0 is outlined in Section 3.5.4 of Chapter 3. For the heat transfer coefficient (h), the method for obtaining and implementation within ANSYS® FLUENT® 15.0 is outlined below.

A simplified heat exchanger is shown in Fig. 4.11, with the upper channel containing air and the lower channel containing the radiator coolant,

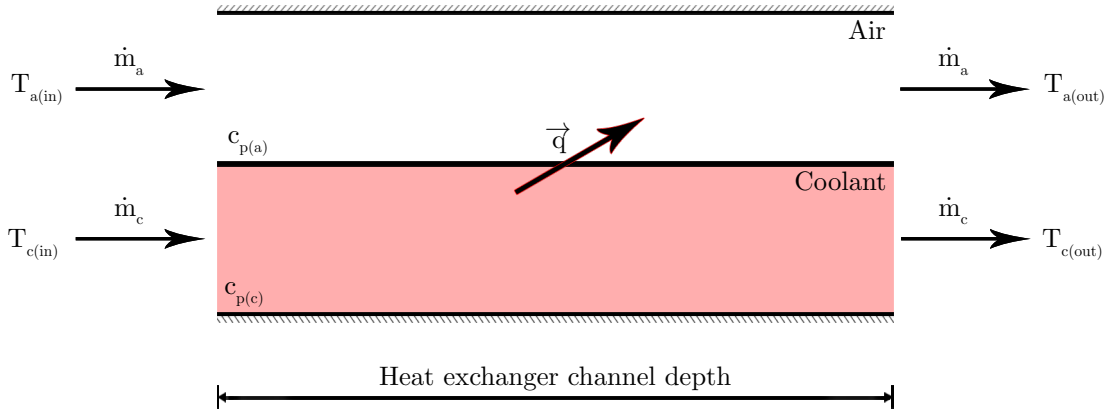

Figure 4.11 Heat flux ($\vec{q}$) nomenclature for a simple heat exchanger.

where $T_{\mathrm{a(in)}}$ is the inlet temperature of the air, $\dot{m}_a$ is the mass flux of the air, $c_{p(\mathrm{a})}$ is the heat capacity of the air, $T_{\mathrm{a(out)}}$ is the outlet temperature of the air, $T_{\mathrm{c(in)}}$ is the inlet temperature of the coolant, $\dot{m}_c$ is the mass flux of the coolant, $c_{p(\mathrm{c})}$ is the heat capacity of the coolant, $T_{\mathrm{c(out)}}$ is the outlet temperature of the coolant and $\vec{q}$ is the heat flux. For a typical heat exchanger, $T_{\mathrm{a(in)}} < T_{\mathrm{a(out)}}$ and $T_{\mathrm{c(in)}} > T_{\mathrm{c(out)}}$.

The heat flux ($\vec{q}$) within the channel is given by

$$\vec{q} = \frac{\dot{m}_{\mathrm{c}} c_{\mathrm{p(c)}} \Delta T}{A}, \tag{4.1}$$

where $\Delta T = T_{\mathrm{a(out)}} - T_{\mathrm{a(in)}}$ and $T_{\mathrm{a(out)}}$ is calculated by using Eq. (4.1) with $\dot{m}_{\mathrm{a}}$ and $c_{\mathrm{p(a)}}$. The reference area A of the radiator core was $0.1511\,\mathrm{m}^2$. The heat transfer coefficient (h) used within ANSYS® FLUENT® 15.0 is given by

$$h = \frac{\vec{q}}{(T_{\mathrm{c(in)}} - T_{\mathrm{a(out)}})}. \tag{4.2}$$

4.5.1 Numerical Simulation of Heat Transfer within an Automotive Radiator

Figure 4.12 shows the heat flux ($\overrightarrow{q}$), also referred to as heat dissipation as a function of tunnel velocity (v) for each radiator inclination angle.

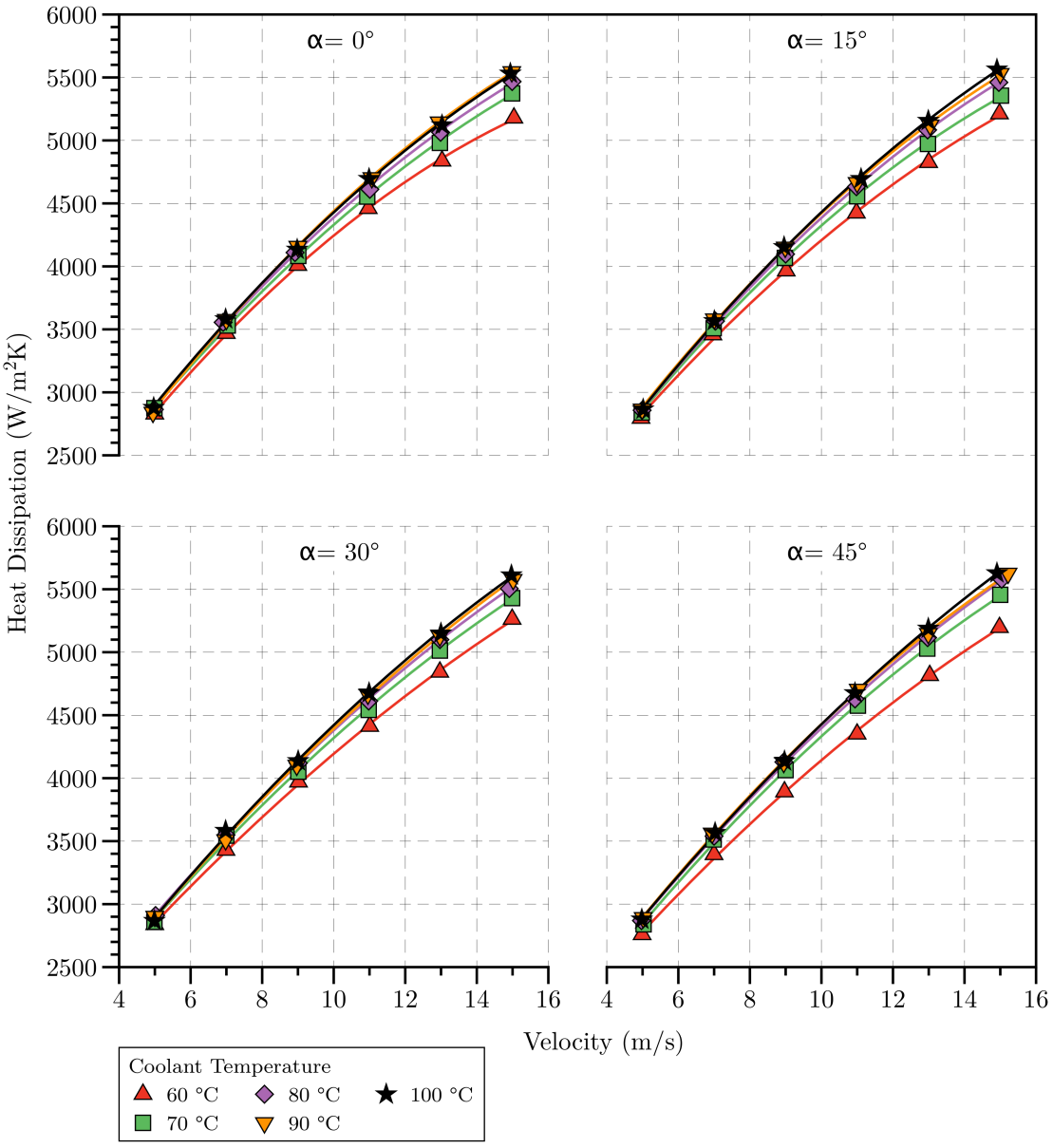

Figure 4.12 Heat dissipation vs. velocity (v) for various coolant temperatures at various angles of inclination (α).

ANSYS® FLUENT® 15.0 uses the polynomial coefficients obtained from the fit of h vs. v in conjunction with the coefficients obtained from the fit of $\Delta P/q$ vs. v. The coefficients for $\Delta P/q$ and h for a coolant temperature of 100 °C and 0° inclination are shown in Fig. 4.13.

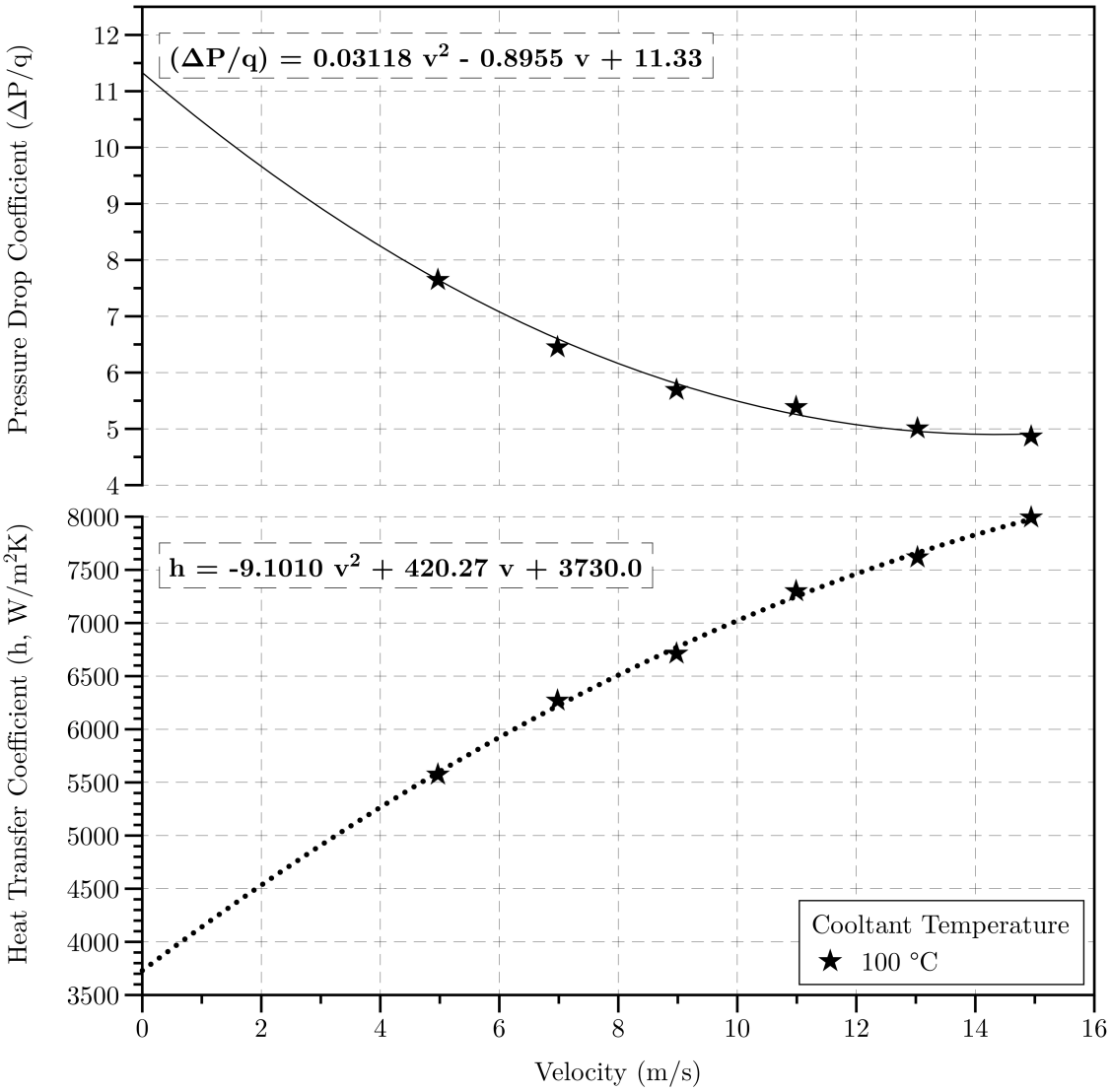

Figure 4.13 Pressure drop coefficient ($\Delta P/q$) and heat transfer coefficient (h) inputs for CFD.

The resulting simulated data from Fig. 4.11 is shown in Table 4.6. From the data obtained from numerical simulation, the maximum error of 2.7% obtained for

the pressure drop occurred at 7 m/s. This error was higher than that obtained in Chapter 3 for the porous media boundary condition (approximately 1%). This was due to the interpolation used in the radiator jump being with respect to $\Delta P/q$ compared to ΔP used within the porous media calculation.

Table 4.6 Experimental and numerical pressure drops (ΔP) and heat rejection ($\overrightarrow{q}A$).

	Experimental		CFD	
Velocity (m/s)	ΔP (Pa)	Heat Rejection (kW)	ΔP (Pa)	Heat Rejection (kW)
4.97	112	32.6	112	33.1
6.98	186	40.6	191	40.3
8.98	272	46.5	278	47.0
10.99	385	52.9	377	52.9
13.03	504	57.5	500	58.1
14.94	643	62.4	652	62.4

The maximum error on the heat rejection was 1.6% at 5 m/s. One major downside with the model implementation within ANSYS® FLUENT® 15.0 is that the radiator is modelled as a discontinuity and as such, the geometry of the radiator is not considered. Attempting to model the inclination of the radiator, results in large errors on both the pressure drop and heat transfer. These errors occur due to the model requiring the air flow to be perpendicular to the coolant flow. This requirement is present in the radiator boundary condition as well as in the Grouped and Ungrouped Macro model. The only model without this requirement is the Dual Cell model which simulates the coolant flow within the geometry using a separate mesh. The Dual Cell model will still, however, suffer from errors on the pressure drop unless the geometry of the radiator is also modelled.

4.6 Chapter Conclusions

The main aim of this chapter was to establish a relationship between the pressure drop and heat transfer properties of a generic full scale automotive radiator as a function of the angle of inclination. Additionally, the present chapter investigated the use of computational fluid dynamics for modelling the tested heat exchanger. Based on the results obtained in this study the following conclusions can be drawn:

- An increase in coolant temperature corresponded to an increase in the pressure drop (ΔP) for all angles of inclination (α) tested. For the highest coolant temperature tested (100 °C), the pressure drop of the heated cases was greater than the unheated case by approximately 8% for inclination angles of 0° and 15°. This different climbed to 10% for 30° of inclination, but fell to 6% for the 45° case.

- The heat rejection of the coolant is dependent of both the angle of inclination of the radiator and the velocity (v). Increasing the velocity increases the heat rejection. Inclination of the radiator at lower velocities decreases the heat rejection, however, at larger velocities the heat rejection increases with inclination. At higher velocities, the radiator with the highest overall heat transfer for higher velocities was 30°. The most efficient radiator inclination angle defined in terms of largest heat rejection : lowest pressure drop, however, was the 0° inclined radiator.

- In order to capture the effects of heat when modelling a heat exchanger at subscale, the decrease in required porosity (β) must be calculated. For 15 m/s (approximately 34 mph) this equated to an approximate 4% decrease in porosity for all angles of inclination (α) tested.

- The radiator boundary conditions in ANSYS® FLUENT® 15.0 can be used to model automotive heat exchangers with known pressure drop ($\Delta P/q$) and heat transfer (h) coefficients. The model, however, does not take into account the radiator inclination and instead, requires the radiator to be modelled as a discontinuity with the coolant flow perpendicular to the air flow. The CFD results at zero degree inclination agreed well with the experimental data. The maximum error on the pressure drop (ΔP) was 2.7% at approximately 9 m/s and the maximum error on the heat rejection was 1.6% at approximately 5 m/s. These errors arose due to the use of a second order polynomial fit through the experimental data. The error on the pressure drop was larger than that achieved using the porous media boundary condition in Chapter 3 as the pressure drop coefficient ($\Delta P/q$) was used instead of the pressure drop (ΔP).

This page intentionally left blank.

Chapter 5

Radiator Matrix Channel Flow

The modelling of heat exchanger air flow characteristics for both wind tunnel testing and numerical simulation requires an in-depth understanding of the heat transfer properties and how they impact on the pressure drop across the radiator.

In view of this, the previous two chapters established a relationship between the pressure drop (ΔP) and heat transfer of a full and sub-scale automotive radiator at various angles of inclination (α). It was found that there was a difference of up to 10% between the unheated and heated pressure drops across the full scale automotive radiator.

In order to quantify this difference, the current chapter aims to determine the effect of heat transfer on the developing velocity profile within an individual channel from the core of an automotive radiator matrix. Laser Doppler Anemometry (LDA) measurements are compared to numerical Computational Fluid Dynamics (CFD) simulations made in ANSYS® FLUENT® 15.0 using the Reynolds-Averaged Navier-Stokes (RANS) Standard $k-\omega$ and Transition SST $k-\omega$ turbulence models.

5.1 Introduction

With wind tunnel testing playing an integral part of vehicle development it is of vital importance for scale models to accurately capture full scale fluid flow phenomena. Development using a scale model within a wind tunnel requires a thorough understanding of the Reynolds number (Re) effects that occur from the similarity parameters. In addition, differences between the full scale and model scale affect both the flow and aerothermodynamic characteristics. This study aims to investigate the heat transfer effects of a scaled channel from an automotive heat exchanger.

Primary research was carried out by Beauvais [107] who investigated effects of the local flow field on the radiator fin's ability to conduct heat. He studied the flow and heat transfer characteristics of flat fins at 10 times scale in a laminar flow

regime. The measurements and visual studies provided detailed information of the velocity profile, boundary layer thickness and the types of flow patterns created in the fin's passage.

Al-Bakhit et al. [108] numerically simulated the flow field in a heat exchanger to determine the impact of different flow parameters on heat transfer and the accuracy of assuming a constant overall heat transfer coefficient (h). The paper further examined the validity of the thin wall assumption (variation of temperature in z-direction was neglected) in the entrance region. The analyses carried out were for developing flows in parallel flow heat exchangers with ducts of the same aspect ratio. The velocity field was assumed to be fully developed, while the thermally developing flow in the two ducts was investigated. The paper concluded that for conventional heat exchangers the thin wall assumption is a reasonable approximation and thus, the performance of the heat exchanger is primarily dependent on the flow in the ducts. This necessitates the examination of the impact of the developing flow velocity profile on the heat exchanger performance.

Al-Bakhit et al. [109] continued numerical investigation into the entrance and wall conduction effects of laminar developing flow within a parallel plate heat exchanger. It was shown that there was a significant change in the heat exchanger effectiveness (ε) in the developing region depending on the thermal conductivity of the material used for the heat exchanger. It was therefore established that to accurately represent the heat transfer of a heat exchanger, one must use three-dimensional geometry. In using three-dimensional geometry and thus accounting for the variation in the overall heat transfer coefficient (h), the numerical heat exchanger length required to reach the maximum possible effectiveness is greatly reduced.

Hasan et al. [110] carried out numerical simulations of three-dimensional developing flows and conjugate heat transfer of a Counter Flow Microchannel Heat Exchanger (CFMCHE). The study was conducted in order to determine the effect of the size and shape of the channel on its performance. Various shapes such as square, iso-triangular, circular and trapezoidal were investigated. The results from the experiments showed that for the same volume of heat exchanger, incrementing the number of channels (and therefore the surface area available for conduction), increased both the effectiveness (ε) of the exchanger and the pressure drop (ΔP). Furthermore, circular channels gave the best overall hydraulic and thermal performance amongst the various tested channel shapes.

Bejan et al. [58] carried out a series of studies pertaining to the optimal spacing of parallel plates cooled by forced convection. They first studied the optimal board-to-board spacing and maximum achievable rate of heat transfer from a package (stack) of parallel boards cooled by laminar forced convection. The optimal spacing was found to be the proportional to the board length raised to the power of 1/2. The maximum total heat transfer rate was found to be proportional to the pressure head

maintained across the stack, $\Delta P^{1/2}$.

Next Bejan et al. [59] addressed the optimum arrangement of stacked parallel plates in free stream cooling. They found that for laminar flow, for Reynolds numbers up to 400, the optimum spacing was equidistant. It was also found that if the free stream and overall dimensions of the stack are specified, there was a resultant optimal number of plates that minimised the overall thermal resistance that occurred between the stack and the free stream.

In order to numerically model a stack with more plates than the optimum number, Bejan et al. [59] determined that the stack could be modelled as a porous medium with Darcy flow. The resulting computations were determined to be computationally quicker and permitted a study on the effect of the fluid/solid thermal conductivity ratio.

Furthermore, Bello-Ochende et al. [60] studied the maximum heat transfer density for plates with multiple lengths in forced convection. They showed that the heat transfer density can be increased beyond the known level for parallel plates with optimal spacing. The paper investigated the technique of inserting smaller plates into the entrance region, which were shown to have thinner boundary layers that fit in the unused isothermal entry flow. Bello-Ochende et al. [60] found that repeating this technique resulted in a sequence of multi-scale flow structures with progressively higher heat transfer densities.

5.2 Mechanisms of Heat Transfer

Flow in the inlet of a straight channel with flat parallel walls assumes that the velocity in the inlet section is uniformly distributed over its width. Due to viscous friction, boundary layers will be formed on both walls and their thickness will increase in the downstream direction. At small distances from the inlet section, the boundary layers grow in the same manner as the growth along a flat plate at zero incidence. The resulting velocity profile consists of two boundary-layer profiles on the two walls joined in the centre by a line of constant velocity [111]. Since the volume of the flow must be the same for every section (closed system), the decrease in the rate of flow near the walls (no-slip condition) must be compensated for by a corresponding increase near the axis (momentum conservation). Thus the boundary layer is formed under the influence of an accelerated external flow, as distinct from the case of the flat plate. For the present study of automotive heat exchangers a number of aerothermal constrains can be imposed. Vehicle velocities vary between 60 mph (26.8 m/s) for average single carriageway within the United Kingdom to 200 mph (89.4 m/s) for a Formula 1 vehicle on a race track. With average radiator matrix core channels being 20 mm long with a 5 mm height [112], this results in a

Reynolds number (Re) range between Re = 4.0×10^4 (v = 30 m/s) to Re = 1.0×10^5 (v = 75 m/s).

Reynolds number is defined as

$$\mathrm{Re} = \frac{\rho v L}{\mu} = \frac{vL}{\nu}, \tag{5.1}$$

where v is the freestream velocity, L is the channel length and the kinematic viscosity of dry air is $\nu = 1.5 \times 10^{-5}$ m^2 s^{-1} at 20 °C. For developing flow, a local Reynolds number (Re_x) is introduced, based on the distance traversed (x) channel length (L). The local Reynolds number is therefore given by

$$\mathrm{Re}_x = \frac{\rho v x}{\mu} = \frac{vx}{\nu}, \tag{5.2}$$

Further constraints can be placed on the maximum temperature that the heat exchangers can reach. Typical automotive cooling fluids operate at around 100 °C (373.15 K). This is possible due to the fact that the cooling systems are pressurised and allow for the liquids to circulate without reaching their boiling point.

The Nusselt number is the ratio between convective and conductive heat transfer and is defined as

$$\mathrm{Nu} = \frac{hx}{k}, \tag{5.3}$$

where h is the convective heat transfer coefficient, x is the characteristic length and k is the thermal conductivity of the fluid. The convective heat transfer coefficient is defined as

$$h = \frac{\overrightarrow{q}}{\Delta T}, \tag{5.4}$$

where $\overrightarrow{q}$ is the heat flux and ΔT is the temperature difference between the plate and the fluid. The laminar local Nusselt number is given by [113]

$$(\mathrm{Nu}_x)_{\mathrm{lam.}} = 0.023\mathrm{Re}_x^{0.8}\mathrm{Pr}^{0.3}, \tag{5.5}$$

where Pr is the Prandtl number and has a value of Pr = 0.713 for dry air at 20 °C. Based on these assumptions the laminar Nusselt number for a 20 mm channel length has a range between Nu = 95 (v = 30 m/s) to Nu = 200 (v = 75 m/s).

For turbulent flow in heat transfer, experimental investigation by Reynolds et al. [72] related the local turbulent Nusselt number as

$$(\mathrm{Nu}_x)_{\mathrm{turb.}} = 0.0296\mathrm{Re}_x^{0.8}\mathrm{Pr}^{0.6}\left(\frac{T_{\mathrm{Plate}}}{T_{\mathrm{Air}}}\right)^{-0.4}, \tag{5.6}$$

where T_{Plate} is the temperature of the heated surface and T_{Air} is the temperature of the free stream fluid. Based on these assumptions the turbulent Nusselt number for a 20 mm channel heated to 373.15 K with a freestream air temperature of 293.15 K has a Nusselt number in the range, Nu = 108 (v = 30 m/s) to Nu = 219 (v = 75 m/s).

5.3 Experimental Methodology

The purpose of the experiment was to obtain data in order to validate the Computational Fluid Dynamics (CFD) turbulence model. The experiment was conducted using a blower wind tunnel at the Centre for Defence Engineering at Cranfield University. A custom working section was fabricated from medium-density fibre board which contained a single glass wall to accommodate the use of a laser for velocity measurements. Additionally the top and bottom walls were fabricated from aluminium to replicate the surface roughness and heat transfer properties of automotive radiator. The working section had a height (y) of 135 mm, width (z) of 160 mm and length (x) of 600 mm, thus having approximately the same aspect ratio as an average radiator matrix core channel [112]. A schematic of the blower wind tunnel working section arrangement is presented in Fig. 5.1.

The channel of the working section was heated by two OMEGA® OMEGALUX silicone rubber fibreglass insulated flexible heater mats adhered to the aluminium faces. The heating mats are of a wire-wound element design with a power density of 15.5 kW m^{-2} with an accuracy of ± 1 °C.The temperature was measured using five OMEGA® self-adhesive K-type thermocouples. The temperature output was controlled using OMEGA® CN79000 1/32 DIN Dual-Zone Controllers with Fuzzy Logic with an accuracy of ± 0.1 °C. The temperature used for the heated case was 100 °C.

Wind tunnel velocity was Reynolds number corrected at 150 rpm (approximately 4 m/s, Re = 1.6×10^5) using a Dewetron signal conditioning rack with barometer and temperature controller boards with a Eurotherms driver unit. The velocity measurements were conducted using Laser Doppler Anemometry (LDA). This was achieved using Dantec FibreFlow LDA optics set up as a 1D system with a 310 mm focal length probe and bespoke $x-y-z$ traverse. The laser used was an ILA 5500A air-cooled multi-line Argon Ion with a 500 mW power output.

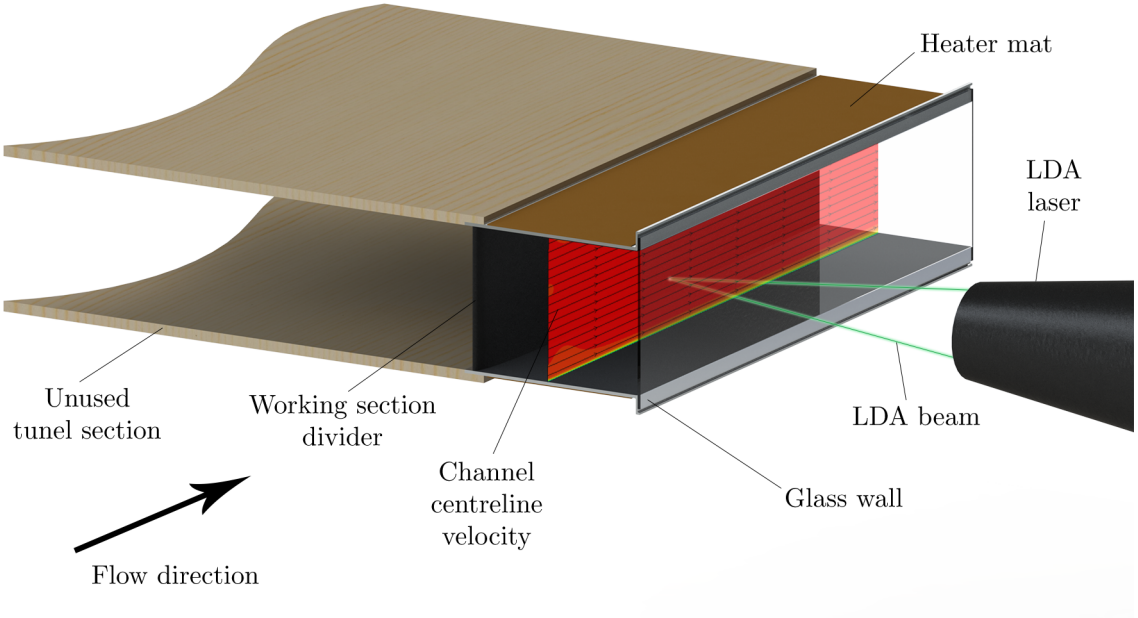

Figure 5.1 Render of Cranfield University Shrivenham's blower wind tunnel working section.

The processor used was a BSA Enhanced with a calibration factor of 4.318 (m/s) / MHz with record length of 64 and a 10 µs record interval, 10 dB gain and 6 dB pedestal attenuation, with 5,000 samples per point. This set-up has an estimated uncertainty of between 1-2% in mean velocity $\left(\overline{U}\right)$ and 3% of rms velocity (u_{rms}). This former estimate is based on comparisons with an equivalent pitot-static measurement.

5.4 Numerical Simulation Methodology

The study was carried out with a three-dimensional CFD simulation of parallel plate channels. It was intended to give a detailed flow field study of the velocity distribution within the channel, as well as the heat transfer effects when the channel is heated.

The discretised meshes were generated using ANSYS® ICEM CFD™, while the simulations were performed in ANSYS® FLUENT® 15.0. The simulations were run on 16 cores (dual Intel E5-2660 Sandy Bridge processors) from Astral II, Cranfield University's supercomputer. Simulations were performed until residuals dropped to $\leq 10^{-6}$. In addition, mass and energy flux were monitored to provided additional confirmation of solution convergence. Each simulation required approximately 8,000 iterations for convergence.

A grid convergence study was carried out in order confirm that any results were independent of grid spacing. This was achieved using 3 meshes with 4.1×10^5, 1.6×10^6, 6.4×10^6 grid cells respectively. The 1.6 and 6.4 million grid cell cases exhibited no variance in the centreline velocity profiles and thus the lower mesh size was use for the simulations (see Appendix F for further information).

The lengths used within the computational notation are normalised with respect to the experimental lengths; the length (x) of 600 mm, height (y) of $\pm$ 67.5 mm and width (z) of $\pm$ 80 mm. This equates to a normalised centre point within the computational domain of (0.5, 0.0, 0.0) for (x/L, y/H, z/W).

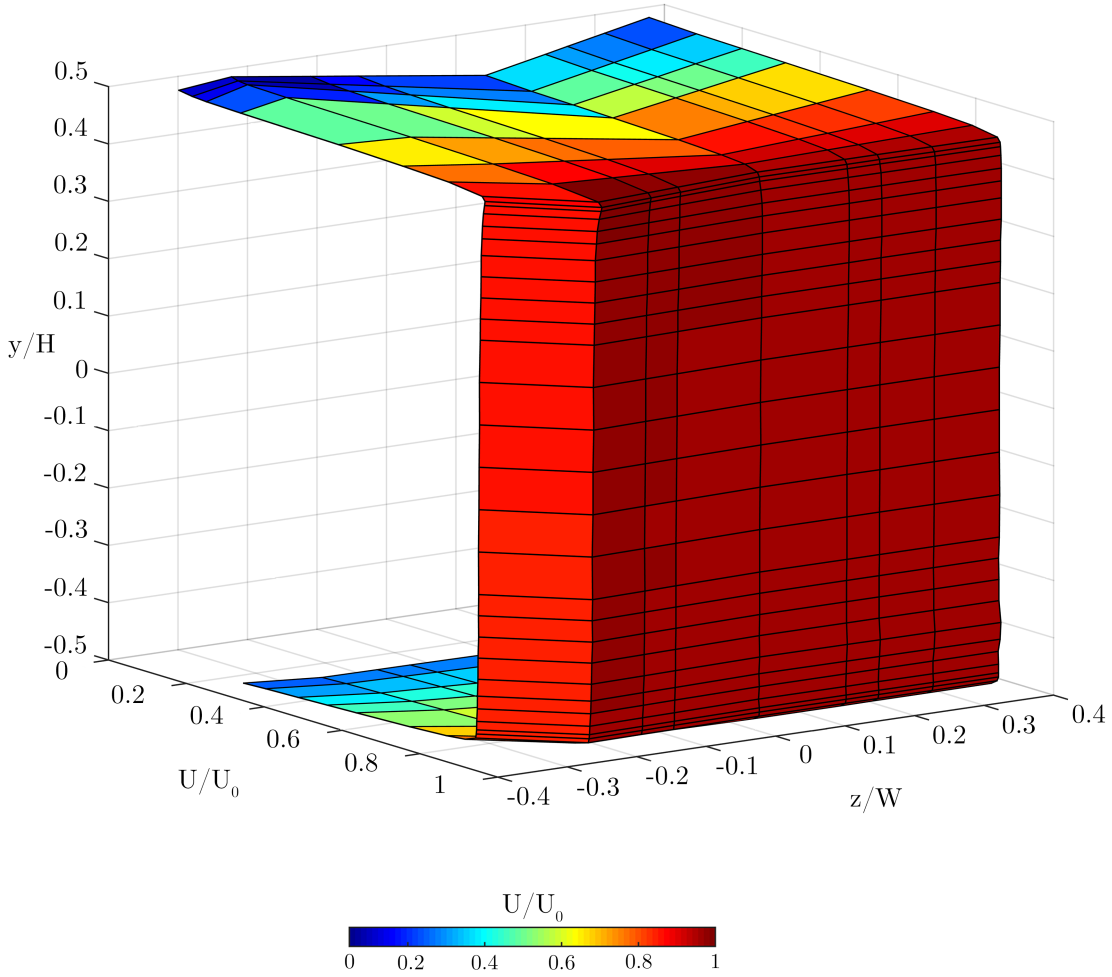

Figure 5.2 Surface plot of normalised (U/U_0) inlet velocity profile.

The node spacing of the chosen mesh was 313 nodes in the length (x) direction, 83 in the width (z) direction and 62 height (y). This equated to a total of 1,610,698

nodes and or to approximately 1 node every 2 mm in the physical domain. This node spacing corresponded to an average dimensionless wall distance (y^+) of ≤ 0.3. This value for y^+ ensured the viscous sublayer was captured and as a result, wall functions were not used, further information is available in Section F.8 of Appendix E.

The simulations were run using the Reynolds-Averaged Navier-Stokes (RANS) Transition SST $k-\omega$ turbulence model [96] shown in Eqs. (5.10) and (5.11). The inlet velocity (shown in Fig. 5.2) and turbulent kinetic energy (k) profiles used within the simulations were obtained from the experimental LDA measurements. The inlet velocity was approximately 4 m/s during the experimental tests with a maximum inlet turbulence intensity (I) of 1.3%. The numerical simulations and experimental results were normalised with respect to the average centreline velocity shown in Fig. 5.2.

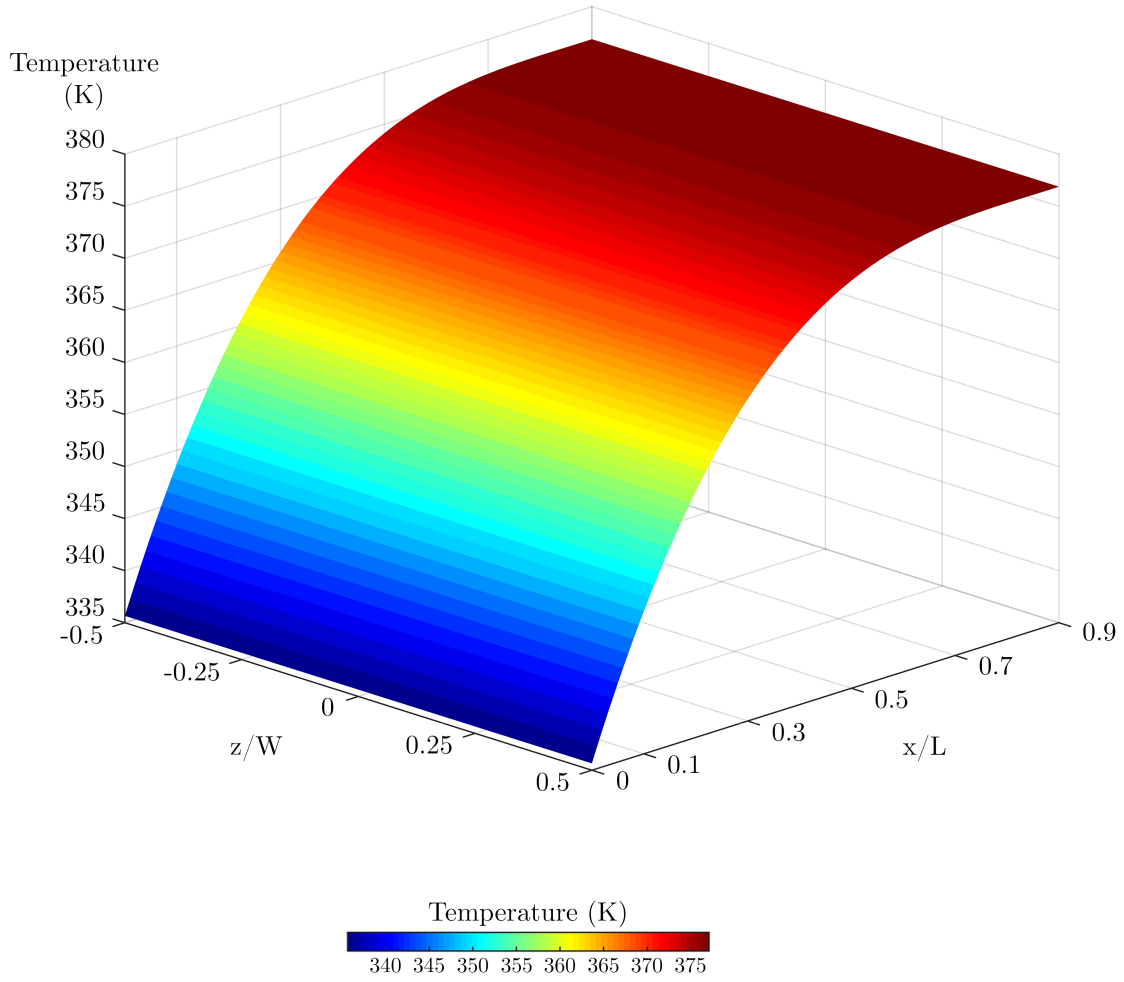

Figure 5.3 Surface plot of upper/lower channel wall temperature profile.

The Reynolds-Averaged Navier-Stokes equation for an incompressible Newtonian fluid is given by [114]

$$\rho\overline{u_j}\frac{\partial\overline{u_i}}{\partial x_j} = \rho\overline{f_i} + \frac{\partial}{\partial x_j}\left[-\overline{p}\delta_{ij} + \mu\left(\frac{\partial\overline{u_i}}{\partial x_j} + \frac{\partial\overline{u_j}}{\partial x_i}\right) - \rho\overline{u_i'u_j'}\right], \tag{5.7}$$

where f_i is a vector of external forces.

Within ANSYS® FLUENT® 15.0 the turbulent kinetic energy (k) and specific dissipation rate (ω) are given by the two transport equations

$$\frac{\partial}{\partial t}(\rho k) + \frac{\partial}{\partial x_i}(\rho k u_i) = \frac{\partial}{\partial x_j}\left(\Gamma_k\frac{\partial k}{\partial x_i}\right) + G_k - Y_k + S_k, \tag{5.8}$$

$$\frac{\partial}{\partial t}(\rho\omega) + \frac{\partial}{\partial x_j}(\rho\omega u_j) = \frac{\partial}{\partial x_j}\left(\Gamma_\omega\frac{\partial\omega}{\partial x_j}\right) + G_\omega - Y_\omega + D_\omega + S_\omega, \tag{5.9}$$

respectively, where G_k represents the generation of turbulent kinetic energy due to the mean velocity gradients, G_ω represents the generation of ω. Γ_k and Γ_ω represent the effective diffusivity of k and ω, respectively and Y_k and Y_ω represent the dissipation of k and ω, respectively. S_k and S_ω are user-defined source terms and D_ω is the cross-diffusion term.

For the Transition SST $k-\omega$ RANS turbulence model, two additional transport equations are used in addition to the SST $k-\omega$ equations. The two additional transport equations are for the intermittency (γ) and the transition momentum thickness Reynolds number ($R\tilde{e}_{\theta t}$), given by

$$\frac{\partial(\rho\gamma)}{\partial t} + \frac{\partial(\rho U_j\gamma)}{\partial x_j} = P_{\gamma1} - E_{\gamma1} + P_{\gamma2} - E_{\gamma2} + \frac{\partial}{\partial x_j}\left[\left(\mu + \frac{\mu_t}{\sigma_\gamma}\right)\frac{\partial\gamma}{\partial x_j}\right], \tag{5.10}$$

$$\frac{\partial(\rho R\tilde{e}_{\theta t})}{\partial t} + \frac{\partial(\rho U_j R\tilde{e}_{\theta t})}{\partial x_j} = P_{\theta t} + \frac{\partial}{\partial x_j}\left[\sigma_{\theta t}\left(\mu + \mu_t\right)\frac{\partial R\tilde{e}_{\theta t}}{\partial x_j}\right], \tag{5.11}$$

respectively, where $P_{\gamma1,2}$, $E_{\gamma1,2}$ are transition source terms and $P_{\theta t}$ is a transition momentum thickness Reynolds number source term. For further information on the implementation of the Transition SST $k-\omega$ RANS models within ANSYS® FLUENT® 15.0 see [96], for further information on the model's background see Langtry et al. [115].

Sutherland's law (shown in Eq. (5.12)) was used for the viscosity formulation, while the incompressible idea gas equation (shown in Eq. (5.13)) was used for the density. The inlet temperature of the freestream flow was set to 293.15K (20 °C). The surface temperature for the heated case used the experimental heat profile shown in Fig. 5.3. For the additional heated cases, the surface temperature was assumed to be uniform at 393.15 K (120 °C) and 413.15 K (140 °C), respectively. In

addition a uniformly heat four sided channel at 373.15 K (100 °C) was also investigated.

Sutherland's law with three coefficients is given by

$$\mu = \mu_0 \left(\frac{T}{T_0} \right)^{3/2} \frac{T_0 + S}{T + S}, \tag{5.12}$$

where μ is the fluid viscosity, μ_0 is the reference viscosity, T is the static temperature, T_0 is the reference temperature and S is the effective temperature (Sutherland constant).

The incompressible ideal gas equation is given by

$$\rho = \frac{p}{\frac{R}{M_W} T}, \tag{5.13}$$

where p is the local pressure, R is the ideal gas constant ($R \simeq 8.314\,\mathrm{J\,K^{-1}\,mol^{-1}}$) and M_W is the molecular weight of the gas.

5.5 Experimental and Numerical Results

5.5.1 Numerical Turbulence Model Selection

Figure 5.4 shows the developing boundary layer profile for both the unheated (blue) and heated (red) velocity profiles. Experimental measurements were taken at horizontal displacements of 50 mm, 175 mm, 300 mm, 425 mm and 500 mm downstream from the inlet, corresponding to $x/L = 0.1$, 0.3, 0.5, 0.7 and 0.9, respectively. The velocity profiles were extracted along the centreline $(z/W) = 0$ of the channel.

Figure 5.4 shows that at the first measured location of 0.1 x/L, the unheated case has a normalised centreline velocity of 1.028. The midpoint measurement location (0.5 x/L) has a normalised velocity of 1.058. The final measured location (0.9 x/L) has a normalised centreline velocity of 1.074.

The corresponding values for the heated (temperature profile shown in Fig. 5.3) case are 1.030, 1.065 and 1.088 for x/L locations of 0.1, 0.5 and 0.9, respectively. This equates to a centreline velocity increase at 0.9 x/L of 1.5% due to heat addition.

Figure 5.5 shows the corresponding developing boundary layer velocity profile for the simulated data of that presented in Fig. 5.4. Two RANS models were compared, the Standard $k - \omega$ (Fig. 5.5a) and the Transition Shear Stress Transport $k - \omega$ (Trans. SST $k - \omega$, shown in Fig. 5.5b). The unheated channel for both turbulence models is shown as a solid blue line and the heated channel as a dashed red line.

Tables 5.1 and 5.2 show the summarised data of the boundary layer growth and centreline velocity increase for the unheated and heated channel, respectively.

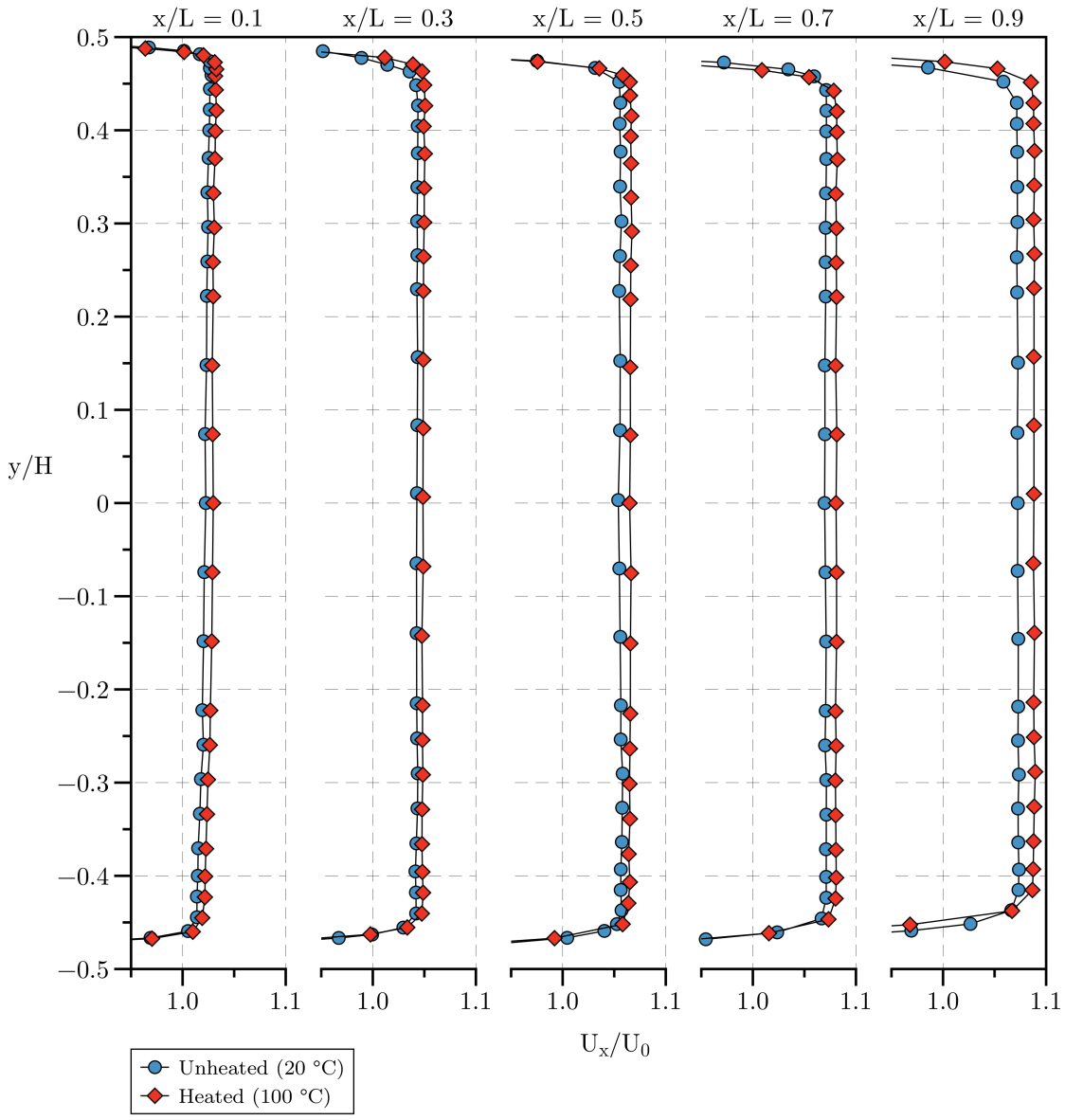

Figure 5.4 Experimental LDA velocity profiles for normalised downstream (x/L) measured locations for an unheated and heated channel.

The tables show an increase in both the boundary layer thickness (δ) and normalised centreline velocity (U_x/U_0) with increased distance along the channel. The Transition SST $k-\omega$ turbulence model more closely matches the overall trend of the experimental data. The Standard $k-\omega$ turbulence model matches closer to the experimental normalised centreline velocity increase, however, overpredicts the

boundary layer growth by over 2.5 times the experimental data. The difference in boundary layer thickness was negligible for the experimental and simulated data between the heated and unheated cases.

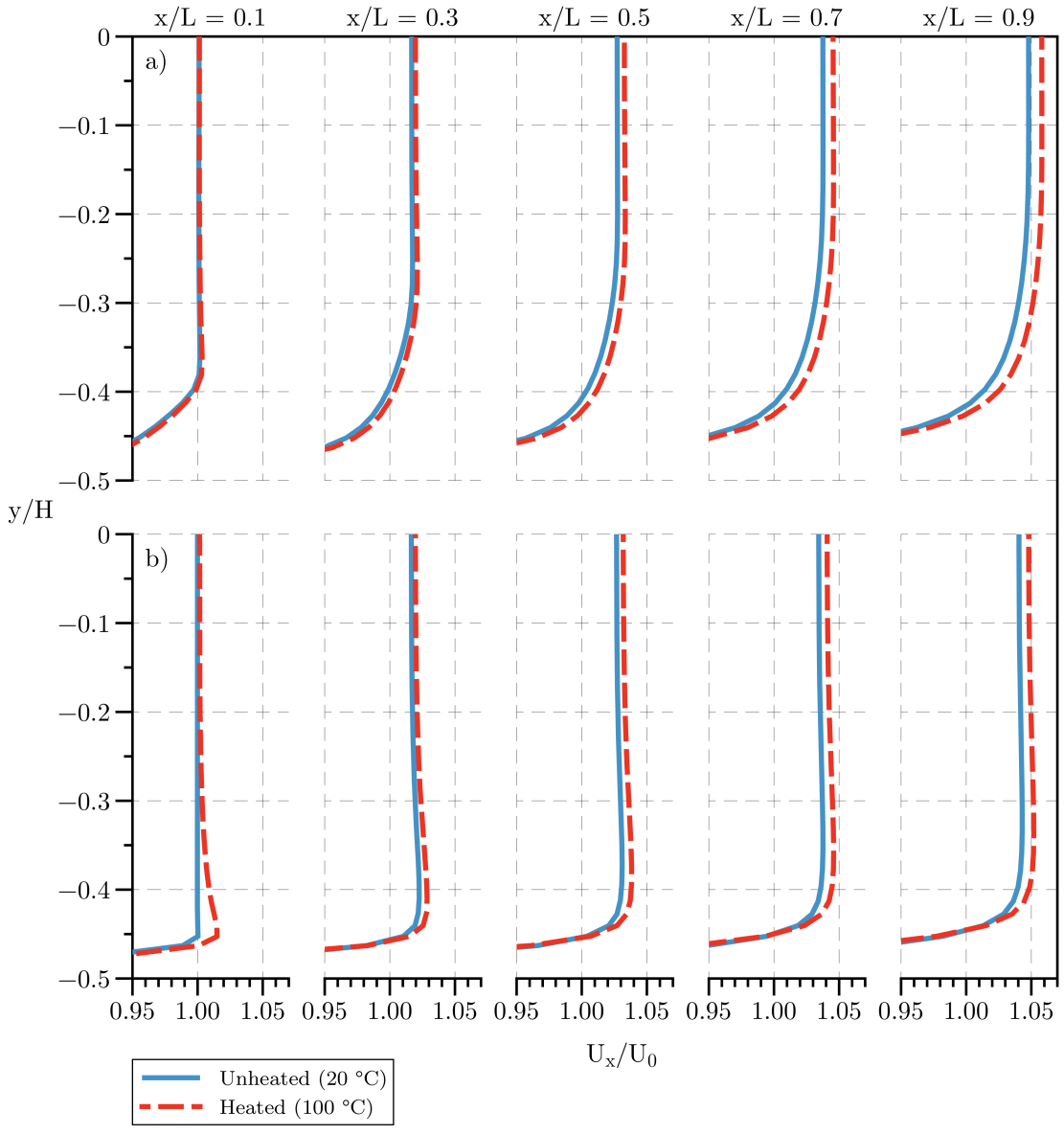

Figure 5.5 Computational Fluid Dynamics (CFD) simulated velocity profiles for normalised downstream (x/L) measured locations for an unheated and heated channel. Upper plot (a) is the Standard $k-\omega$ turbulence model and the lower plot (b) is the Transition SST $k-\omega$ turbulence model.

The velocity overshoot shown in Fig. 5.5b at $x/L = 0.1$ is not a numerical effect but a physically valid result. The overshoot is discussed in more detail on page 95.

Table 5.1 Boundary layer growth and centreline normalised velocity (U_x/U_0) development for experimental and numerically simulated data on an unheated channel.

Unheated							
		Experimental		$k-\omega$		Trans. SST $k-\omega$	
x/L	Re_x	δ (m)	U_x/U_0	δ (m)	U_x/U_0	δ (m)	U_x/U_0
0.0	0.0	0.005	1.000	0.005	1.000	0.005	1.000
0.1	15,712.8	0.004	1.028	0.012	1.001	0.005	1.001
0.3	47,650.0	0.006	1.044	0.018	1.017	0.006	1.016
0.5	79,095.1	0.006	1.058	0.021	1.027	0.008	1.027
0.7	110,565.0	0.007	1.071	0.023	1.038	0.009	1.034
0.9	142,576.6	0.009	1.074	0.024	1.048	0.010	1.041

Table 5.2 Boundary layer growth (δ) and centreline normalised velocity (U_x/U_0) development for experimental and numerically simulated data on a heated channel.

Heated							
		Experimental		$k-\omega$		Trans. SST $k-\omega$	
x/L	Re_x	δ (m)	U_x/U_0	δ (m)	U_x/U_0	δ (m)	U_x/U_0
0.0	0.0	0.005	1.000	0.005	1.000	0.005	1.000
0.1	15,712.8	0.004	1.030	0.012	1.001	0.005	1.002
0.3	47,650.0	0.006	1.049	0.018	1.020	0.006	1.020
0.5	79,095.1	0.006	1.065	0.021	1.033	0.008	1.032
0.7	110,565.0	0.007	1.081	0.023	1.045	0.009	1.041
0.9	142,576.6	0.009	1.088	0.024	1.058	0.010	1.048

The final measurement location (0.9 x/L) from Tables 5.1 and 5.2 is presented graphically in Fig. 5.6. The figure shows that at the first measured location of 0.1 x/L, the unheated case has a normalised centreline velocity of 1.000. The midpoint measurement location (0.5 x/L) has a normalised velocity of 1.027. The final measured location (0.9 x/L) has a normalised centreline velocity of 1.041.

The Standard $k-\omega$ model predicts the final velocity increase due to heat addition to be 1.0% compared to the Transition SST $k-\omega$ model's prediction of 0.7%. The closer approximation of the Standard $k-\omega$ model is due to a more turbulent boundary profile resulting in increased heat transfer over the more laminar prediction of the Transition SST $k-\omega$ model. This is further illustrated in Fig. 5.7, which shows the local Nusselt number as a function of the local Reynolds number.

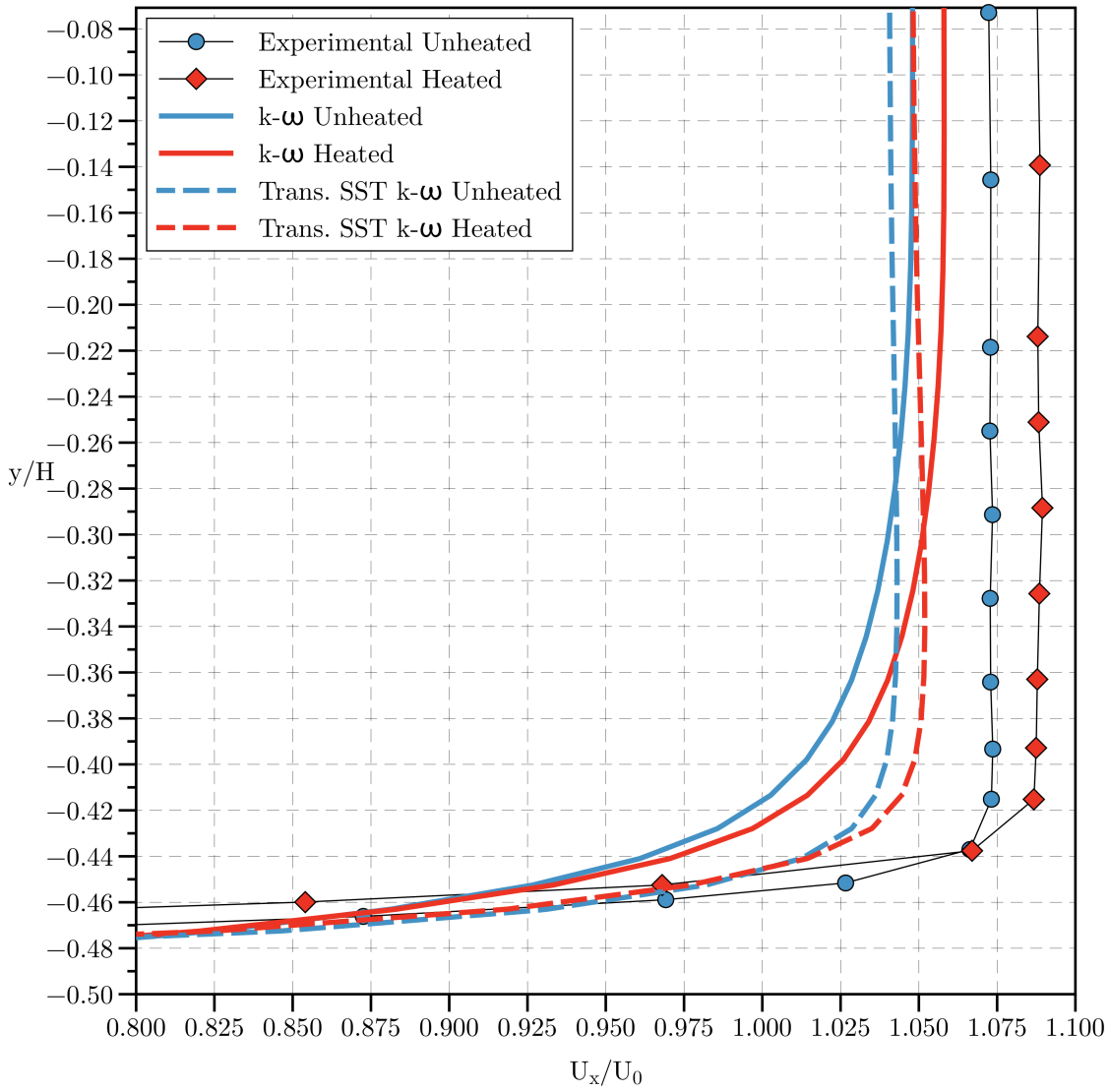

Figure 5.6 Experimental and CFD (Standard $k-\omega$ is plotted as solid lines and Transition SST $k-\omega$ is plotted as dashed lines) boundary layer profiles at 0.9 x/L, for an unheated and heated channel.

The Standard $k-\omega$ turbulence model (using the experimental turbulence intensity of 1.3%) is in good agreement to previously obtained experimental data of Reynolds et al. [72] at a turbulence intensity level of 3%. The Transition SST $k-\omega$ (at a turbulence intensity of 1.3%), is closer to the empirical laminar heat transfer suggest by Incropera et al. [113].

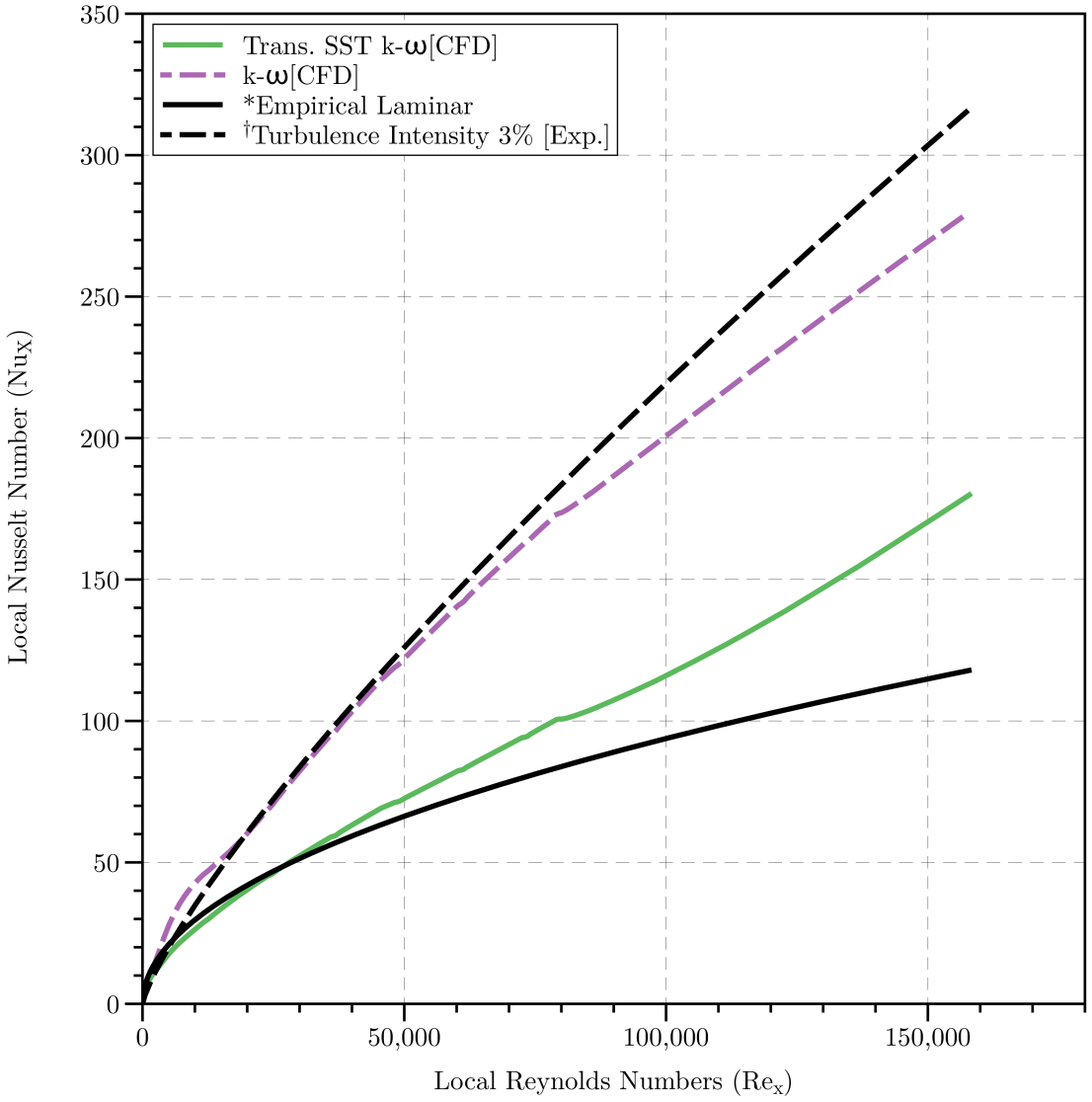

Figure 5.7 Local Nusselt number vs. local Reynolds number for *laminar, reproduced from Incropera et al. [113], CFD ($k-\omega$ is dashed purple line and Transition SST $k-\omega$ is solid green line) and †turbulent flow, reproduced from Reynolds et al. [116].

Due to the Transition SST $k-\omega$ matching closer to the experimental boundary layer growth, this model was chosen for the heat-transfer study. Comparison at the measured locations with the experimental data is shown in Fig. 5.11. Whist the Transition SST $k-\omega$ is more accurate in predicting the flow within the channel than the Standard $k-\omega$ model, there is still a discrepancy between the turbulence model and the experimental data. Figure 5.8 shows the dimensionless velocity profiles for the experimental and CFD results.

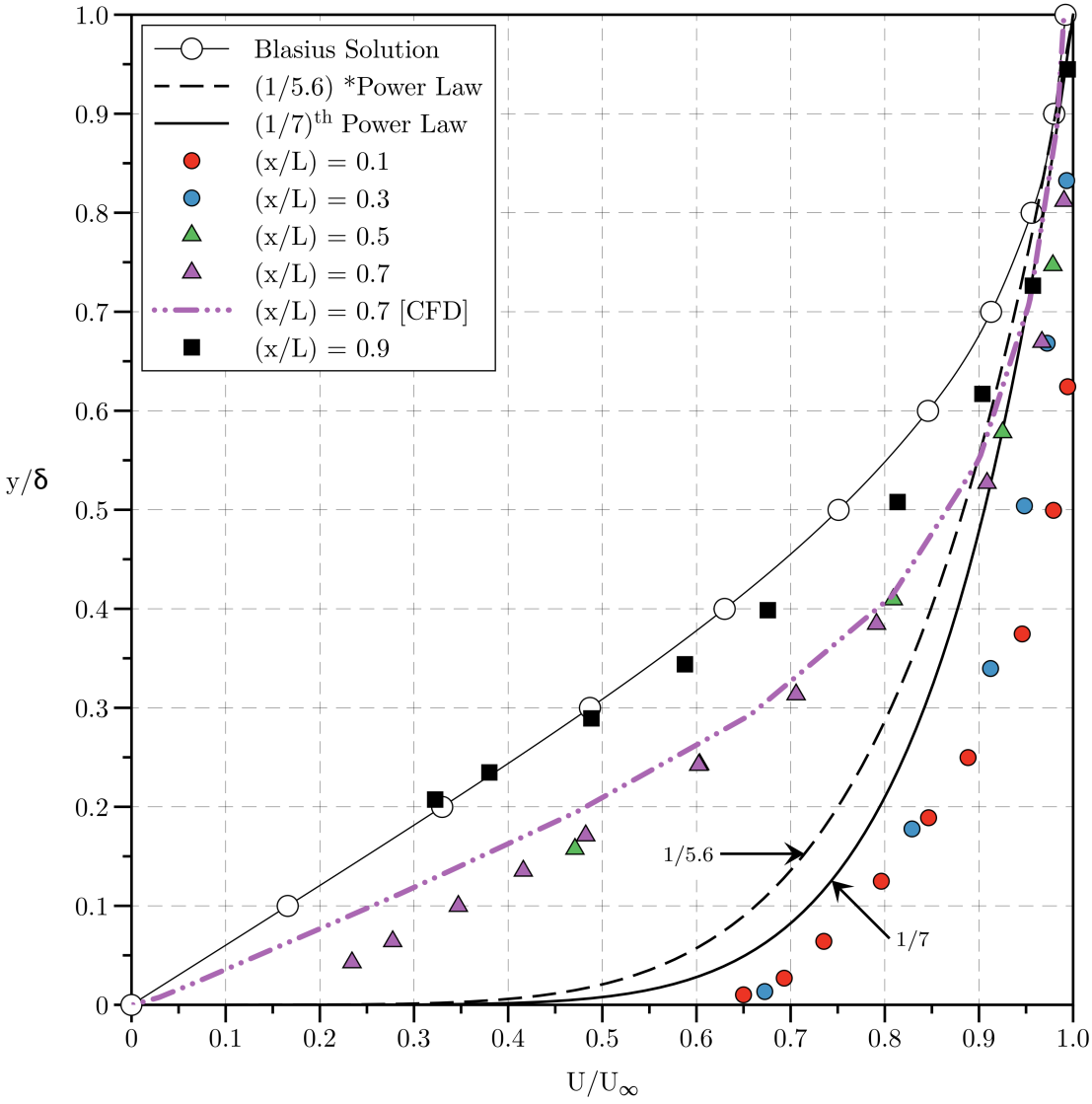

Figure 5.8 Dimensionless laminar and turbulent channel velocity profiles, *reproduced from Reynolds et al. [116].

The entrance region ($x/L = 0.0 \rightarrow 0.3$) to the channel, shows the dimensionless velocity profile is highly turbulent and is in good agreement with experimental data obtained by Prandtl [117] and Reynolds et al. [116]. This is also reflected by a higher centreline turbulence intensity (I) of approximately 2.8% compared to the channel average of approximately 1.0% (shown in Fig. 5.10). This suggests an entrance region effect most likely caused by the geometry of the working section and the physical attachment of the reduced working section to the wind tunnel. As the flow develops within the channel ($x/L = 0.3 \rightarrow 0.9$), the rms ($u_{rms}$) and subsequently the turbulence intensity (I) decreases (shown in Fig. 5.10). This reduction in turbulence intensity is due to the viscous dissipation of the entrance turbulence. This effect is also present on automotive radiators, radiator manufacturers overcome this dissipation via the addition of louvres to the channels used in the radiator. An example of a radiator louvres is shown in Fig. 5.9. The louvres act to increase the overall surface area available for heat transfer and maintain a turbulent boundary layer within the channel to aid in heat transfer.

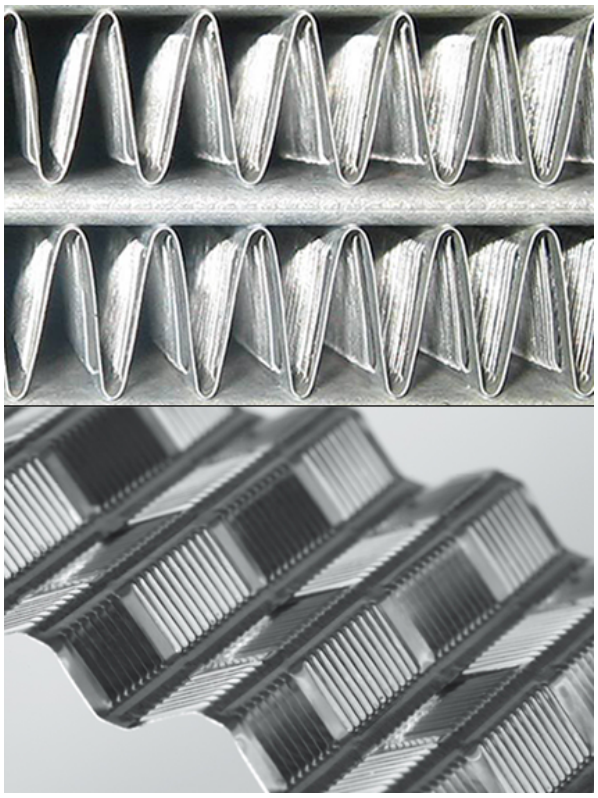

Figure 5.9 Radiator louvres used for increasing heat transfer [118].

The remaining flow reduces in turbulence intensity towards a transitional profile, the CFD profile extracted at $x/L = 0.7$ is in good agreement with this. The CFD

simulation used the velocity inlet (U_0) and rms (u_{rms}) values obtained from the experimental inlet of the working section. This inlet section had a reduced turbulence level of 1.04% compared to the maximum of 2.8% of the working section. The CFD therefore does not capture the temporary turbulent disturbance present near the inlet. The CFD representation can therefore be assumed to model the average effects within the channel assuming no entry length effects.

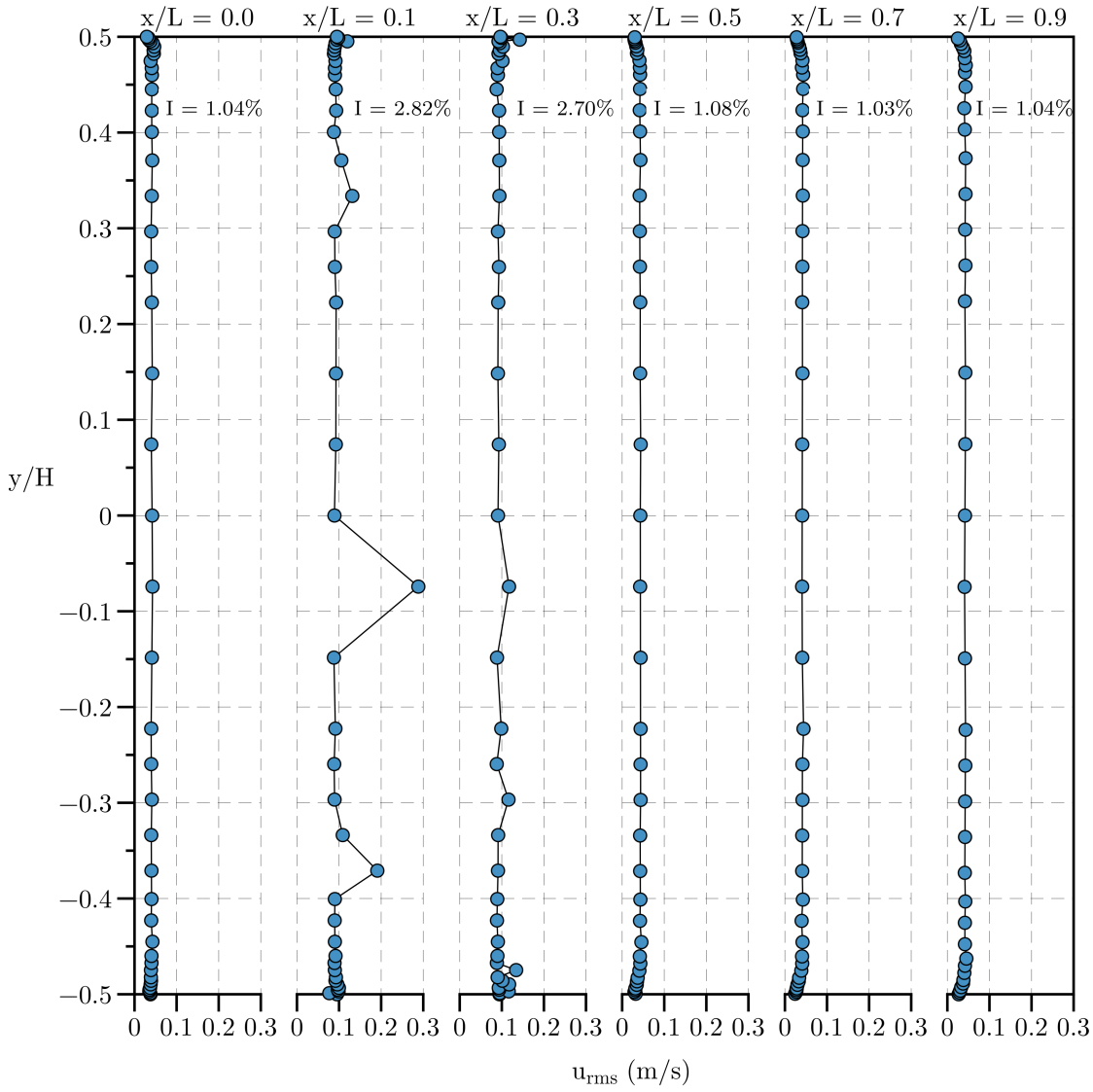

Figure 5.10 Experimental turbulence intensity (I) and rms velocity (u_{rms}) values for the downstream measured locations (x/L).

5.5.2 Developing Heated Channel Flow

5.5.2.1 Velocity Development within the Channel

The experimental and CFD simulated data for four downstream measured locations is shown in Fig. 5.11.

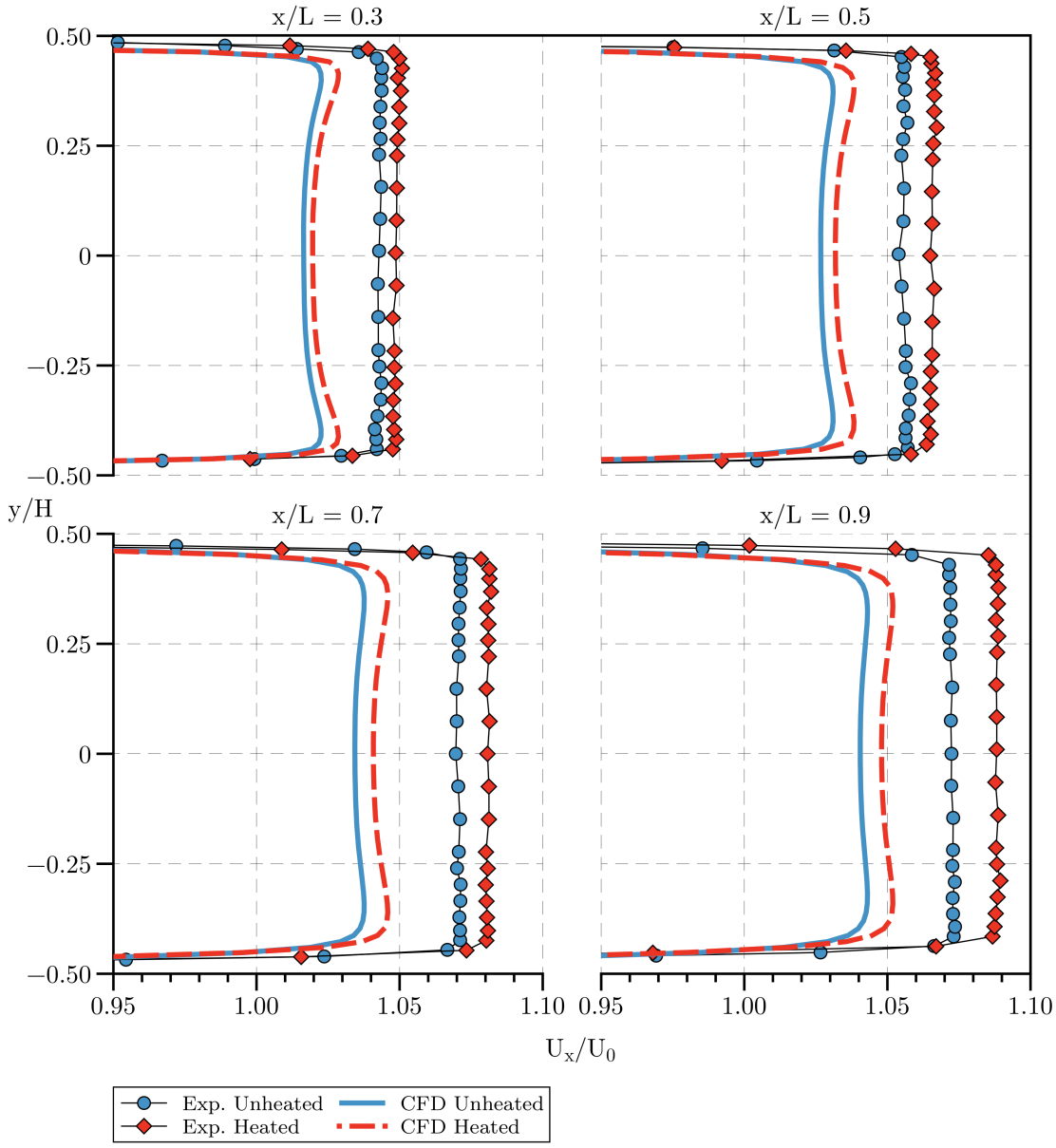

Figure 5.11 Experimental and CFD velocity profiles for downstream measured locations (x/L) for an unheated and heated channel.

Figure 5.11 shows at the four measured locations (0.3, 0.5, 0.7 and 0.9 x/L) that the CFD under predicts the centreline velocity for both the unheated and heated cases. The final measured location (0.9 x/L) has an experimental unheated and heated value of 1.074 and 1.088, respectively (1.5% due to heat addition).

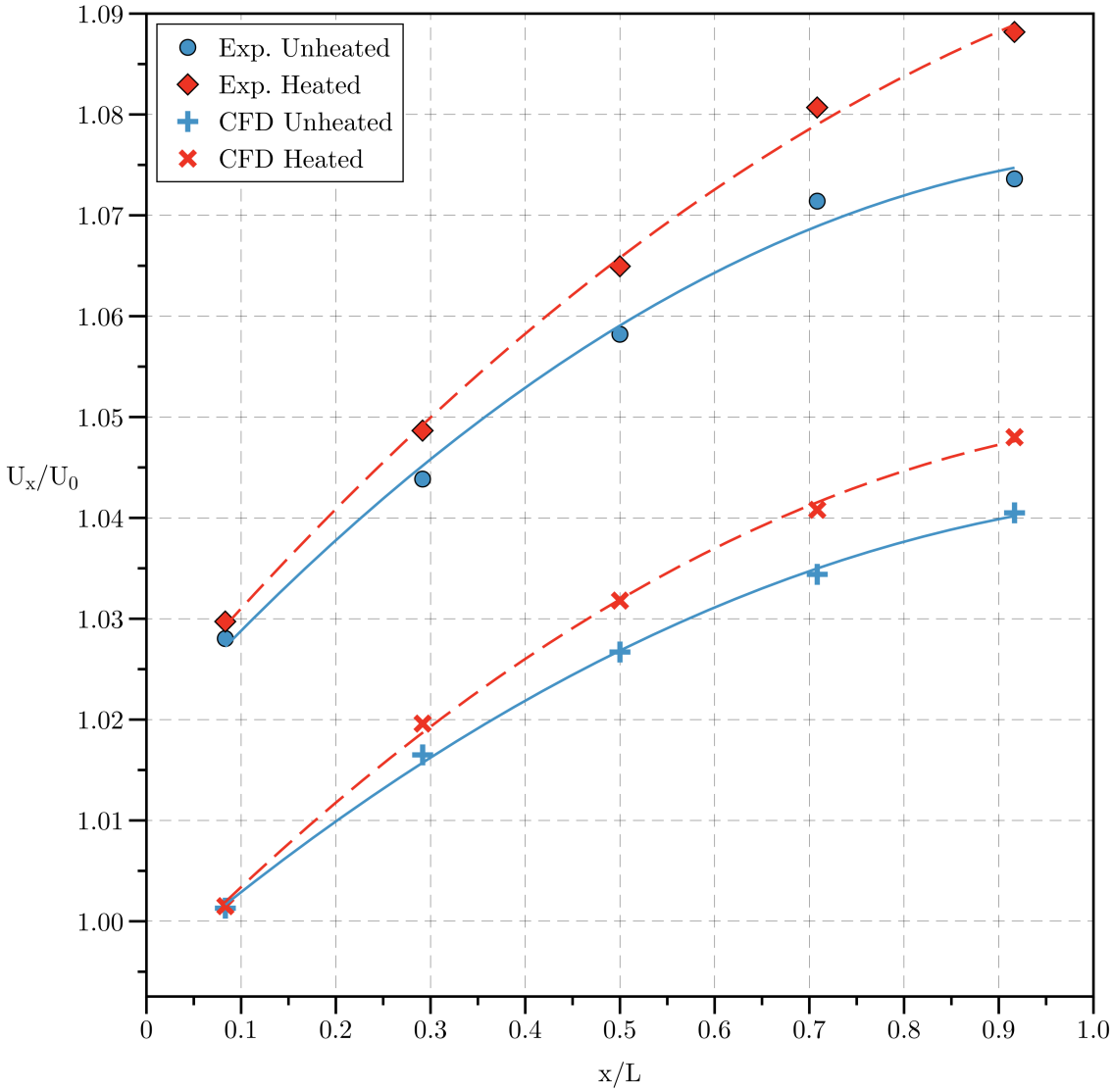

Figure 5.12 Centreline velocity for experimental and CFD data at downstream measured locations (x/L) for an unheated and heated channel.

The corresponding CFD value for the unheated case are 1.041 (-3.1% compared to experimental) and heated case 1.048 (-3.7% compared to experimental). The

experimental data showed a centreline velocity increase of 1.5% compared to the CFD predicted value of 0.7% due to heat addition, as shown in Fig. 5.12.

The heat transfer for the CFD simulations is presented in Table 5.3. The table shows the boundary layer growth for a heated channel for both the experimental and CFD data. The experimental and CFD data both predicted little variation in the boundary layer growth between the unheated and heated cases. The difference in thickness was within experimental measurement error and therefore, only the heated cases are reported.

The Transition SST $k-\omega$ correctly predicts the growth in boundary layer thickness, with a final thickness (δ) at $x/L = 0.9$ of 9 mm for experimental and 10 mm for CFD.

Table 5.3 Boundary layer growth (δ) and heat transfer (h) for experimental and numerically simulated developing channel flow.

		Experimental	CFD (Trans. SST $k-\omega$)				
x/L	Re_x	δ (m)	δ (m)	$\overrightarrow{q}$(W/m^2)	h	Nu_x	St_x
0.0	0.0	0.005	0.005	7,310.5	102.3	0.0	-
0.1	15,712.8	0.004	0.005	1,113.0	14.1	34.6	0.0031
0.3	47,650.0	0.006	0.006	874.7	9.5	70.8	0.0021
0.5	79,095.1	0.006	0.008	817.0	8.1	100.5	0.0018
0.7	110,565.0	0.007	0.009	741.2	7.3	126.1	0.0016
0.9	142,576.6	0.009	0.010	743.4	7.2	161.5	0.0016

Figure 5.11 shows that the computational results do not obtain their maximum velocity at the centreline. This phenomenon has been observed by several authors [119–123]. The velocity overshoots, close to the wall surface, occur due to the relatively large shear stresses in the entrance region of the developing flow. In solving the Navier-Stokes equations this generates a valid, physical solution that can be observed experimentally [124]. This effect, however, is missed by boundary layer theory.

Boundary layer theory splits the fluid flow within the channel into an inner flow (boundary layer) and an outer flow (accelerating core flow). The inner flow is were the boundary layer equations are valid, in the outer layer flow, however, boundary layer theory [111] assumes that the boundary layer is of negligible thickness in comparison to the channel height. In reality, however, the outer flow (close to the edge of the boundary layer) is displaced by the finite thickness of the boundary layer and is therefore accelerated. The velocity profile at the edge of the boundary layer

is therefore slightly greater than 1.0 (U_x/U_0). Far from the edge of the boundary layer, the core flow in the centre of the channel decays to $U_x/U_0 = 1.0$.

Certain authors assume the centreline velocity to be equal to the maximum of the overshoot [122], whilst others [121] assume the effect to be a local overshoot in the boundary layer.

If the velocity profile is assumed to be linear (at the point of maximum overshoot), the corresponding normalised velocities (measured at $x/L = 0.3$, 0.5, 0.7 and 0.9) are 1.001, 1.031 and 1.043, respectively for the unheated case. For the heated case, the corresponding values are 1.051 (+1.5% over unheated), 1.040 (+0.7% over unheated) and 1.052 (+0.9%). Whilst this provides a closer match to the experimental heat transfer of 1.5%, the remaining analysis will focus on the centreline values.

5.5.2.2 Thermal Development within the Channel

The CFD calculated thermal boundary layer (δ_H) profiles are shown in Fig. 5.13 as a function of downstream distance (x/L).

The measured boundary layer thicknesses for the velocity (δ) and thermal (δ_T) are shown in Table 5.4. Due to the temperature on the heated channels varying as a function of the downstream distance (x/L), the thermal boundary layer thickness (δ_H) was measured with respect to the surface temperature at each measured location rather than a uniform temperature.

Table 5.4 CFD velocity (δ) and thermal (δ_T) boundary layer thickness as a function of Reynolds number (Re).

x/L	Re_x	δ (m)	δ_T (m)	$\frac{\delta}{\delta_T}$
0.0	0.0	0.005	0.003	2.03
0.1	15,712.8	0.005	0.005	0.88
0.3	47,650.0	0.006	0.007	0.84
0.5	79,095.1	0.008	0.009	0.84
0.7	110,565.0	0.009	0.009	1.01
0.9	142,576.6	0.010	0.011	0.96

Pohlhausen [125] found an empirical relationship for laminar flow between the ratio of the developing velocity and thermal boundary layers, given by

$$\frac{\delta}{\delta_T} = \mathrm{Pr}^{1/3} = (0.713)^{1/3} = 0.89, \tag{5.14}$$

where Pr = 0.713 for dry air at 20 °C.

Incropera et al. [113] stated that for turbulent flow, this ratio $\left(\frac{\delta}{\delta_T}\right)$ is approximately 1.0. From Table 5.4 the ratio between the velocity and thermal boundaries varies between a laminar and turbulent solution, with the thermal boundary layer being thicker than the velocity boundary layer after $x/L = 0.3$.

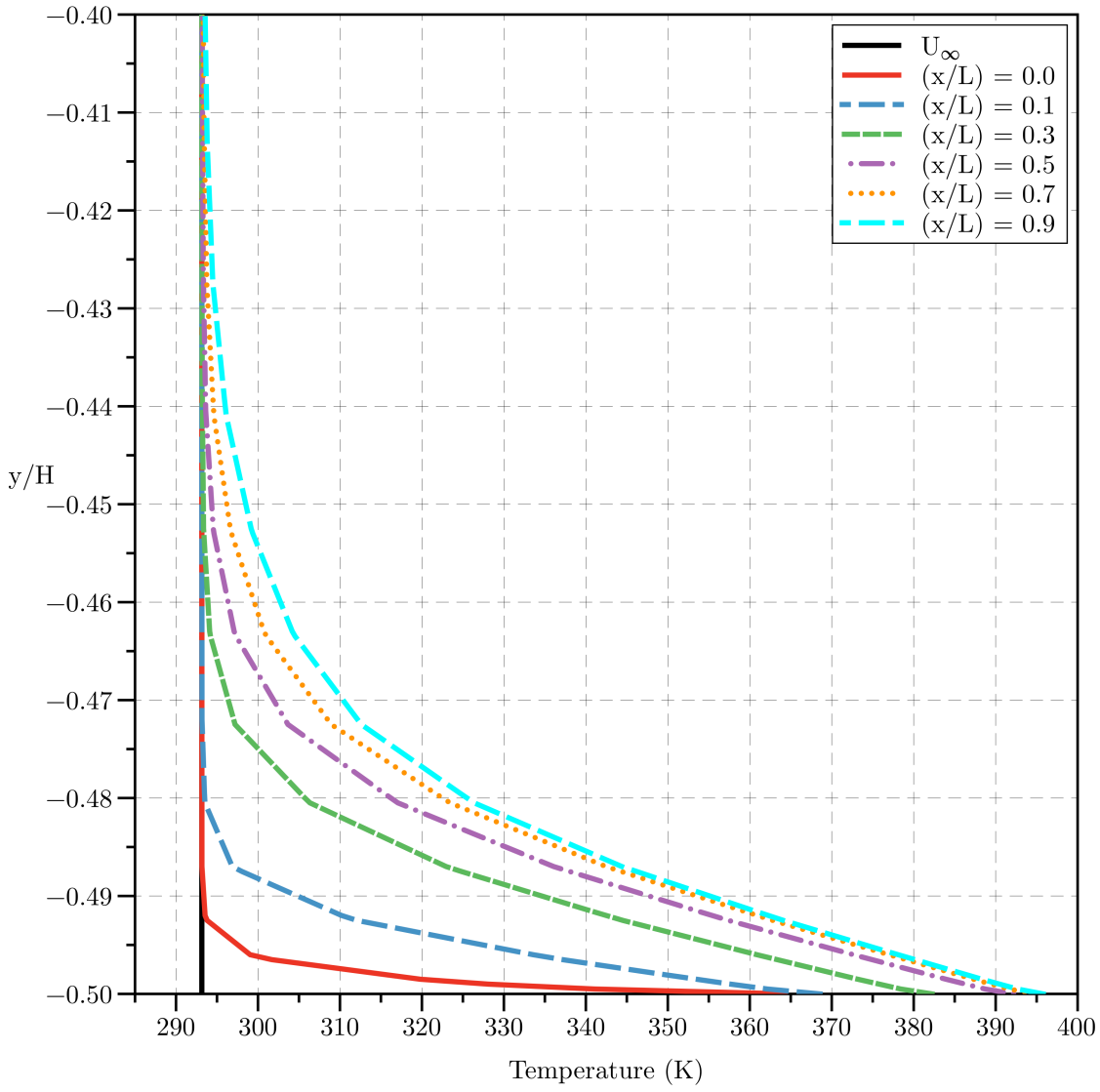

Figure 5.13 Computational Fluid Dynamics (CFD) thermal boundary layer (δ_T) vs. channel height (y/H) for downstream measured locations (x/L).

5.5.3 Flow Development within a Fully Heated Channel

Heat exchangers rarely contain insulated materials separating the channels. Even poor heat conductors (such as wood and glass) used within the experiment conduct heat to a certain extent.

The measurement technique of Laser Doppler Anemometry (LDA) placed a constraint on the experiment. The laser used within the experiment required the geometry to have at least one single wall with good optical transmission properties. This requirement, however, is not present on actual heat exchangers.

A second CFD simulation was therefore performed whereby the wood and glass materials were replaced by aluminium, resulting in four walls heated to a uniform temperature of 373.15K (100 °C). In addition, the original simulation was re-run with a uniform temperature of 393.15K and 413.15K (120 °C and 140 °C, respectively) on the aluminium walls.

Figure 5.14 shows the CFD results obtained for unheated (solid blue line), heated (120 °C, dashed red line), heated (140 °C, dotted red line) and heated (100 °C on four aluminium walls, solid black line). The corresponding heat flux ($\overrightarrow{q}$) and heat transfer coefficient (h) data is shown in Table 5.5.

Table 5.5 Heat transfer (h) for numerically simulated developing channel flow of varying channel wall temperatures.

		120 °C		140 °C		[1]100 °C	
x/L	Re_x	$\overrightarrow{q}$ (W/m^2)	h	$\overrightarrow{q}$ (W/m^2)	h	$\overrightarrow{q}$ (W/m^2)	h
0.0	0.0	9953.3	99.5	11895.6	99.1	7997.6	100.0
0.1	15,712.8	1303.8	13.0	1539.8	12.8	1062.6	13.3
0.3	47,650.0	855.4	8.6	1011.0	8.4	698.3	8.7
0.5	79,095.1	732.8	7.3	869.5	7.2	595.7	7.4
0.7	110,565.0	695.6	7.0	830.7	6.9	560.3	7.0
0.9	142,576.6	698.3	7.0	838.7	7.0	557.2	7.0

The results obtained show that additional heat increases the centreline velocity at each of the measured locations. At a downstream location of 0.3 x/L the heated case of 120 °C and 140 °C correspond to centreline velocity increases of 0.3% and

[1]Heated on all four walls of the channel.

0.4% over the unheated CFD case, respectively. The channel with four heated sides at 100 °C resulted in an increase of 0.5% over the unheated CFD case.

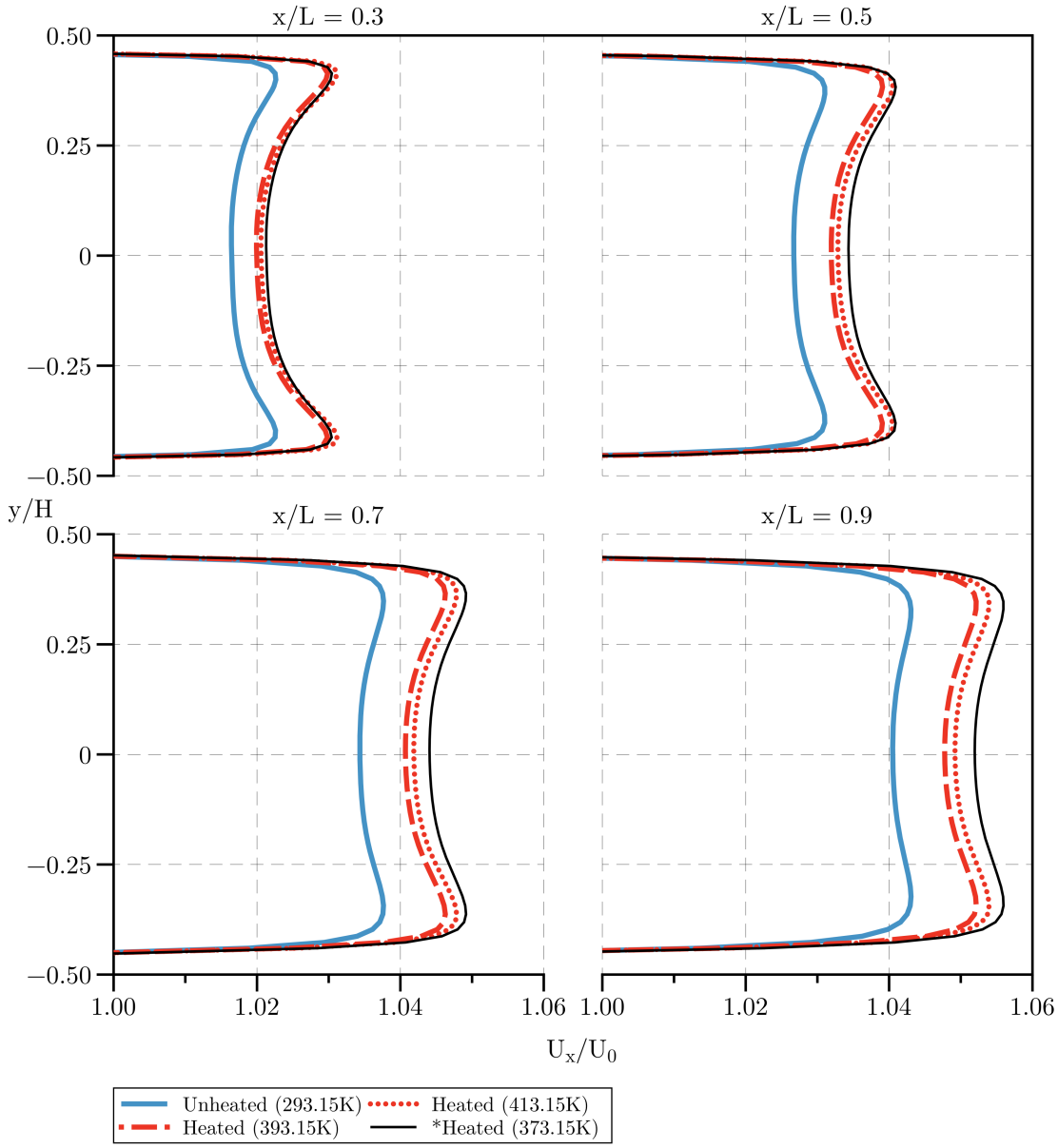

Figure 5.14 Computational Fluid Dynamics (CFD) normalised centreline velocities (Ux/U_0) for downstream measured locations (x/L) for an unheated and various heated cases. *Heated on all four walls of the channel.

At 0.5 x/L the velocity increases for 120 °C and 140 °C are 0.5% and 0.6%, respectively. The four heated sides had a velocity increase of 0.7% over the unheated

case.

At 0.7 x/L the velocity increase for 120 °C and 140 °C are 0.6% and 0.7%, respectively. The four heated sides had a velocity increase of 0.9% over the unheated case

At the final measured location of 0.9 x/L, the centreline velocity increases for 120 °C and 140 °C were 0.7% and 0.8%, respectively, with the four sided case producing the largest increase of 1.1%. The heat transfer coefficient (h) for the four walls at 100 °C is higher than for the dual walls heated to higher temperatures (120 °C and 140 °C). This is despite the total heat flux ($\overrightarrow{q}$) for the 100 °C four heated walls being lower than the 120 °C and 140 °C walls. This is due to the wall having twice the surface area with which to transfer heat and as a result, is able to transfer more overall heat along the channel resulting in the greatest velocity increase.

5.6 Chapter Conclusions

The main aim of this chapter was to investigate the effects of hydrodynamically and thermally developing fluid flow within a simplified radiator channel. It was established from Chapter 4 that the pressure drop (ΔP) across an automotive radiator increased when heated. The mechanisms behind this increase in pressure drop were therefore investigated. Due to the complex geometry associated with an automotive heat exchanger, a simplified (without louvres) channel from a typical automotive radiator was used for the experimental and numerical investigations.

Experimental measurements were taken on the channel using Laser Doppler Anemometry and the results were compared with numerical simulation using various Reynolds-Averaged Navier-Stokes (RANS) turbulence models.

Based on results from this study, the following conclusions can be drawn:

- The results obtained from experimental testing indicate that for an unheated channel, the hydrodynamically developing flow increased the centreline velocity by 7% over the inlet velocity ($U_x/U_0 = 1.07$). When two sides of the channel were heated to approximately 100 °C, the centreline velocity further increased to 9% resulting in an increase of 1.5% over the unheated case.

- Numerical simulations using the Standard $k-\omega$ and Transition SST $k-\omega$ turbulence models found that the Standard $k-\omega$ turbulence model more accurately matched the increase in centreline velocity due to heat. The Standard $k-\omega$ turbulence model produced a centreline velocity increase of 1.0% compared to the inlet velocity (U_0) whereas the Transition SST $k-\omega$ produced an increase of 0.7% over the inlet velocity. The reason for the velocity increase difference between models was that the Standard $k-\omega$ model used a fully turbulent profile for the heat transfer compared to a profile between laminar and fully turbulent used by the Transition SST $k-\omega$.

- The Standard $k-\omega$ model predicted a boundary layer growth 2.5 times larger than the experimental data. The Transition SST $k-\omega$, however, was more accurate in predicting the boundary layer growth predicting a thickness of 10 mm compared to the experimental thickness of 9 mm close to the end of the channel ($x/L = 0.9$). The Transition SST $k-\omega$ turbulence model, however, underpredicted the centreline velocity increase due to the addition of heat, predicting an increase of 0.7% in the centreline velocity at $x/L = 0.9$ compared to 1.5% obtained from experimental measurements at the same location.

- Based on the Transition SST $k-\omega$ model predicting a more accurate boundary layer growth and matching the shape profile (y/δ) of the experimental data,

this turbulence model was found to be the most accurate representation of a hydrodynamically and thermally developing flow within a channel.

- Numerical simulations using the Transition SST $k - \omega$ turbulence mode with wall temperatures of 120 °C and 140 °C found centreline velocity increase of 0.7% and 0.8%, respectively over the unheated case. Extension into all four sides of the channel being heated to 100 °C indicated an estimated centreline velocity increase of 1.1% over the unheated case, compared to 0.7% when only two of the sides were heated.

Chapter 6

Conclusions and Future Work

6.1 Conclusions

6.1.1 Initial Project Objectives

The project objectives outlined at the beginning of this research were:

Experimental

- To determine the relationship between the pressure drop (ΔP) and porosity (β) for porous media as a function of the angle of inclination (α).
- To investigate the relationship between pressure drop (ΔP) and inclination angle (α) for a full scale radiator and the effect of heat transfer on this relationship.
- To determine the effective porosity ($\beta_{\text{eff.}}$) required to account for the change in the pressure drop (ΔP) due to heat transfer.
- To investigate the heat rejection performance of the radiator as a function of the inclination angle.
- To calculate the pressure drop and heat transfer coefficients required for numerical simulation.
- To investigate the mechanisms behind the increase in pressure drop due to heat addition.

Computational Fluid Dynamics

- To use the relationship between pressure drop (ΔP) and porosity (β) obtained from the experimental data to simulate porous media.
- To investigate the numerical methodology of simulating inclined porous media.
- To accurately simulate the aerodynamic and thermal properties of a full scale radiator.
- To simulate the effects of inclination on the numerical model.
- To simulate simultaneously developing hydrodynamic and thermal channel flow associated with a matrix channel within an automotive radiator.

6.1.2 Summary of Project Findings

The relationship between the pressure drop coefficient ($\Delta P/q$) and porosity (β) was established experimentally in a duct blower wind tunnel at Cranfield University. Screens of variable porosity (β) in the range $0.41 \leq \beta \leq 0.76$ were investigate from 7 m/s up to a maximum velocity of 35 m/s. This equated (based on screen thickness) to a Reynolds number (Re) range of $200 \leq \text{Re} \leq 2100$. In addition, the effect of screen inclination on the pressure drop coefficient was investigate for inclination angles (α) of 0°, 15°, 30° and 45°.

For screen porosities of $\beta \geq 0.5$, the pressure drop coefficient ($\Delta P/q$) was found to be independent of Reynolds number above $\text{Re} = 500$. Below this critical Reynolds number, the measured pressure drop coefficient decreased exponentially with an increase in screen porosity. This trend was valid for all angles of inclination tested. In addition, for a given porosity, $\Delta P/q$ was found to reduce as the angle of inclination increased. The magnitude of this effect became smaller as the porosity increased until a threshold value of $\beta = 0.6$ beyond which $\Delta P/q$ was observed to be independent of the angle of inclination (α).

The screen permeability (K) was found to increase with both increasing screen porosity and angle of inclination. When a honeycomb screen was used to investigate the influence of screen thickness, the permeability was found to increase with screen depth. Mathematical relationships were obtained for the both screen pressure drop coefficient and the permeability based on the experimental data at 0° incidence, which compared well with a priori data obtained during the literature review. These mathematical relationships were extended to incorporate the effect of screen inclination on the pressure drop.

In order to simulate porous media within computational programs, the relationship between the pressure drop (ΔP) and the velocity normal to the media

is required. This relationship can be estimated as a second order polynomial fit through the experimental data. The coefficients obtained from this fit are commonly referred to as the Forchheimer coefficients. The standard linear regression model (ordinary least squares, OLS) used to obtain the Forchheimer equation coefficients makes strong assumptions about the behavior of the errors more specifically, that the errors have constant variance (σ^2). A constant error on the variance is known as homoscedasticity, for experimental measurements, however, it is common that the variance of the errors is related to the underlying measurement. This relationship is known as heteroscedasticity and in order to correct for this, the use of weighting applied to the data, known as weighted least squares (WLS), is required. The most common form of weighting is the Heteroscedastic-Consitent Errors (HCE) proposed by White [101], whereby the weight of the data is inversely proportional to the variance. Upon testing the sampled data using the Breusch-Pagan test [99], it was found that the errors on the experimental data were heteroscedastic. These heteroscedastic errors arose due to the accuracy in measuring the pressure through use of a thin membrane piezoelectric pressure transducer. The accuracy in the deflection of the membrane was nonlinear with respect to the applied pressure force.

It was found that the use of weighted least squares (WLS) for weighting the sampled data improved the accuracy of the calculated Forchheimer coefficients.

The porous jump boundary conditions available in ANSYS® FLUENT® 15.0 were used to model thin membranes with known velocity vs. pressure-drop characteristics. The Computational Fluid Dynamics (CFD) results matched closely with the experimental data, with only slight variation due the use of the polynomial coefficients from the experimental data. In contrast, the simulation results varied from the experimental data when only the material thickness (Δm) value was modified and not the corresponding porous jump coefficients.

From the results of the porous media, investigation extended into the relationship between the pressure drop (ΔP) and the heat transfer coefficient (h) for a generic full scale automotive radiator. This variation was also investigated as a function of the angle of inclination of the radiator (α). The radiator was tested at angles of inclination of 0°, 15°, 30° and 45°, for wind tunnel velocities up to 15 m/s. This corresponded to a maximum Reynolds number of Re = 13000 based on the thickness of the radiator. Coolant temperatures of 60 °C, 70 °C, 80 °C, 90 °C and 100 °C were used at a fixed coolant flow rate of $12\,\mathrm{l\,min^{-1}}$. The tests were conducted using an automotive radiator test rig and blower wind tunnel at a dedicated radiator test facility, Young Calibration. Correlating the radiator test results to the results obtained from the porous media study, found that for 15 m/s (approximately 34 mph) a 4% decrease in porosity was required to mach the pressure drop difference between the heated and unheated radiator. The 4% difference in porosity was obtained for all angles of inclination (α) tested. It is therefore possible to account in subscale

for the thermal effects due to heat addition on a full scale heat exchanger via modification of the porosity (β) to an effective porosity ($\beta_{eff.}$) of the material used in subscale. ANSYS® FLUENT® 15.0 was again employed for the modelling of the experimentally tested heat exchanger.

It was found from experimental testing, that an increase in coolant temperature corresponded to an increase in the pressure drop (ΔP) for all angles of inclination tested. For the highest coolant temperature tested (100 °C), the pressure drop of the heated cases was greater than the unheated case by approximately 8% for inclination angles of 0° and 15°. This difference climbed to 10% for 30° of inclination, but fell to 6% for the 45° case. The heat rejection of the coolant is dependent of both the angle of inclination of the radiator and the velocity. Increasing the velocity increases the heat rejection. Inclination of the radiator at lower velocities decreases the heat rejection, however, at larger velocities the heat rejection increases with inclination. At higher velocities, the radiator with the highest overall heat transfer for higher velocities was 30°. The most efficient radiator inclination angle defined in terms of largest heat rejection : lowest pressure drop, however, was the 0° inclined radiator.

The radiator boundary condition within ANSYS® FLUENT® 15.0 were used to model the generic automotive heat exchanger. The pressure drop coefficients ($\Delta P/q$) and heat transfer coefficients (h) from the experimental data were used within the numerical radiator model. The model, however, did not take into account the radiator geometry or inclination and instead required the heat exchanger to be modelled as a discontinuity with the coolant flow perpendicular to the air flow. The CFD results at zero degree inclination agreed well with the experimental data, the maximum error on the pressure drop (ΔP) was 2.7% at approximately 9 m/s and the maximum error on the heat rejection was 1.6% at approximately 5 m/s. These errors arose again, due to the second order polynomial fit through the experimental data. The error on the pressure drop was larger than that achieved using the porous media boundary condition earlier as the pressure drop coefficient ($\Delta P/q$) was used instead of the pressure drop (ΔP).

From testing the automotive full scale radiator, it was found that the pressure drop (ΔP) increased with the addition of heat. An experiment was therefore conducted to investigate the effects of heat addition on a developing channel flow. The channel comprised of two aluminium channels separated vertically by one wooden and one glass wall. Two electrical heaters were used to heat the aluminium walls to approximately 100 °C, to represent the flow of the coolant. The channel was a simplified representation of a single channel from a radiator matrix. Experimental measurements were taken at Cranfield University Shrivenham, using Laser Doppler Anemometry (LDA) and a blower wind tunnel. The Reynolds number (Re) based on the 600 mm channel length and a tunnel velocity of 4 m/s was Re = 160000. This Reynolds number corresponded to that of a full scale radiator at approximately 165

mph (73.8 m/s).

The results from the experimental test indicated that without the addition of heat, the developing flow within the channel accelerated by approximately 7% over the velocity of the inlet. The addition of heat resulted in an additional velocity increase over the unheated case of approximately 1.5%, resulting in a final flow velocity of 9% over the inlet velocity.

The experimental data was compared with numerical simulations performed in ANSYS® FLUENT® 15.0 using the Standard $k-\omega$ and Transition SST $k-\omega$ turbulence models. The Standard $k-\omega$ turbulence model more accurately matched the increase in centreline velocity due to heat, with an increase of 1.0% compared to the Transition SST $k-\omega$ value of 0.7%. The Standard $k-\omega$ model used a turbulent profile for the heat transfer compared to a more laminar profile for the Transition SST $k-\omega$. The Standard $k-\omega$ model, however, predicted a boundary layer growth 2.5 times larger than the experimental data. The Transition SST $k-\omega$ was more accurate in predicting the boundary layer growth with a prediction of 10 mm compared to the experimental thickness of 9 mm, close to the end of the channel ($x/L = 0.9$).

The turbulence model, however, underpredicted the centreline velocity increase due to the addition of heat. The model predicted the heat to account for an increase of 0.7% in the centreline velocity compared to 1.5% obtained from the experiment.

The numerical simulations were then extended to include two additional temperatures of 120 °C and 140 °C. This addition of heat resulted in a final centreline velocity increase of 0.7% and 0.8%, respectively over the unheated case. Finally, investigation was extended into additional heating on the sides of the channel. This was not possible to test experimentally (due to the use of wooden and glass walls required by the LDA instrumentation) and therefore was a purely simulated experiment. The results from this simulation indicated an increase of 1.1% over the unheated case compared to 0.7% when only two of the sides were heated.

6.1.3 Conclusions Summary

A summary of the results unique to this thesis are

- A relationship was established between the pressure drop coefficient (ΔP) and the screen porosity (β) as a function of the angle of inclination (α).
- The use of Weighted Least Squares (WLS) was found to correct for heteroscedasticity in the measured values. This weighting was then used to obtain improved Forchheimer coefficients.
- The pressure drop (ΔP) for a full scale automotive radiator increases with the addition of heat and the angle of inclination (α). An increase was found

of between 6-10% over the unheated radiator depending, upon the angle of inclination.

- The heat rejection of a full scale automotive radiator varies with both the velocity (v) and angle of inclination (α), with inclination providing a larger heat rejection at 15 m/s.
- In order to capture the effects of heat when modelling a heat exchanger at subscale, the decrease in porosity must be accounted for. At 15 m/s (33.6 mph) this equated to an approximate 4% decrease in porosity (β) for all angles of inclination (α) tested.
- Experimental modelling of the geometry of a simplified radiator channel resulted in a centreline velocity increase of 1.5% over the unheated case.

6.2 Recommendations for Future Work

Whilst substantial findings have been made within this thesis, there is still scope for future work. The primary areas that require further investigation are as follows:

- Investigation into the effects of combining multiple sheets of varying porosities (β) and honeycombs, in an effort to match the full scale pressure drops (ΔP) at a subgrid scale.
- To improve the numerical modelling of porous media using a user-defined function (UDF) within ANSYS® FLUENT® 15.0 to correct for the presence of the geometry. In addition, to provide a table to input the pressure drops (ΔP) and pressure drop coefficients ($\Delta P/q$) as a function of the inclination of the media (α).
- To improve the numerical modelling of the radiator boundary condition within ANSYS® FLUENT® 15.0. This can again be achieved with a user-defined function to amend the velocity flow field close to the discontinuity in order to take into account the inclination of the heat exchanger.
- Radiator channels feature louvres to maintain a turbulent boundary layer within the channel. Experimental measurements of a heated channel with louvres would provide more accurate heat transfer characteristics. The corresponding numerical model should also provide closer agreement as the channel would not be within the transitioning flow regime.

This page intentionally left blank.

References

[1] W.M. Kays and A.L. London. *Compact Heat Exchangers*. Krieger Publishing Company, 3rd edition, 1998.

[2] M. Plitkins. A 2004 Ferrari F2004 Formula 1 right side panel radiator. `http://www.atspeedimages.com`, 2015.

[3] H.N. Gupta. *Fundamentals of Internal Combustion Engines*, page 29. PHI Learning, 2nd edition, 2013.

[4] V.A.W. Hillier. *Fundametals of Motor Vehicle Technology*. Nelson Thornes, 1st edition, 1991.

[5] Second Chance Garage. Automotive cooling systems. `http://www.secondchancegarage.com/public/cooling-system.cfm`, 2015.

[6] Cooling Standards Comittee. Coolants for internal combustion engines. *SAE Technical Standard J814*, 2013.

[7] Emercedesbenz. Karl Benz automotive patent. `http://www.emercedesbenz.com/Apr06/04MercedesToShowcaseNewMuseumAtTechnoClassica2006.html`, 2006.

[8] G & B. Automotive aluminium radiator. `http://gbradiator.com/wp-content/uploads/2015/06/aluminum-car-radiator.jpg`, 2015.

[9] S. Stafford. Heat exchanger simulation in wind tunnel models. *SAE Technical Paper 983039*, 1998. doi: 10.4271/983039.

[10] R.H. Barnard and N. Ledakis. Physical modeling and optimisation of radiator cooling flow systems. In *MIRA International Aerodynamics Conference*, 1998.

[11] M.G. Paish and W.R. Stapleford. A study to improve the aerodynamics of vehicle cooling systems. In *MIRA Report*, 1967.

[12] R.A. Bowman, A.C. Mueller, and W.M. Nagle. Mean temperature difference in design. *Transactions of the A.S.M.E*, 62(4):283–294, 1940.

[13] R.A. Beard and G.J. Smith. A method of calculating the heat dissipation from radiators to cool vehicle engines. *SAE Technical Paper 710208*, 1971. doi: 10.4271/710208.

[14] K.E. Emmenthal and W.H. Hucho. A rational approach to automotive radiator systems design. *SAE Technical Paper 740088*, 1974. doi: 10.4271/740088.

[15] J.P. Chiou. The effect of the flow nonuniformity on the sizing of the engine radiator. *SAE Technical Paper 800035*, 1980. doi: 10.4271/800035.

[16] W. Eichlseder and G. Raab. Calculation and design of cooling systems. *SAE Technical Paper 931088*, 1993. doi: 10.4271/931088.

[17] W.M. Nagle. Mean temperature difference in multipass heat exchangers. *Ind. Eng. Chem.*, 25(6):604–609, 1933. doi: 10.1021/ie50282a003.

[18] R.A. Bowman. Mean temperature difference correction in multipass exchangers. *Ind. Eng. Chem.*, 28(5):541–544, 1936. doi: 10.1021/ie50317a009.

[19] K. Fellague, S. Hu, and D. Willoughby. Determination of the effects of inlet air velocity and temperature distributions on the performance of an automotive radiator. *SAE Technical Paper 940771*, 1994. doi: 10.4271/940771.

[20] Cooling Standards Comittee. Engine cooling system field test (air-to-boil). *SAE Technical Standard J819*, 2009.

[21] Cooling Standards Comittee. Coolants for internal combustion engines. *SAE Technical Standard J814*, 2013.

[22] C. Kurland. Computer program for engine cooling radiator selection. *SAE Technical Paper 710209*, 1971. doi: 10.4271/710209.

[23] F. Tenkel. Computer simulation of automotive cooling systems. *SAE Technical Paper 740087*, 1974. doi: 10.4271/740087.

[24] J. Mosier and F. Jarrett. Cooling system analysis. *SAE Technical Paper 740689*, 1974. doi: 10.4271/740689.

[25] A. Costelli, P.Gabriele, and D.Giordanengo. Experimental analysis of engine cooling systems. *SAE Technical Paper 790397*, 1979. doi: 10.4271/790397.

[26] J. Williams. An automotive front-end design approach for improved aerodynamics and cooling. *SAE Technical Paper 850281*, 1985. doi: 10.4271/850281.

[27] K. Chapman, J. Johnson, and E. Chiang. The use of the vehicle engine cooling system simulation as a cooling system diesel tool. *SAE Technical Paper 880600*, 1988. doi: 10.4271/880600.

[28] H.J. Emmelmann and H. Bernebur. Aerodynamic drag and engine cooling-conflicting goals? In *SAE International Congress and Exposition*, 1990.

[29] A. Ecer, C. Toksoy, V. Rubek, R. Hall, G.Gezmisoglu, V. Parliarulo, S. Caruso, and J. Azzali. Air flow and heat transfer analysis of an automotive engine radiator to calculate air-to-boil temperature. *SAE Technical Paper 951015*, 1995. doi: 10.4271/951015.

[30] D.G. Stratton, R.E. Stringer, and S.R.G. Taylor. Air flow and heat transfer analysis of an automotive engine radiator to calculate air-to-boil temperature. *Proceedings of the Institution of Mechanical Engineers: Automobile Division*, 180(1):221–235, 1965. doi: 10.1243/PIME˙AUTO˙1965˙180˙023˙02.

[31] M.G. Paish. A rational approach to the aerodynamics of engine cooling system design. *Proceedings of the Institution of Mechanical Engineers: Automobile Division*, 183(1):69–84, 1968. doi: 10.1243/PIME˙AUTO˙1968˙183˙014˙02.

[32] T.G. Hird, O.W. Johnson, and B. Pitt. Aerodynamic improvements to car radiator performance using a wind tunnel facility. In *9^{th} Australian Fluid Mechanics Conference*, 1980.

[33] C. Lin, J.W. Saunders, S. Watkins, and L. Mole. Increased productivity - use of specific dissipation to evaluate vehicle engine cooling. *SAE Technical Paper 970137*, 1997. doi: 10.4271/970137.

[34] C. Lin, J.W. Saunders, and S. Watkins. Effect of cross-winds on motor car engine cooling. *SAE Technical Paper 970138*, 1997. doi: 10.4271/970138.

[35] C. Lin, J.W. Saunders, and S. Watkins. The effect of changes in ambient and coolant radiator inlet temperatures and coolant flowrate on specific dissipation. *SAE Technical Paper 2000-01-0579*, 2000. doi: 10.4271/2000-01-0579.

[36] E.Y. Ng, P.W. Johnson, S. Watkins, and L. Grant. Wind-tunnel tests of vehicle cooling system performance at high blockage. *SAE Technical Paper 2000-01-0351*, 2000. doi: 10.4271/2000-01-0351.

[37] E.Y. Ng, S. Watkins, P. Johnson, and L. Mole. Use of a pressure-based technique for evaluating the aerodynamics of vehicle cooling systems. *SAE Technical Paper 2002-01-0712*, 2002. doi: 10.4271/2002-01-0712.

[38] Road Vehicle Aerodynamics Forum Committee. Cooling flow measurement techniques. *SAE Technical Standard J2082*, 2015.

[39] J.W. Oler, C.M. Roseberry, D.P. Jordan, and J.E. Williams. Ram-recovery coefficient correlations for automotive cooling airflows. *SAE Technical Paper 910309*, 1991. doi: 10.4271/910309.

[40] L. Christoffersen, D. Söderblom, L. Löfdahl, and A. Jönson. Development of a model scale heat exchanger for wind tunnel models of road vehicles. *SAE Technical Paper 2008-01-0097*, 2008. doi: 10.4271/2008-01-0097.

[41] R. Ruijsink. The use of microprobe system in cooling system development. In *MIRA International Aerodynamics Conference*, 2000.

[42] M. Lyu and Y. Ku. Numerical and experimental study of three dimensional flow in engine room. *SAE Technical Paper 960270*, 1996. doi: 10.4271/960270.

[43] U.W. Schaub and H.N. Charles. Ram air effects on the air side cooling system performance of a typical North American passenger car. *SAE Technical Paper 800032*, 1980. doi: 10.4271/800032.

[44] H. Takahashi, S. Ogino, T. Nishimura, and Y. Okuno. Experimental analysis for the improvement of radiator cooling air intake and discharge. *SAE Technical Paper 920787*, 1992. doi: 10.4271/920787.

[45] F. Browand, B. Marcu, and C. Sharpe. The influence of close-following upon the cooling module air flow. *SAE Technical Paper 981941*, 1998. doi: 10.4271/981941.

[46] M.E. Olson. Aerodynamic effects of front end design on automobile engine cooling systems. *SAE Technical Paper 760188*, 1976. doi: 10.4271/760188.

[47] H. Berneburg and A. Cogotti. Development and use of LDV and other airflow measurement techniques as a basis for the improvement of numerical simulation of engine compartment air flows. *SAE Technical Paper 930294*, 1993. doi: 10.4271/930294.

[48] N.S. Ap. A simple engine cooling system simulation model. *SAE Technical Paper 1999-01-0237*, 1999. doi: 10.4271/1999-01-0237.

[49] J. Williams, D. Karanth, and W. Oler. Cooling inlet aerodynamic performance and system resistance. *SAE Technical Paper 2002-01-0256*, 2002. doi: 10.4271/2002-01-0256.

[50] H. Shimonosono, Y. Shibata, and K. Fujitani. Optimization of the heat flow distribution in the engine compartment. *SAE Technical Paper 930883*, 1993. doi: 10.4271/930883.

[51] A.J. Baxendale and G.W. Carr. Evaluation of CFD for predicting the airflow inside an engine compartment with encapsulation. In *MIRA Vehicle Aerodynamics Conference*, 1996.

[52] A. Cogotti and H. Berneburg. Engine compartment airflow investigations using a laser-doppler-velocimeter. *SAE Technical Paper 910308*, 1991. doi: 10.4271/910308.

[53] J.G. Pharoah and D.A. Hicks. CFD model of an automotive cooling module. In *MIRA Vehicle Aerodynamics Conference*, 1998.

[54] K. Fujikake, H. Katagiri, and Y. Suzuki. Measurement of air velocity distribution and airflow rate through radiator in an automobile. *SAE Technical Paper 780587*, 1978. doi: 10.4271/780587.

[55] S.P. Dudley and R.E. Barry. The measurement of underhood and underbody velocities with the h-meter. *SAE Technical Paper 1999-01-0234*, 1999. doi: 10.4271/1999-01-0234.

[56] T. Hoshino, R. Yoshino, and H. Takada. Improvement of engine cooling performance by cooling airflow visualization. *SAE Technical Paper 811392*, 1981. doi: 10.4271/811392.

[57] A.J. Fowler, G.A. Ledezma, and A. Bejan. Optimal geometric arrangement of staggered plates in forced convection. *International Journal of Heat and Mass Transfer*, 40(8):1795–1805, 1997. doi: 10.1016/S0017-9310(96)00251-7.

[58] A. Bejan and E. Sciubba. The optimal spacing of parallel plates cooled by forced convection. *International Journal of Heat and Mass Transfer*, 35(12): 3259–3264, 1992. doi: 10.1016/0017-9310(92)90213-C.

[59] A.M. Morega, A. Bejan, and S.W. Lee. Free stream cooling of a stack of parallel plates. *International Journal of Heat and Mass Transfer*, 38(3):519–531, 1995. doi: 10.1016/0017-9310(94)00123-D.

[60] T. Bello-Ochende and A. Bejan. Maximal heat transfer density: Plates with multiple lengths in forced convection. *International Journal of Thermal Sciences*, 43(12):1181–1186, 2004. doi: 10.1016/j.ijthermalsci.2004.05.002.

[61] N. Haidar and E. Draper. Computational modelling of the underbonnet cooling flow characteristics of the new Daewoo van. In *2nd MIRA International Aerodynamics Conference on Vehicle Aerodynamics*, 1998.

[62] T. Yasuki, T. Nishimura, T. Abe, and J. Takamitsu. Prediction of the airflow through automotive radiators using 3-dimensional analysis. *SAE Technical Paper 932889*, 1993. doi: 10.4271/932889.

[63] M. Pervaiz, R. Brewster, R. Ross, W. Bauer, and H. Reister. Numerical methodology for automotive radiator and condenser simulations. *SAE Technical Paper 971840*, 1997. doi: 10.4271/971840.

[64] J. Williams and G. Vemaganti. CFD quality - a calibration study for front-end cooling airflow. *SAE Technical Paper 980039*, 1998. doi: 10.4271/980039.

[65] H. Beamer, D. Ghosh, K. Bellows, and L. Huang. Applied CFD and experiment for automotive compact heat exchanger development. *SAE Technical Paper 980426*, 1998. doi: 10.4271/980426.

[66] R. Andra, E. Hytopoulos, K. Kumar, and R. Sun. The effect of boundary and geometry simplification on the numerical simulation of front-end cooling. *SAE Technical Paper 980395*, 1998. doi: 10.4271/980395.

[67] Y.L. Lee and Y.T Hong. Analysis of engine cooling including flow nonuniformity over a radiator. *International Journal of Vehicle Design*, 24(1):121–135, 2000. doi: 10.1504/IJVD.2000.001877.

[68] B. Uhl, F. Brotz, J. Fauser, and U. Krüger. Development of engine cooling systems by coupling CFD simulation and heat exchanger analysis programs. *SAE Technical Paper 2001-01-1695*, 2001. doi: 10.4271/2001-01-1695.

[69] B. Shome and R. Joshi. CFD based air-to-boil temperature prediction for sport utility vehicle radiator. *SAE Technical Paper 2006-01-3266*, 2006. doi: 10.4271/2006-01-3266.

[70] M.J. Gartner, C.R. Wilhelm, K.L. Gage, M.C. Fabrizio, and W.R. Wagner. Modeling flow effects on thrombotic deposition in a membrane oxygenator. *Artificial Organs*, 24(1):29–36, 2000. doi: 10.1046/j.1525-1594.2000.06384.x.

[71] M. Teitela, D. Dvorkina, Y. Haima, J. Tannyb, and I. Seginer. Comparison of measured and simulated flow through screens: Effects of screen inclination and porosity. *Biosystems Engineering*, 104(3):404–416, 2009. doi: 10.1016/j.biosystemseng.2009.07.006.

[72] G.B. Schubauer, W.G Spangenberg, and P.S. Klebanoff. Aerodynamic characteristics of damping screens. In *NASA Technical Report*, 1950.

[73] G.I. Taylor. Air resistance of a flat plate of very porous material. In *Aeronautical Research Council Reports and Memoranda*, 1944.

[74] G.I. Taylor and R.M. Davies. The aerodynamics of porous sheets. In *Aeronautical Research Council Reports and Memoranda*, 1944.

[75] W.D. Baines and E.G. Paterson. An investigation of flow through porous screens. *Transactions of the American Society of Mechanical Engineers*, 73 (1):467–480, 1965.

[76] P.J.G. Carrothers and W.D. Baines. Forces on screens inclined to a fluid flow. *Journal of Fluids Engineering*, 97(1):116–117, 1975. doi: 10.1115/1.3447186.

[77] A.J. Reynolds. Flow deflection by gauze screens. *Journal of Mechanical Engineering Science*, 11(3):290–294, 1969. doi: 10.1243/JMES˙JOUR˙1969˙011˙036˙02.

[78] J.K. Koo and D.F. James. Fluid flow around and through a screen. *Journal of Fluid Mechanics*, 60(3):513–538, 1973. doi: 10.1017/S0022112073000327.

[79] T.J. O'Hern and J.R. Torczynski. Reynolds number dependence of the drag coefficient for laminar flow through fine-scale screens. In *National Fluid Dynamics Congress*, Los Angeles, California, US, 1992.

[80] E. Brundrett. Prediction of pressure drop for incompressible flow through screens. *Journal of Fluid Eng.*, 115(2):1–4, 1992. doi: 10.1115/1.2910130.

[81] A.F. Miguel. Airflow through porous screens: from theory to practical considerations. *Energy and Buildings*, 28(1):63–69, 1998. doi: 10.1016/S0378-7788(97)00065-0.

[82] A. Ito and K.P. Garry. Pressure measurements around a two-dimensional gauze at incidence. *Journal of Fluids and Structures*, 12(2):171–181, 1998. doi: 10.1006/jfls.1997.0134.

[83] F.G. O'Neill. Source models of flow through and around screens and gauzes. *Ocean Engineering*, 33(14):1884–1895, 2006. doi: 10.1016/j.oceaneng.2005.10.009.

[84] Z. Dong, W. Luo, G. Qian, and H. Wang. A wind tunnel simulation of the mean velocity fields behind upright porous fences. *Ocean Engineering*, 146(1): 82–93, 2007. doi: 10.1016/j.agrformet.2007.05.009.

[85] Z. Dong, W. Luo, G. Qian, P. Lu, and H. Wang. A wind tunnel simulation of the turbulence fields behind upright porous wind fences. *Journal of Arid Environments*, 74(2):193–207, 2010. doi: 10.1016/j.jaridenv.2009.03.015.

[86] D.L. Valera, F.D. Molina, A.J. Alvarez, J.A. López, J.M. Terrés-Nicoli, and A. Madueño. Contribution to characterisation of insect-proof screens: Experimental measurements in wind tunnel and CFD simulation. *ISHS Acta Horticulturae*, 691(1):441–448, 2005. doi: 10.17660/ActaHortic.2005.691.53.

[87] M. Teitel. Using computational fluid dynamics simulations to determine pressure drops on woven screens. *Biosystems Engineering*, 105(2):172–179, 2010. doi: 10.1016/j.biosystemseng.2009.10.005.

[88] M. Teitel. On the applicability of the Forchheimer equation in simulating flow through woven screens. *Biosystems Engineering*, 109(2):130–139, 2011. doi: 10.1016/j.biosystemseng.2011.02.009.

[89] H. Darcy. *Les fontaines publiques de la ville de Dijon*. Victor Dalmont, 1st edition, 1856.

[90] D.A. Nield and A. Bejan. *Convection in Porous Media*. Springer, 4th edition, 2013.

[91] P. Forchheimer. Wasserbewegung durch boden. *Z. Vereines Deutscher Ingenieur*, 45(1):1782–1788, 1901.

[92] K. Vafai. *Handbook of Porous Media*. CRC Press, 3rd edition, 2015.

[93] W. Dierickx. Flow reduction of synthetic screens obtained with both a water and airflow apparatus. *Journal of Agricultural Engineering Research*, 71(1): 67–73, 1998. doi: 10.1006/jaer.1998.0299.

[94] P. Muñoz, J.I. Montero, A. Antón, and F. Giuffrida. Effect of insect-proof screens and roof openings on greenhouse ventilation. *Journal of Agricultural Engineering Research*, 73(2):171–178, 1999. doi: 10.1006/jaer.1998.0299.

[95] J. Flores-Velazquez and J.I.] Montero. Computational Fluid Dynamics (CFD) study of large scale screen houses. In *International Workshop on Greenhouse Environmental Control and Crop Production in Semi-Arid Regions*, 2008.

[96] ANSYS. *Fluent Version 15.0 Release Manual*. ANSYS Inc., 2013.

[97] I. Idelchik. *Handbook of Hydraulic Resistance*. CRC Press Inc., 3rd edition, 2005.

[98] Q.F. Hou, B.Y. Guo, L.F. Li, and A.B. Yu. Numerical simulation of gas flow in an electrostatic precipitator. In *7th International Conference on CFD in the Minerals and Process Industries*, Australia, 2009.

[99] T.S. Breusch and A.R. Pagan. A simple test for heteroskedasticity and random coefficient variation. *Econometrica*, 47(5):1287–1294, 1979. doi: 10.2307/1911963.

[100] K. Gerova, S. Velikov, and K.P. Garry. The effects of porosity and inclination on the pressure drop across porous screens and honeycombs used for heat exchanger simulations in wind tunnel studies. *SAE Int. J. Passeng. Cars - Mech. Syst.*, 6(2):483–494, 2013. doi: 10.4271/2012-01-2340.

[101] H. White. A heteroskedasticity-consistent covariance matrix estimator and a direct test for heteroskedasticity. *Econometrica*, 48(4):817–838, 1980.

[102] J. Williams, S. Watkins, and C. Dixon. Reduced drag and adequate cooling for passenger vehicles using variable area front air intakes. *SAE Technical Paper 2006-01-0342*, 2006. doi: 10.4271/2006-01-0342.

[103] L. Christoffersen, D. Söderblom, L. Löfdahl, and A. Jönson. Development of a model scale heat exchanger for wind tunnel models of road vehicles. *SAE Technical Paper 2008-01-0097*, 2008. doi: 10.4271/2008-01-0097.

[104] K. Gerova and A. Savill. On optimum choice of Forchheimer equation coefficients for computational fluid dynamics simulation of heat exchangers. *SAE Int. J. Passeng. Cars - Mech. Syst.*, 8(2):779–785, 2015. doi: 10.4271/2015-01-9110.

[105] L. Henriksson, E. Dahl, P. Gullberg, and A. Contet. Experimental investigation of heat transfer rate and pressure drop through angled compact heat exchangers relative to the incoming airflow. *SAE Int. J. Commer. Veh.*, 7(2): 448–457, 2014. doi: 10.4271/2014-01-2337.

[106] M. Kim, B. Youn, and C. Bullard. Effect of inclination on the air-side performance of a brazed aluminum heat exchanger under dry and wet conditions. *International Journal of Heat and Mass Transfer*, 44(24):4613–4623, 2001. doi: 10.1016/S0017-9310(01)00104-1.

[107] F.N. Beauvais. An aerodynamic look at automotive radiators. *SAE Technical Paper*, 1965. doi: 10.4271/650470.

[108] H. Al-Bakhit and A. Fakheri. Numerical simulation of heat transfer in simultaneously developing flows in parallel rectangular ducts. *Applied Thermal Engineering*, 26(5-6):596–603, 2006. doi: 10.1016/j.applthermaleng.2005.07.002.

[109] H. Al-Bakhit and A. Fakheri. Entrance and wall conduction effects in parallel flow heat exchangers. In *5th International Conference on ECUCHE*, pages 93–99, 2005, Holoken, New Jersey, USA.

[110] M.I. Hasan, A.A. Rageb Rageb, and M. Yaghoubi. Investigation of a counter flow microchannel heat exchanger performance with using nanofluid as a coolant. *International Journal of Thermal Science*, 2(3):35–43, 2012. doi: 10.4236/jectc.2012.23004.

[111] H. Schlichting and K. Gersten. *Boundary-Layer Theory*, pages 186–187. Springer, 7th edition, 2000.

[112] A.P. Fraasl. *Heat Exchanger Design*, page 276. Wiley-Interscience, 2nd edition, 1989.

[113] F.P. Incropera and D.P. Dewitt. *Introduction to Heat Transfer*, page 370. Wiley, 4th edition, 2002.

[114] J.D. Anderson. *Computational Fluid Dynamics*, page 76. McGraw-Hill Higher Education, 6th edition, 1995.

[115] R.B. Langtry and F.R. Menter. Transition modeling for general CFD applications in aeronautics. In *43rd AIAA Aerospace Sciences Meeting and Exhibit*, pages 1–14, 2005, Reno, Nevada, USA.

[116] W.C. Reynolds, W.M. Kays, and S.J. Kline. Heat Transfer in the Turbulent Incompressible Boundary Layer. Technical report, National Aeronautics and Space Administration, 1958.

[117] L. Prandtl. *Aerodynamic Theory*. Juilius Springer, 3rd edition, 1935.

[118] Daiwa Racing Labo. Radiator fin geometry. `http://www.daiwaracinglabo.com`, 2015.

[119] H. Morihara and R. Ta-Shun Cheng. Numerical solution of the viscous flow in the entrance region of parallel plates. *Journal of Computational Physics*, 11(4):550–572, 1973. doi: 10.1016/0021-9991(73)90137-X.

[120] F. Durst, S. Ray, B. Ünsal, and O.A. Bayoumi. The development lengths of laminar pipe and channel flows. *Journal of Fluids Engineering*, 127(6): 1154–1160, 2005. doi: 10.1115/1.2063088.

[121] M. Darbandi and E. Schneider. Numerical study of the flow behaviour in the uniform velocity entry flow problem. *Numerical Heat Transfer, Part A: Applications: An International Journal of Computation and Methodology*, 34 (5):479–494, 1998. doi: 10.1080/10407789808913999.

[122] H.S. Heaton, W.C. Reynolds, and W.M. Kays. Heat transfer in annular passages. Simultaneous development of velocity and temperature fields in laminar flow. *International Journal of Heat and Mass Transfer*, 7(7):763–781, 1964. doi: 10.1016/0017-9310(64)90006-7.

[123] G.E. Karniadakis, A. Beskok, and N. Aluru. *Microflows: Fundamentals and Simulation*, page 140. Springer, 2nd edition, 2002.

[124] J. Gartner and M. Amitay. Effect of boundary layer thickness on secondary structures in a short inlet curved duct. *International Journal of Heat and Fluid Flow*, 50(1):467–478, 2014. doi: 10.1016/j.ijheatfluidflow.2014.10.016.

[125] E.Pohlhausen. Der Wärmeaustausch zwischen festen Körpern und Flüssigkeiten mit kleiner reibung und kleiner Wärmeleitung. *Zeitshrift für Angewandte Mathematik und Mechanik*, 1(2):115–121, 1921. doi: 10.1002/zamm.19210010205.

[126] E.M. Smith. *Advances in Thermal Design of Heat Exchangers*. Wiley-Blackwell, 1st edition, 2005.

[127] T.G. Beckwith, R.D. Marangoni, and J.H. Lienhard V. *Mechanical Measurements*. Pearson Education, 6th edition, 2007.

[128] Pyle. Pyle pma82 digital anemometer. `http://www.pyleaudio.com`, 2015.

[129] United Sensor Corp. Kiel probe. `http://www.unitedsensorcorp.com/kiel.html`, 2015.

[130] DIY Drones. Pitot-static probe. `http://www.diydrones.com`, 2015.

[131] TSI. Thermal anemometry probe. `http://www.tsi.com/Products/_Product-Components/Thermal-Anemometry-Probes.aspx`, 2015.

[132] Y. Yeh and H. Cummins. Localized fluid flows measurements with he-ne laser spectrometer. *Applied Physics Letters*, 1(4):176–178, 1964. doi: 10.1063/1.1753925.

[133] Dantec Dynamics. Measurement principles of LDA. `http://www.dantecdynamics.com/measurement-principles-of-lda`, 2015.

[134] P. Günther, T. Pfister, and J.Czarske. Laser doppler distance sensor using phase evaluation. *Optics Express*, 17(4):2611–2622, 2009. doi: 10.1364/OE.17.002611.

[135] J. Boussinesq. Essai sur la théorie des eaux courantes. In *Mémoires présentés par divers savants à l'Académie des Sciences*, 1877.

[136] MathWorks. Curve Fitting Toolbox (CFT). `http://www.uk.mathworks.com/products/curvefitting`, 2015.

[137] Evgenia Vogiatzi. Heteroscedastic errors. `http://www.oocities.org/qecon2002/founda10.html`, 2015.

[138] DENSO Europe. Denso reduced thickness radiator. `http://denso-europe.com/denso-slashes-size-and-weight-of-radiator-by-40-percent`, 2015.

[139] Dr. M. Finnis. Cranfiled University Shrivenham blower tunnel schematic. Personal communication, 10/11/2015.

[140] Omega Engineering. Omega Engineering SRFG flexible silicon heater mats. `http://www.omega.co.uk/pptst/SRFR_SRFG.html`, 2015.

Appendix A

Governing Equations

A.1 Log Mean Temperature Difference

In order to determine the mean temperature difference for heat transfer between two fluids the following equation is used [126]

$$\dot{Q} = US\Delta\theta_m, \tag{A.1}$$

where $\Delta\theta_m$ is the mean temperature difference between the fluids, U is the overall heat-transfer coefficient and S is the surface area.

The use of Eq. (A.1) requires the following assumptions:

- both fluids have steady mass flow rates ($\dot{m}_h$, $\dot{m}_c$)
- both fluids have constant specific heats (C_h, C_c)
- constant overall heat-transfer coefficient (U)
- negligible heat loss to surroundings

For an element of δS,

$$\delta\dot{Q} = U\delta S\Delta\theta_m, \tag{A.2}$$

also considering each fluid

$$\delta\dot{Q} = \dot{m}_h C_h(-\delta T_h) = \dot{m}_c C_c(\pm\delta T_c). \tag{A.3}$$

The increment in temperature $\Delta\theta$ is therefore

$$\delta(\Delta\theta) = \delta(T_h - T_c) = (\delta T_h - \delta T_c) = \left[\frac{-1}{\dot{m}_h C_h} - \frac{\pm 1}{\dot{m}_c C_c}\right] U\delta S\Delta\theta. \tag{A.4}$$

Thus,

$$\frac{\delta(\Delta\theta)}{\Delta\theta} = \left[\frac{-1}{\dot{m}_h C_h} - \frac{\pm 1}{\dot{m}_c C_c}\right] U\delta S. \tag{A.5}$$

Integrating between stations 1 and 2 gives

$$\ln\frac{\Delta\theta_2}{\Delta\theta_1} = \left[\frac{-1}{\dot{m}_h C_h} - \frac{\pm 1}{\dot{m}_c C_c}\right] US, \tag{A.6}$$

also integration of Eq. (A.2), gives

$$\Delta\theta_2 - \Delta\theta_1 = \left[\frac{-1}{\dot{m}_h C_h} - \frac{\pm 1}{\dot{m}_c C_c}\right] \dot{Q}. \tag{A.7}$$

Combining Eqs. (A.6) and (A.7) gives

$$\dot{Q} = US\frac{\Delta\theta_2 - \Delta\theta_1}{\ln\frac{\Delta\theta_2}{\Delta\theta_1}}. \tag{A.8}$$

Comparing Eq. (A.8) with Eq. (A.1), $\Delta\theta_m$ can be written as the logarithmic mean temperature difference ($\Delta\theta_{\text{lmtd}}$)

$$\Delta\theta_{\text{lmtd}} = US\frac{\Delta\theta_2 - \Delta\theta_1}{\ln\frac{\Delta\theta_2}{\Delta\theta_1}}. \tag{A.9}$$

A.2 ε-NTU Method

The assumptions presented in the previous section for calculating the Log Mean Temperature Difference (LMTD) also hold true for the ε-NTU method.

The basic definition for the effectiveness of any ε-type heat exchanger [1] is

$$\varepsilon = f\left(\text{NTU}, \frac{C_{\min}}{C_{\max}}, \text{flow arrangement}\right), \tag{A.10}$$

where NTU is the number of heat transferred units, defined as

$$\text{NTU} = \frac{UA}{C_{\min}} = \frac{1}{C_{\min}}\int_0^A U dA, \tag{A.11}$$

where U is the overall thermal conductance, A is the heat transfer area. $C_{\min}$ is defined as the smaller of the C_h and C_c magnitudes, where C_h and C_c are the flow stream capacity rates of the cold and hot side fluid, respectively.

For cross-flow where both fluids remain unmixed, the ε-NTU relationship is defined [113] as

$$\varepsilon = 1 - \exp\left[\frac{1}{C_r}(\mathrm{NTU}^{0.22})\{\exp[-C_r(NTU)^{0.78}] - 1\}\right], \tag{A.12}$$

where C_r is the heat capacity ratio, defined as

$$C_r = \frac{C_{\min}}{C_{\max}}. \tag{A.13}$$

A.3 Air-to-Boil Temperature

As defined in SAE's standard [6] the Air-to-Boil (ATB) temperature is the ambient air temperature that will cause the cooling system to boil when the machine is operated under specified conditions and modes of operation. This is usually at the maximum productivity.

The ATB temperature is expressed as

$$\mathrm{ATB} = T_{\mathrm{BP}} - (T_{\mathrm{ci}} - T_{\mathrm{ai}}), \tag{A.14}$$

where T_{BP} is the coolant boiling point, T_{ci} is the coolant radiator inlet temperature and T_{ai} is the ambient temperature after the cooling system has stabilised. All temperatures are measured in degrees Celsius.

The standard also specifies testing restrictions including not running a cooling test if the ambient temperature is below 24 °C (297.15 K) and not testing if the wind velocity exceeds 6 mph (2.8 m/s) unless the wind is at 90° to the test course. Furthermore the machine being tested needs to be operating under a steady load and speed conditions.

A.4 Specific Dissipation

A change in Specific Dissipation (SD) can be used to determine the heat transfer variation of automobile radiators at constant conditions. It is defined [30] as the heat transfer rate of a heat exchanger divided by the maximum temperature difference across the heat exchanger. It is given by

$$SD = \frac{Q}{T_{\mathrm{hot(in)}} - T_{\mathrm{cold(in)}}}, \tag{A.15}$$

where Q is the heat exchanger heat transfer rate and $T_{\mathrm{hot(in)}}$ and $T_{\mathrm{cold(in)}}$ are the hot and cold inlet temperatures respectively.

Equation (A.14) can also be rewritten as

$$SD = \frac{Q}{Q_{\max}} \cdot C_{\min} = \varepsilon \times C_{\min}, \tag{A.16}$$

where $Q_{\max}$ is the maximum possible heat transfer rate, ε is the heat exchanger heat transfer effectiveness and $C_{\min}$ is the minimum capacity rate.

For an air-cooled cross-flow heat exchanger, $C_{\min}$ is defined as

$$C_{\min} = \dot{m}_a C_{p,a} = A_a V_a \rho_a C_{p,a}, \tag{A.17}$$

for a radiator

$$Q_{\max} = \dot{m}_a C_{p,a} (T_{\mathrm{ci}} - T_{\mathrm{ai}}). \tag{A.18}$$

$$\varepsilon = \frac{Q}{Q_{\max}} = \frac{\dot{m}_c C_{p,c} (T_{ci} - T_{co})}{\dot{m}_a C_{p,a} (T_{ci} - T_{ai})}. \tag{A.19}$$

Appendix B

Experimental Techniques

B.1 Propeller Anemometry

Propeller anemometers (sometimes referred to as vane/pinwheel/turbine anemometers) have been extensively employed for measuring air speeds [127]. In effect, the device is simply a windmill consisting of a rotor shaft supported by a hub. A series of blades are attached to a surrounding ring. A proximity detector mounted on this ring is then used to measure the rotor blade passing frequency. The rotation speed of each propeller gives an indication of the average velocity of a given circular area. The anemometers can be used individually or arranged in either a rake or square grid. An example of a typical digital propeller anemometer is shown in Fig. B.1.

One of the advantages of using vane anemometers is that they measure velocity directly, eliminating the need of pressure and temperature corrections. This allows for the direct comparison between results obtained in wind tunnels and those obtained on road in different ambient conditions.

Figure B.1 An example of a propeller anemometer [128].

B.2 Pitot Tubes

The primary use of pressure measurements at a point in fluid is to determine flow conditions, i.e. the velocity. The most basic instrument available for this is the pitot tube. It is used to measure total pressure only. The pitot tube consists of a tube pointing directly into the fluid flow. As the tube fills out with fluid, it is gradually brought to rest as there is no outlet to allow flow to continue. The measured pressure at that point is the total pressure or pitot pressure. A drawback of the pitot tube is its sensitivity to alignment with the flow direction. A variation of the pitot tube, the kiel probe (shown in Fig. B.2) avoids this problem by using a shroud to protect the primary tube.

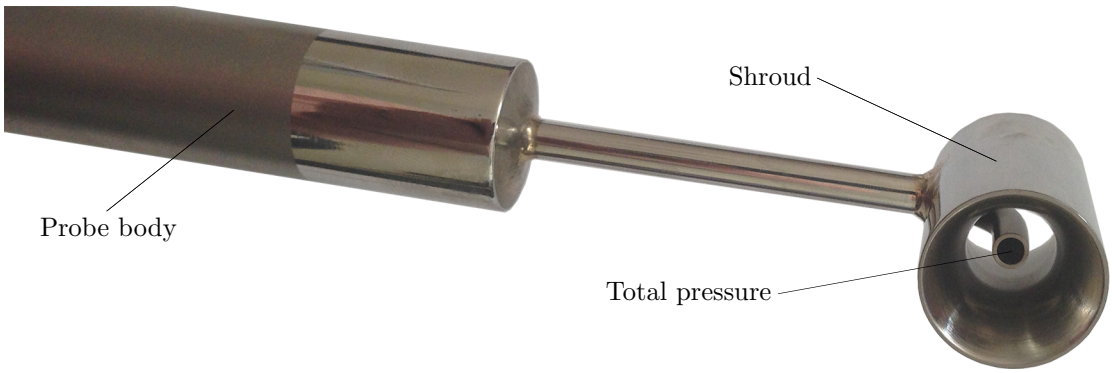

Figure B.2 An example of a kiel probe [129].

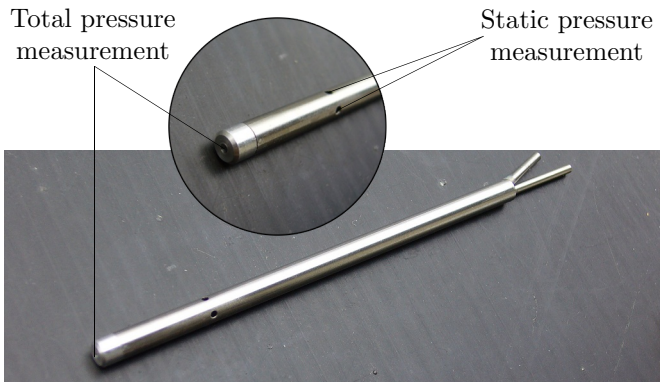

Figure B.3 An example of a pitot-static probe [130].

In order to determine the fluid velocity the dynamic pressure is needed. This is the difference between the total and the static pressure. A combined probe that measures both these pressures is called a pitot-static tube (shown in Fig. B.3). It consists of two coaxial tubes. The inner tube faces the flow and measures total pressure, the other tube is open to the stream only through small static orifices. The dynamic pressure (q) is then determined using a diaphragm inside an enclosed container. The deflection of the diaphragm is proportional to the dynamic pressure. Furthermore, multi-hole arrangements usually found on aeroplanes are capable of measuring 3D flow fields and can simultaneously measure: yaw, roll and pitch.

B.3 Hot-Wire Anemometry

In many instances it is necessary to have instantaneous measurements of velocities in turbulent flows. A standard method of measuring such fluctuating quantities is

thermal anemometry.

A heated object in a moving stream loses heat at a rate proportional to the fluid velocity. Thus, if a heated wire is placed in a moving fluid, its temperature fluctuations will be a measure of the variation in the velocity of the fluid. If the flow velocity acting at the wire changes, the convective heat transfer coefficient changes and the wire temperature will consequently change.

The most commonly used thermal velocity probes are the hot wire and hot-film ones. The hot-wire probe consists of a fine wire mounted between supports and exposed to the flow. Typically, the wire is 4–10 µm in diameter, 1 mm in length and made of platinum or tungsten. A variation of the single component hot-wire probe is the X-wire probe. It has two orthogonal sensors mounted at 45° to the flow. A three component hot-wire probe can also be constructed as shown in Fig. B.4).

Figure B.4 Thermal three component anemometer probe [131].

Since the wires in hot-wire probes are extremely fragile, they should only be used in clean gas flows. For all other flow applications hot-film probes are recommended. They consist of a quartz fibre suspended between prongs with a platinum film coated onto the fibre surface. Typical diameter of such wires is 25–150 µm.

B.4 Laser Doppler Anemometry

Invented in 1964 by Yeh et al. [132], the helium laser doppler anemometer is a widely used tool for the study of fluid dynamics. It is a non-intrusive technique that obtains flow velocity information. Some of the main advantages of this method are the high spatial and temporal resolution and the lack of need for calibration.

An interesting element of the set-up is the use of a Bragg cell as the beam splitter. This is a glass crystal with a vibrating piezoelectric crystal attached. This results in the vibrations generating acoustic waves which act as an optical grid.

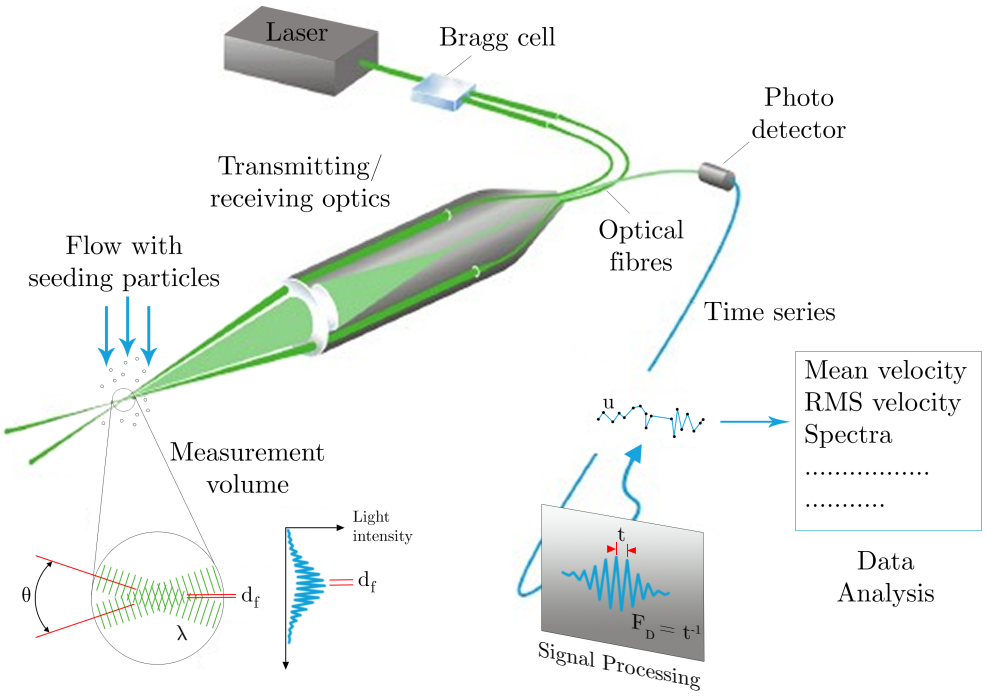

Figure B.5 The principles behind Laser Doppler Anemometry (LDA) measurement [133].

In order for any measurement to be performed tracer particles are needed in the flow. Flow velocity information is collected by means of the light scattered by the seeding as they move through the probe volume. The scattered light contains a Doppler shift. The Doppler shift of the scattered waves is proportional to the velocity of the scattering particle and thus the velocity of the fluid.

A receiver lens is used to collect the scattered light, which is then passed through an interference filter so that only the required wave length is passed and focused on the photo-detector. This removes noise from ambient light and from other wavelengths. The photo-detector converts the fluctuating light intensity into an electrical signal knows as the Doppler burst. The Doppler bursts are then filtered and amplified in the signal processor in order to determine the Doppler frequency. This is often achieved using a Fast Fourier Transform (FFT) algorithm.

In order to measure three velocity components we require three beam pairs.

Two pairs are emitted from a 2D probe and one pair from a 1D probe. The two probes need to be placed in such a way that their intersection volumes coincide. It is important to note that the velocity components measured by the beams from the 2D probe are orthogonal while the third velocity component has to be orthogonalized by software. To obtain a three velocity component measurement one can use two separate probes measuring two separate and one common velocity, where all the beams intersect in a common volume as shown in the example set-up in Fig. B.6. In such a set-up different wavelengths are used in order to separate the measured components as well as photo-detectors with appropriate interference filters to detect the scattered light from the different wavelengths.

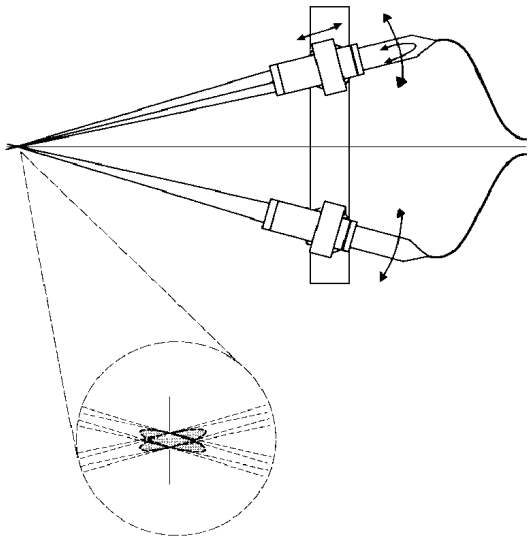

Figure B.6 Laser doppler velocimetry measurement system [134].

Appendix C

Computational Fluid Dynamics Modelling

C.1 Reynolds-Averaged Navier-Stokes

Reynolds-Averaged Navier-Stokes (RANS) equations are time averaged equations for the motion of fluid flow. They arise from a Reynolds decomposition whereby an instantaneous quantity is decomposed into its time-averaged and time varying quantitates. RANS equations are not a closed set and as a result it is not possible to solve for Reynolds stresses directly. Turbulence models are therefore required to represent the Reynolds stresses. RANS models are currently the most widely used algorithms present in commercial code. Extensive testing and validation with fast implementation make them ideal for both research and for commercial applications.

The RANS model is based on Reynolds decomposition where the flow is divided into a mean and fluctuating part given by

$$\tilde{P} = \overline{P} + p, \tag{C.1}$$

$$\tilde{u_i} = \overline{U_i} + u_i, \tag{C.2}$$

and

$$\tilde{\Phi} = \overline{\Phi} + \phi, \tag{C.3}$$

where p and u are the pressure and velocity respectively, Φ can be another quantity in the flow field such as temperature. These modified variables are then substituted into the Navier-Stokes Equations and averaged in time.

The Navier-Stokes equations for incompressible fluids, written in tensor notation can be expressed as

$$\frac{\partial u_i}{\partial x_i} = 0, \tag{C.4}$$

and

$$\frac{\partial u_i}{\partial t} + u_j \frac{\partial u_i}{\partial x_j} = f_i - \frac{1}{\rho}\frac{\partial p}{\partial x_i} + v\frac{\partial^2 u_i}{\partial x_j \partial x_j}. \tag{C.5}$$

Substituting into the Navier-Stokes equations (Eq. (C.4)) and taking an ensemble average, yields the Reynolds-Averaged Navier-Stokes equations

$$\frac{\partial \overline{u_i}}{\partial x_i} = 0, \tag{C.6}$$

and

$$\frac{\partial \overline{u_i}}{\partial t} + \overline{u_j}\frac{\partial \overline{u_i}}{x_j} + \overline{u'_j \frac{\partial u'_i}{\partial x_j}} = \overline{f_i} - \frac{1}{\rho}\frac{\partial \overline{p}}{\partial x_i} + v\frac{\partial^2 \overline{u_i}}{\partial x_j \partial x_j}. \tag{C.7}$$

Defining the mean rate of stress tensor as

$$\overline{S_{ij}} = \frac{1}{2}\left(\frac{\partial \overline{u_i}}{\partial x_j} + \frac{\partial \overline{u_j}}{\partial x_i}\right). \tag{C.8}$$

Substituting Eq. (C.8) into Eq. (C.7) and removing the time dependence of resulting terms yields

$$\rho\frac{\partial \overline{u}_j \overline{u}_i}{\partial x_j} = \rho\overline{f_i} + \frac{\partial}{\partial x_j}\left[-\overline{p}\delta_{ij} + 2\mu\overline{S}_{ij} - \rho\overline{u'_i u'_j}\right]. \tag{C.9}$$

The above equations are unclosed because they contain terms of unknown fluctuating components. The Reynolds stresses contained within these fluctuating components must therefore be modelled in order to solve the equations.

Boussinesq [135] employed a hypothesis to relate the Reynolds stress to the mean velocity gradients

$$-\rho\overline{u'_i u'_j} = \mu_t\left(\frac{\partial u_i}{\partial x_j} + \frac{\partial u_j}{\partial x_i}\right) - \frac{2}{3}\left(\rho k + \mu_t\frac{\partial u_k}{\partial x_k}\right), \tag{C.10}$$

where μ_t is the turbulent viscosity. The Boussinesq hypothesis is used in the Spalart-Allmaras model, the $k-\varepsilon$ models, and the Standard $k-\omega$ models.

RANS models can be classified into three main categories, they are as follows:

- Linear eddy-viscosity models
  - Algebraic (zero equation models)
  - Single equation models
  - Two equation models
- Non-linear eddy viscosity
- Second Moment Closure Models (SMCM)

C.2 RANS Two Equation Models

Computational Fluid Dynamics (CFD) used within industry focuses on the families contained within the two equation models. The two equation models use the Boussinesq assumption to compute the local conditions for the Reynolds stresses. In reality, the Reynolds stresses could be convected by both the mean and the fluctuating velocities. The two equation models are used despite their known limitations as they offer reduced computational cost over the second moment closure models (SMCM).

The two main families of the two equation models are $k-\varepsilon$ and $k-\omega$. Details about the performance and limitation of each family are listed below.

C.2.1 $k-\varepsilon$

One of the more common families of turbulence models is the $k-\varepsilon$ model. Two extra equations are solved to represent the flow turbulence. The two transported variables are k and ε, the turbulent kinetic energy and the turbulent dissipation, respectively.

The $k-\varepsilon$ family consists of three sub models: Standard, RNG and Realizable. The Standard model was the primary model developed and is widely used in engineering calculations due to its robustness.

The RNG model contains an additional term in the turbulent dissipation equation enabling higher accuracy in strained flows.

The Realizable model is the latest model to be developed, it introduces a newer formulation for turbulent viscosity and dissipation rate. The Realizable $k-\varepsilon$ model

more accurately models the spreading rate of both planar and round jets. In addition it also performs well in flows containing rotation, separation, recirculation or boundary layers under strong adverse pressure gradients.

Transport Equation

The transport equations for the Standard $k-\varepsilon$ model are given by

$$\frac{\partial(\rho k)}{\partial t}+\frac{\partial(\rho k u_j)}{\partial x_j}=\frac{\partial}{\partial x_i}\left[\left(\mu+\frac{\mu_t}{\sigma_k}\right)\frac{\partial k}{\partial x_j}\right]+G_k+G_b-\rho\epsilon-Y_M+S_k, \quad \text{(C.11)}$$

and

$$\frac{\partial(\rho\epsilon)}{\partial t}+\frac{\partial(\rho\epsilon u_j)}{\partial x_j}=\frac{\partial}{\partial x_j}\left[\left(\mu+\frac{\mu_t}{\sigma_\epsilon}\right)\frac{\partial\epsilon}{\partial x_j}\right]+C_{1\epsilon}\frac{\epsilon}{k}(G_k+C_{3\epsilon}G_b)-C_{2\epsilon}\rho\frac{\epsilon^2}{k}+S_\epsilon, \quad \text{(C.12)}$$

with constants: $C_{1\epsilon}=1.44$, $C_{2\epsilon}$ =1.92 and turbulent Prandtl numbers: σ_ϵ =1.3, σ_k =1. S_ϵ and S_k are the source terms. G_k is the production of turbulent kinetic energy, given by: $G_k=-\rho\overline{u_i'u_j'}\frac{\partial u_j}{\partial x_i}=\mu_t S^2$, where S is the strain-rate tensor: $S=\sqrt{2S_{ij}S_{ij}}$ and the turbulent viscosity, μ_t is calculated as: $\mu_t=\rho C_\mu\frac{k^2}{\epsilon}$. C_μ is a constant with a value of 0.09. Y_M accounts for compressibility effects and is modelled as: $Y_M=2\rho\epsilon M_t^2$, where M_t is the turbulent Mach number defined as: $M_t=\sqrt{\frac{k}{a^2}}$. The turbulent viscosity (μ_t) is given by: $\mu_t=\rho C_\mu\frac{k^2}{\epsilon}$.

C.2.2 $k-\omega$

The second most common family of turbulence models is the $k-\omega$ model. Two equations are again solved to represent the flow turbulence. The two transported variables are k, the turbulent kinetic energy and ω, the specific dissipation rate. The Standard model was the primary model developed and is widely used in engineering calculations for internal flows due to its superior performance of wall-bounded flows.

Transport Equation

$$\frac{\partial}{\partial t}(\rho k)+\frac{\partial}{\partial x_i}(\rho k u_i)=\frac{\partial}{\partial x_j}\left(\Gamma_k\frac{\partial k}{\partial x_i}\right)+G_k-Y_k+S_k, \quad \text{(C.13)}$$

$$\frac{\partial}{\partial t}(\rho\omega)+\frac{\partial}{\partial x_i}(\rho\omega u_i)=\frac{\partial}{\partial x_j}\left(\Gamma_\omega\frac{\partial\omega}{\partial x_i}\right)+G_\omega-Y_\omega+S_\omega, \quad \text{(C.14)}$$

respectively, where S_ω is a user-defined source term, G_k represents the generation of turbulent kinetic energy due to the mean velocity gradients, G_ω represents the generation of ω. Γ_k and Γ_ω represent the effective diffusivity of k and ω, respectively.

Effective Diffusivity

The effective diffusivities for k and ω are given by

$$\Gamma_k = \mu + \frac{\mu_t}{\sigma_k}, \tag{C.15}$$

$$\Gamma_\omega = \mu + \frac{\mu_t}{\sigma_\omega}, \tag{C.16}$$

where σ_k and σ_ω are the turbulent Prandtl number for k and ω, respectively. The turbulent viscosity (μ_t) is computed combining k and ω by: $\mu_t = \alpha^* \frac{\rho k}{\omega}$. Y_k and Y_ω represent the dissipation of k and ω, respectively.

Low Reynolds Number Correction

The coefficient α^*, if enabled (if disabled $\alpha^* = \alpha^*_\infty = 1$) within ANSYS® FLUENT® 15.0 (low Re correction) is given by

$$\alpha^* = \alpha^*_\infty \left(\frac{\alpha^*_0 + Re_t/R_k}{1 + Re_t/R_k} \right). \tag{C.17}$$

Production of k

The production of turbulent kinetic energy is denoted by G_k within ANSYS® FLUENT® 15.0. The exact transport of k is given by

$$G_k = -\rho \overline{u_i' u_j'} \frac{\partial u_j}{\partial x_j}. \tag{C.18}$$

ANSYS® FLUENT® 15.0 evaluates G_k in a manner consistent with the Boussinesq hypothesis,

$$G_k = \mu_t S^2, \tag{C.19}$$

where $S \equiv \sqrt{2 S_{ij} S_{ij}}$.

Production of ω

The production of ω within ANSYS® FLUENT® 15.0 is given by

$$G_\omega = \alpha \frac{\omega}{k} G_k, \tag{C.20}$$

where

$$\alpha = \frac{a_\infty}{\alpha^*}\left(\frac{a_0 + Re_t/Re_\omega}{1 + Re_t/R_\omega}\right), \tag{C.21}$$

where $R_\omega = 2.95.\alpha^*$ and Re_t is given by

$$Re_t = \frac{\rho k}{\mu\omega}. \tag{C.22}$$

Dissipation of k

The dissipation of k is given by: $Y_k = \rho\beta^* f_{\beta^*} \cdot k\omega$, where

$$f_{\beta^*} = \begin{cases} 1 & \chi_k \leq 0 \\ \frac{1+680\chi_k^2}{1+400\chi_k^2} & \chi_k > 0 \\ , \end{cases} \tag{C.23}$$

$$\chi_k \equiv \frac{1}{\omega^3}\frac{\partial k}{\partial x_j}\frac{\partial \omega}{\partial x_j}, \tag{C.24}$$

$$\beta^* = 0.09\left(\frac{4/15 + (Re_t/8)^4}{(1 + (Re_t/8)^4}\right). \tag{C.25}$$

Dissipation of ω

The dissipation of ω is given by $Y_\omega = \rho\beta f_\beta \cdot \omega^2$, where

$$f_\beta = \frac{1 + 70\chi_\omega}{1 + 80\chi_\omega}, \tag{C.26}$$

$$\chi_\omega = \left|\frac{\Omega_{ij}\Omega_{ji}S_{ki}}{(0.09\omega)^3}\right|, \tag{C.27}$$

$$\Omega_{ij} = \frac{1}{2}\left(\frac{\partial u_i}{\partial x_j} - \frac{\partial u_j}{\partial x_i}\right). \tag{C.28}$$

C.2.3 Shear-Stress Transport (SST) $k - \omega$

Transport Equations

The SST $k-\omega$ turbulence model has transport equations similar to the Standard $k - \omega$ model, given by

$$\frac{\partial}{\partial t}(\rho k) + \frac{\partial}{\partial x_i}(\rho k u_i) = \frac{\partial}{\partial x_j}\left(\Gamma_k \frac{\partial k}{\partial x_i}\right) + G_k - Y_k + S_k, \tag{C.29}$$

$$\frac{\partial}{\partial t}(\rho \omega) + \frac{\partial}{\partial x_j}(\rho \omega u_j) = \frac{\partial}{\partial x_j}\left(\Gamma_\omega \frac{\partial \omega}{\partial x_j}\right) + G_\omega - Y_\omega + D_\omega + S_\omega, \tag{C.30}$$

where G_k and G_ω are calculated in the same manner as the Standard $k-\omega$ model mentioned earlier. S_k and S_ω are user defined source terms.

Effective Diffusivity

The effective diffusivities within the Standard $k-\omega$ model in ANSYS® FLUENT® 15.0 is given by

$$\Gamma_k = \mu + \frac{\mu_t}{\sigma_k}, \tag{C.31}$$

$$\Gamma_\omega = \mu + \frac{\mu_t}{\sigma_\omega}, \tag{C.32}$$

where σ_k and σ_ω are the turbulent Prandtl numbers for k and ω, respectively. The turbulent viscosity is given by u_t and is calculated as

$$\mu_t = \frac{\rho k}{\omega} \frac{1}{\max\left[\frac{1}{\alpha^*}, \frac{SF_2}{a_1 \omega}\right]}, \tag{C.33}$$

where S is the strain rate magnitude defined earlier and

$$\sigma_k = \frac{1}{f_1/\sigma_{k,1} + (1-F_1)/\sigma_{k,2}}, \tag{C.34}$$

$$\sigma_\omega = \frac{1}{f_1/\sigma_{\omega,1} + (1-F_1)/\sigma_{\omega,2}}, \tag{C.35}$$

the blending functions F_1 and F_2 are given by

$$F_1 = tanh(\Phi_1^4), \tag{C.36}$$

where

$$\Phi_1 = \min\left[\max\left(\frac{\sqrt{k}}{0.09\omega y}, \frac{500\mu}{\rho y^2 \omega}\right), \frac{4\rho k}{\sigma_{\omega,2} D_\omega^+ y^2}\right], \tag{C.37}$$

$$D_\omega^+ = \max\left[2\rho \frac{1}{\omega, 2}\frac{1}{\omega}\frac{\partial k}{\partial x_j}\frac{\partial \omega}{\partial x_j}, 10^{-10}\right], \tag{C.38}$$

$$F_2 = tanh(\Phi_2^2), \tag{C.39}$$

$$\Phi_2 = \left[2\frac{\sqrt{k}}{0.09\omega y}, \frac{500\mu}{\rho y^2 \omega} \right], \tag{C.40}$$

where y is the distance to the surface and D_ω^+ is the positive portion of the cross-diffusion term.

Production of k

The term G_k is the production of turbulent kinetic energy within the SST $k-\omega$ model and is defined in the same manner as the Standard $k-\omega$ model.

Production of ω

The production of ω is given by G_ω given by

$$G_\omega = \frac{\alpha}{\nu_t} G_k, \tag{C.41}$$

where this formulation differs from the Standard $k-\omega$. In the Standard $k-\omega$ model α_∞ is a constant, however, in the SST $k-\omega$ model it is given by

$$\alpha_\infty = F_1 \alpha_{\infty,1} + (1 - F_1)\alpha_{\infty,2}, \tag{C.42}$$

where

$$\alpha_{\infty,1} = \frac{\beta_i, 1}{\beta_\infty^*} - \frac{(0.41)^2}{\sigma_{w,1}\sqrt{\beta_\infty^*}}, \tag{C.43}$$

$$\alpha_{\infty,2} = \frac{\beta_i, 2}{\beta_\infty^*} - \frac{(0.41)^2}{\sigma_{w,2}\sqrt{\beta_\infty^*}}, \tag{C.44}$$

Dissipation of k

Within the SST $k-\omega$ model, Y_k is the dissipation of the turbulent kinetic energy and is defined in the same manner as the Standard $k-\omega$ model. The difference between the two models is in the evaluation of the f_{β^*} term. In the Standard $k-\omega$ model it is defined as a piecewise function. For the SST $k-\omega$ model, however, it is a constant equal to 1, therefore

$$Y_k = \rho\beta^* k\omega. \tag{C.45}$$

Dissipation of ω

Within the SST $k-\omega$ model, Y_ω is the dissipation of ω and is defined in the same manner as the Standard $k-\omega$ model. The difference between the two models is in the evaluation of the f_β term, in the Standard $k-\omega$ it is calculated, however, in the SST $k-\omega$ model it is a constant equal to 1, therefore Y_ω is given by

$$Y_\omega = \rho\beta_i\omega^2, \tag{C.46}$$

with β_i given by

$$\beta_i = F_1\beta_{i,1} + (1-F_1)\beta_{i,2}. \tag{C.47}$$

Cross Diffusion Modification

The SST $k-\omega$ model is based on the Standard $k-\omega$ model and the Standard $k-\varepsilon$ model. To blend the two models, the Standard $k-\varepsilon$ has been transformed in ANSYS® FLUENT® 15.0 to models based on k and ω, which leads to the introduction of a cross-diffusion term (D_ω) given by

$$D_\omega = 2(1-F_1)\rho\frac{1}{\omega\sigma_{\omega,2}}\frac{\partial k}{\partial x_j}\frac{\partial\omega}{\partial x_j}. \tag{C.48}$$

C.2.4 Transition (SST) $k-\omega$

The Transition SST $k-\omega$ by Langtry et al. [115], uses the original SST $k-\omega$ model coupled with two other transport equations. Intermittency and transition onset criteria in terms of momentum-thickness Reynolds number. This model is useful for standard bypass transition as well as low freestream turbulence environments.

Transport Equations

The transport equations for intermittency (γ) and transition momentum thickness Reynolds number ($R\tilde{e}_{\theta t}$) are given by

$$\frac{\partial(\rho\gamma)}{\partial t} + \frac{\partial(\rho U_j\gamma)}{\partial x_j} = P_{\gamma1} - E_{\gamma1} + P_{\gamma2} - E_{\gamma2} + \frac{\partial}{\partial x_j}\left[\left(\mu + \frac{\mu_t}{\sigma_\gamma}\right)\frac{\partial\gamma}{\partial x_j}\right], \tag{C.49}$$

$$\frac{\partial(\rho R\tilde{e}_{\theta t})}{\partial t} + \frac{\partial(\rho U_j R\tilde{e}_{\theta t})}{\partial x_j} = P_{\theta t} + \frac{\partial}{\partial x_j}\left[\sigma_{\theta t}\left(\mu+\mu_t\right)\frac{\partial R\tilde{e}_{\theta t}}{\partial x_j}\right], \tag{C.50}$$

respectively.

The transition source terms are given by

$$P_{\gamma 1} = C_{a1} F_{length} \rho S \left[\gamma F_{onset}\right]^{c\gamma 3}, \tag{C.51}$$

$$E_{\gamma 1} = C_{e1} P_{\gamma 1} \gamma, \tag{C.52}$$

where S is the strain rate magnitude, F_{length} is an empirical calculation that controls the length of the transition region. The destruction/relaminarization sources are given by

$$P_{\gamma 2} = C_{a2} \rho \Omega \gamma F_{turb}, \tag{C.53}$$

$$E_{\gamma 2} = C_{e2} P_{\gamma 2} \gamma, \tag{C.54}$$

where Ω is the vorticity magnitude. The transition onset is defined within ANSYS® FLUENT® 15.0 using

$$Re_{\nu} = \frac{\rho y^2 S}{\mu}, \tag{C.55}$$

$$R_T = \frac{\rho k}{\mu \omega}, \tag{C.56}$$

$$F_{onset1} = \frac{Re_{\nu}}{2.193 Re_{\theta c}}, \tag{C.57}$$

$$F_{onset2} = \min(\max(F_{onset1}, F_{onset4}), 2.0), \tag{C.58}$$

$$F_{onset3} = \max\left(1 - \left(\frac{R_T}{2.5}\right)^3, 0\right), \tag{C.59}$$

$$F_{onset4} = \max(F_{onset2} - F_{onset3}, 0), \tag{C.60}$$

$$F_{turb} = e^{-\left(\frac{R_T}{4}\right)^4}, \tag{C.61}$$

where y is the wall distance and $Re_{\theta c}$ is the critical Reynolds number where the intermittency first starts to increase in the boundary layer.

The source terms for the transition momentum thickness Reynolds number $R\tilde{e}_{\theta t}$ are given by

$$P_{\theta t} = c_{\theta t} \frac{\rho}{t} (Re_{\theta t} - R\tilde{e}_{\theta t})(1.0 - F_{\theta t}), \tag{C.62}$$

$$t = \frac{500\mu}{\rho U^2}, \tag{C.63}$$

$$F_{\theta t} = \min\left(\max\left(F_{wake}e^{\left(-\frac{y}{\delta}\right)^4}, 1.0 - \left(\frac{\gamma - 1/50}{1.0 - 1/50}\right)^2\right), 1.0\right), \tag{C.64}$$

$$\theta_{BL} = \frac{R\tilde{e}_{\theta t}\mu}{\rho U}, \tag{C.65}$$

$$\delta_{BL} = \frac{15}{2}\theta_{BL}, \tag{C.66}$$

$$\delta = \frac{50\Omega y}{U}\delta_{BL}, \tag{C.67}$$

$$Re_\omega = \frac{\rho\omega y^2}{\mu}, \tag{C.68}$$

$$F_{wake} = e^{-\left(\frac{Re_\omega}{1E+5}\right)^2}. \tag{C.69}$$

The model contains three empirical correlations. The transition onset $Re_{\Theta t}$, the length of transition F_{length} and $Re_{\Theta c}$, the critical point at which the model is activated.

SST Transport Equation Coupling

The transition model interacts with the SST turbulence model by modification of the k-equation as follows

$$\frac{\partial}{\partial t}(\rho k) + \frac{\partial}{\partial x_i}(\rho k u_i) = \frac{\partial}{\partial x_j}\left(\Gamma_k \frac{\partial k}{\partial x_j}\right) + G_k^* - Y_k^* + S_k, \tag{C.70}$$

where

$$G_k^* = \gamma_{eff}\tilde{G}_k, \tag{C.71}$$

$$Y_k^* = \min\left(\max\left(\gamma_{eff}, 0.1\right), 1.0\right) Y_k, \tag{C.72}$$

where $\tilde{G}_k$ and Y_k are the original production and destruction terms of the SST model mentioned earlier.

C.3 Upwind Discretisation Scheme

By default, ANSYS® FLUENT® 15.0 stores discrete values of the cell-centred value (ϕ) at the cell centre. For convection terms face values (ϕ_f) are required. Interpolation over cell centre values are therefore conducted. This is achieved through the use of an upwind discretisation scheme. An upwind discretisation scheme derives the face value (ϕ_f) from the upwind cells relative to the normal velocity (v).

For second order accuracy, the cell faces are computed using a multidimensional linear reconstruction.

High-order accuracy is achieved via a Taylor series expansion of the cell-centred solution about the cell centroid.

For a second-order upwind discretisation, ϕ_f is calculated by

$$\phi_{f,SOU} = \phi + \nabla\phi \cdot \overrightarrow{r}, \tag{C.73}$$

where ϕ and $\nabla\phi$ are the cell-centred value and upstream cell gradient and $\overrightarrow{r}$ is the displacement vector from the upstream cell centroid to the face centroid. $\nabla\phi$ is maxima/minima limited such that no new extremum values are introduced.

C.4 SIMPLE Pressure-Velocity Coupling

SIMPLE or Semi-Implicit Method for Pressure-Linked Equations is an iterative algorithm designed to relate velocity and pressure corrections to enforce mass conservation and obtain the pressure field. This correction is required for incompressible flows where pressure does not explicitly appear in the continuity equation. The algorithm is designed to calculate the pressure and velocity at different nodes in the control volume. The calculation at different nodal points removes the effect that a non-uniform pressure field can act like a uniform one. As a result, the scalar variables such as pressure and density at ordinary points but with velocity components on staggered grids centred on the cell face.

Appendix D

Subscale Heat Exchangers

D.1 Wind Tunnel Arrangement

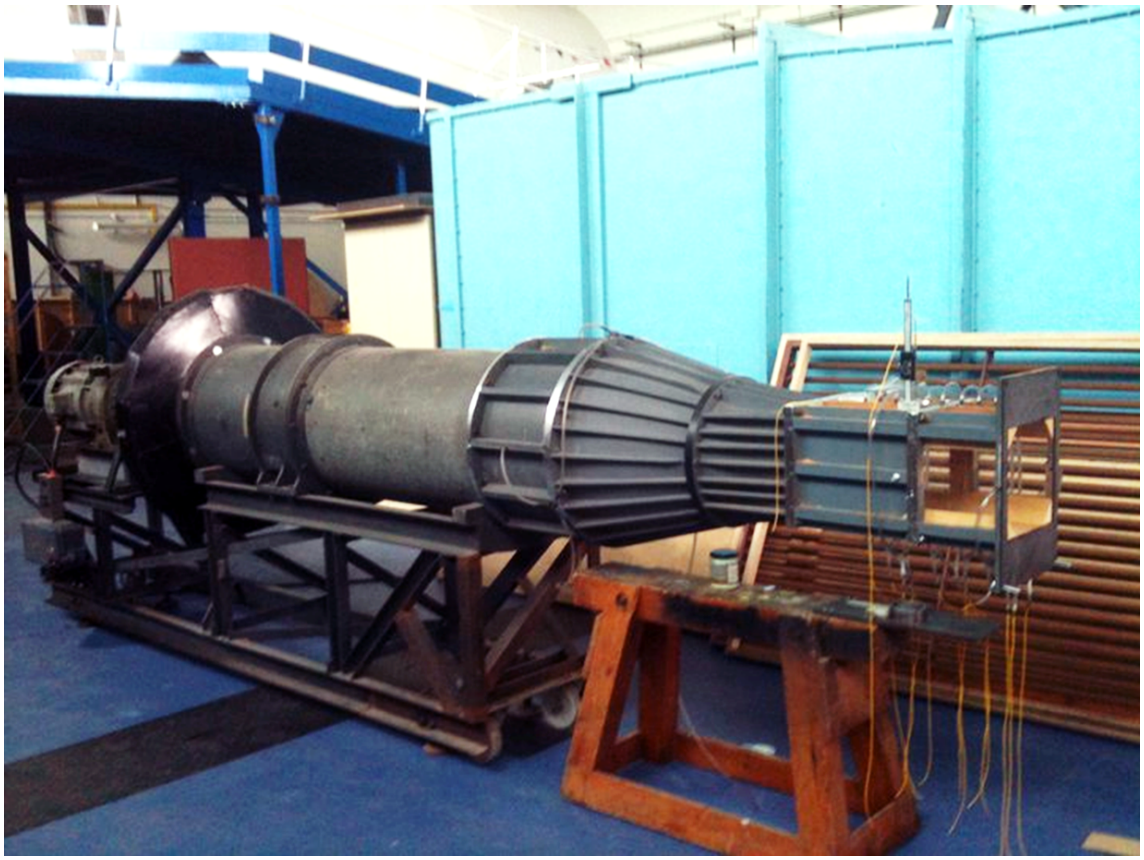

Figure D.1 Cranfield University's blower wind tunnel.

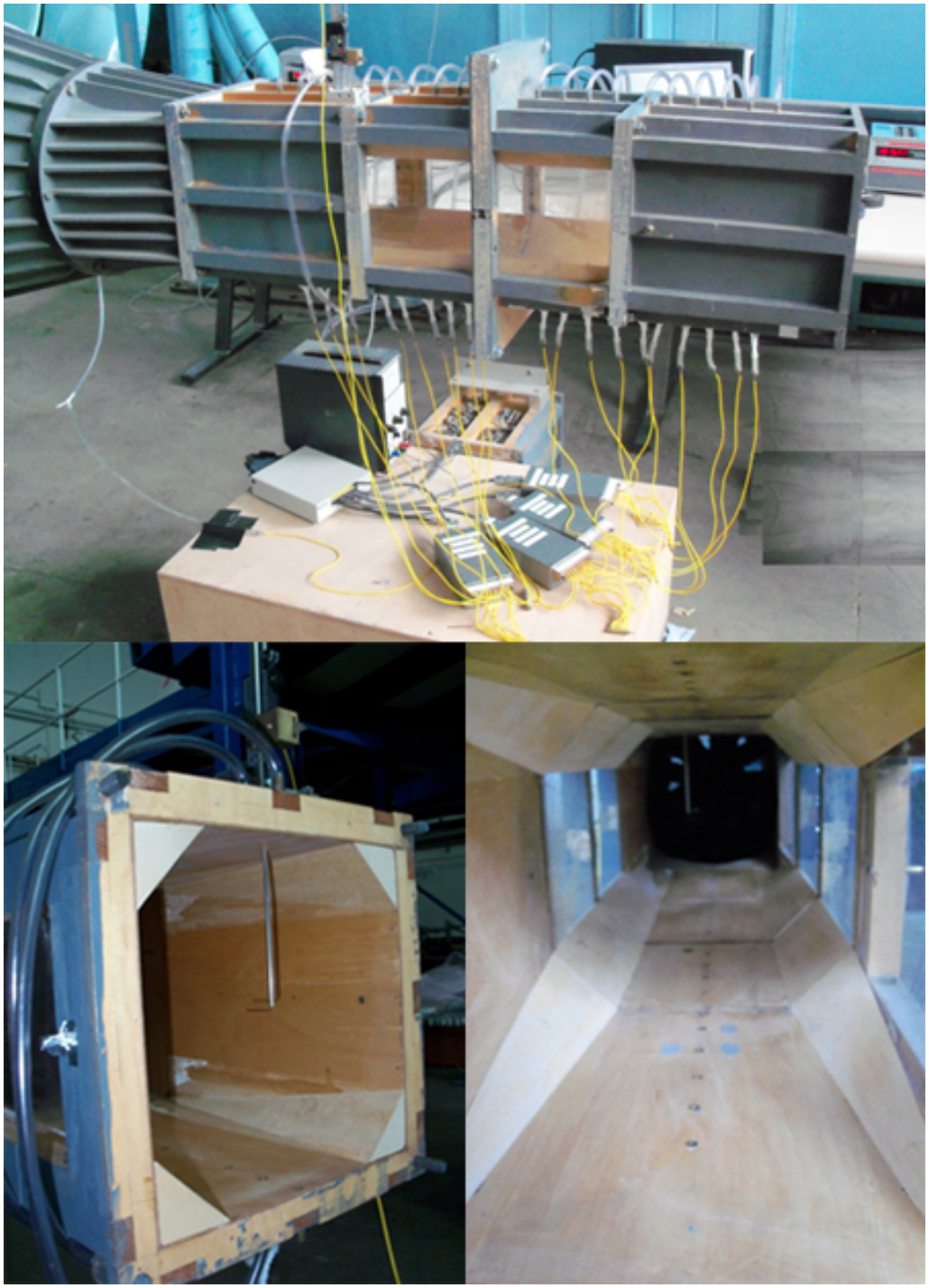

Figure D.2 Interior of Cranfield University's blower wind tunnel and working section.

D.2 Working Section Renderings

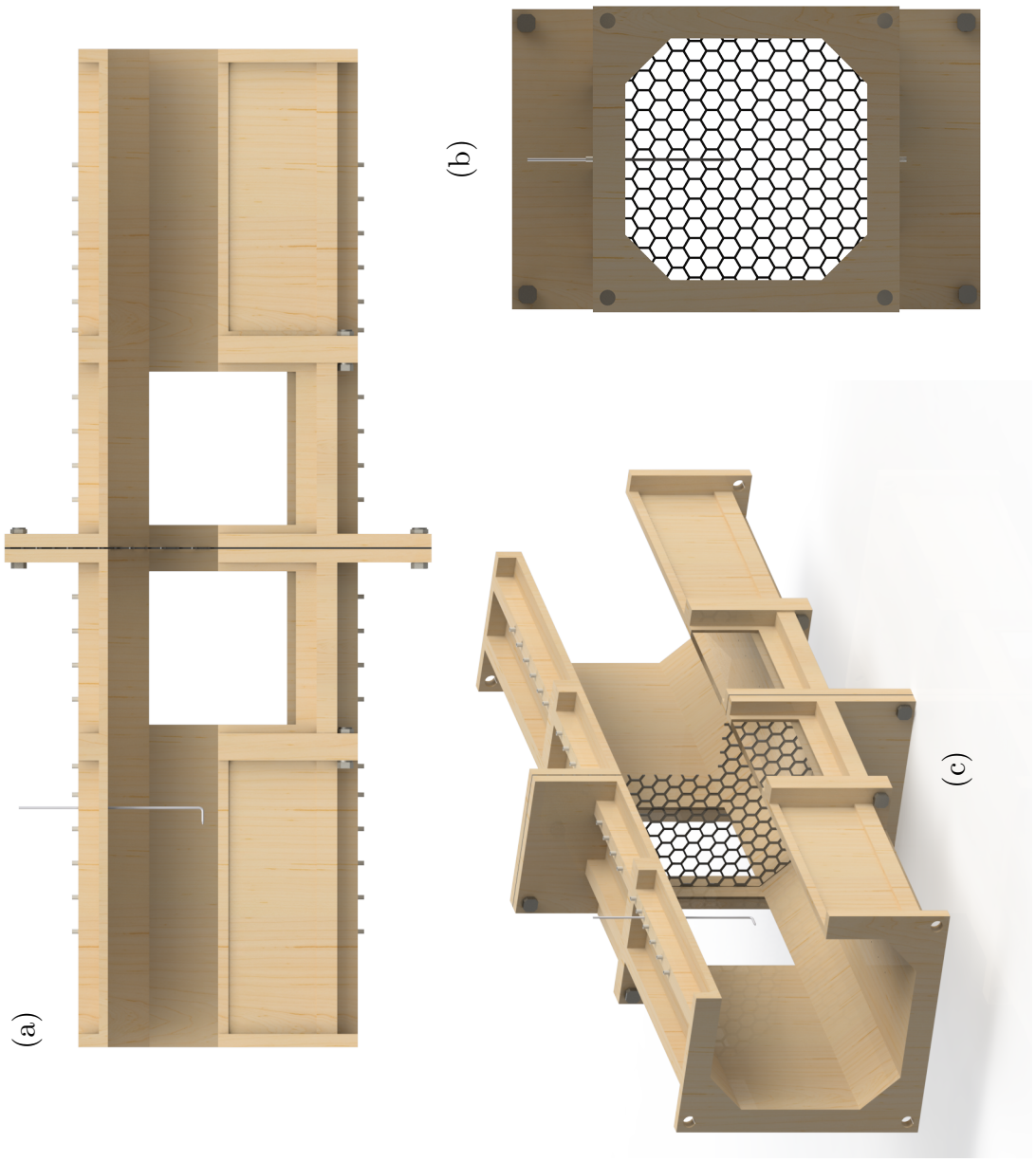

Figure D.3 Render of Cranfield University's blower wind tunnel, (a) side view, (b) front view and (c) 3/4 view.

D.3 Wind Tunnel Schematic

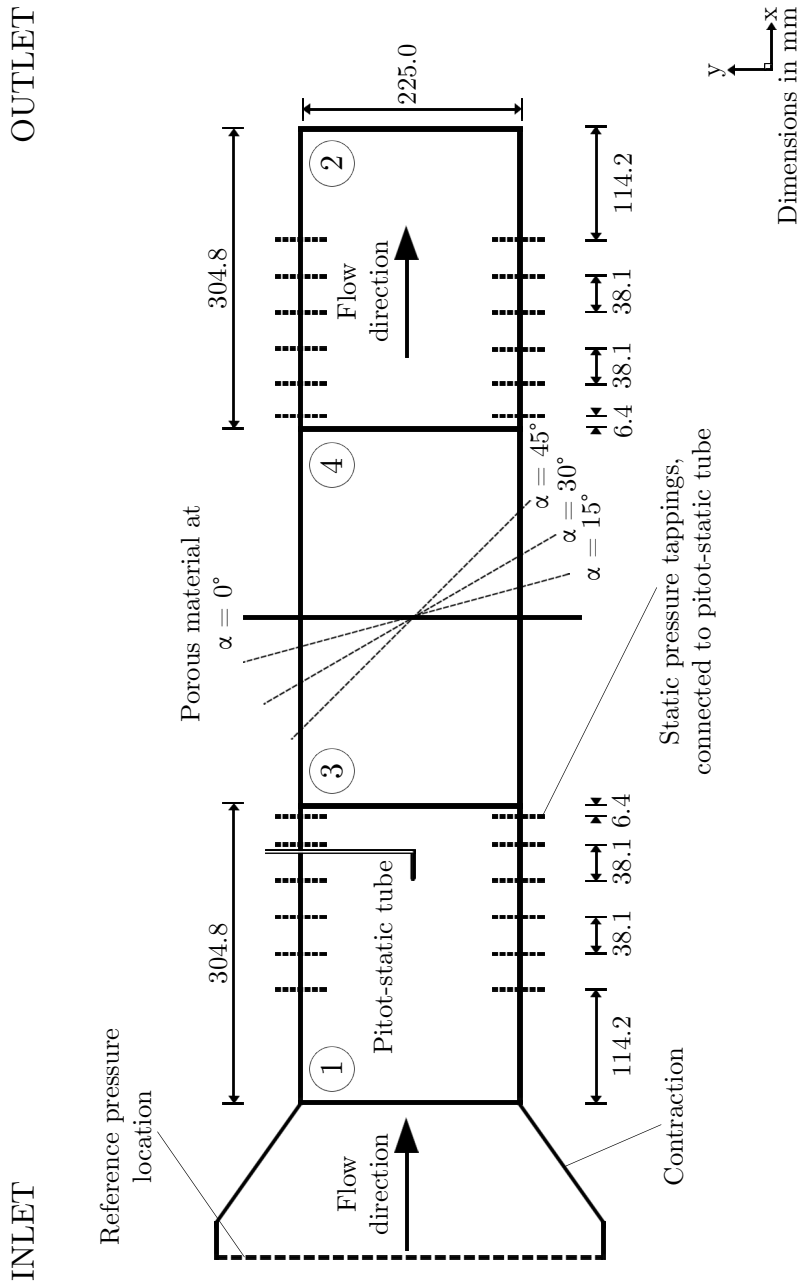

Figure D.4 Schematic of Cranfield University's blower wind tunnel working section.

D.4 Schematics of the Working Sections

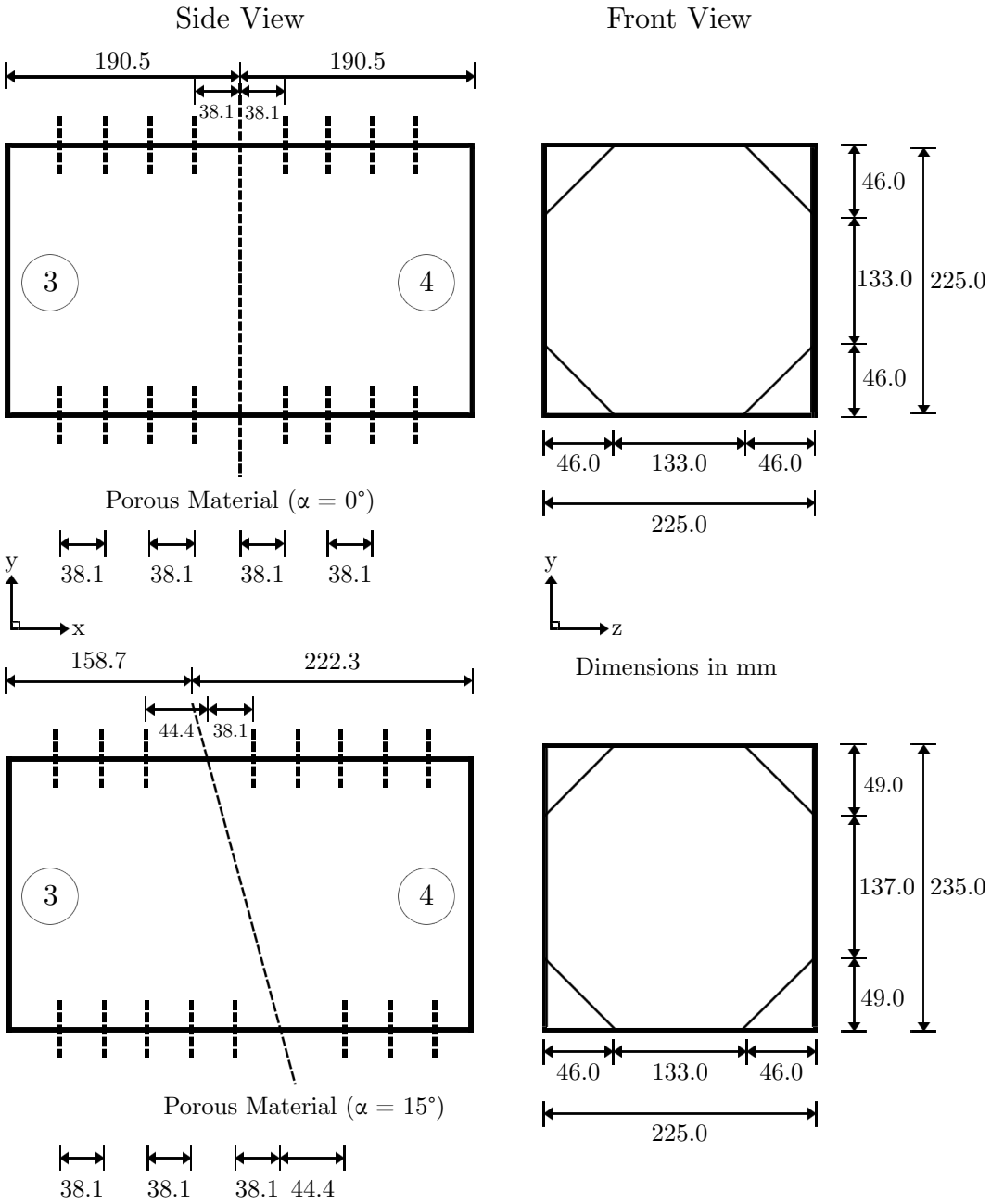

Figure D.5 Schematic of the working sections for inclination angles of $\alpha = 0°$ (upper) and $\alpha = 15°$ (lower).

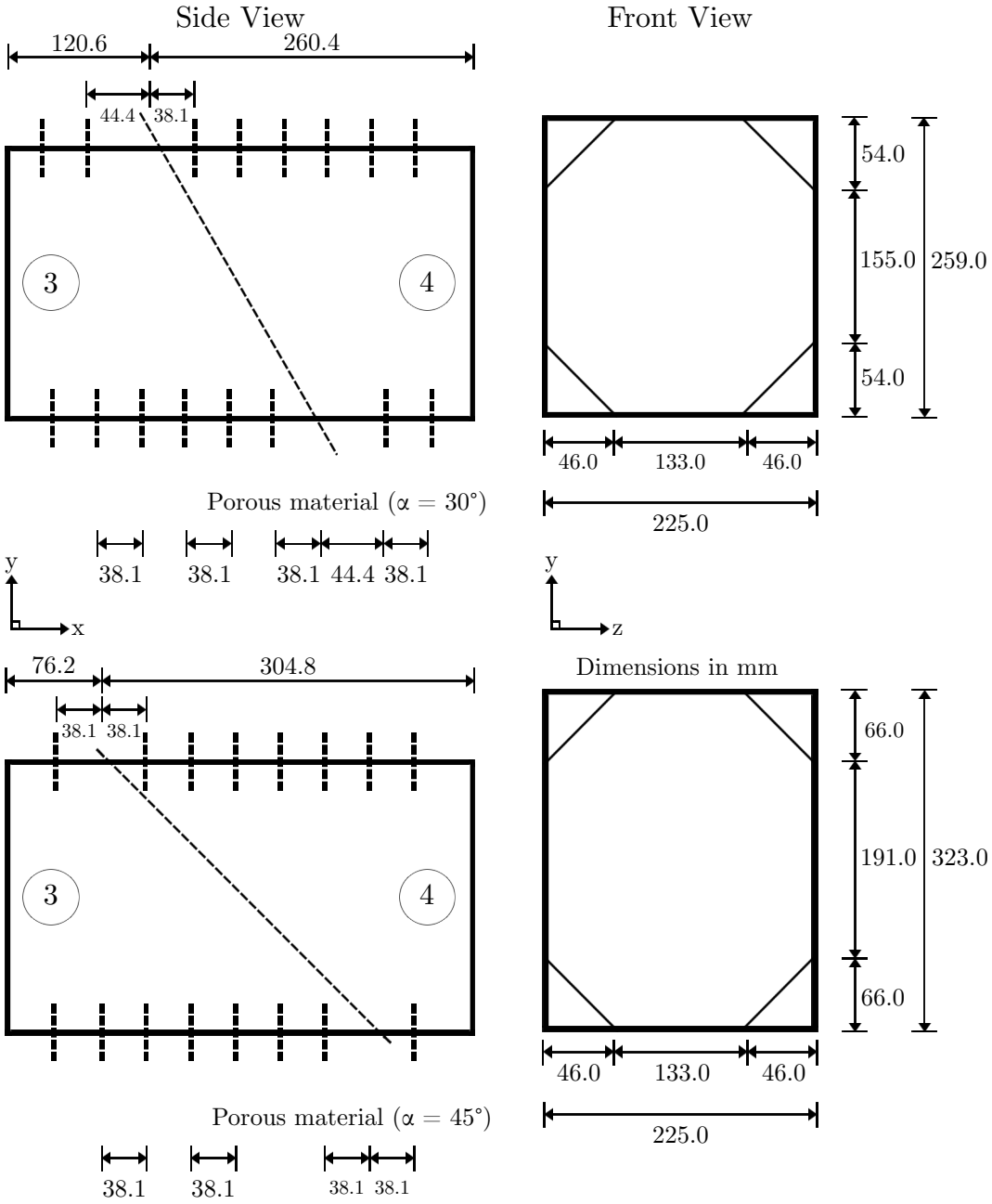

Figure D.6 Schematic of the working sections for inclination angles of $\alpha = 30°$ (upper) and $\alpha = 45°$ (lower).

D.5 Velocity Profiles

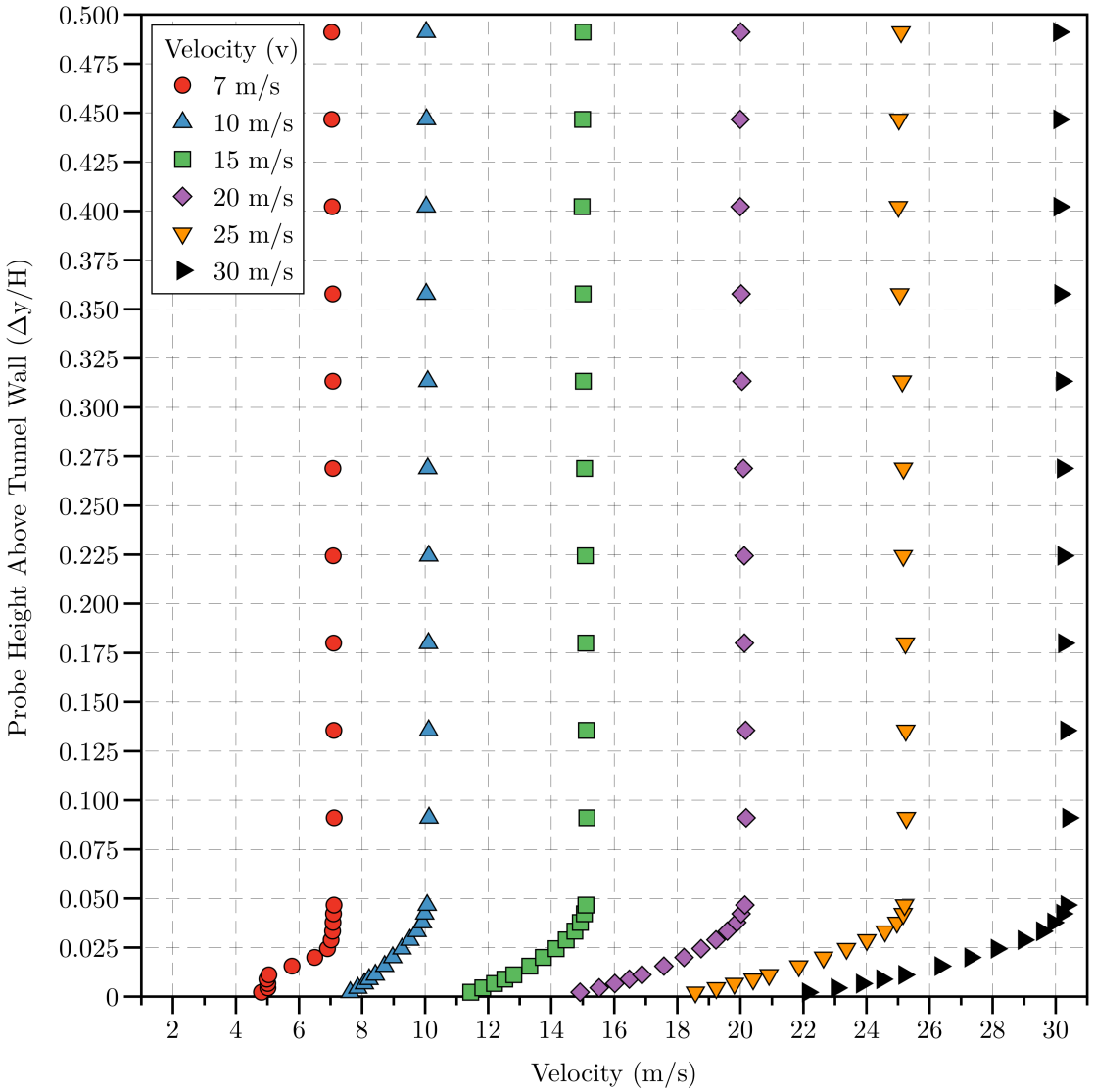

Figure D.7 Cranfiled blower wind tunnel velocity profiles for various velocities (v).

D.6 Repeatability Test

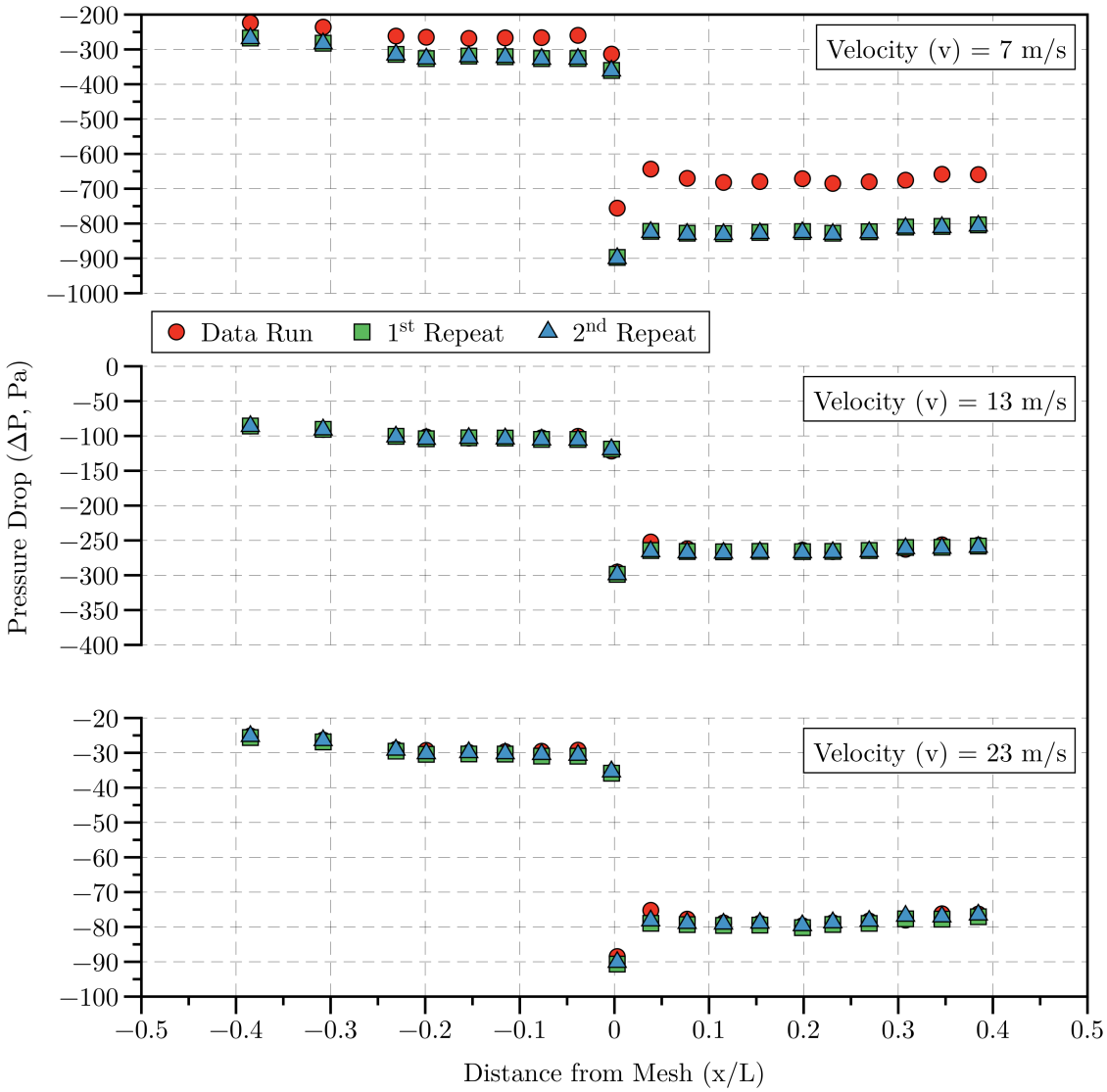

Figure D.8 Blower wind tunnel repeatability tests for various velocities (v), angle of inclination (α) = 0° and porosity (β) = 0.66.

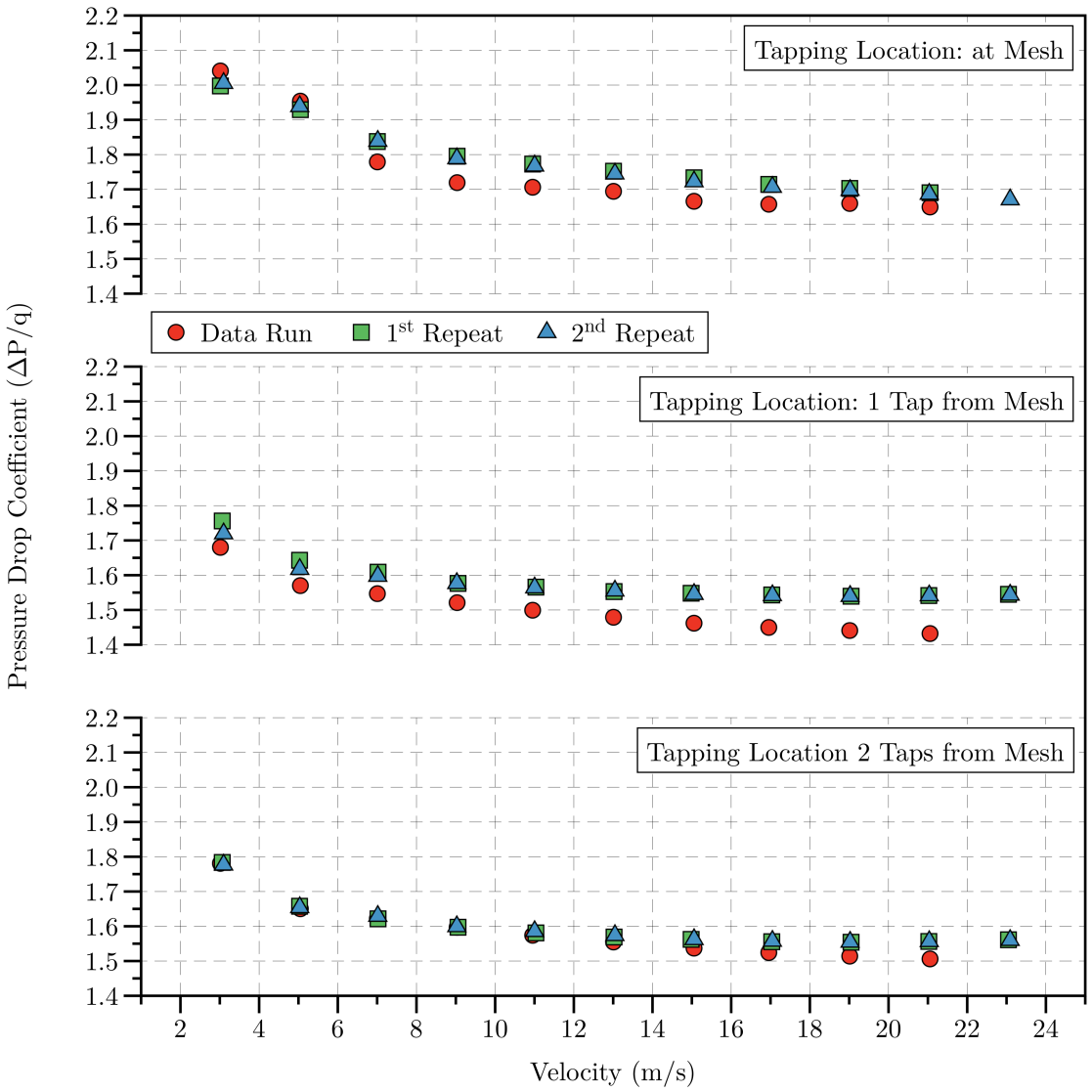

Figure D.9 Blower wind tunnel repeatability tests for ports close to the porous media as a function of velocity (v), angle of inclination (α) = 0° and porosity (β) = 0.66.

D.7 Error Analysis

Wind tunnel velocity can be determined from pitot-static probe measurements through Eq. (D.1), where q is the dynamic pressure and equals the difference of total and static pressure

$$v = \sqrt{\left(\frac{2q}{\rho}\right)}. \tag{D.1}$$

The relative error measurement in the velocity ($\Delta v/v$) is given by

$$\frac{\Delta v}{v} = \sqrt{\left(\frac{1}{2}\frac{\Delta q}{q}\right)^2 + \left(\frac{1}{2}\frac{\Delta \rho}{\rho}\right)^2}, \tag{D.2}$$

where the relative error of the air density ($\Delta\rho/\rho$) is given by

$$\frac{\Delta \rho}{\rho} = \sqrt{\left(\frac{\Delta P}{P}\right)^2 + \left(\frac{\Delta T}{T}\right)^2}, \tag{D.3}$$

where the errors specified by the manufacturers are $\Delta P = \pm 15\,\text{Pa}$ on the barometer (GE Druck DPI 141) and $\Delta T = \pm 0.5\,\text{K}$ on the thermometer. For the purpose of these calculations the experimentally recorded maximum barometric pressure and ambient temperature of $P = 99\,693\,\text{Pa}$ and $T = 288\,\text{K}$, respectively, will be used to determine the relative error in the air density. The error on the fluid density is therefore given by

$$\frac{\Delta \rho}{\rho} = \sqrt{\left(\frac{15}{99693}\right)^2 + \left(\frac{0.5}{288}\right)^2} = 0.00174. \tag{D.4}$$

The maximum relative error of the pressure transducers specified by the manufacturer is $\pm 0.3\%$ of the pressure measurement. The maximum dynamic pressure measured at 35 m/s is: $q = 750\,\text{Pa}$. The corresponding error is therefore

$$\frac{\Delta q}{q} = 0.3\% = 2.25\ \text{Pa}. \tag{D.5}$$

The error on the velocity measurement is given by

$$\frac{\Delta v}{v} = \sqrt{\left(\frac{1}{2}\frac{2.25}{750}\right)^2 + \left(\frac{1}{2}(0.00174)\right)^2} = 0.17\%. \tag{D.6}$$

A sample calculation of the relative error of the pressure drop coefficient ($\Delta P/q$) for a 50% porosity mesh (β) at a 0° inclination (α) is presented.

For the maximum wind tunnel speed of 21 m/s the dynamic pressure (q) and the pressure drop (ΔP) was measured to be $q = 270\,\text{Pa}$ and $\Delta P = 442\,\text{Pa}$, respectively.

The relative error is therefore given by

$$\frac{\Delta(\Delta P/q)}{\Delta P/q} = \sqrt{\left(\frac{\Delta(\Delta P)}{\Delta P}\right)^2 + \left(\frac{\Delta q}{q}\right)^2}, \tag{D.7}$$

$$\frac{\Delta(\Delta P/q)}{\Delta P/q} = \sqrt{\left(\frac{1.326}{442}\right)^2 + \left(\frac{0.81}{270}\right)^2} = 0.43\%. \tag{D.8}$$

D.8 Pressure Drop Distribution

The results for the longitudinal pressure distribution along the duct show a consistent trend which is qualitatively similar for all screens tested. An example for a mesh of porosity $\beta = 0.64$ at 0° and 45° is shown in Fig. D.10 and Fig. D.11, respectively, where the non-dimensional coordinate (x/L) is used to describe the longitudinal distance from the start of the working section (x) relative to its total length (L). Generally, the pressure drop occurs in close proximity to the screen and its magnitude increases with wind tunnel velocity. The newly established lower static pressure remains approximately constant downstream of the screen for the remainder of the working section up to its end at $x/L = 1$ and then slowly increases with distance. The same trend is observed upstream of the mesh. These changes in static pressure away from the mesh are due to variable cross section of the duct, Sections 1 and 2, which have corner fillets of longitudinally decreasing (with distance from the working section) cross sectional area.

As a result of the duct-type working section arrangement, when the mesh is inclined, differences in top and bottom pressure distribution occur in close proximity to the screen. These differences are of greater magnitude with increasing speed (v) and angle of inclination (α). This is possibly due to a difference in the effective mesh inclination angle relative to the incoming flow (streamlines are aligned with the duct walls) between the top and bottom of the working section. For example, as shown in Fig. D.11 for an inclination of 45°, the mesh at the ceiling is inclined with the flow direction and at the floor, it is inclined against the flow direction.

This results in a noticeably greater pressure drop across the mesh at the floor ($x/L = 0.19$) compared to the ceiling ($x/L = -0.19$). Sufficiently far away from the mesh (upstream of $x/L = -0.2$ and downstream of approximately $x/L = 0.2$) the pressures on top and bottom even out as the flow symmetry in vertical direction within the duct is restored.

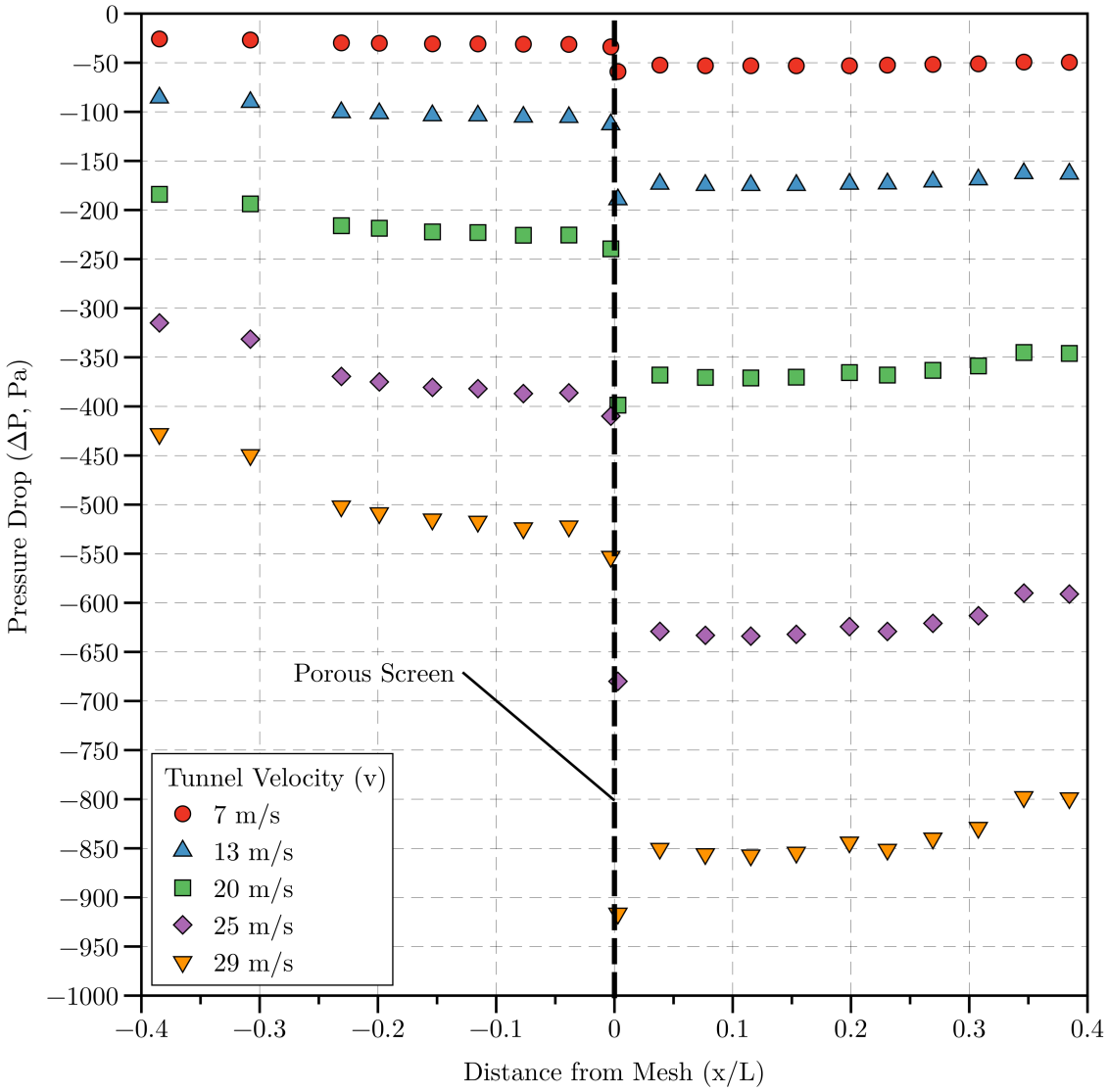

Figure D.10 Static pressure drop (ΔP) for various velocities (v), angle of inclination (α) = 0° and porosity (β) = 0.64.

$x-axis$: longitudinal distance along the wind tunnel centre line non-dimensionalized by the tunnel length, working section starts at $(x/)L = -0.19$ and ends at $(x/L) = 0.19$.
$y-axis$: pressure difference between the local static pressures (upstream and downstream of the screens) and the reference ring static pressure in the contraction, screen angle as shown in Figs. D.10 and D.11.

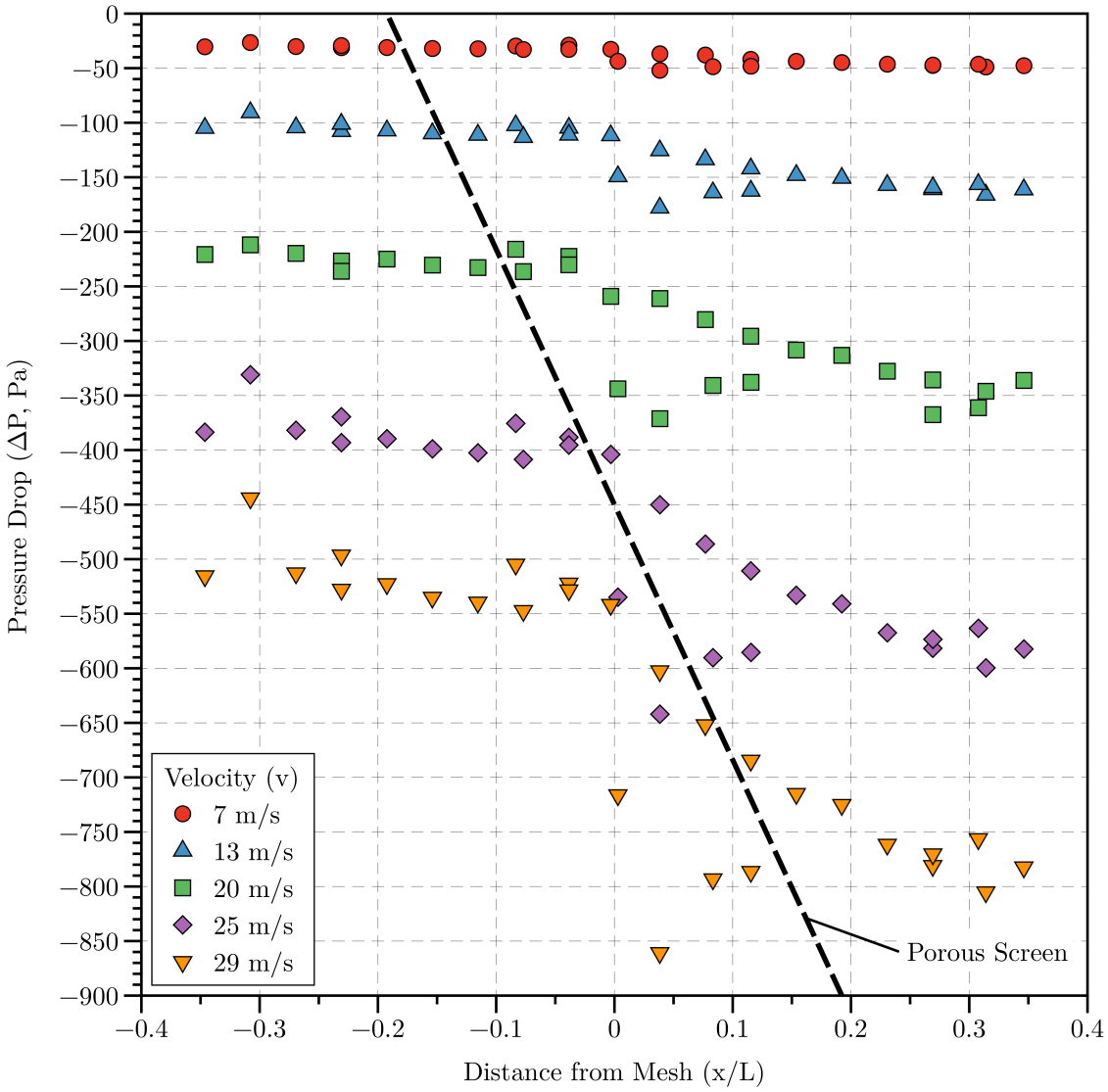

Figure D.11 Static pressure drop (ΔP) for various velocities (v), angle of inclination (α) = 45° and porosity (β) = 0.64.

D.9 Pressure Drop vs. Velocity Graphs

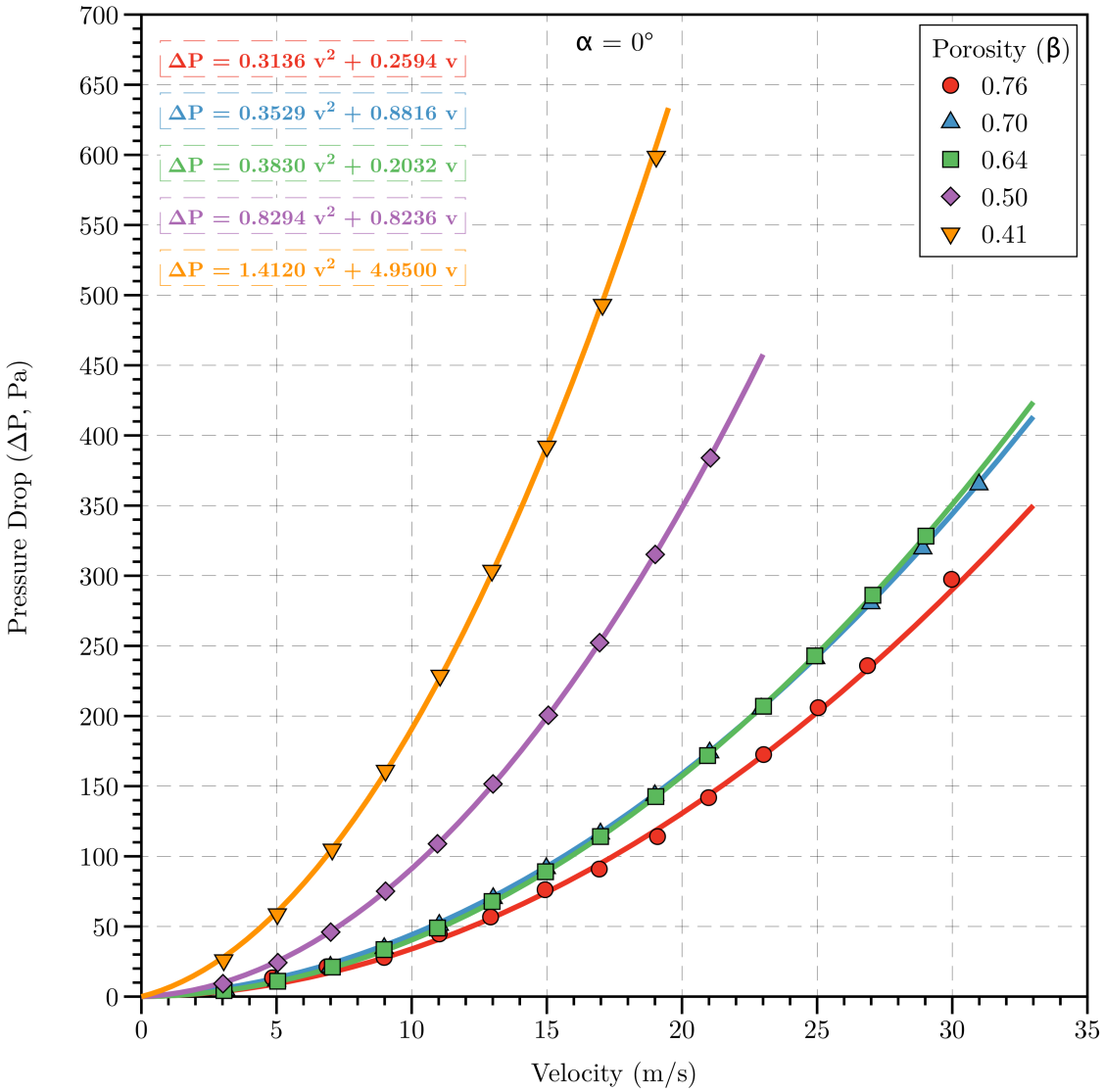

Figure D.12 Pressure drop (ΔP) vs. velocity (v) for various porosities (β), angle of inclination (α) = 0°.

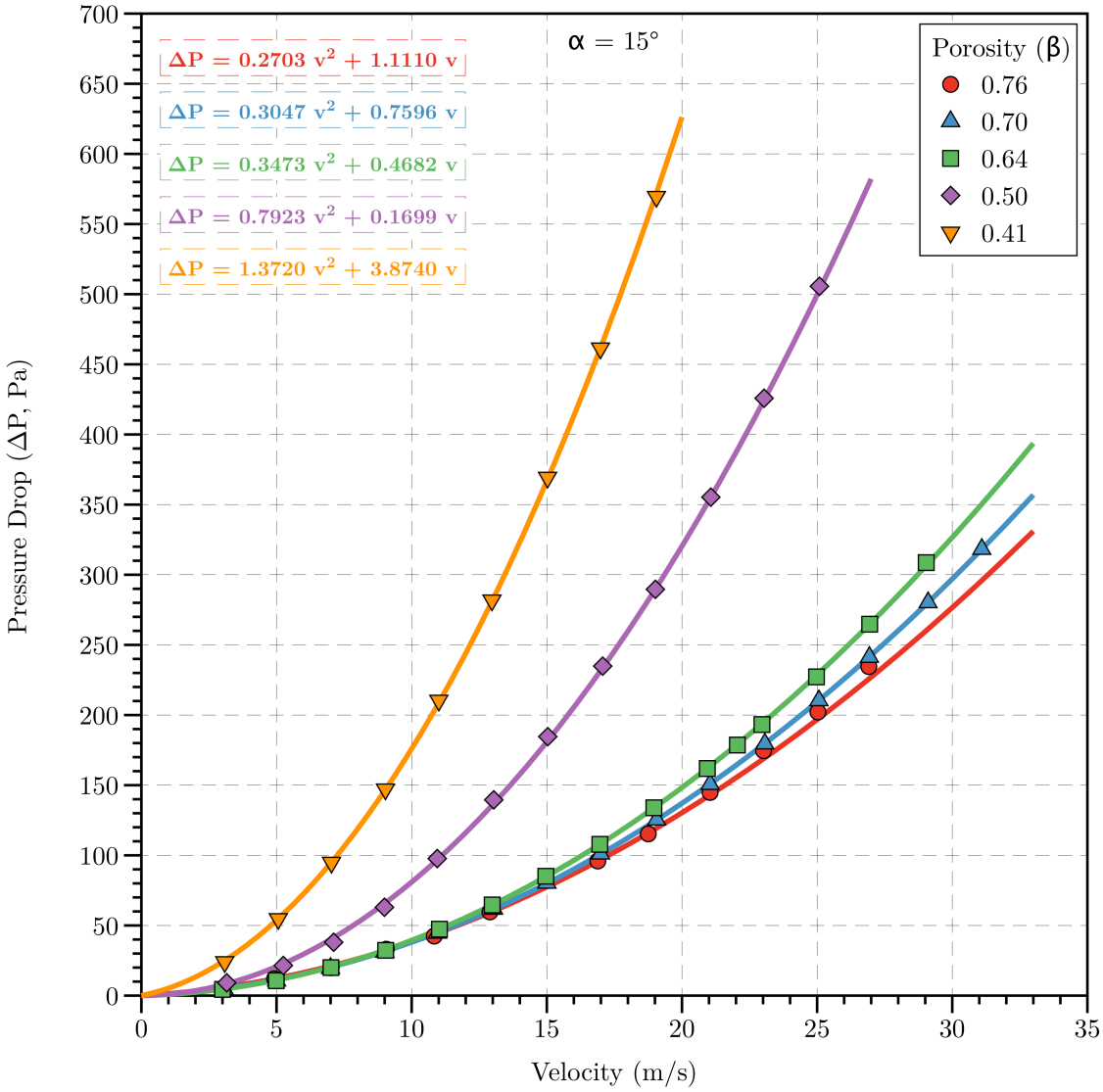

Figure D.13 Pressure drop (ΔP) vs. velocity (v) for various porosities (β), angle of inclination (α) = 15°.

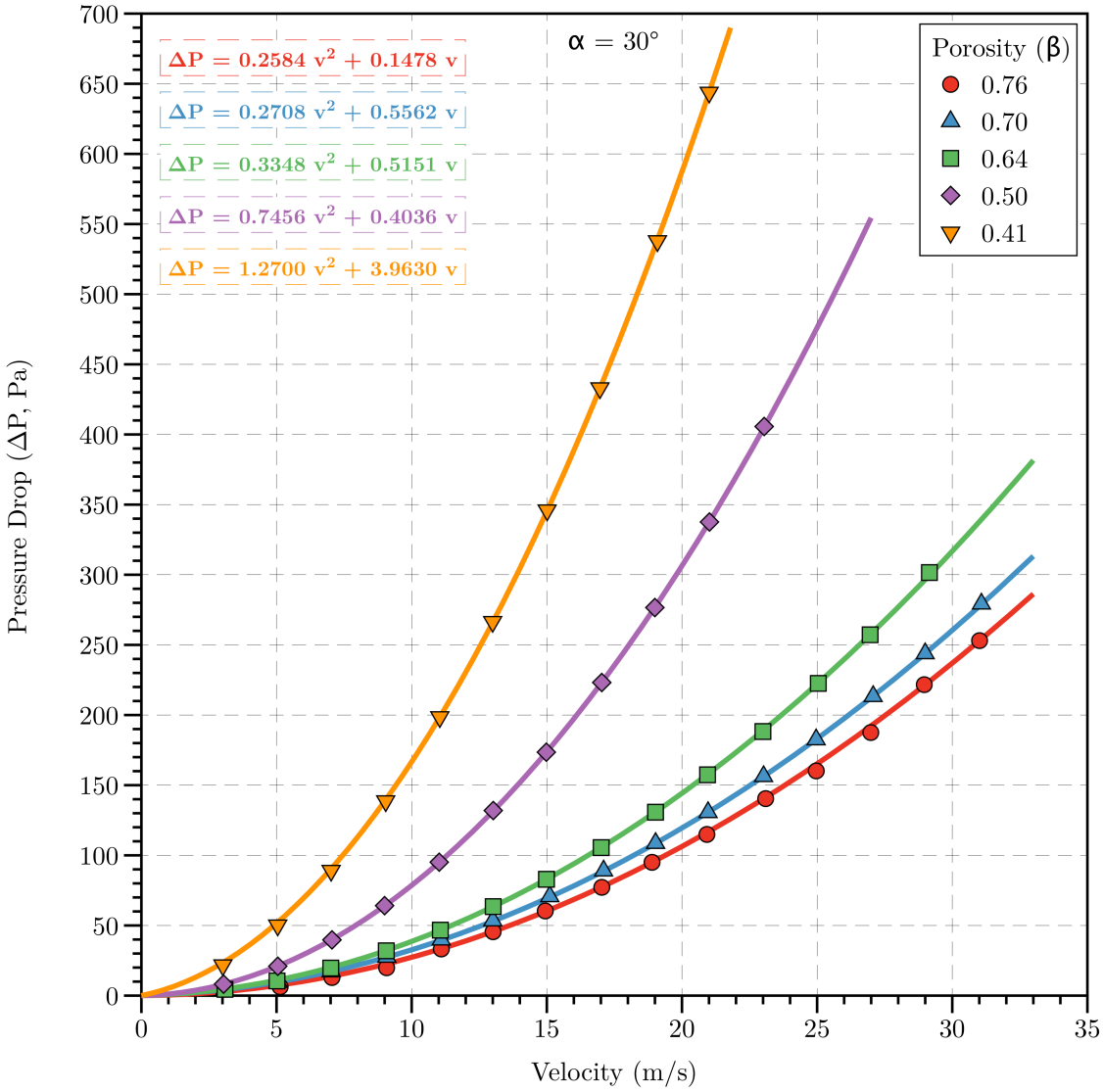

Figure D.14 Pressure drop (ΔP) vs. velocity (v) for various porosities (β), angle of inclination (α) = 30°.

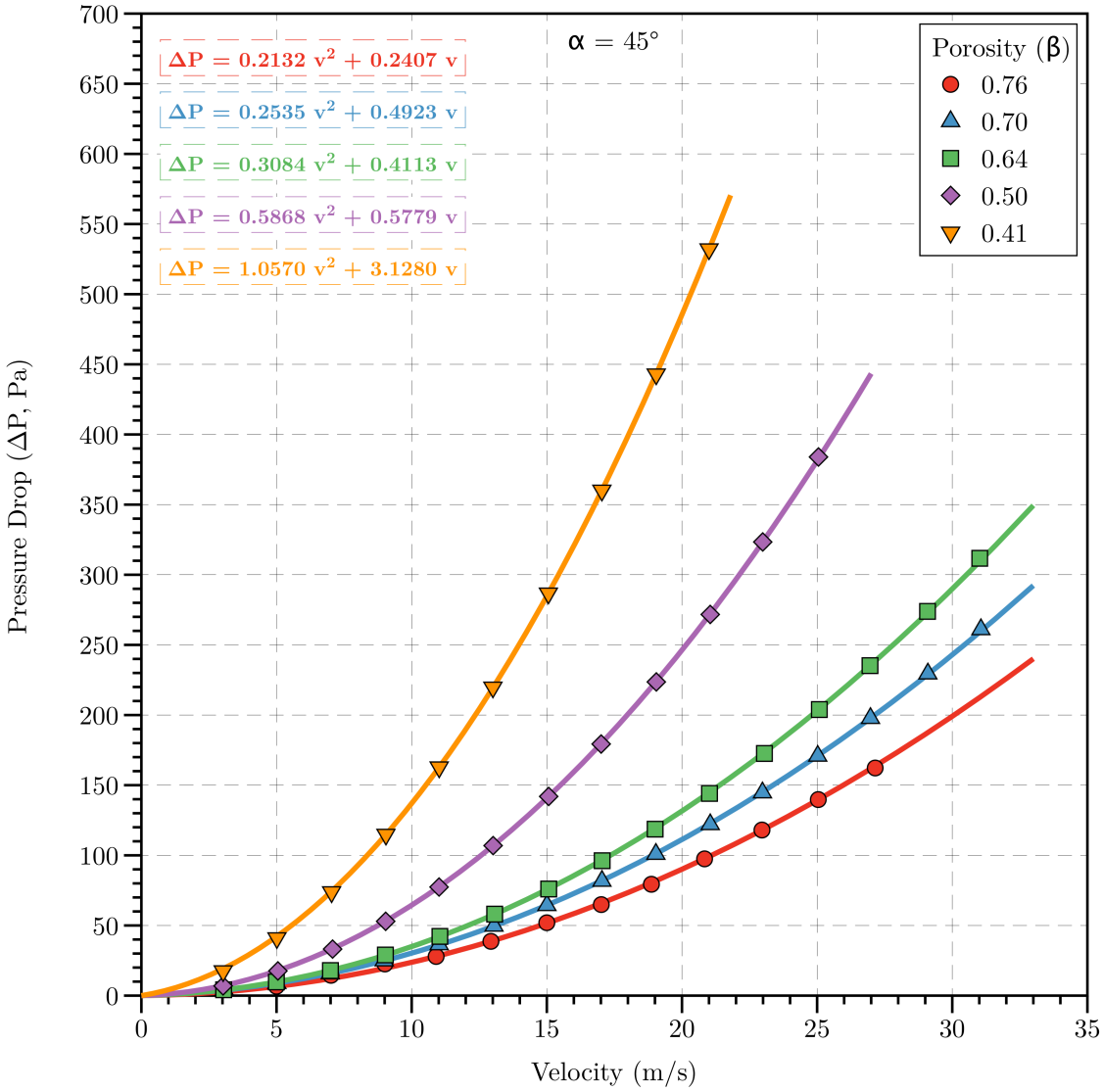

Figure D.15 Pressure drop (ΔP) vs. velocity (v) for various porosities (β), angle of inclination (α) = 45°.

D.10 Permeability Calculations

Table D.1 Permeability calculations for porous media.

ρ ($\mathrm{kg\,m^{-3}}$)	Thickness (m)	T (K)	Porosity (β)	a	b	R^2	K ($\times 10^{-8}$)	Y
			($\alpha = 0°$)					
1.21	0.0006	290.70	0.41	1.3046	7.1259	1.00	0.15	0.0699
1.21	0.0005	291.32	0.50	0.8133	1.2267	1.00	0.74	0.1155
1.22	0.0002	291.45	0.64	0.3811	0.2283	1.00	1.59	0.1975
1.22	0.0012	291.05	0.70	0.2719	1.0737	1.00	1.69	0.0290
1.22	0.0020	289.05	0.76	0.3652	0.1523	0.99	2.36	0.0230
			($\alpha = 15°$)					
1.20	0.0006	290.88	0.41	1.319	5.6848	1.00	19.3	0.0842
1.20	0.0005	290.67	0.50	0.7816	1.2387	0.99	0.73	0.1110
1.21	0.0002	291.85	0.64	0.3510	0.2952	1.00	1.23	0.1609
1.21	0.0012	291.45	0.70	0.2857	0.9747	1.00	2.23	0.0234
1.22	0.0020	288.75	0.76	0.3009	0.4252	1.00	8.46	0.0359
			($\alpha = 30°$)					
1.20	0.0006	293.24	0.41	1.2559	4.4153	1.00	0.25	0.0866
1.20	0.0005	291.85	0.50	0.7459	0.4011	1.00	2.26	0.1866
1.20	0.0002	292.60	0.64	0.3387	0.4238	1.00	8.58	0.1310
1.20	0.0012	292.39	0.70	0.2693	0.6103	1.00	3.57	0.0354
1.21	0.0020	290.15	0.76	0.2566	0.1873	1.00	19.30	0.0464
			($\alpha = 45°$)					
1.21	0.0006	288.15	0.41	1.0455	3.4762	1.00	0.31	0.0805
1.20	0.0005	288.43	0.54	0.5911	0.4824	1.00	1.86	0.1340
1.20	0.0012	290.29	0.64	0.3162	0.1733	1.00	2.09	0.1910
1.20	0.0012	298.24	0.70	0.2576	0.3643	1.00	5.94	0.0436
1.22	0.0020	289.65	0.76	0.2159	0.0429	1.00	84.10	0.0814

Table D.2 Permeability calculations for porous media (continued).

ρ (kg m^{-3})	Thickness (m)	T (K)	Porosity (β)	a	b	R^2	K ($\times 10^{-8}$)	Y
			($\alpha = 0°$)					
1.21	0.005	292.00	0.20	0.0400	0.0726	1.00	12.5	0.00233
1.21	0.010	292.00	0.40	0.0470	1.1900	1.00	15.2	0.00151
1.21	0.020	292.00	0.80	0.0700	0.9200	1.00	39.4	0.00181

D.11 Curve Fitting in MATLAB

D.11.1 Linear Least Squares

The Curve Fitting Toolbox™ (CFT) within MATLAB® uses linear least-squares to fit a linear model to sample data. A linear model is defined as an equation that is linear in the coefficients. For a sample data set containing n sample points that can be modeled by a first degree polynomial

$$y = p_1 x + p_2. \tag{D.9}$$

In order to solve Eq. (D.9) for the unknown coefficients (p_1 and p_2), one can write a system (S) of n simultaneous linear equation equations in the two unknowns, shown in Eq. (D.10). If n is greater than the number of unknowns the system is called overdetermined.

$$S = \sum_{i=1}^{n} (y_i - (p_1 x + p_2))^2. \tag{D.10}$$

The least-squares fitting process minimises the squared sum of the residuals. The coefficients are therefore determined by differentiating S with respect to each parameter and equating the result to zero, therefore

$$\frac{\partial S}{\partial p_1} = -2 \sum_{i=1}^{n} x_i (y_i - (p_1 x + p_2)) = 0, \tag{D.11}$$

$$\frac{\partial S}{\partial p_2} = -2 \sum_{i=1}^{n} y_i (y_i - (p_1 x + p_2)) = 0. \tag{D.12}$$

The estimates of the true parameters are usually represent by b, substituting b_1 and b_2 for p_1 and p_2 into Eq. (D.11) and Eq. (D.12), gives

$$\sum_{i=1}^{n} x_i(y_i - (b_1 x + b_2)) = 0, \tag{D.13}$$

$$\sum_{i=1}^{n} y_i(y_i - (b_1 x + b_2)) = 0. \tag{D.14}$$

The normal equations are given by

$$b_1 \sum x_i^2 + b_2 \sum x_i = \sum x_i y_i, \tag{D.15}$$

$$b_1 \sum x_i + n b_2 = \sum y_i, \tag{D.16}$$

where the summations are from $i = 1$ to n and are omitted for clarity. Solving for b_1 and b_2 gives

$$b_1 = \frac{n \sum x_i y_i - \sum x_i \sum y_i}{n \sum x_i^2 - \left(\sum s_i\right)^2}, \tag{D.17}$$

$$b_2 = \frac{1}{n}\left(\sum y_i - b_1 \sum x_i\right). \tag{D.18}$$

MATLAB® solves linear models in matrix form, where linear models are expressed as

$$y = X\beta + \epsilon, \tag{D.19}$$

where y is an $n \times 1$ vector of responses, β is an $m \times 1$ vector of coefficients, X is the $n \times m$ model matrix, with ϵ containing the $n \times 1$ errors. For a first-degree polynomial, the n equations in the two unknowns can be expressed in terms of y, X and β by

$$\begin{bmatrix} y_1 \\ y_2 \\ y_3 \\ \cdot \\ \cdot \\ \cdot \\ y_n \end{bmatrix} = \begin{bmatrix} x_1 1 \\ x_2 1 \\ x_3 1 \\ \cdot \\ \cdot \\ \cdot \\ x_n 1 \end{bmatrix} \times \begin{bmatrix} p_1 \\ p_2 \end{bmatrix}. \tag{D.20}$$

The least-squares solution to Eq. (D.20) is the vector b, which estimates the unknown vector of coefficients (β). The normal equations are given by

$$(X^T X)b = X^T y, \tag{D.21}$$

where b is given by

$$b = (X^T X)^{-1} X^T y. \tag{D.22}$$

MATLAB® uses a QR Decomposition [136] based algorithm to solve Eq. (D.22) due to the numerical stability. After solving for b, one can calculate the predicted response values $\hat{y}$ given by

$$\hat{y} = Xb = Hy, \tag{D.23}$$

where

$$H = X(X^T X)^{-1} X^T, \tag{D.24}$$

with the residuals (r) given by the difference between the measured values (y) and the model estimates ($\hat{y}$),

$$r = y - \hat{y} = (1 - H)y. \tag{D.25}$$

D.11.2 Weighted Least Squares

It is usually assumed that the response data was measured with equal accuracy for each sample point (homoscedasticity). This implies that the error estimate therefore has a constant variance. If this is not true an ordinary least squares (OLS) with data that is heteroscedastic will be biased. An example of homoscedasticity and various forms of heteroscedasticity is shown in Fig. D.16.

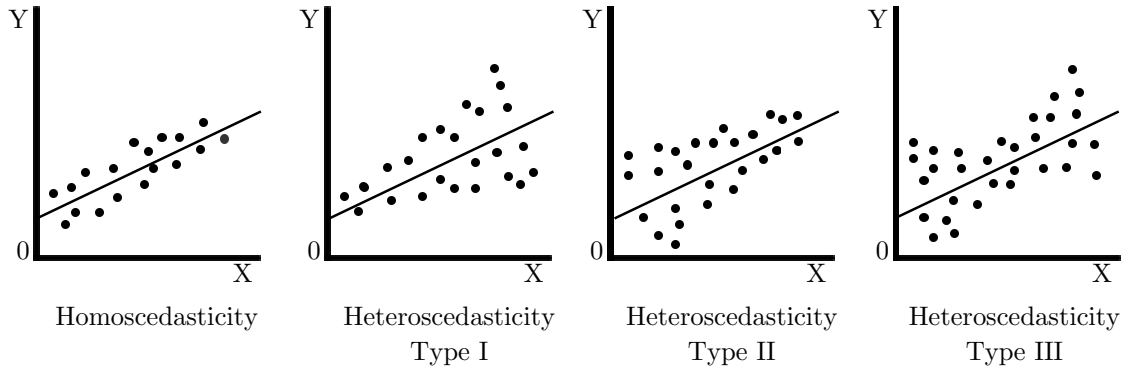

Figure D.16 Homoscedasticity and various types of heteroscedasticity [137].

In order to remove the bias in OLS, weighting is added to the fit via weighted least-squares regression (where a weight w_i is introduced) will provide a better estimate. Weighted least-squares (WLS) regression minimises the error estimate given by

$$s = \sum_{i}^{n} w_i (y_i - \hat{y})^2. \tag{D.26}$$

In matrix form the parameter estimates (b) can be written as

$$b = \hat{\beta} = (X^T W X)^{-1} X^T W y, \tag{D.27}$$

where W is given by the diagonal elements of the weighting matrix w. The most common choice for weighting is White's heteroscedasticity-consistent estimator (HCE), where the residuals are weighted by the inverse of their variance

$$w_i = \frac{1}{\sigma_i^2}, \tag{D.28}$$

where the larger the variance of the observed data point, the lesser the effect of that data point on the fitted curve.

D.12 CFD Details

To establish grid convergence for the 2D simulations used to model porous materials, three numerical domains were chosen. The physical size of the computational domain was chosen as 1.0 m in the horizontal (x-axis) and 0.23 m in the vertical (y-axis). The porous media was placed horizontally ($\alpha = 0°$) at x = 0.5 m.

The initial mesh size (case 1) chosen consisted of 46 nodes along the x-axis and 200 nodes along the y-axis corresponding to 9,200 nodes in the computational domain. The mesh was then refined (case 2) in both the x and y directions to 92 and 400 nodes, respectively, giving a total node count of 36,800. This process was again repeated (case 3) resulting in 147,200 nodes (184 $\times$ 800). The meshes used for the grid convergence study are show in Fig. D.17.

The numerical simulations were compared with experimental data for an inlet velocity of 15 m s^{-1} and a mesh porosity (β) of 50%. The solver parameters used for the simulations are shown in Table D.3, the residuals from the simulation are shown in Fig. D.18.

To check for the influence of the mesh cell sizing, the static pressure drop (ΔP) across the screen was monitored. The pressure drop across the screen was measured at horizontal positions of 0.25 m and 0.75 m at a vertical height above the lower wall of 0.115 m. This pressure drop was calculated for each of the three cases and is shown in Table D.4.

From Table D.4, case 2 (36,800 nodes) shows little with additional refinement to 147,200 nodes there is only a 0.06 Pa variation in the measured pressure drop. Based on this result, the case 2 (36,800 modes) mesh was chosen for the simulations in Chapter 3. The pressure distribution within the computational domain is shown in Fig. D.19.

The meshes used for the simulations in Chapter 3 are shown in Fig. D.20 for screen inclinations (α) of 0°, 15°, 30° and 45°. The corresponding solver parameters are shown in Table D.5. The associated residuals from the simulations are shown in Fig. D.21 and Fig. D.22. The convergence of the pressure drop (Δ P) across the porous jump is shown in Fig. D.23.

D.12.1 Grid Convergence

D.12.1.1 Meshes

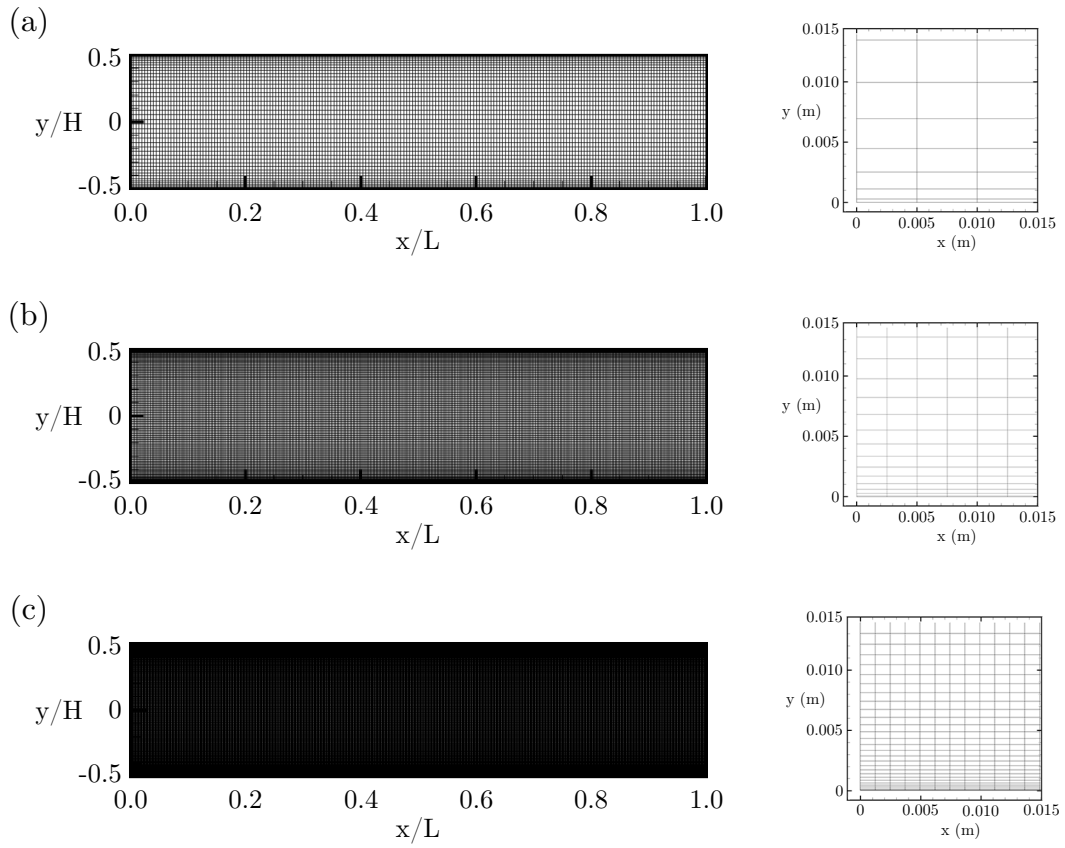

Figure D.17 Computational meshes for (a) 9,200, (b) 36,800 and (c) 147,200 grid cells.

D.12.1.2 Solver Parameters

Table D.3 CFD solver parameters used for the 2D porous media simulations.

General Details	
Solver	ANSYS® FLUENT® 15.0, Pressure Based, Steady, Implicit, Node-Based
Mesh Type	Structured
Number of Cells	Case 1 - 9200 Case 2 - 36800 Case 3 - 147200
Solver Controls	
Turbulence Model	$k-\varepsilon$ (Standard)
Near-Wall Treatment	Standard Wall Treatment
Pressure-Velocity Coupling	SIMPLE
Discretisation (Under Relaxation)	
Gradient	Least Squares Cell Based
Pressure	Second Order (0.3)
Momentum	Second Order Upwind (0.7)
Turbulent Kinetic Energy	Second Order (0.8)
Turbulent Dissipation Rate	Second Order Upwind (0.8)
Materials	
Fluid	Air
Density	$1.225 \times 10^{-3}\,\mathrm{kg\,m^{-3}}$
Viscosity	$1.7894 \times 10^{-5}\,\mathrm{kg\,m^{-1}\,s^{-1}}$
Boundary Conditions	
Inlet	Velocity Inlet ($15\,\mathrm{m\,s^{-1}}$)
Outlet	Pressure Outlet
Top	Wall (Hydrodynamically smooth)
Bottom	Wall (Hydrodynamically smooth)
Screen	Porous Jump: Face Permeability (α_f): $2.21 \times 10^{-8}\,\mathrm{m^2}$ Porous Media Thickness: $0.001\,\mathrm{m}$ Pressure-Jump Coefficient (C_{2f}): $1370\,\mathrm{m^{-1}}$

D.12.1.3 Residuals

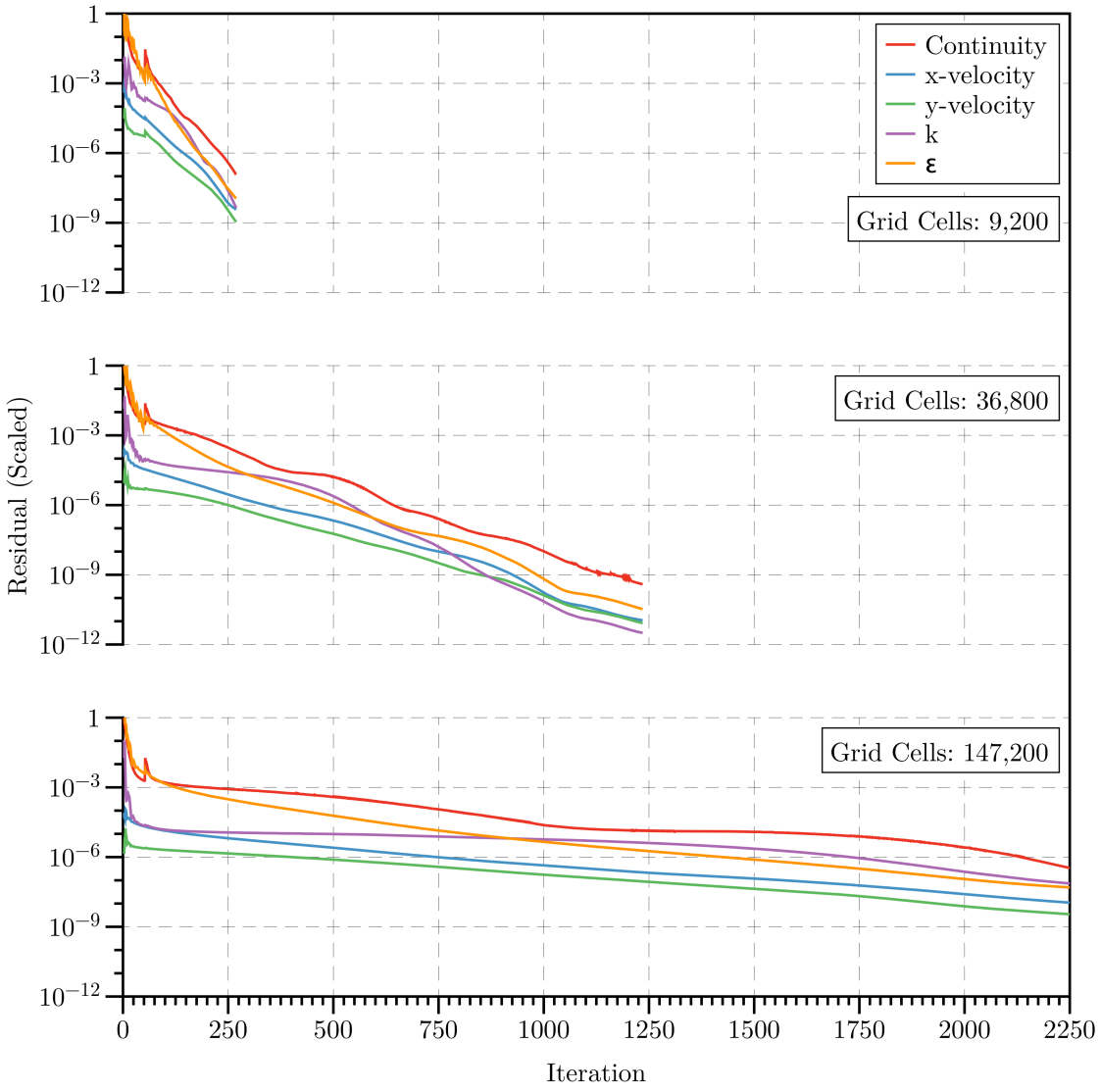

Figure D.18 Scaled residuals for the 2D grid convergence study.

D.12.1.4 Results

Table D.4 CFD grid convergence results.

Grid Size	(x × y) Cell Arrangement	Pressure Drop (ΔP, Pa)
9200	46 × 200	204.93
36800	92 × 400	206.61
147200	184 × 800	206.67

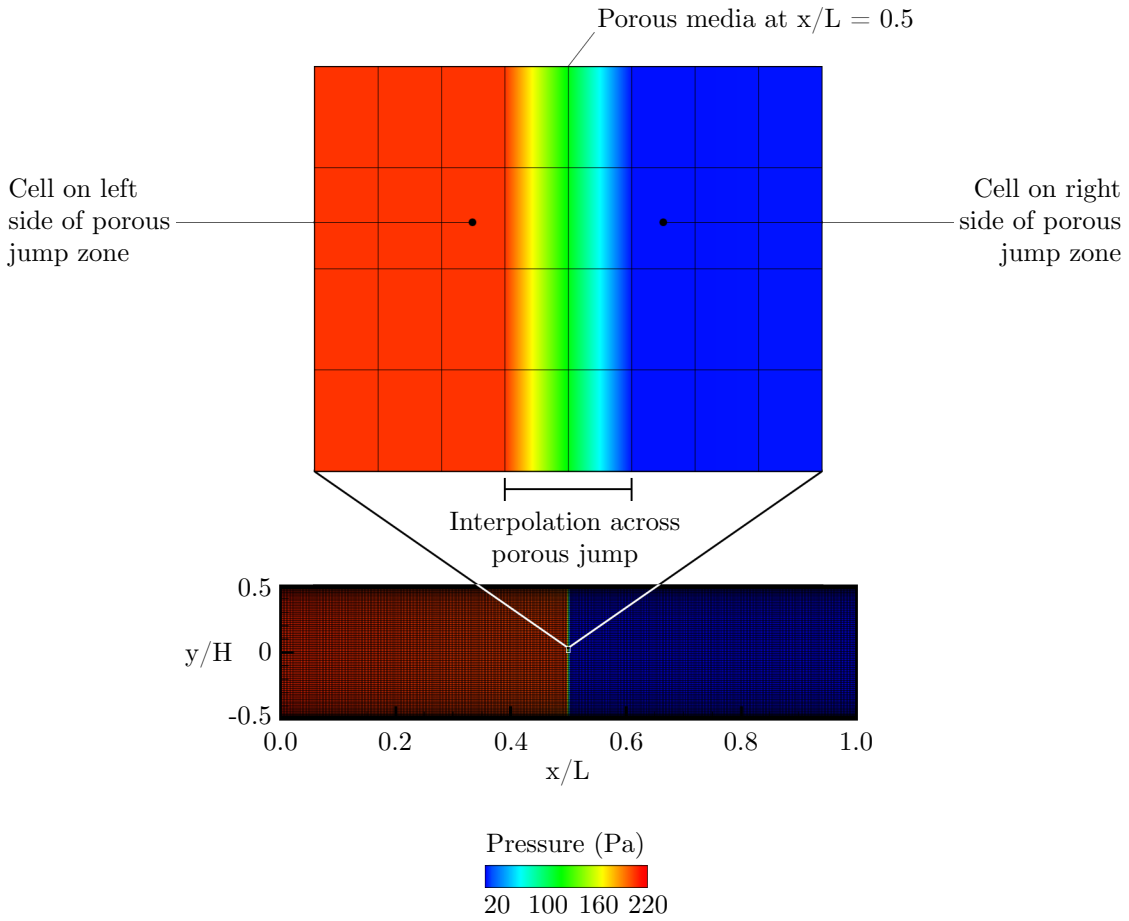

Figure D.19 Pressure distribution within the 2D computational domain.

D.12.2 CFD Results

D.12.2.1 Meshes

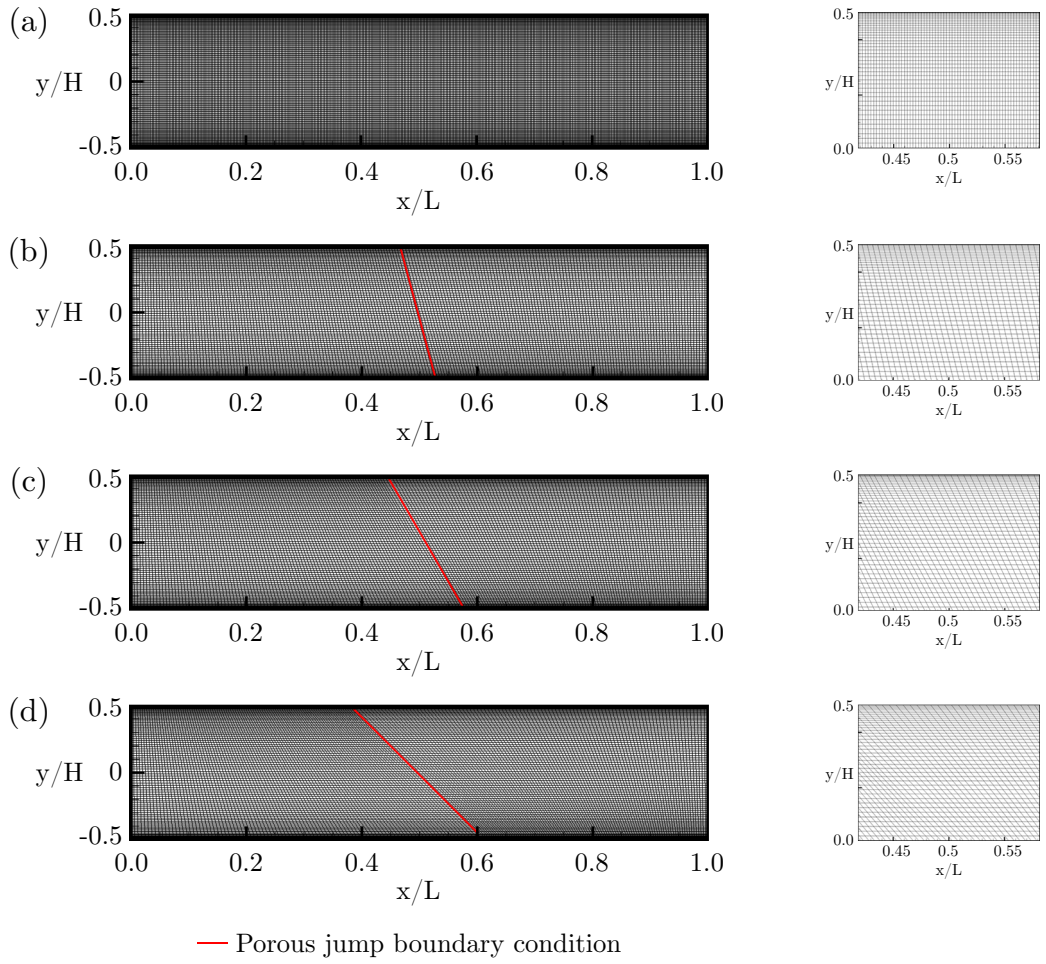

Figure D.20 Computational meshes for porous jump inclination angles of (a) $\alpha = 0°$, (b) $\alpha = 15°$, (c) $\alpha = 30°$ and $\alpha = 45°$.

D.12.2.2 Solver Parameters

Table D.5 CFD solver parameters used for the 2D porous media simulations.

General Details	
Solver	ANSYS® FLUENT® 15.0, Pressure Based, Steady, Implicit, Node-Based
Mesh Type	Structured
Number of Cells	36800
Solver Controls	
Turbulence Model	$k-\varepsilon$ (Standard)
Near-Wall Treatment	Standard Wall Treatment
Pressure-Velocity Coupling	SIMPLE
Discretisation (Under Relaxation)	
Gradient	Least Squares Cell Based
Pressure	Second Order (0.3)
Momentum	Second Order Upwind (0.7)
Turbulent Kinetic Energy	Second Order (0.8)
Turbulent Dissipation Rate	Second Order Upwind (0.8)
Materials	
Fluid	Air
Density	$1.225 \times 10^{-3}\,\mathrm{kg\,m^{-3}}$
Viscosity	$1.7894 \times 10^{-5}\,\mathrm{kg\,m^{-1}\,s^{-1}}$
Boundary Conditions	
Inlet	Velocity Inlet
Outlet	Pressure Outlet
Top	Wall (Hydrodynamically smooth)
Bottom	Wall (Hydrodynamically smooth)
Screen	Porous Jump

D.12.2.3 Residuals

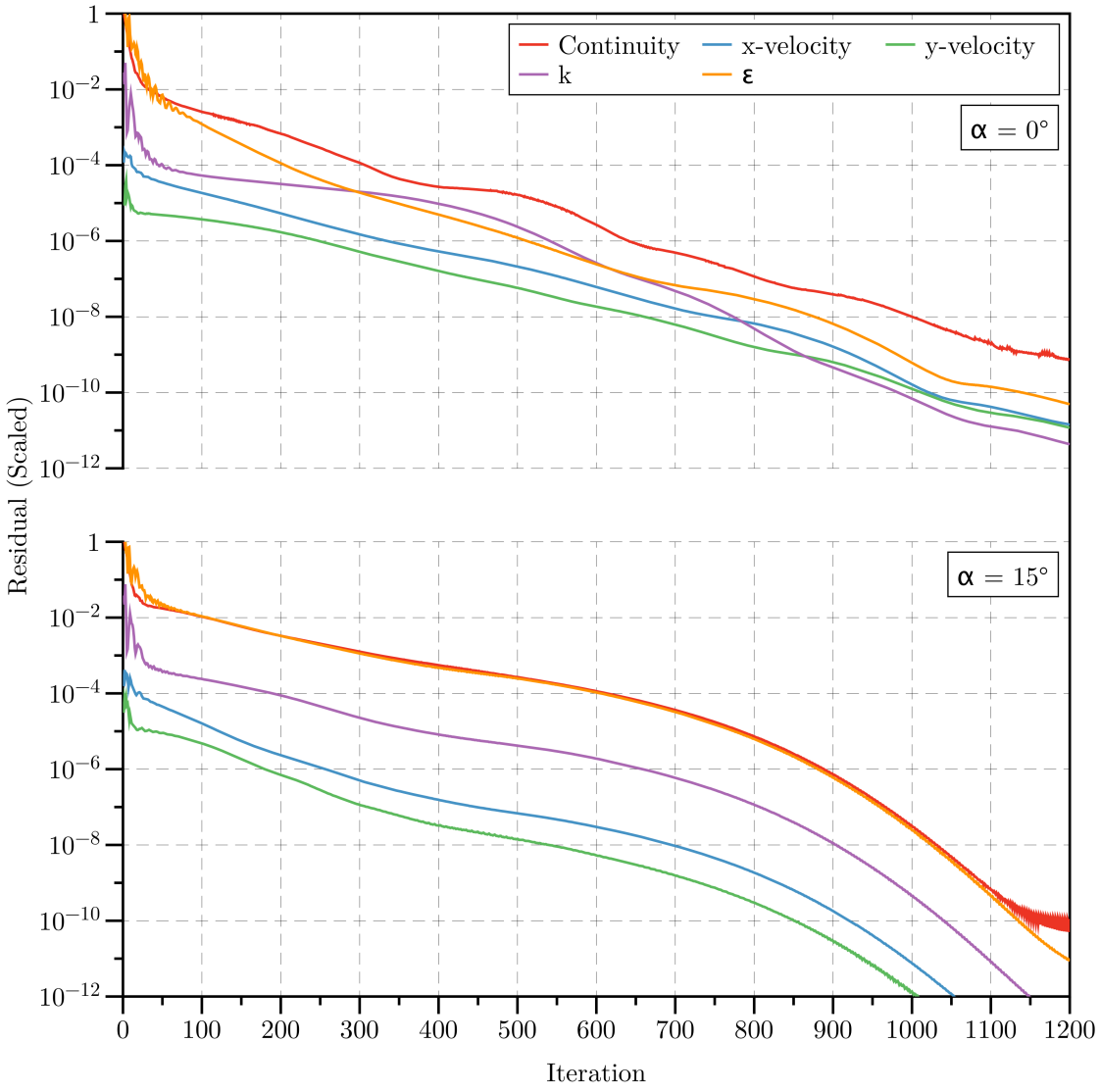

Figure D.21 Scaled residuals for the 2D porous jump simulations for a screen inclination of $\alpha = 0°$ (upper) and $\alpha = 15°$ (lower).

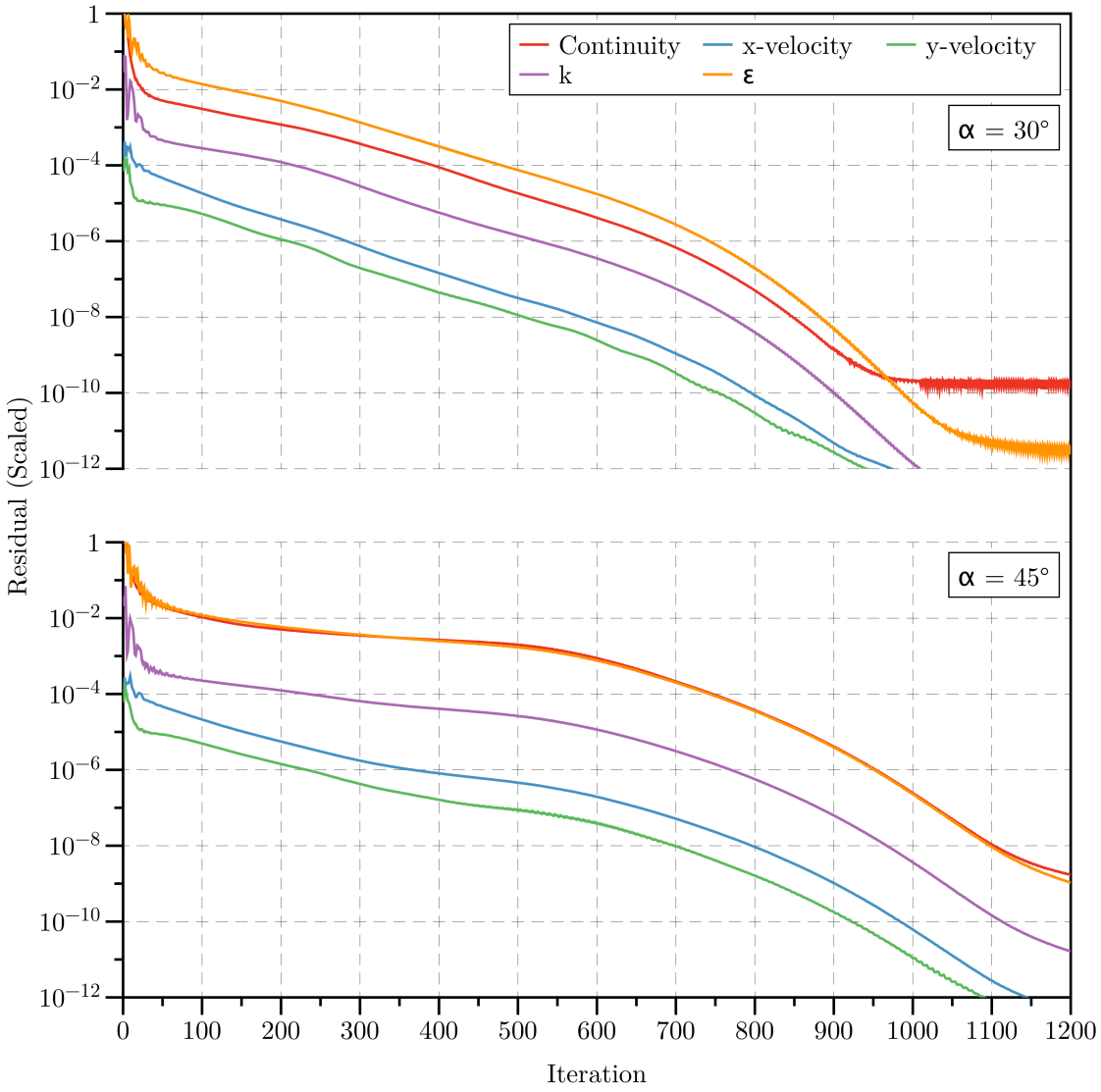

Figure D.22 Scaled residuals for the 2D porous jump simulations for a screen inclination of $\alpha = 30°$ (upper) and $\alpha = 45°$ (lower).

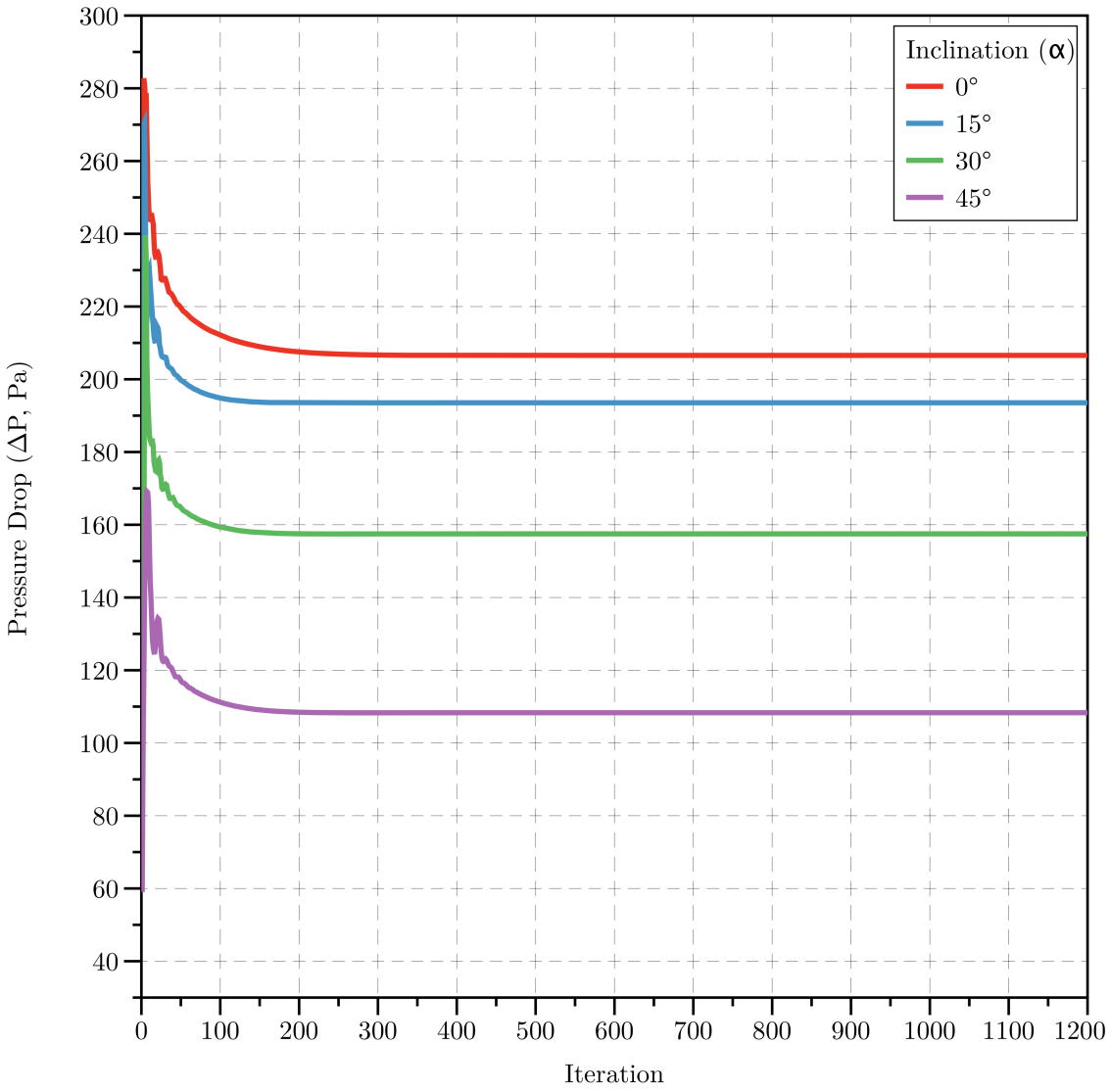

Figure D.23 Facet averaged pressure drop (ΔP) convergence for the 2D porous jump simulations. Screen porosity (β) of 0.50 and inlet velocity (v) of 15 m s^{-1}.

Appendix E

Full Scale Radiator Flow

E.1 Wind Tunnel Arrangement

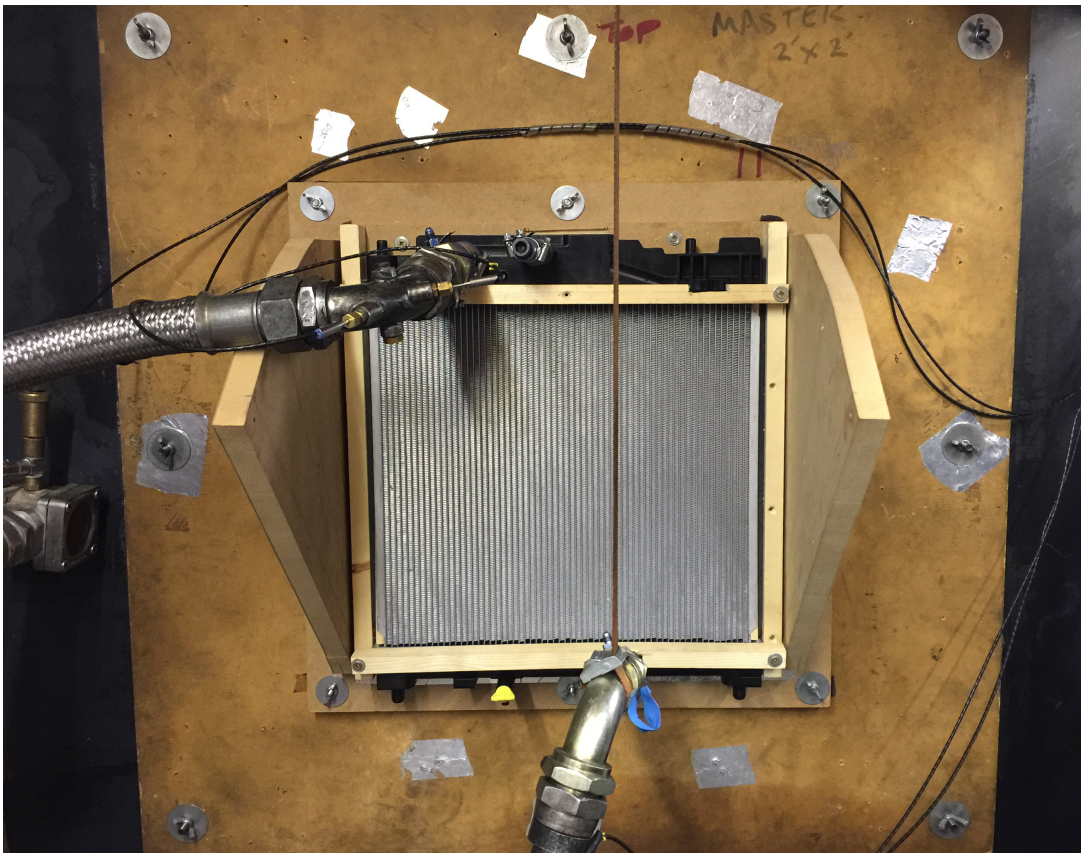

Figure E.1 Hot side view of Young Calibration radiator blower wind tunnel.

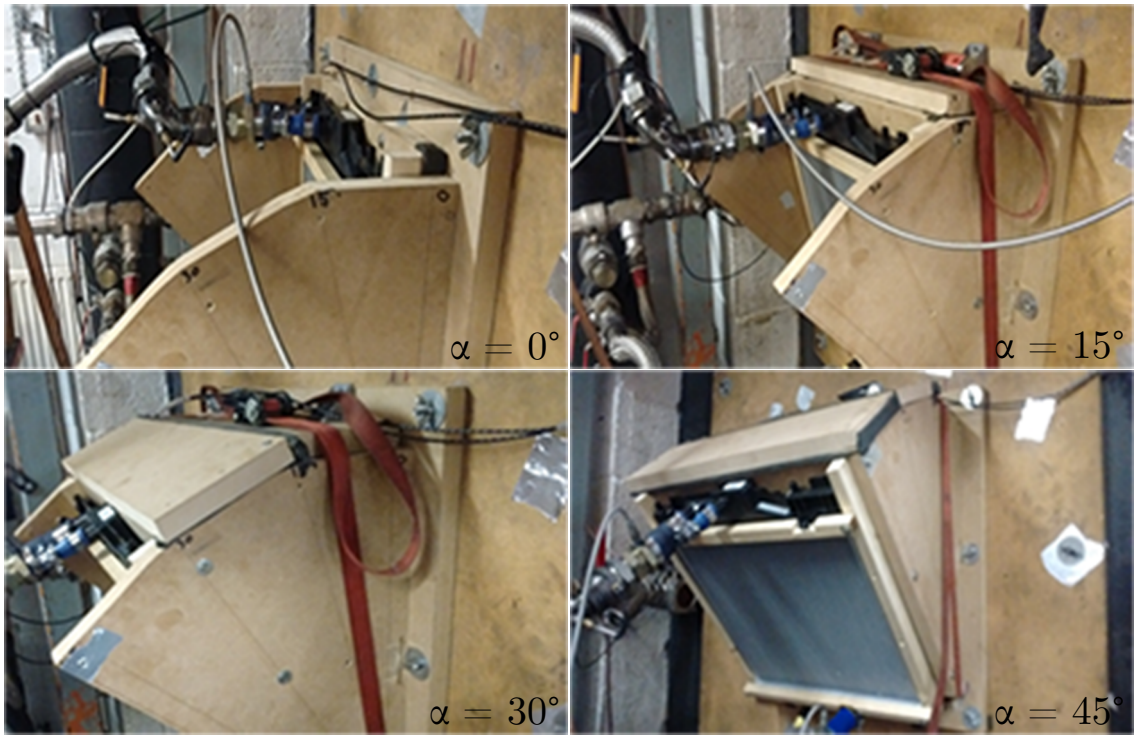

Figure E.2 Angular adjustment within blower wind tunnel.

E.2 Working Section Renderings

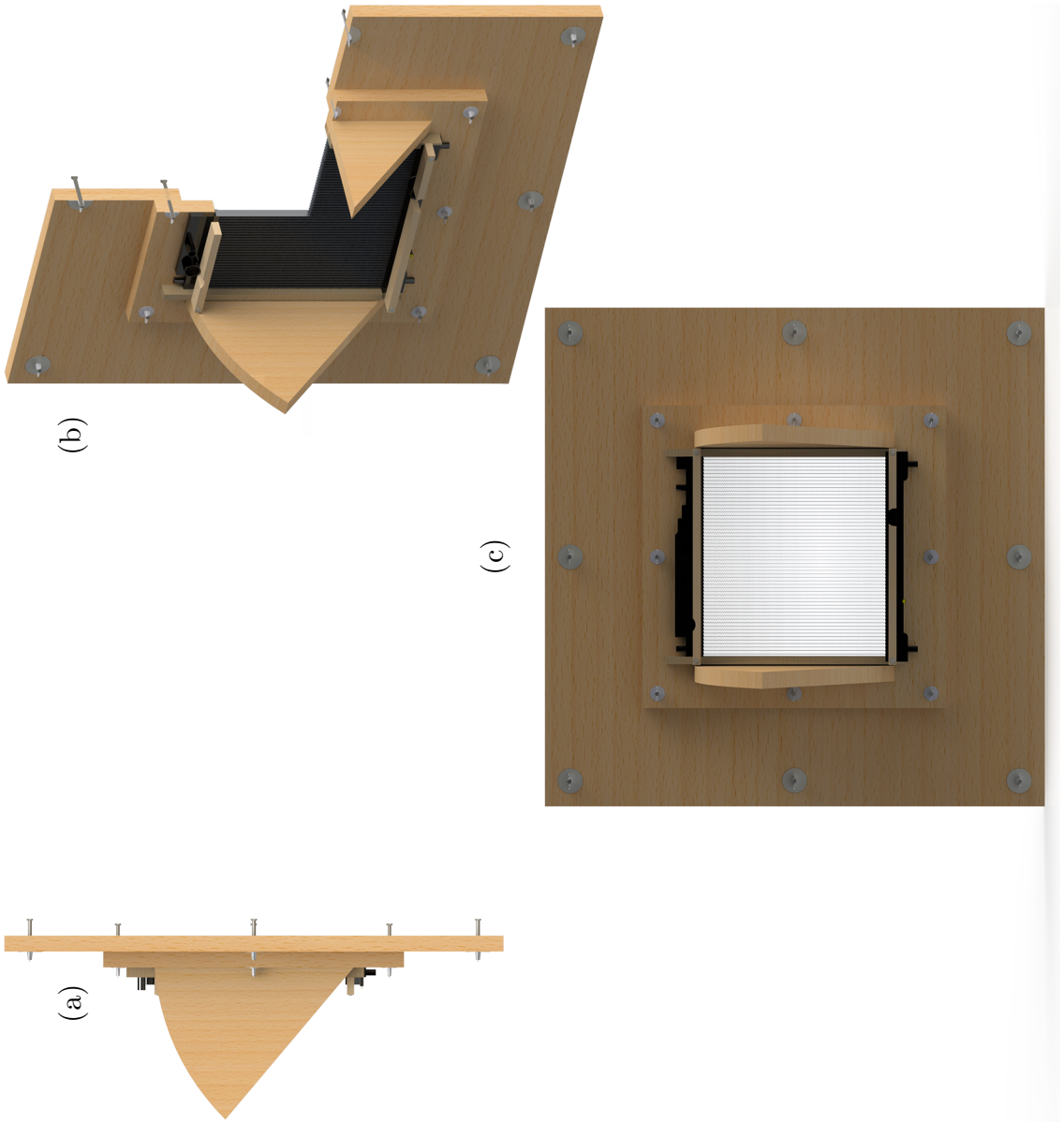

Figure E.3 Render of Young Calibration's radiator working section, (a) side view, (b) 3/4 view and (c) hot side view.

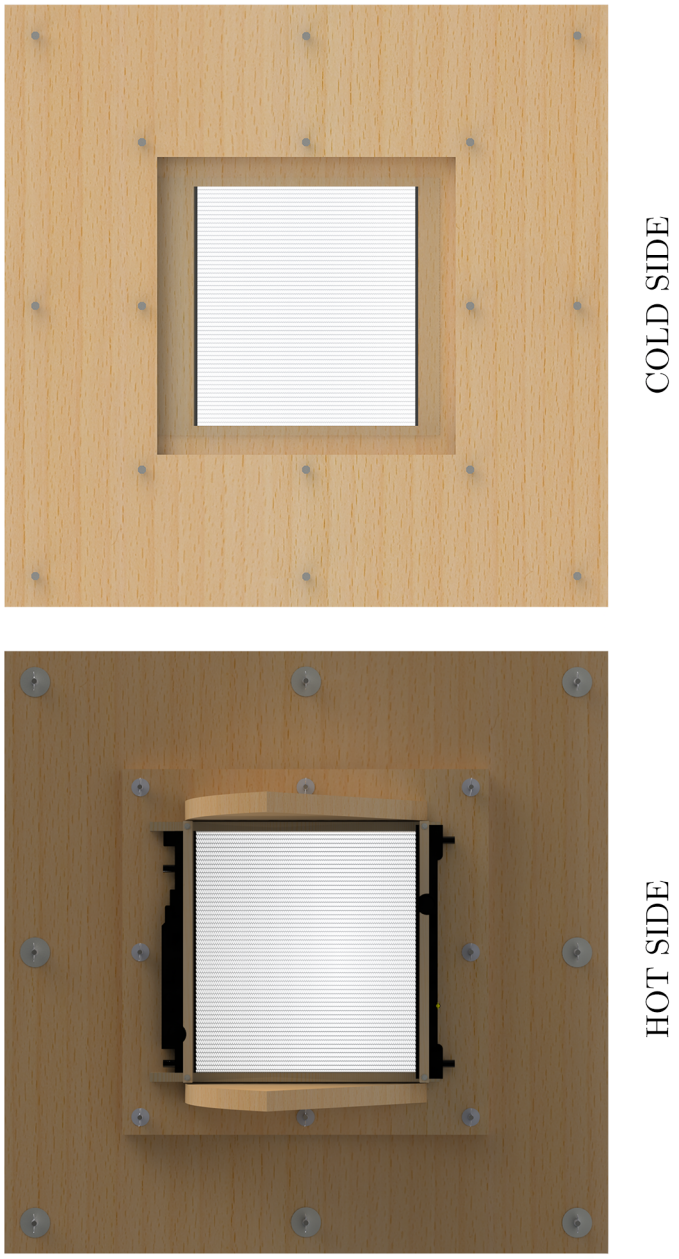

Figure E.4 Render of Young Calibration's radiator working section, hot side (left) and cold side (right) views.

E.3 Wind Tunnel Schematic

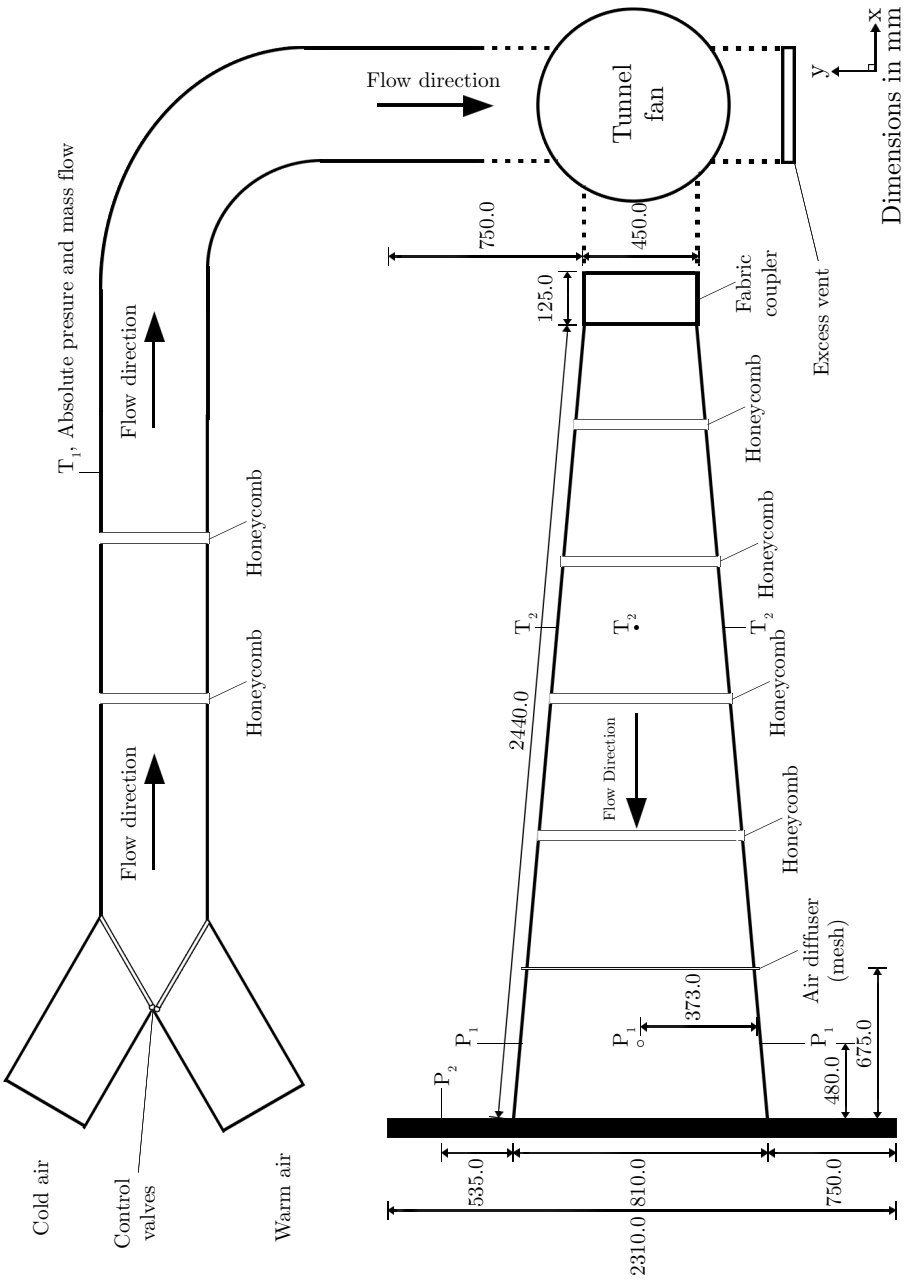

Figure E.5 Schematic of Young Calibration's wind tunnel.

E.4 Schematic of the Working Sections

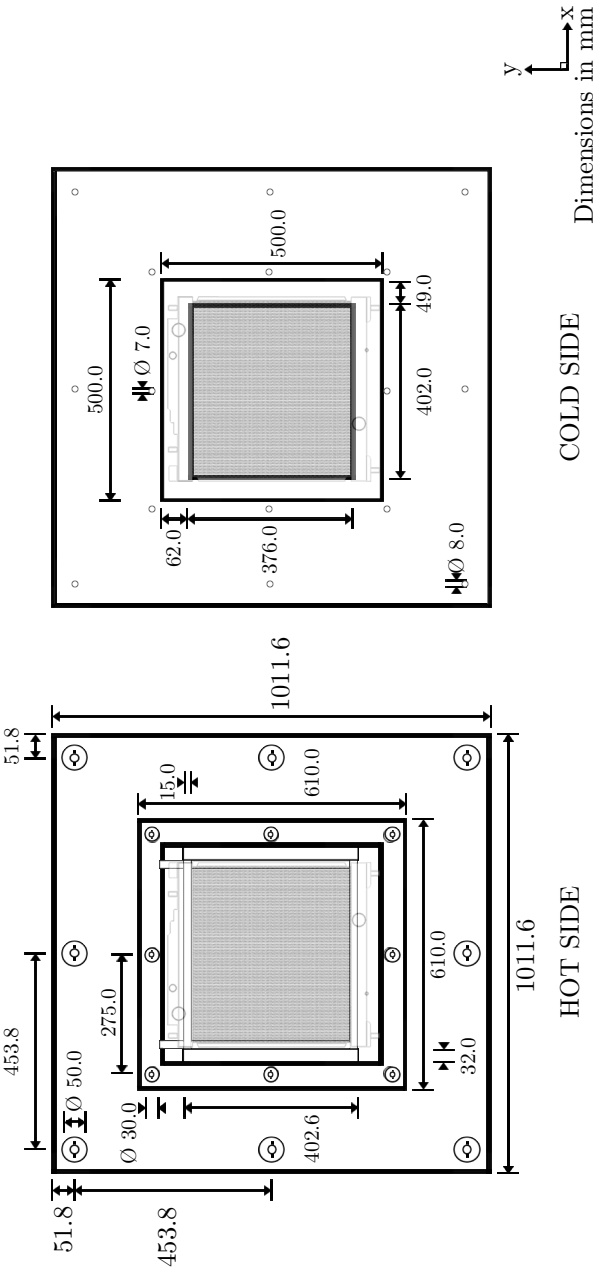

Figure E.6 Schematic of blower wind tunnel working section, hot side (left) and cold side (right) views.

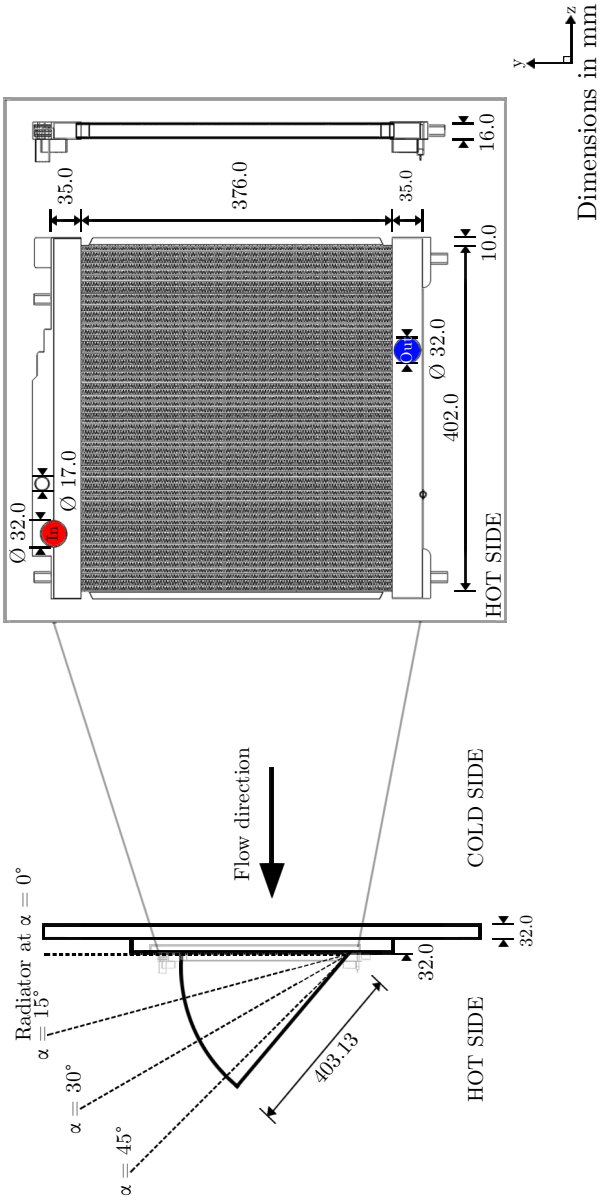

Figure E.7 Schematic of blower wind tunnel working section, side and radiator view.

E.5 DENSO Radiator

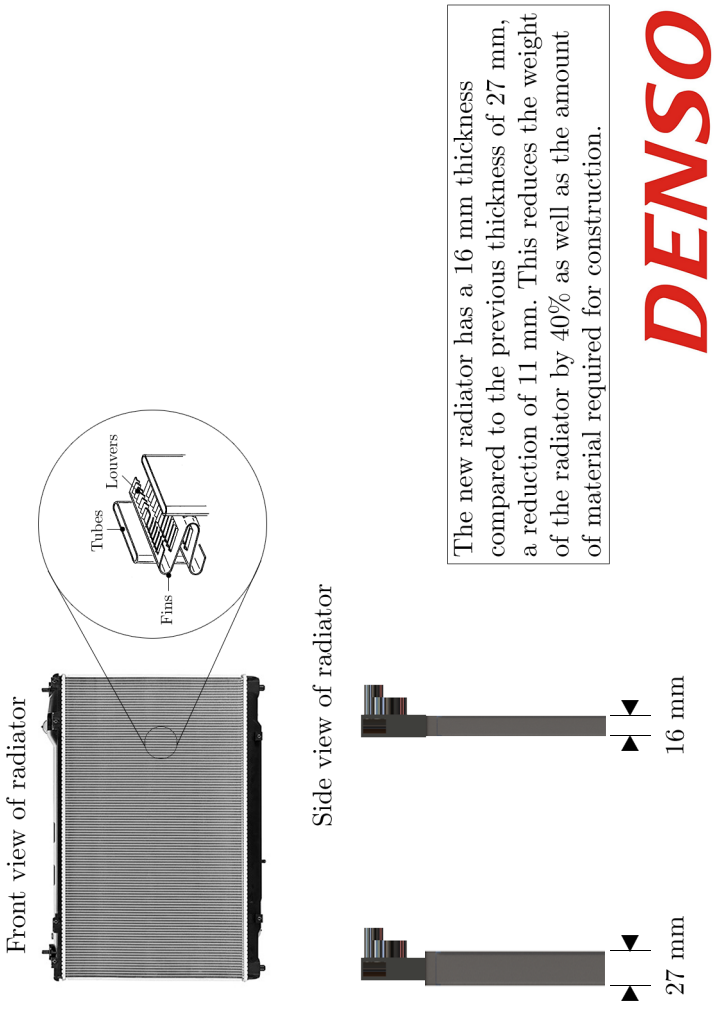

Figure E.8 DENSO [138] reduced thickness radiator used in the experimental tests.

E.6 Radiator Test Report

young CALIBRATION

CERTIFICATE OF TEST

ISSUED BY YOUNG CALIBRATION LIMITED

DATE OF ISSUE 22/10/15 TEST REPORT NUMBER 10788T

Young Calibration Ltd
Unit 4 Ham Business Centre
Brighton Road
Shoreham-by-Sea
West Sussex BN43 6RE

Telephone 01273 455572
Facsimile 01273 454120

Document : YCF/007_a
Issue Number : 1.6

Page 1 of 6 Pages

Approved Signatory

A. Young
J. Powell

Customer	: Cranfield University	
Customer Address	: Wharley End, Cranfield, Bedford, UK	
Customer's Reference No.	: 621535	
Date of Receipt	: 29th Septmeber 2015	
YCL Project Number	: YC/32913	
Test Date	: 19th - 21st October	
Test Performed By	: L. Maidment	
Test Item Manufacturer	: Denso	
Test Item Model Type	: Coolant Radiator	
Serial Number	: DRM50056-11211	
Coolant Flow Test Range	: 120 l/min	Coolant On Temperature : 60, 70, 80, 90 100°C
Mean Radiator Face Velocity Range	: 5,7,9,11,13,15 m/sec	Air On Temperature : 18°C & Ambient
Test Fluid	: Texaco XLC and Water @ 50:50 Volume Mix	
Radiator Matrix Dimensions	: 402 x 376 x 16	Core Area (m2) : 0.151152
Tubes	: 62	
Rows	: 1	
Fin Density (Fins /dM)	: 81 avg	

Installation and Method
The test radiator is mounted centrally in a duct with a nominal cross sectional area of 1.0 m², and sealed to ensure all air passes through the radiator core matrix only. Temperature controlled air is blown through the wind tunnel duct and then through the radiator core matrix. Temperature and pressure measurements are taken upstream and downstream of the radiator and a mean core face velocity is inferred from the mean upstream duct velocity. The radiator was tested at varying angles from 0° - 45° Incline

Temperature controlled coolant is pumped through the radiator, through insulated coolant pipework, and measurements of temperature and pressure are taken within 150 mm upstream and downstream of the radiator inlet and outlet spigots. The coolant flow rate is measured upstream of the radiator. YCL pressure tapping's were used for pressure drop measurements and do not have the ideal 10D/5D upstream/downstream pipe straight lengths, due to minimising of pipe lengths for calorimetric testing.

The radiator core mean face velocity, inlet temperatures and coolant flow test conditions are set, allowed to stabilise, and measurements are recorded. The results are derived from the average of at least 10 readings per condition.

Figure E.9 Young Calibration test certification.

E.6.1 Radiator Data for $\alpha = 0^\circ$

Table E.1 Young Calibration radiator pressure drop (ΔP) for 0° radiator inclination (α).

Tunnel Velocity (m/s)	Air Mass Flow (kg/s)	Inlet Temp. (°C)	Rad. ΔP (Pa)
($\alpha = 0^\circ$, No Coolant)			
4.95	0.92	16.8	86
7.06	1.31	17.3	160
9.03	1.68	17.8	242
10.99	2.05	17.2	337
12.95	2.40	19.3	456
15.01	2.80	17.6	595
($\alpha = 0^\circ$, Coolant Temp. = 60 °C)			
5.00	0.90	25.0	92
7.00	1.27	25.0	164
9.00	1.63	25.0	247
10.97	1.99	24.9	348
13.03	2.37	25.0	477
15.04	2.74	25.1	611
($\alpha = 0^\circ$, Coolant Temp. = 70 °C)			
4.99	0.90	25.0	101
7.04	1.27	25.1	173
9.01	1.63	25.1	258
10.94	1.99	24.9	359
12.97	2.35	25.1	479
14.99	2.73	25.1	622
($\alpha = 0^\circ$, Coolant Temp. = 80 °C)			
4.99	0.90	25.0	104
6.91	1.25	24.9	176
8.92	1.62	24.9	261
11.01	2.00	24.9	368
12.99	2.36	25.1	490
14.99	2.72	25.0	624

Table E.2 Young Calibration radiator pressure drop (ΔP) for 0° radiator inclination (α) (continued).

Tunnel Velocity (m/s)	Air Mass Flow (kg/s)	Inlet Temp. (°C)	Rad. ΔP (Pa)
($\alpha = 0°$, Coolant Temp. = 90 °C)			
4.95	0.90	24.9	107
7.00	1.27	24.9	182
9.00	1.63	25.0	268
11.07	2.01	25.1	379
12.95	2.35	24.8	497
14.98	2.72	24.9	642
($\alpha = 0°$, Coolant Temp. = 100 °C)			
4.97	0.90	24.9	112
6.98	1.26	24.9	186
8.98	1.63	25.0	272
10.99	1.99	25.1	385
13.03	2.36	25.3	504
14.94	2.72	24.9	643

Table E.3 Young Calibration heat transfer data for 0° radiator inclination (α).

Tunnel Velocity (m/s)	Flow Rate (L/min)	Mass Flow (kg/s)	Inlet Temp. (°C)	Outlet Temp. (°C)	ΔP (mbar)	Heat Dissipation $\mathrm{W\,m^{-2}\,K^{-1}}$	Heat Rejection (kW)
($\alpha = 0°$, Coolant Temp. = 60 °C)							
5.00	120.1	2.09	59.6	57.6	706	2829.72	14.8
7.00	119.9	2.09	59.7	57.2	710	3469.36	18.2
9.00	120.0	2.09	59.8	57.0	711	4009.98	21.1
10.97	120.1	2.09	59.5	56.4	712	4461.02	23.3
13.03	120.1	2.09	59.8	56.3	716	4837.73	25.5
15.04	119.9	2.09	59.9	56.2	716	5179.44	27.2
($\alpha = 0°$, Coolant Temp. = 70 °C)							
4.99	120.0	2.08	69.6	67.0	699	2875.23	19.4
7.04	120.0	2.08	70.5	67.2	699	3530.59	24.2
9.01	119.9	2.08	70.1	66.4	700	4083.92	27.8
10.94	120.0	2.08	69.9	65.7	703	4554.91	31.0
12.97	120.0	2.08	69.7	65.1	705	4980.85	33.6
14.99	119.9	2.08	69.7	64.8	706	5373.41	36.2
($\alpha = 0°$, Coolant Temp. = 80 °C)							
4.99	119.8	2.06	79.7	76.5	683	2864.31	23.7
6.91	119.9	2.06	80.3	76.3	684	3555.86	29.8
8.92	120.0	2.06	80.3	75.6	685	4110.50	34.4
11.01	120.0	2.06	80.0	74.8	689	4611.88	38.4
12.99	120.0	2.06	79.9	74.2	689	5064.91	42.0
14.99	120.1	2.07	79.8	73.6	692	5467.41	45.2
($\alpha = 0°$, Coolant Temp. = 90 °C)							
4.95	119.9	2.05	89.6	85.9	667	2841.03	27.8
7.00	120.1	2.05	90.4	85.6	670	3578.25	35.4
9.00	120.1	2.05	89.8	84.3	674	4158.71	40.7
11.07	119.9	2.05	89.6	83.4	673	4703.95	45.8
12.95	120.0	2.05	90.0	83.1	674	5146.32	50.7
14.98	120.0	2.05	90.1	82.8	674	5545.41	54.6
($\alpha = 0°$, Coolant Temp. = 100 °C)							
4.97	120.1	2.04	99.9	95.5	655	2878.68	32.6
6.98	120.1	2.04	100.0	94.5	656	3582.67	40.6
8.98	119.9	2.03	99.5	93.2	658	4134.54	46.5
10.99	120.0	2.04	99.6	92.5	659	4696.78	52.9
13.03	120.0	2.04	99.6	91.9	659	5122.61	57.5
14.94	119.9	2.03	99.5	91.1	663	5532.43	62.4

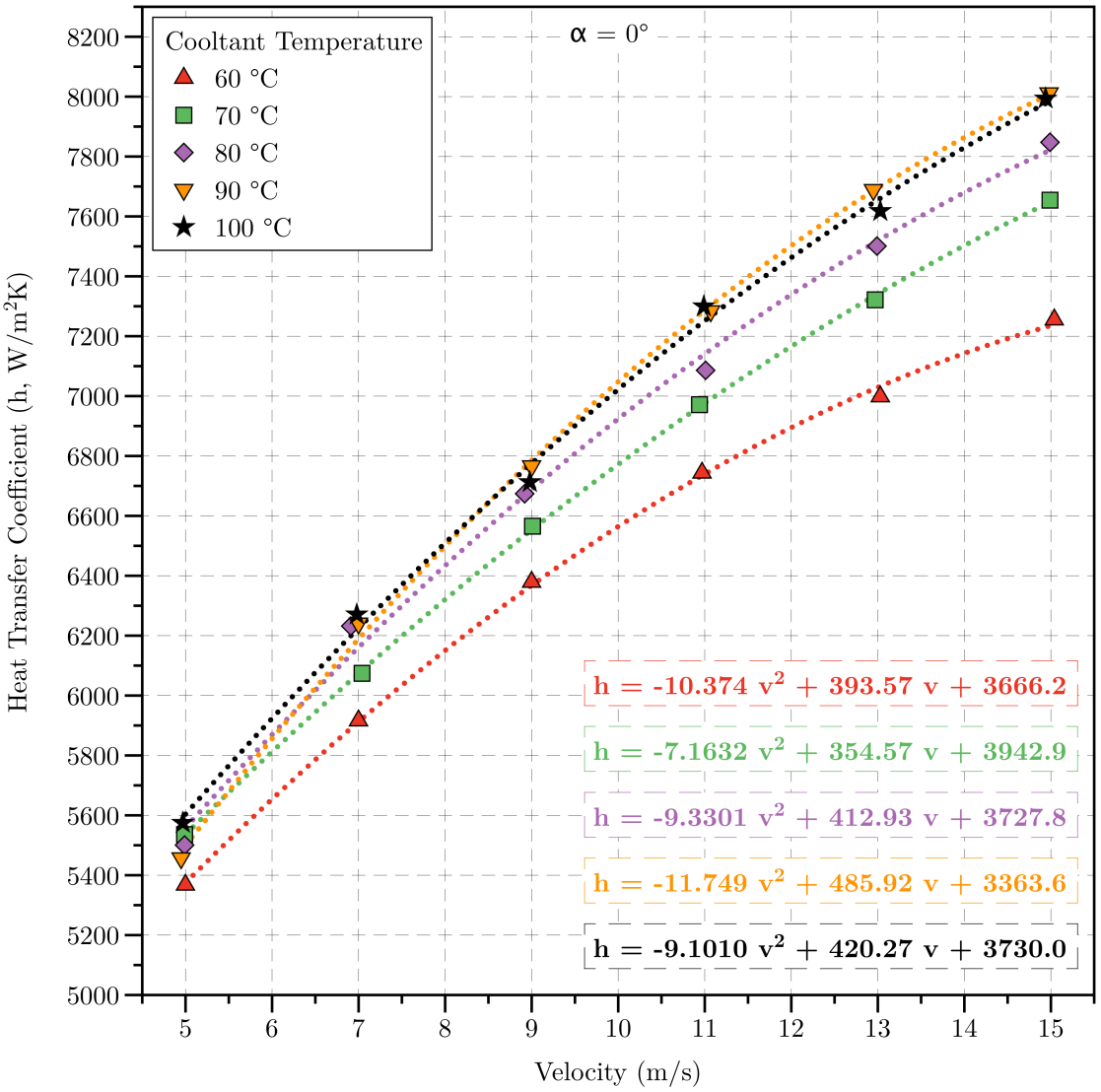

Figure E.10 Heat transfer coefficient (h) vs. velocity (v) for 0° radiator inclination (α).

E.6.2 Radiator Data for $\alpha = 15^{\circ}$

Table E.4 Young Calibration radiator pressure drop (ΔP) for 15° radiator inclination (α).

Tunnel Velocity (m/s)	Air Mass Flow (kg/s)	Inlet Temp. (°C)	Rad. ΔP (Pa)
($\alpha = 15^{\circ}$, No Coolant)			
4.93	0.91	18.4	85
6.98	1.29	17.8	157
8.96	1.66	17.7	236
10.99	2.04	17.7	335
13.01	2.42	18.0	462
14.97	2.79	18.0	599
($\alpha = 15^{\circ}$, Coolant Temp. = 60 °C)			
4.96	0.90	25.2	89
6.97	1.26	25.0	160
9.02	1.63	25.2	248
10.98	1.99	25.1	350
13.00	2.36	25.0	477
14.98	2.72	25.1	614
($\alpha = 15^{\circ}$, Coolant Temp. = 70 °C)			
4.98	0.90	25.0	92
6.99	1.26	25.2	164
8.98	1.62	25.1	254
11.00	1.99	25.0	358
12.98	2.36	25.0	481
15.02	2.73	25.1	620
($\alpha = 15^{\circ}$, Coolant Temp. = 80 °C)			
4.99	0.90	25.0	98
7.04	1.27	25.0	170
9.00	1.63	25.1	256
10.98	1.99	25.1	363
12.97	2.35	25.0	489
14.96	2.72	25.0	632

Table E.5 Young Calibration radiator pressure drop (ΔP) for 15° radiator inclination (α) (continued).

Tunnel Velocity (m/s)	Air Mass Flow (kg/s)	Inlet Temp. (°C)	Rad. ΔP (Pa)
($\alpha = 15°$, Coolant Temp. = 90 °C)			
4.99	0.90	25.2	100
7.01	1.27	25.0	173
8.99	1.63	25.2	260
11.00	1.99	25.1	371
13.04	2.37	25.1	500
15.00	2.72	25.0	641
($\alpha = 15°$, Coolant Temp. = 100 °C)			
5.02	0.91	25.0	104
7.01	1.27	25.1	179
8.96	1.62	25.1	269
11.11	2.01	25.1	383
12.99	2.36	25.1	512
14.91	2.71	24.9	651

Table E.6 Young Calibration heat transfer data for 15° radiator inclination (α).

Tunnel Velocity (m/s)	Flow Rate (L/min)	Mass Flow (kg/s)	Inlet Temp. (°C)	Outlet Temp. (°C)	ΔP (mbar)	Heat Dissipation $\mathrm{W\,m^{-2}\,K^{-1}}$	Heat Rejection (kW)
($\alpha = 15°$, Coolant Temp. = 60 °C)							
4.96	120.0	2.09	59.9	57.9	700	2795.72	14.7
6.97	120.0	2.09	59.9	57.4	704	3458.60	18.2
9.02	120.0	2.09	59.8	57.0	705	3965.39	20.7
10.98	120.0	2.09	59.9	56.7	707	4425.08	23.3
13.00	120.0	2.09	59.8	56.4	708	4826.87	25.4
14.98	120.0	2.09	60.0	56.3	711	5212.64	27.5
($\alpha = 15°$, Coolant Temp. = 70 °C)							
4.98	120.0	2.08	69.6	67.0	692	2839.96	19.1
6.99	120.0	2.08	69.7	66.5	694	3509.15	23.6
8.98	120.0	2.08	69.8	66.1	695	4067.80	27.5
11.00	120.0	2.08	69.8	65.6	698	4557.00	30.9
12.98	119.9	2.08	69.8	65.2	699	4972.40	33.7
15.02	119.9	2.08	69.9	64.9	700	5355.90	36.2
($\alpha = 15°$, Coolant Temp. = 80 °C)							
4.99	120.0	2.06	79.6	76.4	679	2857.85	23.6
7.04	120.0	2.06	79.8	75.8	680	3565.80	29.5
9.00	119.9	2.06	79.7	75.2	682	4098.04	33.9
10.98	120.0	2.06	79.8	74.6	685	4632.74	38.3
12.97	120.1	2.06	79.8	74.1	685	5083.48	42.1
14.96	120.1	2.06	79.8	73.7	687	5460.71	45.2
($\alpha = 15°$, Coolant Temp. = 90 °C)							
4.99	120.0	2.05	89.5	85.8	665	2866.97	27.9
7.01	120.0	2.05	89.6	84.9	665	3582.93	35.0
8.99	120.0	2.05	89.5	84.1	666	4152.53	40.4
11.00	120.0	2.05	89.6	83.5	672	4665.32	45.5
13.04	119.9	2.05	89.9	83.1	669	5122.10	50.2
15.00	120.0	2.05	89.8	82.5	674	5530.93	54.2
($\alpha = 15°$, Coolant Temp. = 100 °C)							
5.02	120.1	2.04	99.7	95.4	651	2865.74	32.4
7.01	120.0	2.04	99.6	94.2	653	3568.15	40.2
8.96	120.0	2.04	99.5	93.2	653	4155.59	46.8
11.11	120.1	2.04	99.8	92.7	655	4696.35	53.1
12.99	120.0	2.04	99.6	91.8	657	5157.41	58.1
14.91	120.1	2.04	99.6	91.2	658	5565.15	62.8

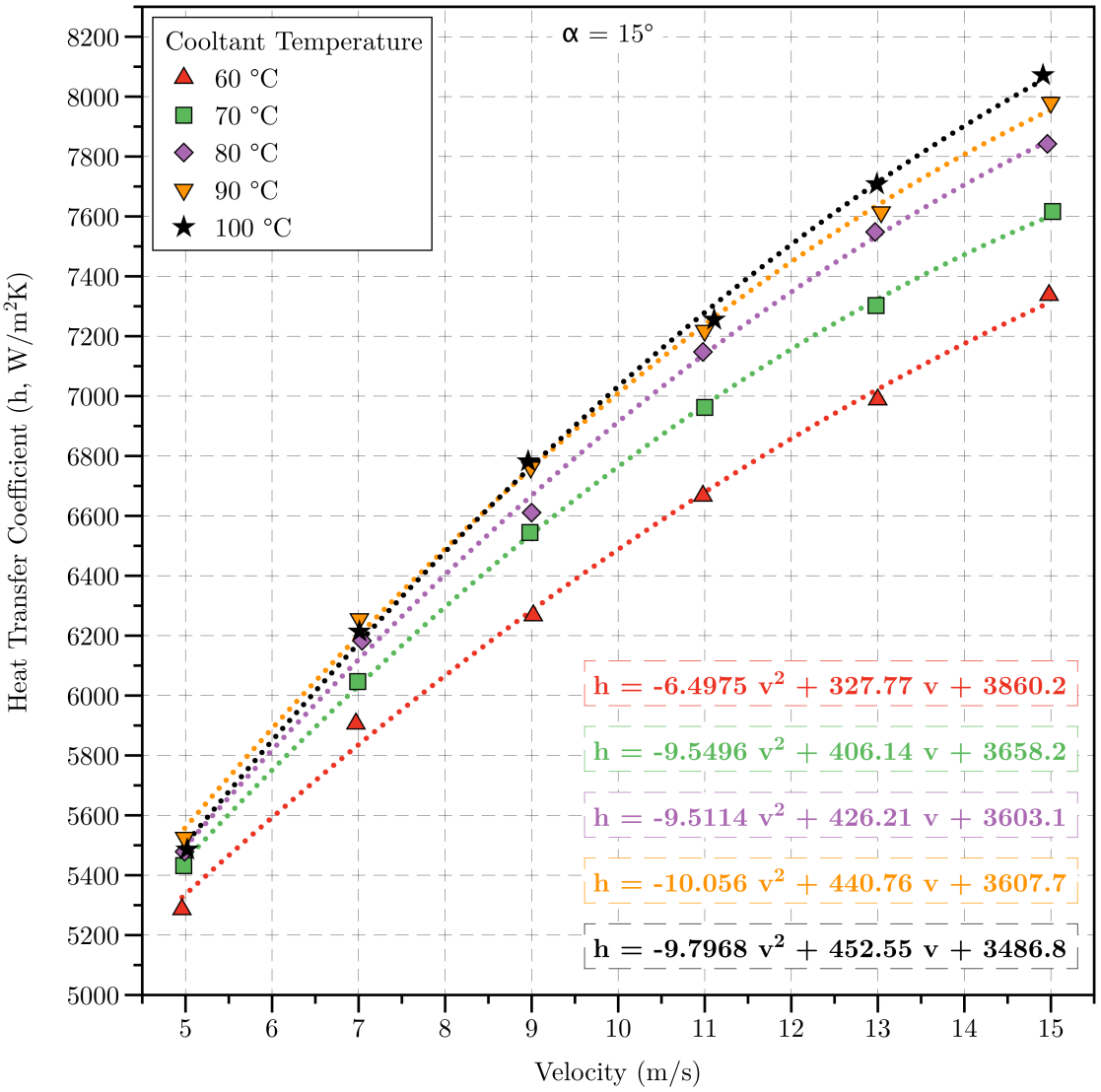

Figure E.11 Heat transfer coefficient (h) vs. velocity (v) for 15° radiator inclination (α).

E.6.3 Radiator Data for $\alpha = 30^{\circ}$

Table E.7 Young Calibration radiator pressure drop (ΔP) for 30° radiator inclination (α).

Tunnel Velocity (m/s)	Air Mass Flow (kg/s)	Inlet Temp. (°C)	Rad. ΔP (Pa)
($\alpha = 30^{\circ}$, No Coolant)			
4.99	0.93	17.8	90
7.00	1.30	17.7	164
8.99	1.67	18.2	250
11.01	2.05	18.5	356
13.00	2.43	17.8	481
14.90	2.79	17.8	615
($\alpha = 30^{\circ}$, Coolant Temp. = 60 °C)			
5.00	0.91	25.2	97
6.99	1.27	25.1	167
9.02	1.64	25.0	255
11.01	2.01	25.0	363
12.97	2.37	25.0	485
14.99	2.74	25.1	638
($\alpha = 30^{\circ}$, Coolant Temp. = 70 °C)			
4.99	0.91	25.2	100
7.00	1.27	25.1	173
9.01	1.64	25.2	261
10.98	2.00	25.0	367
12.97	2.36	25.4	491
14.99	2.74	24.6	650
($\alpha = 30^{\circ}$, Coolant Temp. = 80 °C)			
5.02	0.91	25.1	103
6.99	1.27	25.1	176
9.01	1.64	25.0	267
10.98	2.00	25.0	374
12.97	2.36	25.0	507
14.91	2.72	25.0	650

Table E.8 Young Calibration radiator pressure drop (ΔP) for 30° radiator inclination (α) (continued).

Tunnel Velocity (m/s)	Air Mass Flow (kg/s)	Inlet Temp. (°C)	Rad. ΔP (Pa)
($\alpha = 30°$, Coolant Temp. = 90 °C)			
5.00	0.91	25.1	108
6.98	1.27	25.1	183
8.97	1.63	24.9	273
10.96	1.99	25.1	383
12.97	2.36	25.0	513
15.02	2.74	25.1	666
($\alpha = 30°$, Coolant Temp. = 100 °C)			
4.99	0.90	25.0	112
6.98	1.27	25.0	189
9.01	1.64	25.2	279
10.99	2.00	25.0	391
13.00	2.37	25.2	523
14.97	2.73	25.0	678

Table E.9 Young Calibration heat transfer data for 30° radiator inclination (α).

Tunnel Velocity (m/s)	Flow Rate (L/min)	Mass Flow (kg/s)	Inlet Temp. (°C)	Outlet Temp. (°C)	ΔP (mbar)	Heat Dissipation $\mathrm{W\,m^{-2}\,K^{-1}}$	Heat Rejection (kW)
($\alpha = 30°$, Coolant Temp. = 60 °C)							
5.00	120.0	2.09	60.2	58.2	704	2839.15	15.0
6.99	120.0	2.09	60.4	57.9	706	3429.70	18.3
9.02	119.9	2.09	60.0	57.2	708	3971.48	21.0
11.01	120.0	2.09	59.8	56.6	711	4413.64	23.2
12.97	120.0	2.09	59.8	56.3	712	4843.65	25.5
14.99	120.0	2.09	59.9	56.1	713	5263.17	27.7
($\alpha = 30°$, Coolant Temp. = 70 °C)							
4.99	119.9	2.07	70.3	67.6	696	2860.97	19.5
7.00	120.2	2.08	69.8	66.5	699	3544.20	24.0
9.01	120.0	2.08	70.2	66.5	700	4052.53	27.6
10.98	120.0	2.08	70.0	65.8	702	4542.57	30.9
12.97	120.0	2.08	69.9	65.3	702	5013.23	33.7
14.99	119.9	2.07	69.9	64.8	703	5430.33	37.2
($\alpha = 30°$, Coolant Temp. = 80 °C)							
5.02	120.1	2.07	79.9	76.6	683	2910.12	24.1
6.99	120.0	2.06	80.5	76.5	686	3548.99	29.7
9.01	119.9	2.06	79.9	75.3	686	4119.98	34.2
10.98	120.0	2.06	79.8	74.6	688	4612.56	38.2
12.97	120.0	2.06	79.6	73.9	691	5099.88	42.1
14.91	119.9	2.06	79.7	73.6	691	5505.54	45.6
($\alpha = 30°$, Coolant Temp. = 90 °C)							
5.00	120.2	2.05	90.2	86.3	668	2903.37	28.6
6.98	120.1	2.05	89.5	84.9	672	3510.47	34.2
8.97	120.0	2.05	89.9	84.5	672	4102.60	40.3
10.96	120.1	2.05	90.0	83.8	674	4667.17	45.7
12.97	120.0	2.05	89.5	82.8	675	5129.58	50.0
15.02	120.0	2.05	89.9	82.5	676	5577.36	54.6
($\alpha = 30°$, Coolant Temp. = 100 °C)							
4.99	120.1	2.04	99.8	95.4	656	2868.79	32.4
6.98	119.9	2.03	100.4	94.9	657	3583.76	40.8
9.01	119.9	2.03	100.0	93.7	659	4137.48	46.8
10.99	119.9	2.03	99.6	92.5	660	4677.16	52.7
13.00	120.0	2.04	99.6	91.8	661	5150.94	58.0
14.97	119.9	2.03	99.9	91.3	661	5612.71	63.6

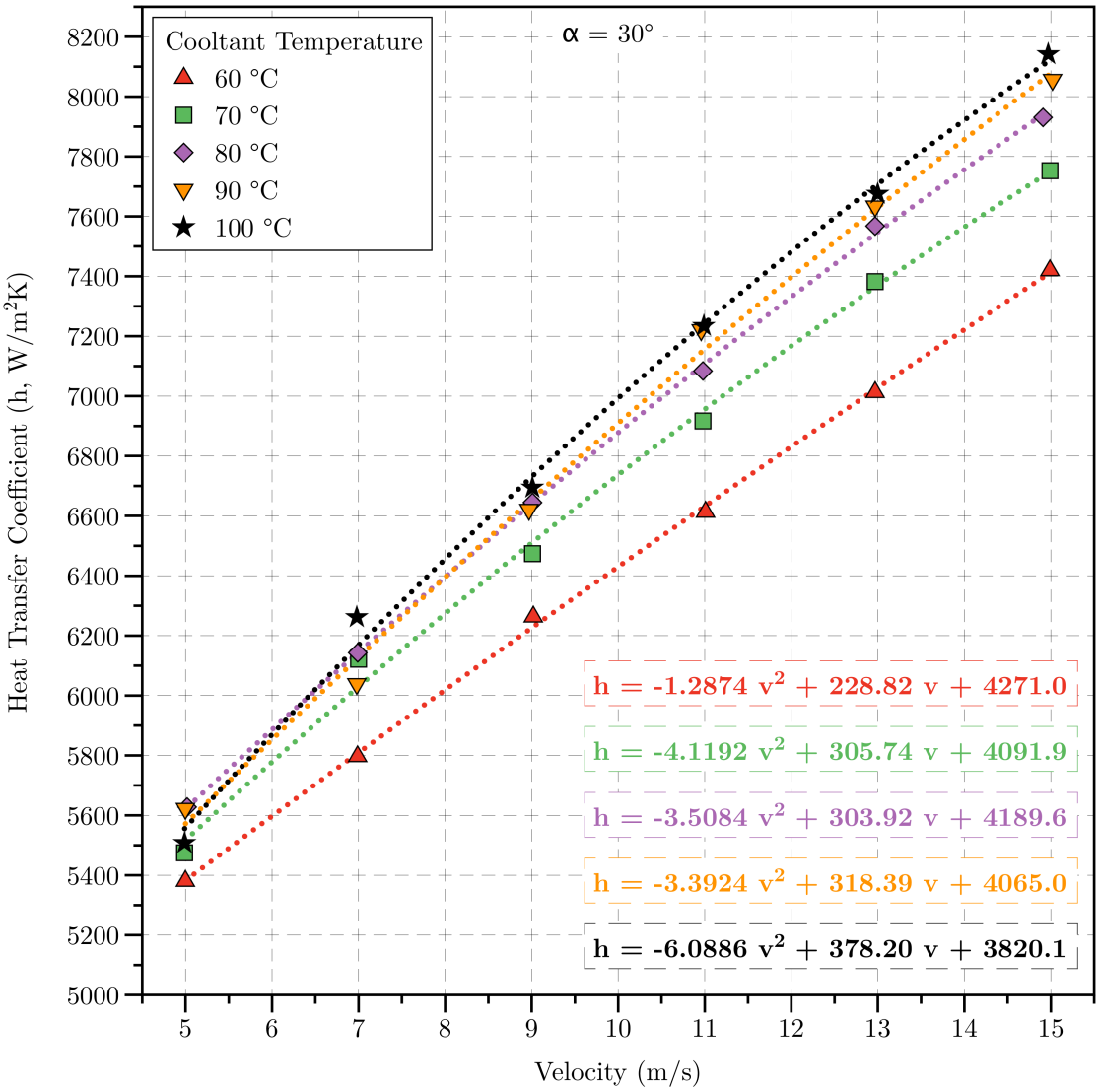

Figure E.12 Heat transfer coefficient (h) vs. velocity (v) for 30° radiator inclination (α).

E.6.4 Radiator Data for $\alpha = 45^{\circ}$

Table E.10 Young Calibration radiator pressure drop (ΔP) for 45° radiator inclination (α).

Tunnel Velocity (m/s)	Air Mass Flow (kg/s)	Inlet Temp. (°C)	Rad. ΔP (Pa)
($\alpha = 45^{\circ}$, No Coolant)			
5.03	0.93	18.2	92
6.99	1.30	17.8	163
9.03	1.68	18.2	254
11.00	2.05	17.8	360
12.95	2.41	18.2	490
15.00	2.79	18.8	642
($\alpha = 45^{\circ}$, Coolant Temp. = 60 °C)			
4.99	0.90	24.8	98
7.00	1.27	25.3	171
8.97	1.63	25.0	260
11.00	2.00	25.0	368
13.03	2.37	24.9	505
14.98	2.73	24.9	653
($\alpha = 45^{\circ}$, Coolant Temp. = 70 °C)			
5.03	0.91	25.0	101
6.99	1.27	25.0	173
9.00	1.63	25.1	263
11.02	2.00	25.1	375
12.96	2.36	25.0	506
15.00	2.73	25.1	662
($\alpha = 45^{\circ}$, Coolant Temp. = 80 °C)			
4.97	0.90	24.9	101
7.00	1.27	24.9	177
8.95	1.62	25.0	269
10.94	1.99	24.9	377
12.97	2.36	24.9	511
15.04	2.74	25.0	678

Table E.11 Young Calibration radiator pressure drop (ΔP) for 45° radiator inclination (α) (continued).

Tunnel Velocity (m/s)	Air Mass Flow (kg/s)	Inlet Temp. (°C)	Rad. ΔP (Pa)
($\alpha = 45°$, Coolant Temp. = 90 °C)			
5.02	0.91	24.9	106
6.95	1.26	24.9	179
8.95	1.62	25.0	270
11.03	2.00	25.1	391
12.99	2.36	25.0	528
15.22	2.77	25.4	687
($\alpha = 45°$, Coolant Temp. = 100 °C)			
4.98	0.90	24.8	106
7.03	1.27	25.1	185
8.97	1.63	25.2	275
10.94	1.99	24.7	388
12.99	2.36	25.1	533
14.91	2.71	25.2	681

Table E.12 Young Calibration heat transfer data for 45° radiator inclination (α).

Tunnel Velocity (m/s)	Flow Rate (L/min)	Mass Flow (kg/s)	Inlet Temp. (°C)	Outlet Temp. (°C)	ΔP (mbar)	Heat Dissipation $\mathrm{W\,m^{-2}\,K^{-1}}$	Heat Rejection (kW)
($\alpha = 45°$, Coolant Temp. = 60 °C)							
4.99	120.1	2.09	60.4	58.4	707	2759.75	14.8
7.00	119.9	2.09	60.2	57.7	704	3394.56	17.9
8.97	120.2	2.09	60.2	57.3	713	3892.93	20.7
11.00	120.0	2.09	60.1	57.0	713	4351.88	23.1
13.03	119.9	2.09	59.8	56.4	714	4816.48	25.4
14.98	120.0	2.09	60.4	56.6	715	5197.69	27.9
($\alpha = 45°$, Coolant Temp. = 70 °C)							
5.03	120.0	2.08	69.9	67.3	698	2839.56	19.3
6.99	120.0	2.08	69.7	66.4	700	3513.62	23.7
9.00	120.0	2.08	69.7	66.0	701	4064.48	27.4
11.02	120.2	2.08	69.8	65.7	705	4575.93	31.0
12.96	120.0	2.08	69.9	65.3	706	5029.16	34.1
15.00	120.0	2.08	69.9	64.9	707	5456.39	37.0
($\alpha = 45°$, Coolant Temp. = 80 °C)							
4.97	119.9	2.06	79.7	76.5	683	2869.37	23.8
7.00	119.9	2.06	79.8	75.9	688	3539.56	29.4
8.95	120.0	2.06	79.9	75.3	689	4128.91	34.3
10.94	120.1	2.06	79.7	74.5	691	4628.78	38.3
12.97	120.0	2.06	79.7	73.9	691	5116.13	42.3
15.04	120.0	2.06	80.0	73.7	691	5579.76	46.4
($\alpha = 45°$, Coolant Temp. = 90 °C)							
5.02	119.9	2.05	89.7	85.9	671	2892.86	28.3
6.95	119.9	2.05	89.7	85.0	673	3563.54	34.9
8.95	119.8	2.05	89.6	84.2	673	4125.06	40.3
11.03	119.9	2.05	89.6	83.4	676	4705.23	45.9
12.99	120.1	2.05	90.5	83.7	677	5148.64	51.0
15.22	120.0	2.05	89.8	82.4	678	5626.81	54.7
($\alpha = 45°$, Coolant Temp. = 100 °C)							
4.98	120.0	2.04	99.6	95.2	657	2880.10	32.5
7.03	120.0	2.04	99.7	94.3	657	3567.36	40.2
8.97	120.0	2.04	99.6	93.3	663	4136.05	46.5
10.94	119.8	2.03	99.6	92.4	663	4677.20	52.9
12.99	120.0	2.04	99.6	91.7	664	5188.91	58.4
14.91	120.0	2.04	99.8	91.3	664	5629.18	63.6

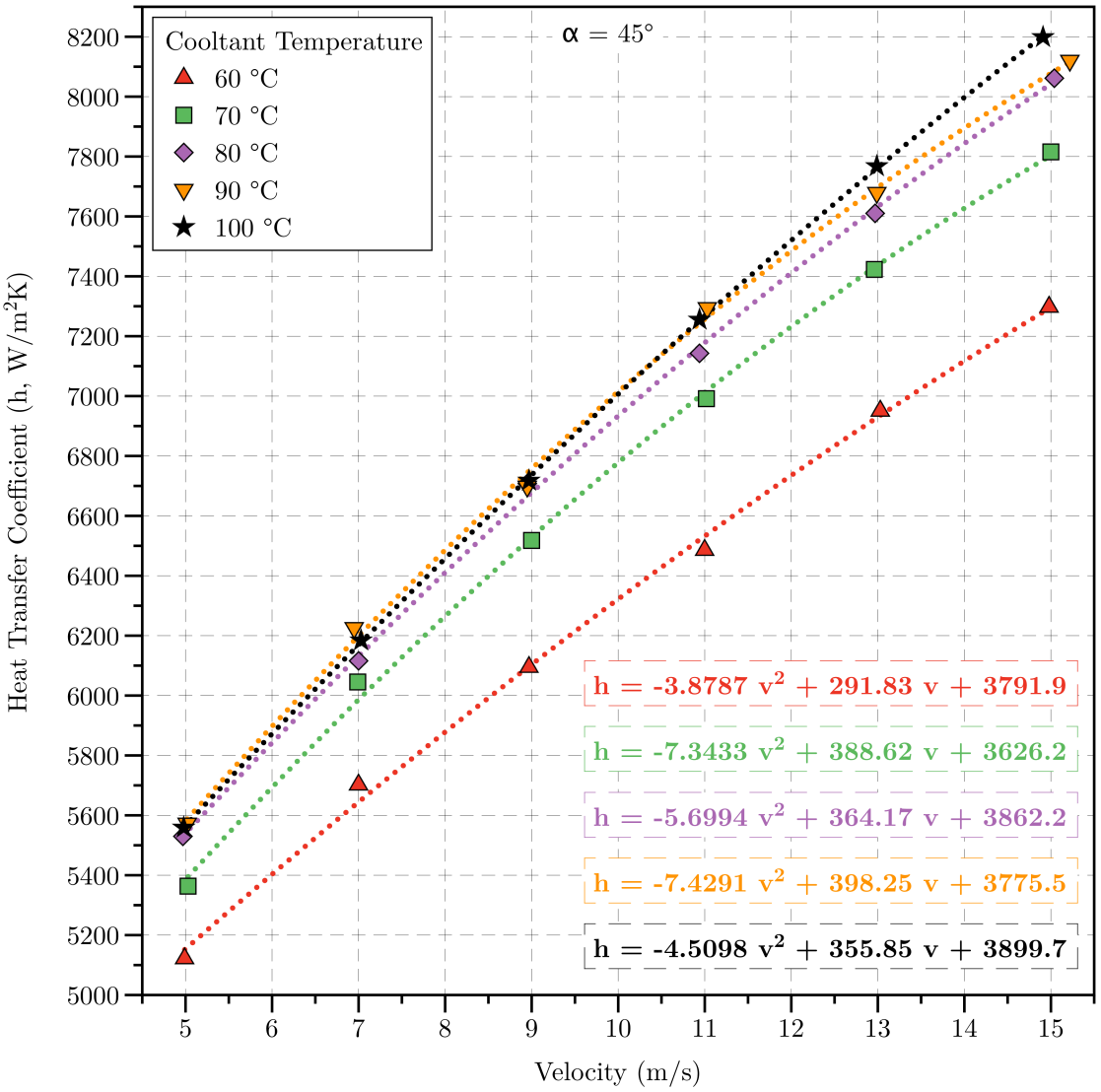

Figure E.13 Heat transfer coefficient (h) vs. velocity (v) for 45° radiator inclination (α).

E.7 Error Analysis

Wind tunnel velocity can be determined from pitot-static probe measurements through Eq. (E.1), where q is the dynamic pressure and equals the difference between the total and static pressure

$$v = \sqrt{\left(\frac{2q}{\rho}\right)}. \tag{E.1}$$

The relative error measurement in the velocity ($\Delta v/v$) is given by

$$\frac{\Delta v}{v} = \sqrt{\left(\frac{1}{2}\frac{\Delta q}{q}\right)^2 + \left(\frac{1}{2}\frac{\Delta \rho}{\rho}\right)^2}, \tag{E.2}$$

where the relative error of the air density ($\Delta\rho/\rho$) is given by

$$\frac{\Delta \rho}{\rho} = \sqrt{\left(\frac{\Delta P}{P}\right)^2 + \left(\frac{\Delta T}{T}\right)^2}, \tag{E.3}$$

where $\Delta P = \pm 15$ Pa is the barometer error on the GE Druck DPI 141 and $\Delta T = \pm 0.5$ K is the thermometer error, where the errors are specified by the respective manufactures. For the purpose of these calculations the experimentally recorded maximum barometric pressure and ambient temperature of $P = 102\,100$ Pa and $T = 298.15$ K, respectively, will be used to determine the relative error in the air density. The error on the density is therefore given by

$$\frac{\Delta \rho}{\rho} = \sqrt{\left(\frac{15}{102100}\right)^2 + \left(\frac{0.5}{298.15}\right)^2} = 0.00168. \tag{E.4}$$

The maximum relative error of the pressure transducers specified by the manufacturer is $\pm 0.5\%$ of the pressure measurement. The maximum error specified for the velocity is $\pm 1\%$ of the velocity measurement.

A sample calculation of the relative error of the pressure drop coefficient for a full scale radiator with a maximum tested velocity of 15 m/s and a pressure drop (ΔP)= 687 Pa is presented. The relative error on the pressure drop coefficient ($\Delta P/q$) is therefore given by

$$\frac{\Delta(\Delta P/q)}{\Delta P/q} = \sqrt{\left(\frac{\Delta(\Delta P)}{\Delta P}\right)^2 + \left(\frac{\Delta q}{q}\right)^2}, \tag{E.5}$$

where,

$$\frac{\Delta q}{q} = \sqrt{2 \cdot \left(\frac{\Delta v}{v}\right)^2 + \left(\frac{\Delta \rho}{\rho}\right)^2}, \tag{E.6}$$

therefore the error on the dynamic pressure (q) is

$$\frac{\Delta q}{q} = \sqrt{2 \cdot \left(\frac{0.15}{15}\right)^2 + (0.00168)^2} = 0.02, \tag{E.7}$$

hence the error on the pressure drop coefficient is

$$\frac{\Delta(\Delta P/q)}{\Delta P/q} = \sqrt{\left(\frac{3.435}{687}\right)^2 + (0.02)^2} = 2.06\%. \tag{E.8}$$

E.8 CFD Details

The physical size of the computational domain was chosen as 2.016 m in the horizontal (x-axis), with the vertical (y-axis) and spanwise (z-axis) dimensions matching that of the physical radiator (0.402 m and 0.376 m, respectively) with the radiator having a thickness of 0.016 m.

The mesh consisted of a total of 2,160,000 nodes arranged as $216 \times 100 \times 100$ in the x, y, z directions, respectively. The mesh used in the radiator CFD simulations is shown in Fig. E.14. The numerical simulations were compared with experimental data for inlet velocities of 4.97, 6.98, 8.98, 10.99, 13.03 and 14.94 $\mathrm{m\,s^{-1}}$. The solver parameters used for the simulations are shown in Table E.13.

To check for solution convergence, in addition to residual monitoring (shown in Fig. E.15 and Fig. E.16), the centreline temperature downstream of the radiator was monitored. The facet-averaged monitor was horizontally located at 0.5 m downstream of the cold-side of the radiator and is shown in Fig. E.17.

E.8.1 CFD Results

E.8.1.1 Mesh

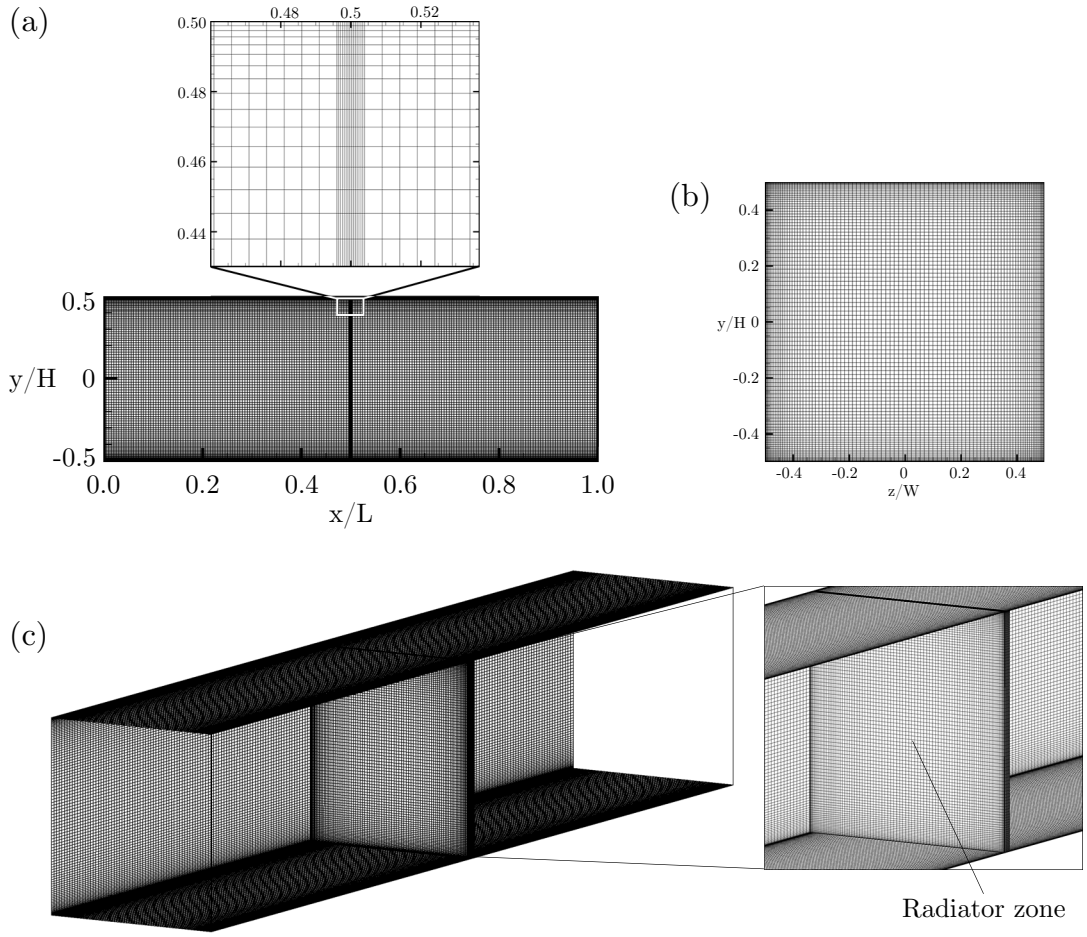

Figure E.14 Computational mesh for radiator model, (a) side view, (b) front view and (c) 3/4 view.

E.8.1.2 Solver Parameters

Table E.13 CFD solver parameters used for the radiator simulations.

General Details	
Solver	ANSYS® FLUENT® 15.0, Pressure Based, Steady, Implicit, Node-Based
Mesh Type	Structured
Number of Cells	2160000
Solver Controls	
Turbulence Model	$k-\varepsilon$ (Standard)
Near-Wall Treatment	Standard Wall Treatment
Pressure-Velocity Coupling	SIMPLE
Discretisation (Under Relaxation)	
Gradient	Least Squares Cell Based
Pressure	Second Order (0.3)
Momentum	Second Order Upwind (0.7)
Turbulent Kinetic Energy	Second Order (0.8)
Turbulent Dissipation Rate	Second Order Upwind (0.8)
Energy	Second Order Upwind
Materials	
Fluid	Air
Density	$1.225 \times 10^{-3}\,\mathrm{kg\,m^{-3}}$
Viscosity	$1.7894 \times 10^{-5}\,\mathrm{kg\,m^{-1}\,s^{-1}}$
Boundary Conditions	
Inlet	Velocity Inlet (4.97, 6.98, 8.98, 10.99, 13.03 and $14.94\,\mathrm{m\,s^{-1}}$)
Outlet	Pressure Outlet
Top / Bottom / Left / Right	Wall (Hydrodynamically smooth)
Radiator	Radiator: Pressure Drop Coefficient (ΔP/q): Polynomial: [1] 11.3, [2] -0.8955 and [3] 0.03118, Heat Transfer Coefficient (h): Polynomial: [1] 3730, [2] 420.27 and [3] -9.101, Temperature (k): 373.15

E.8.2 Residuals

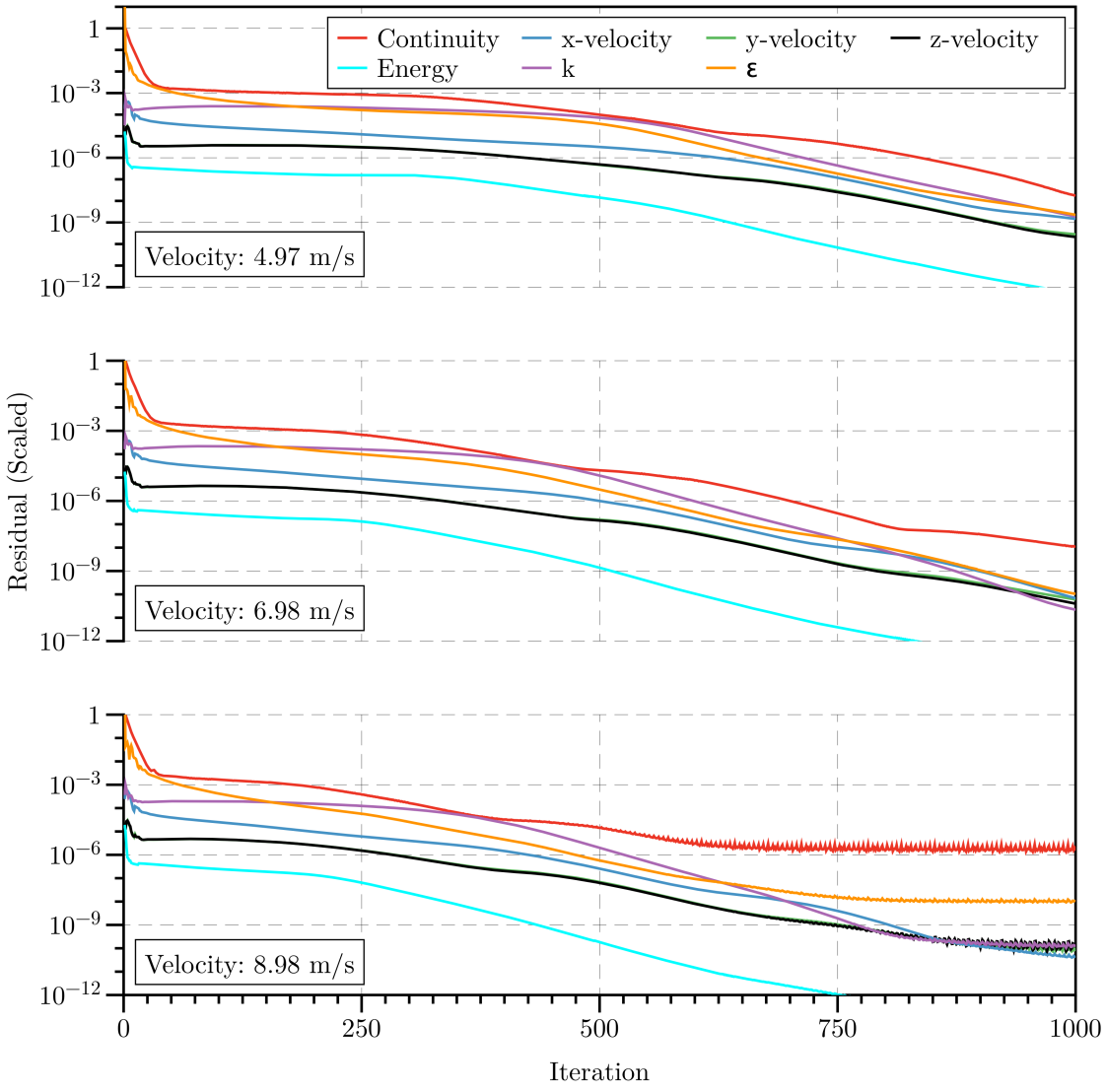

Figure E.15 Scaled residuals for the CFD radiator simulations.

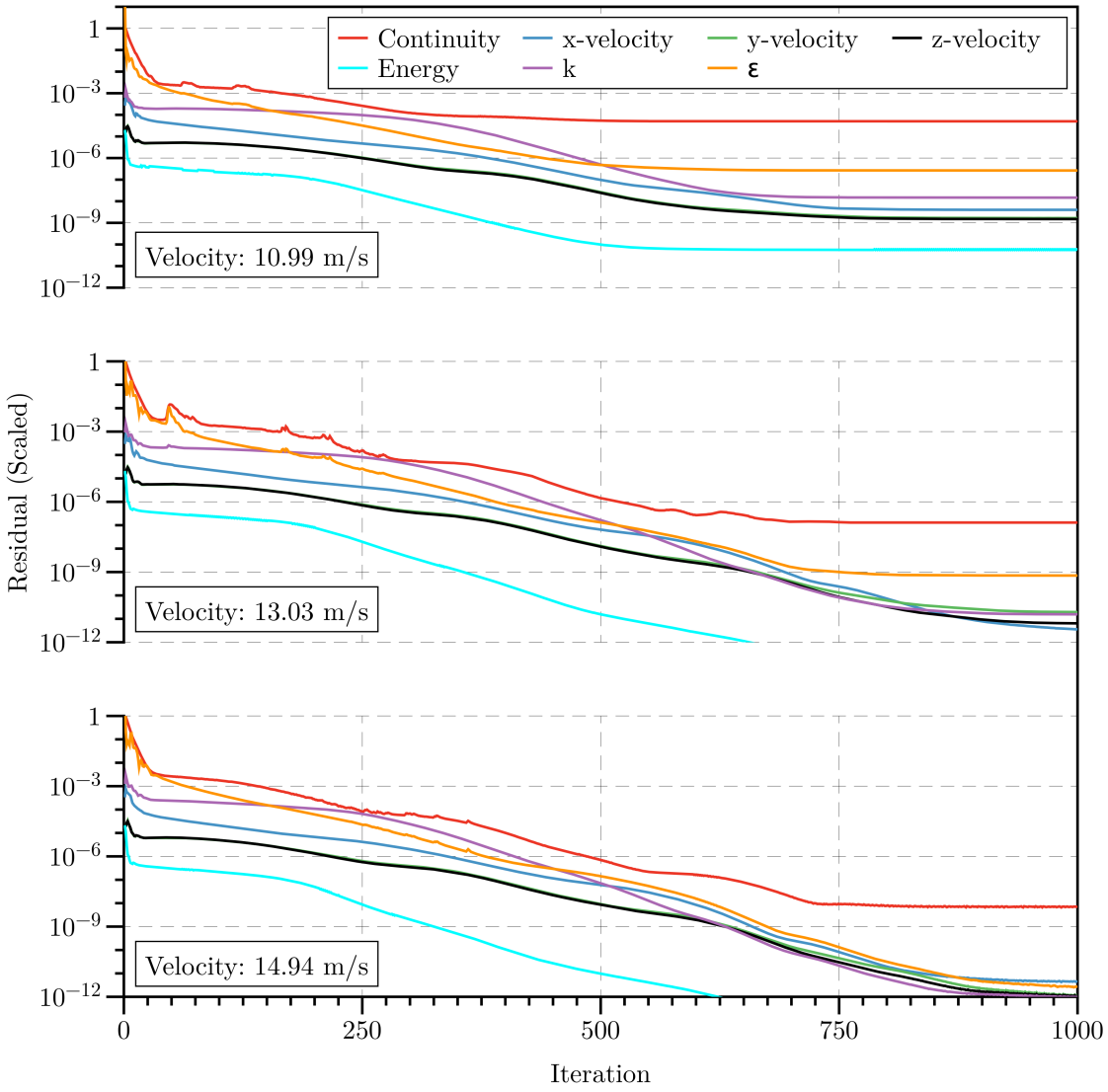

Figure E.16 Scaled residuals for the CFD radiator simulations (continued).

E.8.2.1 Temperature Convergence

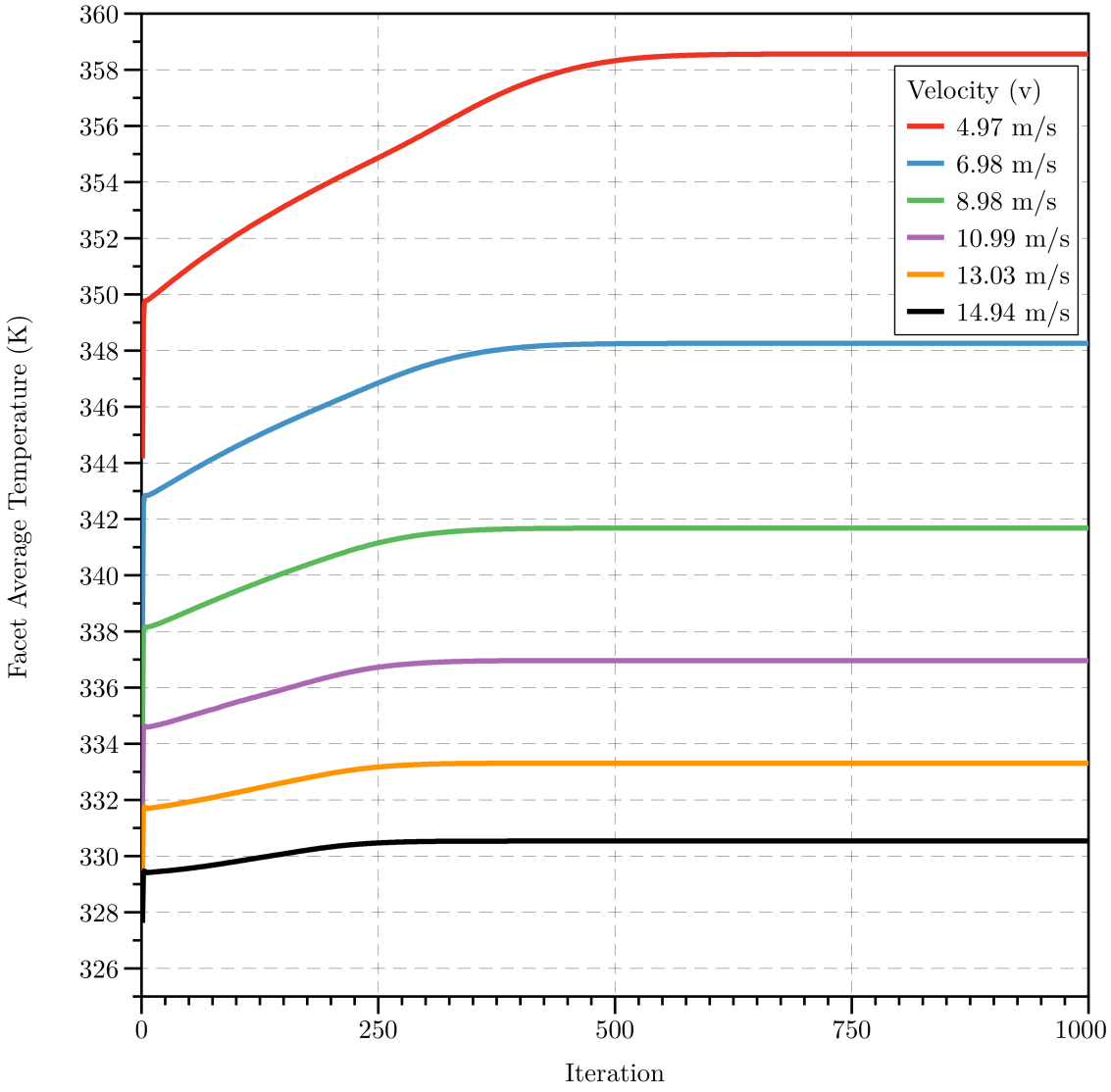

Figure E.17 Facet averaged temperature convergence for the CFD radiator simulations.

This page intentionally left blank.

Appendix F

Radiator Matrix Channel Flow

F.1 Wind Tunnel Arrangement

Figure F.1 Cranfield University's Shrivenham blower wind tunnel, (a) front view of working section, (b) side view of working section and (c) channel view.

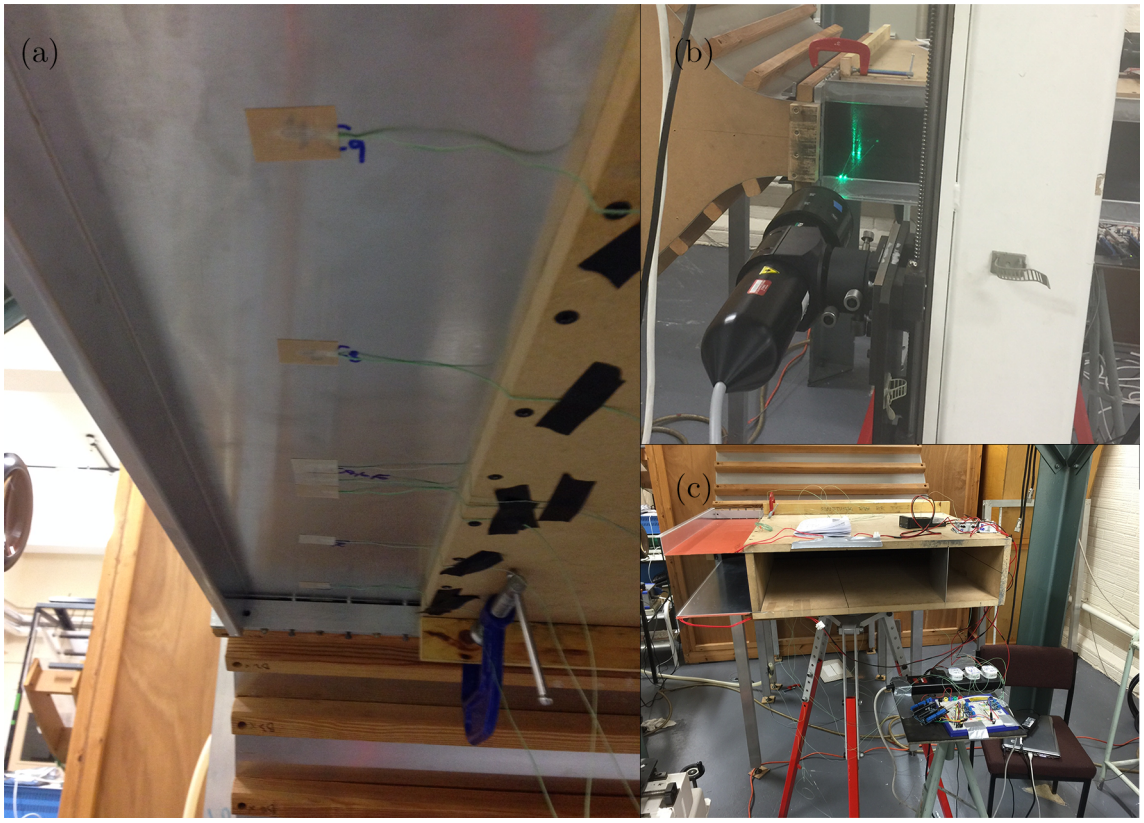

Figure F.2 Cranfield University's Shrivenham blower wind tunnel, (a) view of the thermocouple mounting locations, (b) side view of working section with laser and (c) thermocouple controller wiring.

F.2 Working Section Renderings

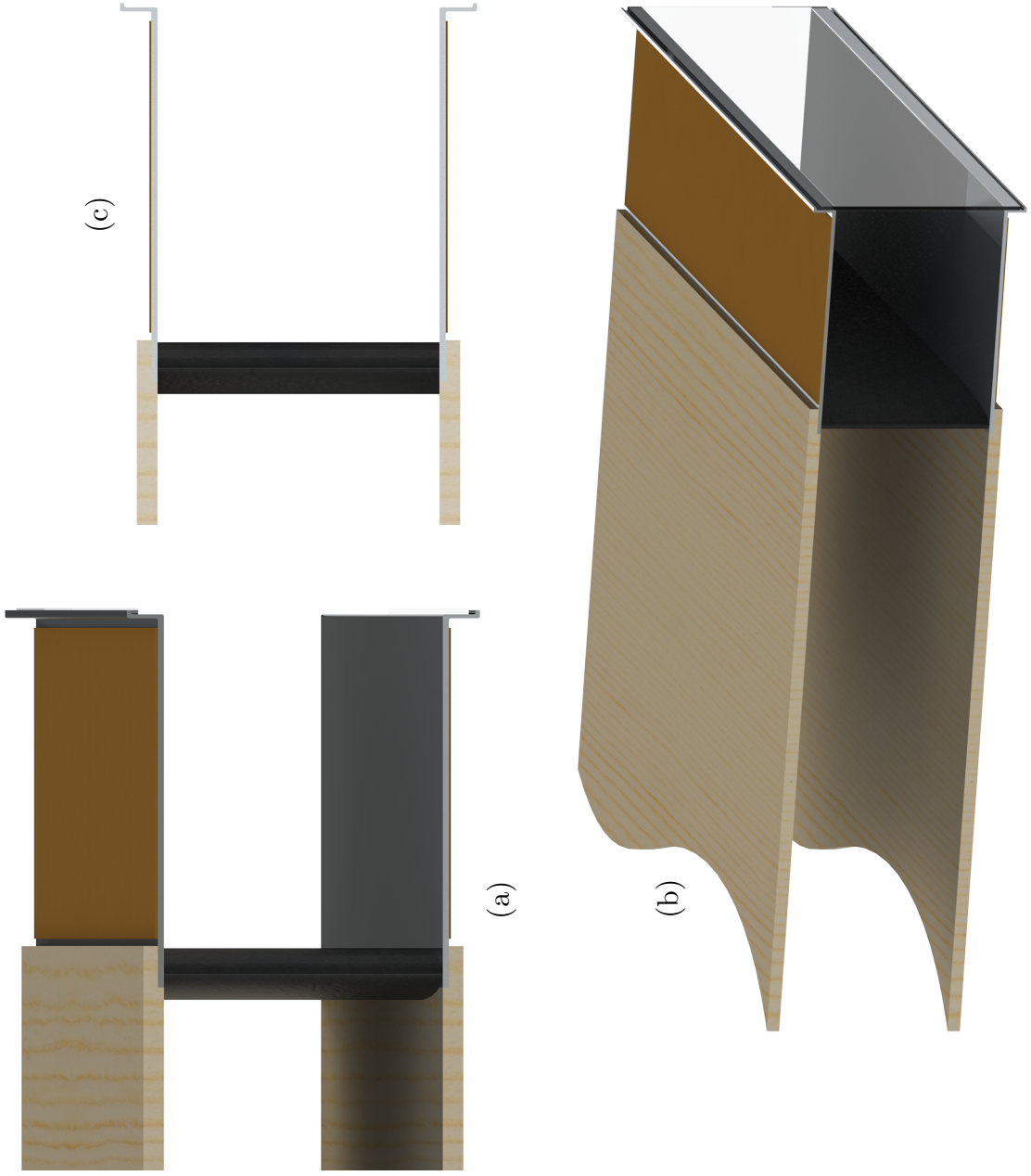

Figure F.3 Render of Cranfield University's Shrivenham blower wind tunnel, (a) channel entrance view, (b) 3/4 view and (c) front view.

F.3 Wind Tunnel Schematic

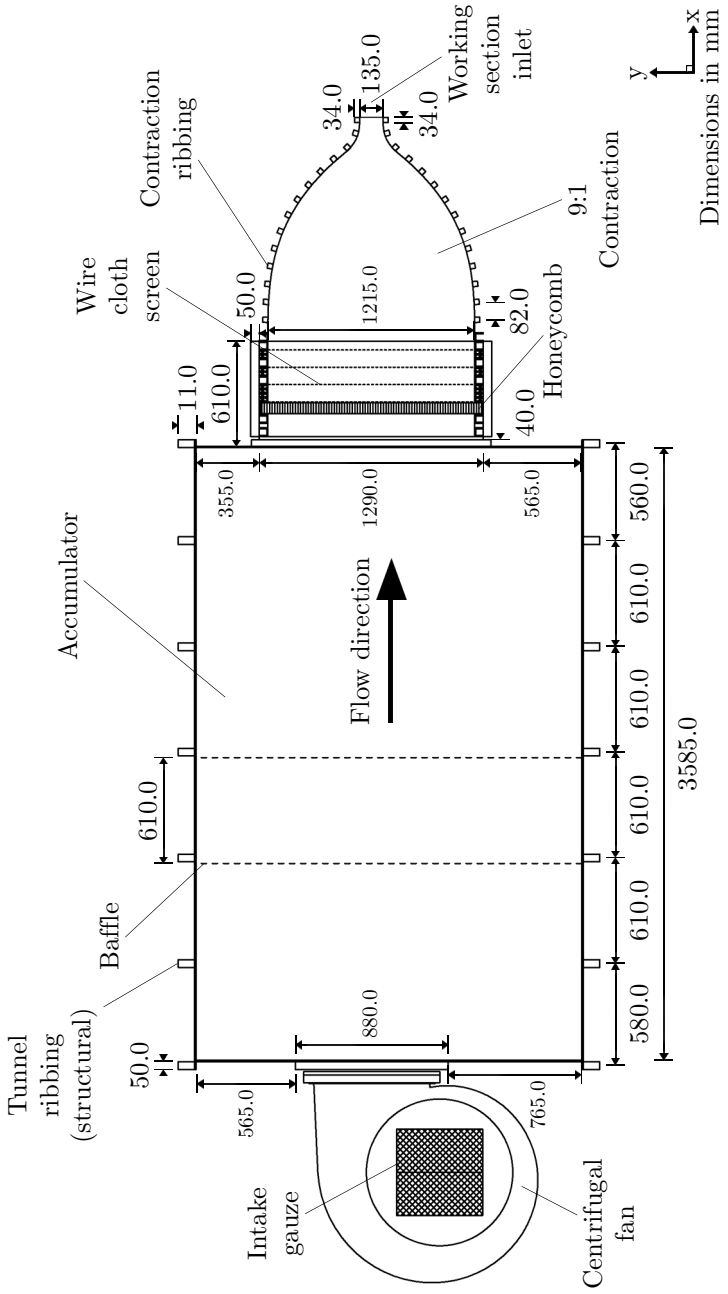

Figure F.4 Schematic of Cranfield University's Shrivenham blower wind tunnel [139].

F.4 Schematics of the Working Section

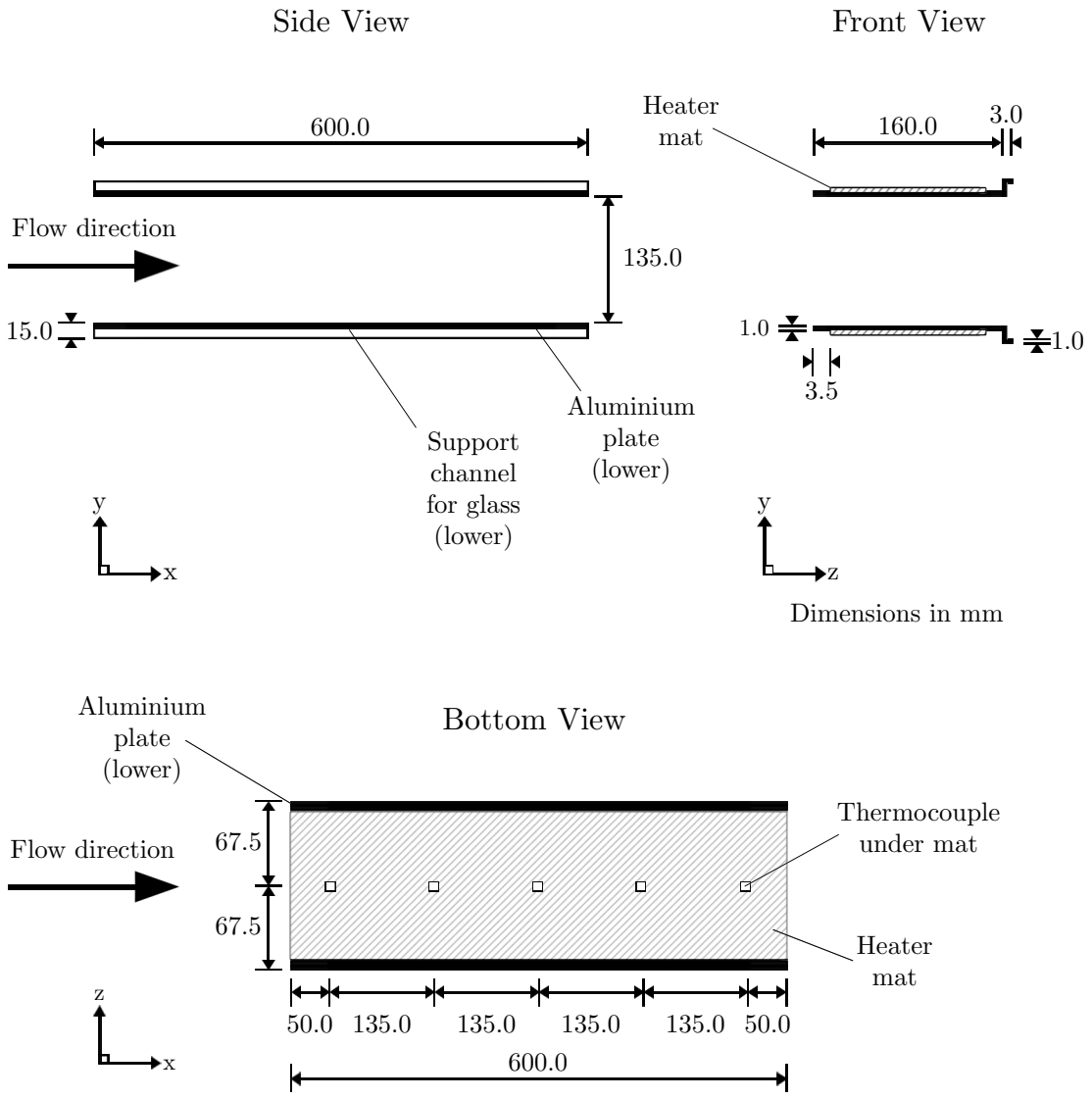

Figure F.5 Schematic of Cranfield University's Shrivenham working section.

F.5 Flexible Heater Specification Sheet

FLEXIBLE HEATERS

FLEXIBLE SILICONE RUBBER FIBERGLASS INSULATED HEATERS

- Lightweight Thin, Flexible
- Available in 2.5, 5 and 10 W/in²
- -56 to 232°C (-70 to 450°F) Operating Temperature
- Etched Foil and Wire Wound Design
- Round or Rectangular Shapes
- Available in 115 or 230** Vac
- Optional Pressure Sensitive Adhesive (PSA)†

SRF Series Starts at **$26**

MADE IN USA — 1 YEAR WARRANTY

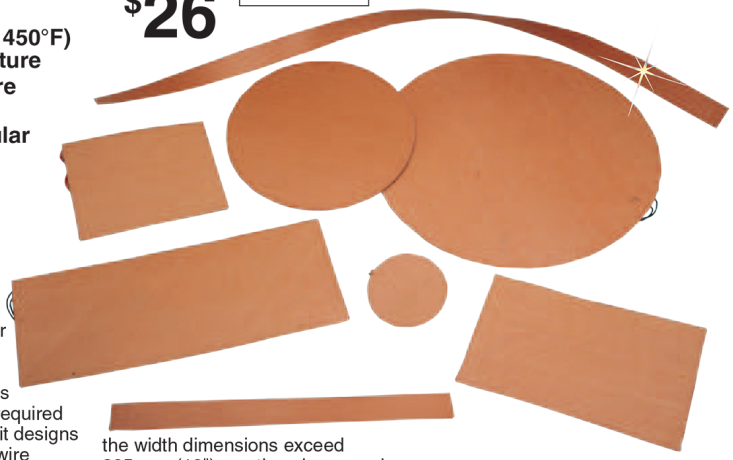

OMEGALUX® silicone rubber fiberglass insulated flexible heaters can improve heat transfer and speed warm-ups where controlled heating is required in confined areas. Two circuit designs are available: etched foil or wire wound. Heaters with etched foil designed elements are available where the length or width dimension is less than 305 mm (12"). All other heaters where both the length and the width dimensions exceed 305 mm (12") use the wire-wound element design. Effect of power density: gentle warming is best done with 2.5 W/in². A good all purpose unit is the 5 W/in². Rapid warm-up and high temperature are achieved with the 10 W/in²; however, temperature must be controlled as the safe maximum operating temperature limit of 232°C (450°F) may be exceeded.

Round Silicone Rubber Heaters

MOST POPULAR MODELS HIGHLIGHTED!

To Order *(Specify Model Number)*

Diameter cm (in)	Total Wattage for Watt Density 2.5 W/in²	5 W/in²	10 W/in²	Without PSA Model No.	Price	With PSA Model No.	Price
7.6 (3)	17.5	35	70	SRFR-3/*	$26	SRFR-3/*-P	$28
10 (4)	31.4	62.8	125.6	SRFR-4/*	32	SRFR-4/*-P	35
13 (5)	49.0	98.15	196.3	SRFR-5/*	39	SRFR-5/*-P	42
15 (6)	70.67	141.3	282.7	SRFR-6/*	40	SRFR-6/*-P	44
18 (7)	96.2	192.4	384.8	SRFR-7/*	44	SRFR-7/*-P	48
20 (8)	125.65	251.3	502.6	SRFR-8/*	48	SRFR-8/*-P	53
23 (9)	157.9	315.8	631.7	SRFR-9/*	53	SRFR-9/*-P	59
25 (10)	196.25	392.5	785	SRFR-10/*	59	SRFR-10/*-P	65
28 (11)	237.45	474.9	949.8	SRFR-11/*	65	SRFR-11/*-P	72
30 (12)	376.8	753.6	1507.2	SRFR-12/*	72	SRFR-12/*-P	79

Comes with complete operator's manual

** Insert watt density: 2 for 2.5 W/in², 5 for 5 W/in² or 10 for 10 W/in².*
*** Most sizes available in 230V. Contact Engineering.*

† Heaters with pressure sensitive adhesive: max operating temperature is 149°C (300°F).

***Ordering Examples: SRFR-3/10,** 7.6 cm (3") diameter heater with a watt density of 10 W/in² and 70 watts of total power, **$26**.*
SFRG-208/10
SRFR-11/10,** 28 cm (11") diameter heater with a 10 W/in², 949 watts **$72.

Figure F.6 OMEGA® SRFG heater specification sheet [140].

F.6 Velocity Profiles

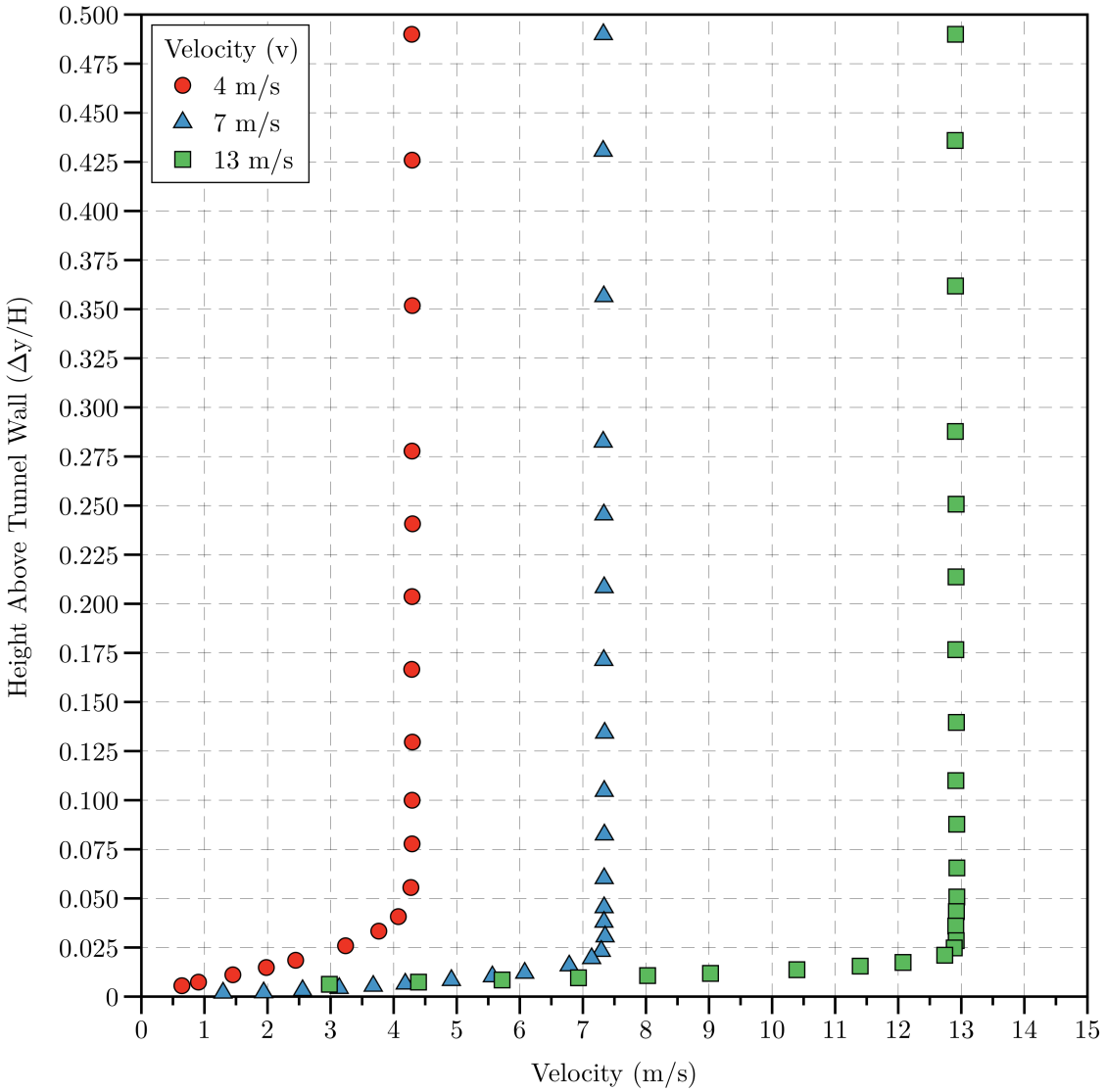

Figure F.7 Shrivenham blower wind tunnel velocity profiles for various velocities (v).

F.7 Error Analysis

The velocity measurements were made using a Dantec FibreFlow Laser Doppler Anemometry (LDA) optics set up as a 1D system with a 310 mm focal length probe and bespoke x-y-z traverse. The maximum error associated with the mean velocity ($\overline{U}$) is given by the manufacturer as

$$\frac{\Delta\overline{U}}{\overline{U}} = 2.0\%, \tag{F.1}$$

the corresponding maximum error associated with the root mean squared (u_{rms}) velocity is given by

$$\frac{\Delta u_{rms}}{u_{rms}} = 3.0\%. \tag{F.2}$$

The OMEGA® self-adhesive K-type thermocouples have an associated error of

$$\frac{\Delta T}{T} = \pm 1.0\text{K}. \tag{F.3}$$

F.8 CFD Details

To establish grid convergence for the 3D simulations used to model a simplified radiator channel, three numerical domains were chosen. The physical size of the simplified channel was 0.600 m in the horizontal (x-axis), 0.135 m in the vertical (y-axis) and 0.160 m in the spanwise (z-axis).

The initial mesh size (case 1) chosen consisted of 157 nodes along the x-axis, 42 nodes along the y-axis and 62 nodes along the z-axis. This equated to a total of 408,828 nodes in the computational domain. The mesh was then refined (case 2) in both the x and y directions to 313 and 83 nodes, respectively, whilst maintaining a spanwise node count of 62, this resulted in a total node count of 1,610,698. This process was again repeated (case 3) in the x and y directions (626 and 166 nodes, respectively) whilst again maintaining a spanwise node count of 62, resulting in 6,442,792 total nodes. The meshes used for the grid convergence study are show in Fig. F.8 and Fig. F.9.

The solver parameters used for the simulations are shown in Table F.1, the residuals from the simulation are shown in Fig. F.9. The dimensionless wall distance (y^+) for a wall-bounded flow is given by

$$y^+ \equiv \frac{u_* y}{\nu}, \tag{F.4}$$

where

$$u_* \equiv \sqrt{\frac{\tau_w}{\rho}}, \tag{F.5}$$

where τ_w is the wall shear stress, ρ is the fluid density at the wall, y is the distance to the nearest wall and ν is the kinematic viscosity of the fluid near the wall.

The variation in the numerical simulations were compared with at a normalised downstream location (x/L) of 0.9. The velocities were normalised with respect to the inlet velocity of $4\,\mathrm{m\,s^{-1}}$, the graphical output from the simutions is shown in Fig. F.12, with the normalised velocity profiles plotted in Fig. F.13. The 1.6×10^6 and 6.4×10^6 meshes (case 2 and case 3, respectively) exhibited no variation in the centreline velocity and as a result the 1.6×10^6 (case 2) mesh was used in the simplified radiator channel simulations.

For the turbulence model comparison, the general solver settings are shown in Table F.2. The turbulence specific solver settings for the Standard $k-\omega$ and Transition SST $k-\omega$ are shown in Table F.3 and Table F.4, respectively. The associated residuals from the heated and unheated, Standard $k-\omega$ and Transition SST $k-\omega$ simulations are shown in Fig. F.14 and Fig. F.15, respectively. The heated (120 K), heated (140 K) and heated (100 K, on all four walls) residuals are shown in Fig. F.16.

In addition to residual monitoring, the convergence of the heat flux ($\overrightarrow{q}$) was monitored at a normalised distance (x/L) of 0.9. The convergence of the heat flux for the heated channel simulations is shown in Fig. F.17.

F.8.1 CFD Grid Convergence

F.8.1.1 Meshes

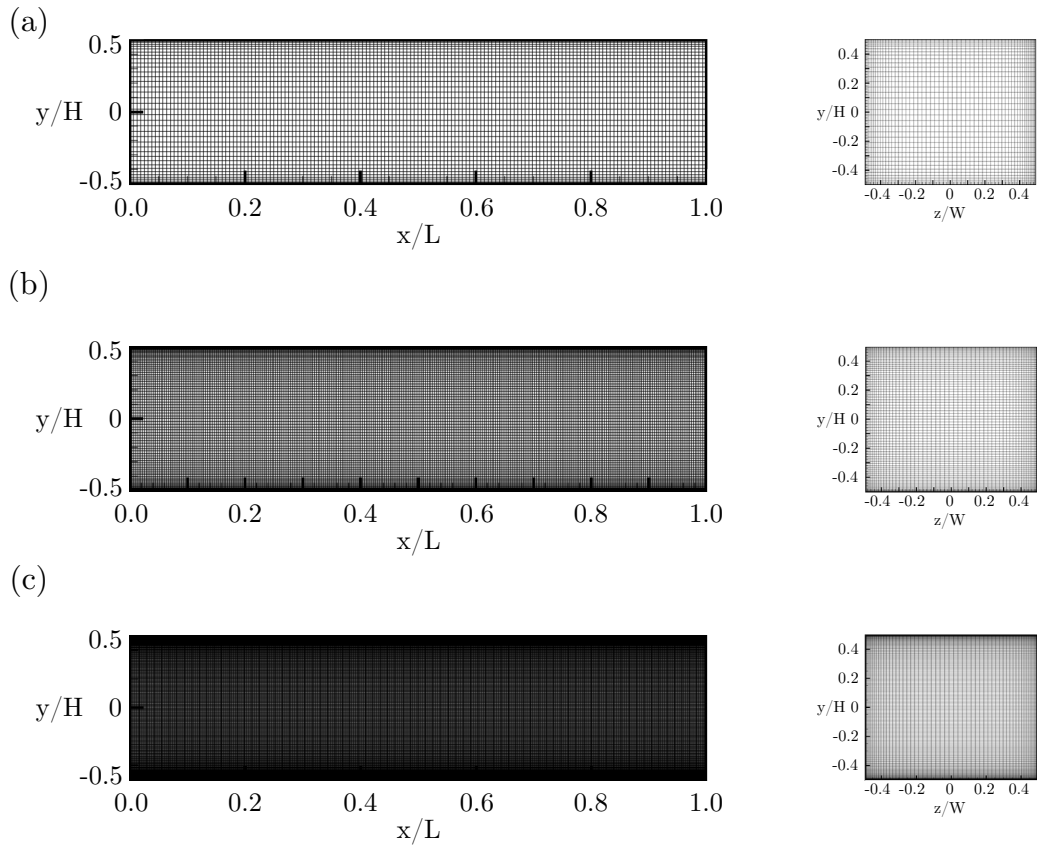

Figure F.8 Computational meshes for (a) 408,828, (b) 1,610,698 and (c) 6,442,792 grid cells.

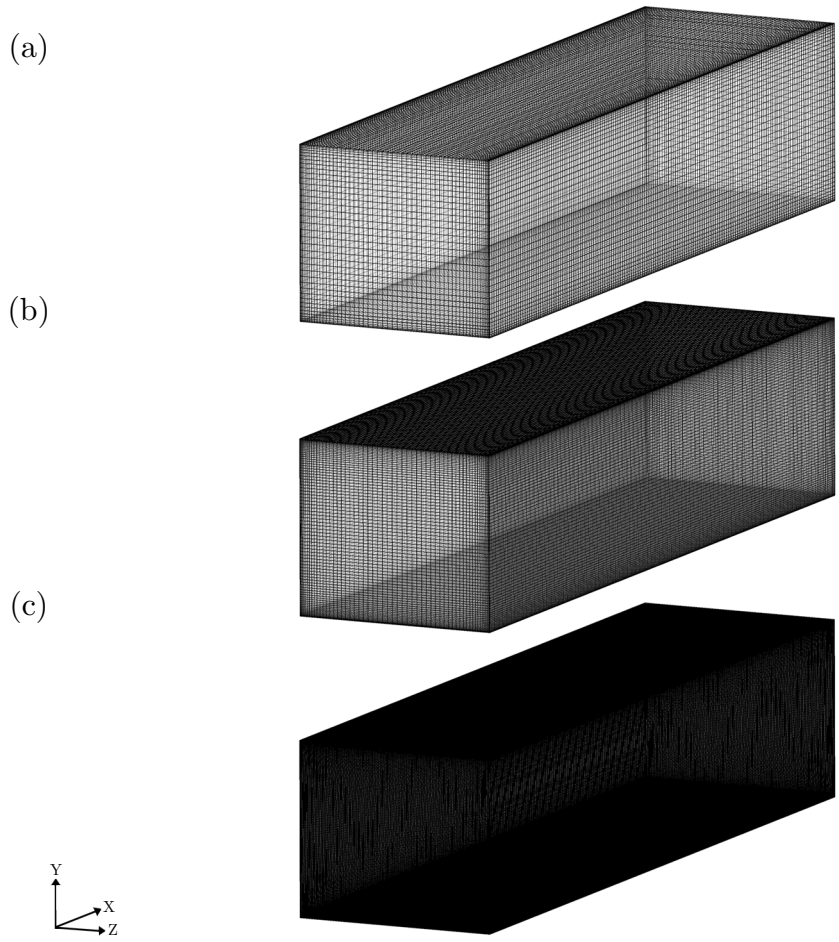

Figure F.9 Computational meshes for (a) 408,828, (b) 1,610,698 and (c) 6,442,792 grid cells (continued).

F.8.1.2 Solver Parameters

Table F.1 CFD solver parameters used in the 3D channel grid convergence simulations.

General Details	
Solver	ANSYS® FLUENT® 15.0, Pressure Based, Steady, Implicit, Node-Based
Mesh Type	Structured
Number of Cells	Case 1 - 408828 Case 2 - 1610698 Case 3 - 6442792
Solver Controls	
Turbulence Model	$k-\omega$ (Standard)
Near-Wall Treatment	Standard Wall Treatment
Pressure-Velocity Coupling	SIMPLE
Discretisation (Under Relaxation)	
Gradient	Least Squares Cell Based
Pressure	Second Order (0.3)
Momentum	Second Order Upwind (0.7)
Turbulent Kinetic Energy	Second Order (0.8)
Turbulent Dissipation Rate	Second Order Upwind (0.8)
Materials	
Fluid	Air
Density	$1.225 \times 10^{-3}\,\mathrm{kg\,m^{-3}}$
Viscosity	$1.7894 \times 10^{-5}\,\mathrm{kg\,m^{-1}\,s^{-1}}$
Boundary Conditions	
Inlet	Velocity Inlet ($4\,\mathrm{m\,s^{-1}}$)
Outlet	Pressure Outlet
Top	Wall (Hydrodynamically smooth)
Bottom	Wall (Hydrodynamically smooth)
Left	Wall (Hydrodynamically smooth)
Right	Wall (Hydrodynamically smooth)

F.8.1.3 Residuals

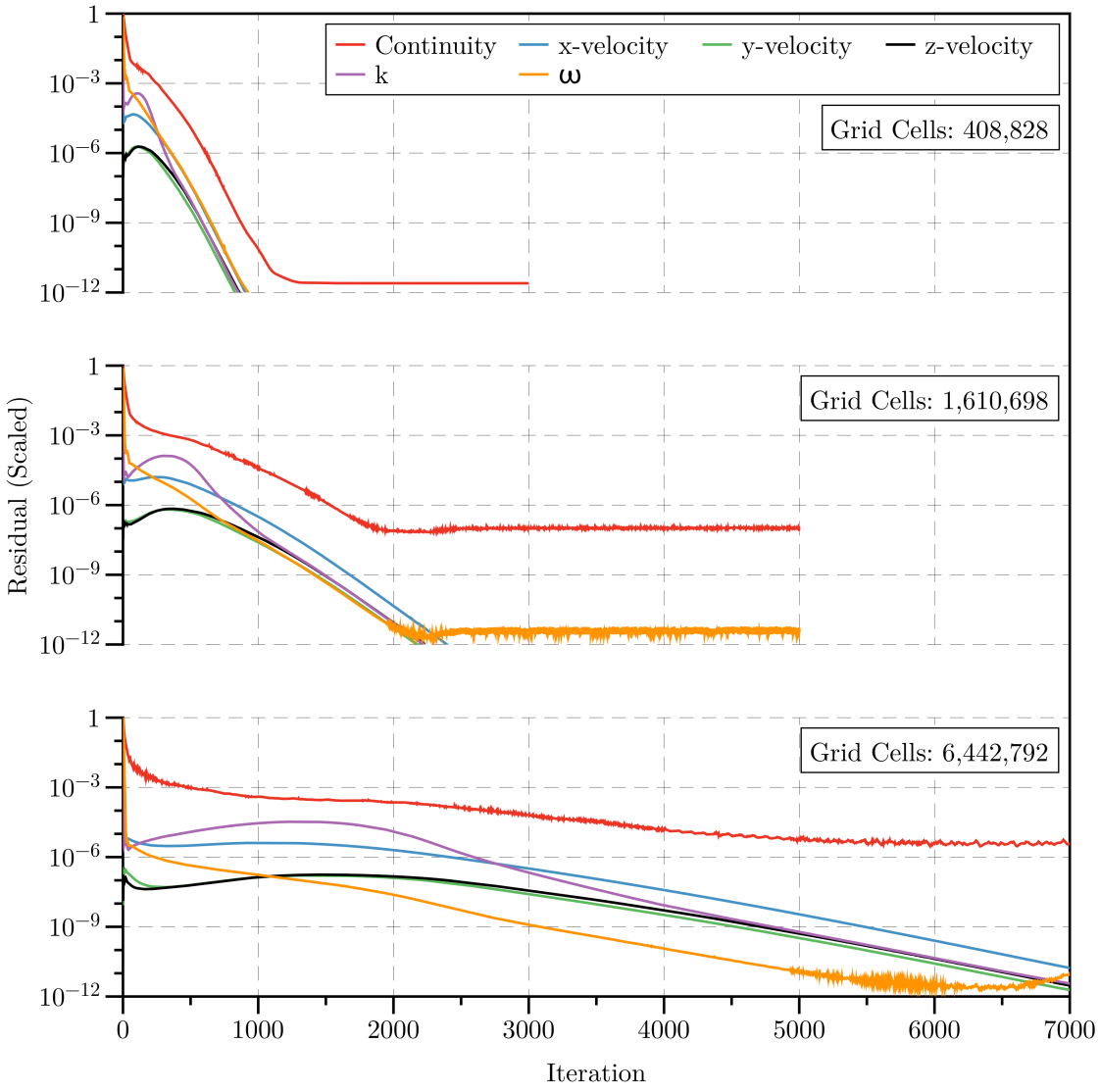

Figure F.10 Scaled residuals for the channel grid convergence.

F.8.1.4 Wall y^+

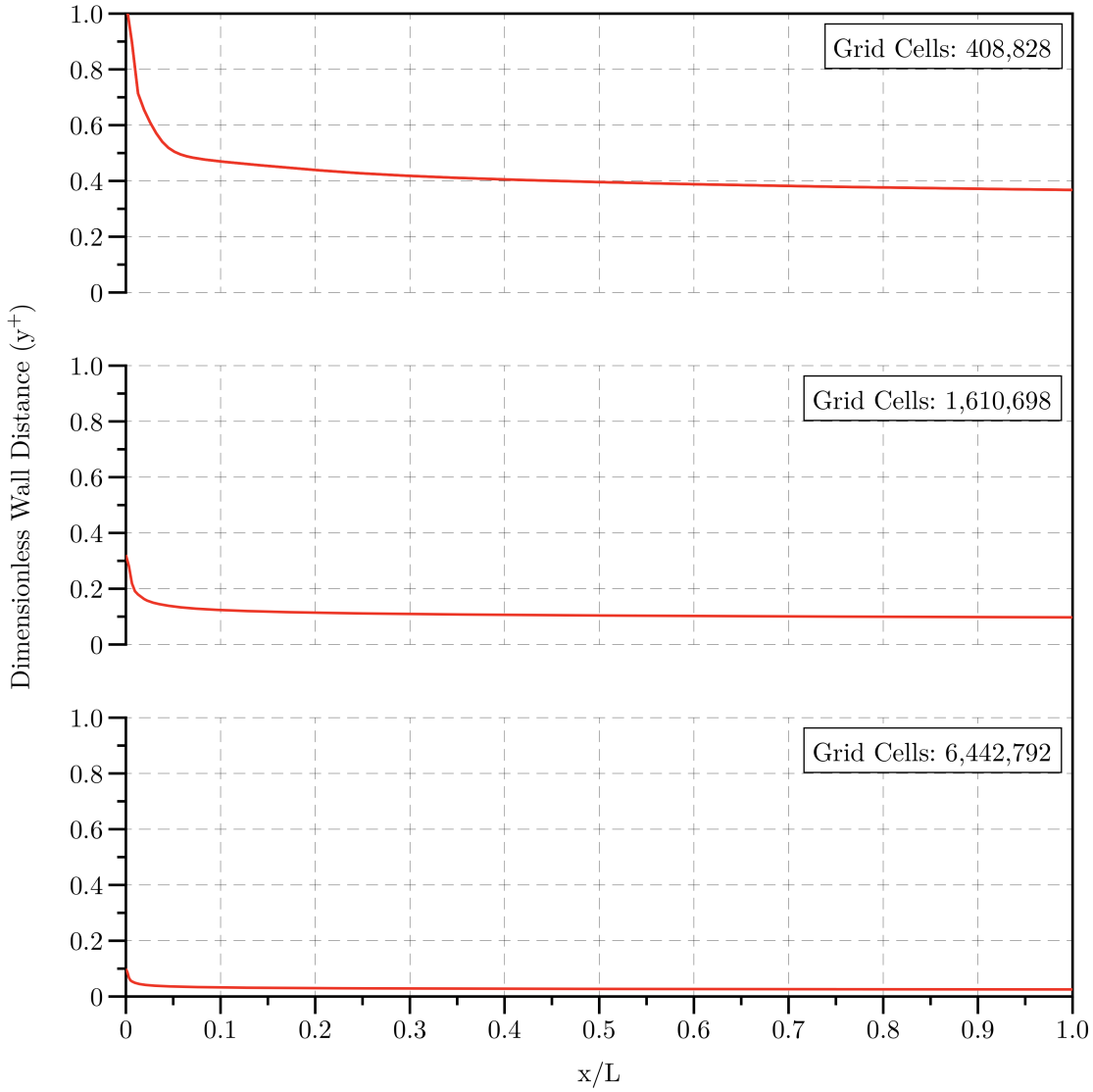

Figure F.11 Dimensionless wall distance (y^+) for the channel grid convergence.

F.8.1.5 Results

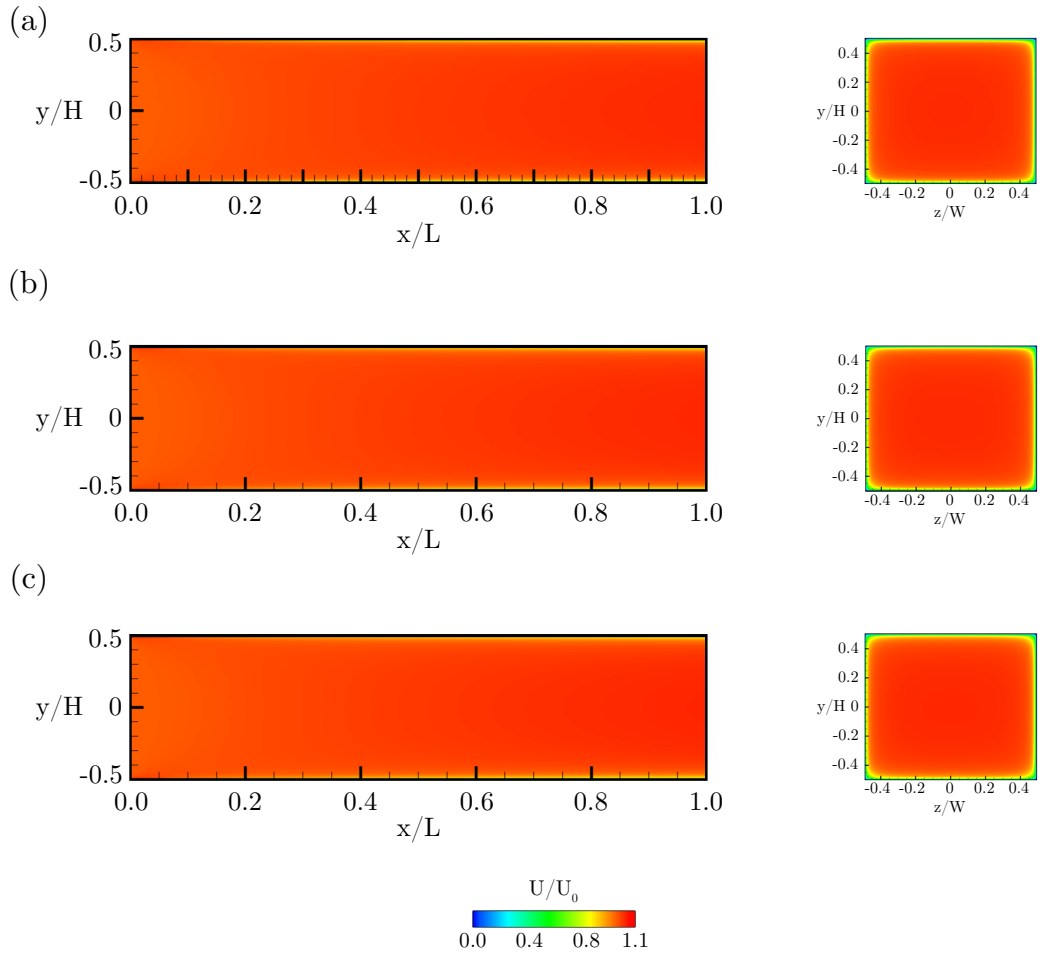

Figure F.12 Velocity fields for (a) 408,828, (b) 1,610,698 and (c) 6,442,792 grid cells.

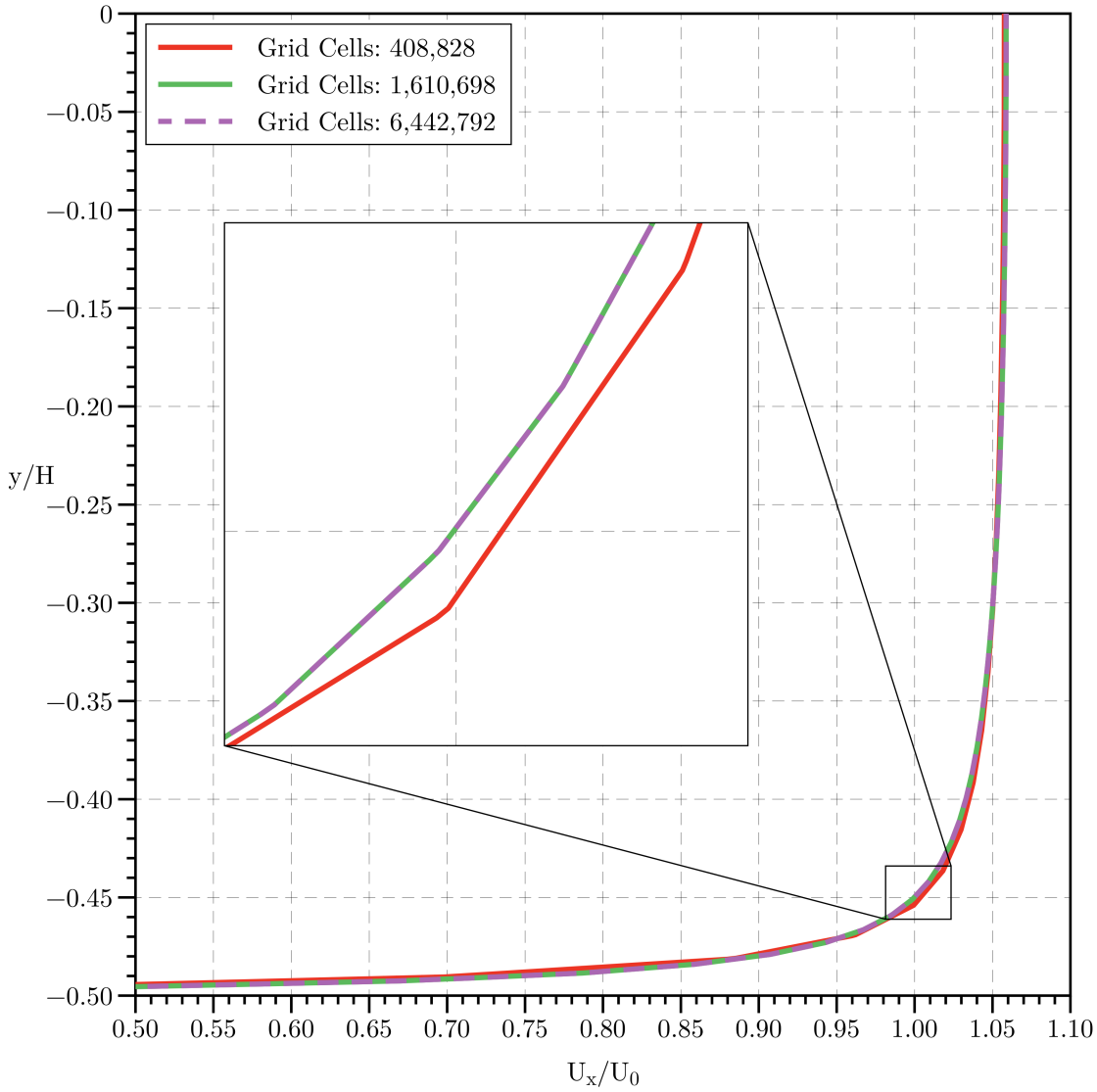

Figure F.13 Normalised centreline velocity (U_x/U_0) profiles for the tested meshes at a normalised downstream (x/L) distance of 0.9.

F.8.2 CFD Results

F.8.2.1 General Solver Parameters

Table F.2 CFD solver parameters used in the 3D channel simulations.

General Details	
Solver	ANSYS® FLUENT® 15.0, Pressure Based, Steady, Implicit, Node-Based
Mesh Type	Structured
Number of Cells	1610698
Materials	
Fluid	Air
Density	Incompressible, ideal gas law
Specific Heat	$1006.43\,\mathrm{J\,kg^{-1}\,K^{-1}}$
Thermal Conductivity	$0.0242\,\mathrm{W\,m^{-1}\,K^{-1}}$
Viscosity	Sutherland law
Molecular Weight	$28.966\,\mathrm{kg\,kmol^{-1}}$
Boundary Conditions	
Inlet	Velocity Inlet (velocity and turbulent kinetic energy profiles, specific dissipation rate of $12.3\,\mathrm{s^{-1}}$)
Outlet	Pressure Outlet
Top	Wall (aluminium with temperature profile)
Bottom	Wall (aluminium with temperature profile)
Left	Wall (wood)
Right	Wall (smooth glass)
Top/Bottom/Left/Right	(Hydrodynamically smooth)

F.8.2.2 Standard $k-\omega$ Solver Parameters

Table F.3 CFD solver parameters used in the 3D $k-\omega$ channel simulations.

Solver Controls	
Turbulence Model	$k-\omega$ (Standard)
$k-\omega$ Options	Low-Re and Shear Flow Corrections
Pressure-Velocity Coupling	SIMPLE
Discretisation (Under Relaxation)	
Gradient	Least Squares Cell Based
Pressure	Second Order (0.3)
Momentum	Second Order Upwind (0.7)
Turbulent Kinetic Energy	Second Order (0.8)
Turbulent Dissipation Rate	Second Order Upwind (0.8)
Specific Dissipation Rate	Second Order Upwind (0.8)
Energy	Second Order Upwind

F.8.2.3 Transition SST $k-\omega$ Solver Parameters

Table F.4 CFD solver parameters used in the 3D Trans. SST $k-\omega$ channel simulations.

Solver Controls	
Turbulence Model	Transition SST
Pressure-Velocity Coupling	SIMPLE
Discretisation (Under Relaxation)	
Gradient	Least Squares Cell Based
Pressure	Second Order (0.3)
Momentum	Second Order Upwind (0.7)
Turbulent Kinetic Energy	Second Order (0.8)
Specific Dissipation Rate	Second Order Upwind (0.8)
Intermittency	Second Order Upwind (0.8)
Momentum Thickness Re	Second Order Upwind (0.8)
Energy	Second Order Upwind

F.8.2.4 Residuals

F.8.2.5 Standard $k-\omega$

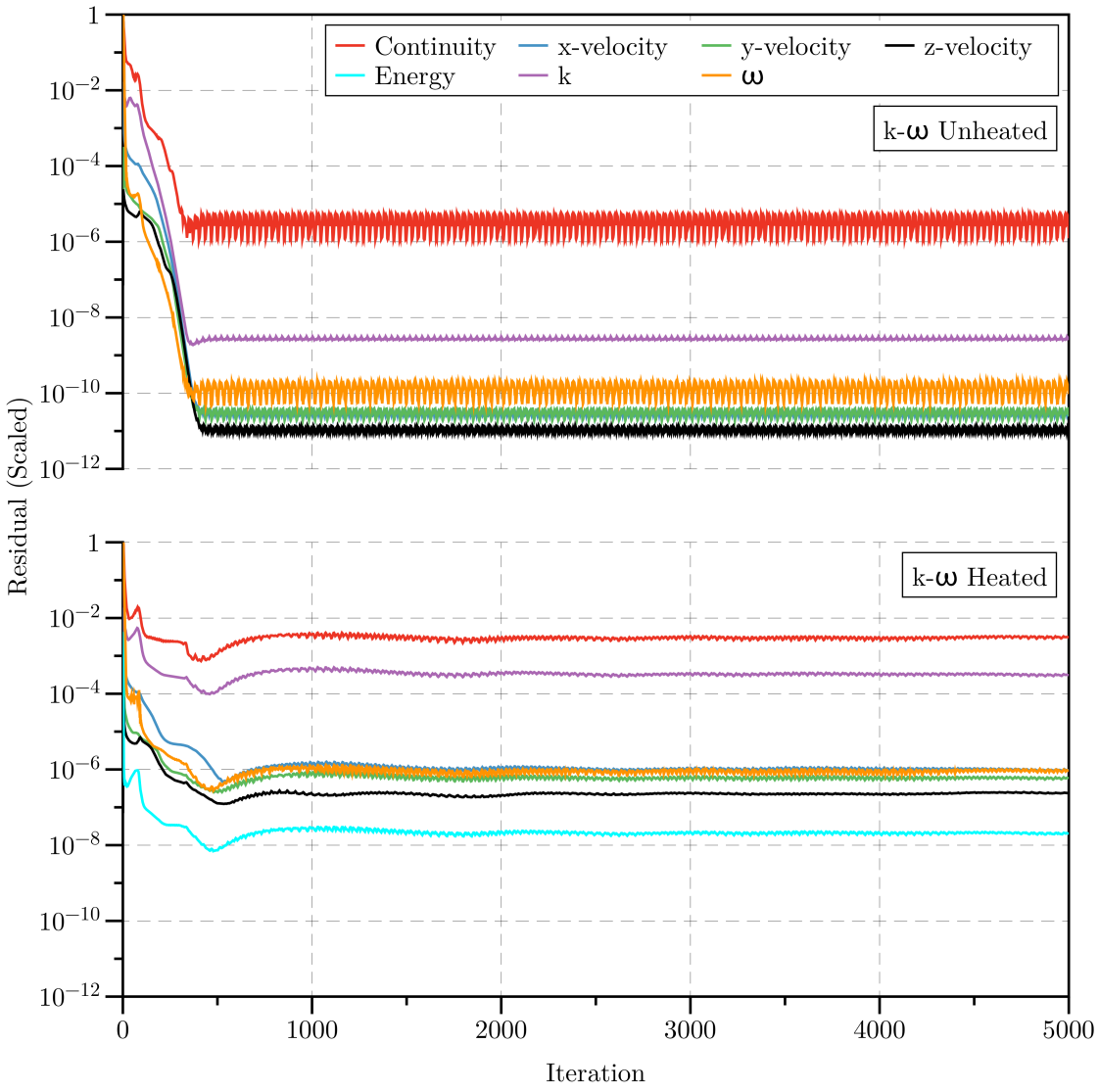

Figure F.14 Scaled residuals for the unheated (upper plot) and heated (lower plot) Standard $k-\omega$ simulations.

F.8.2.6 Trans. SST $k-\omega$

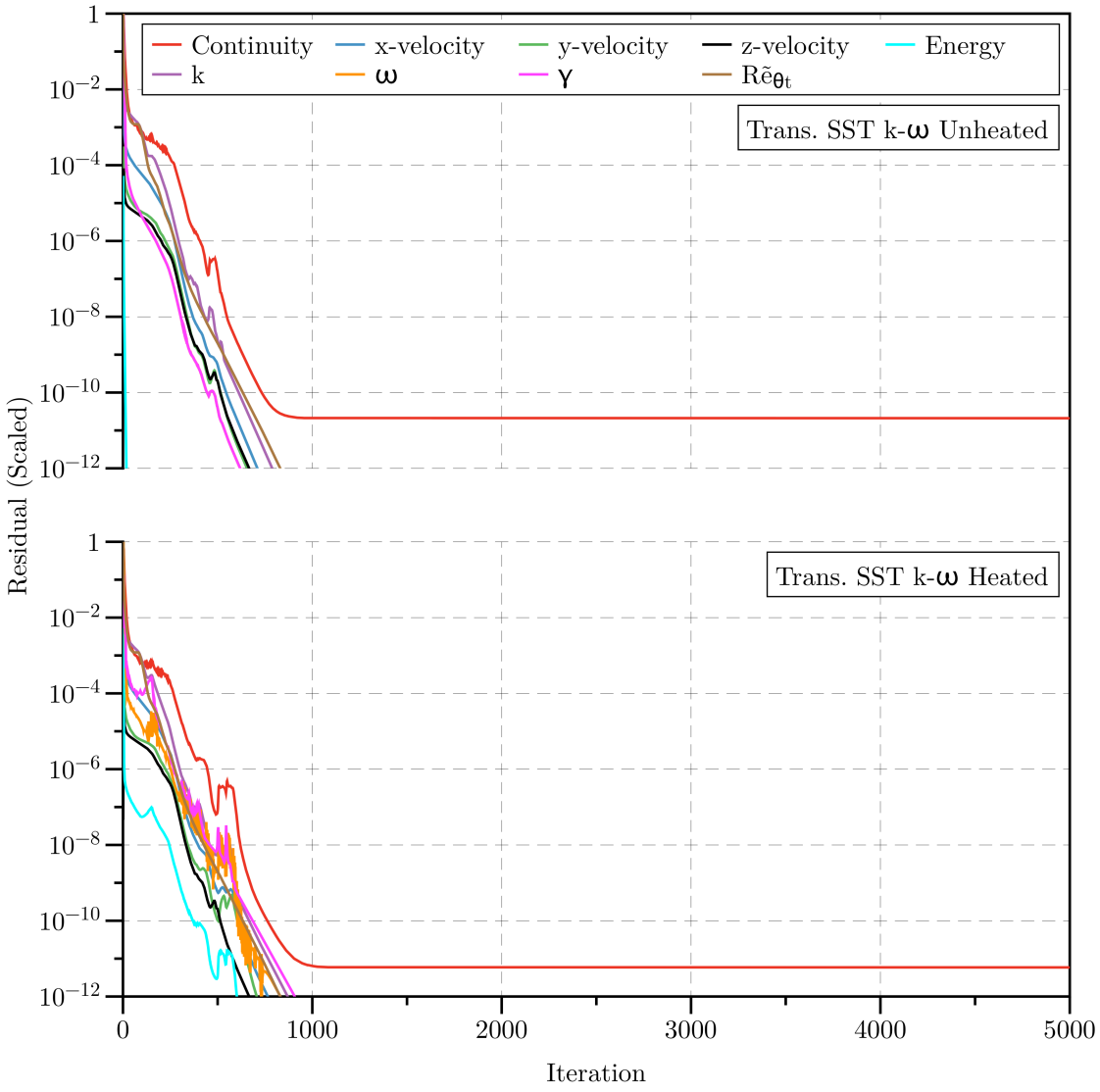

Figure F.15 Scaled residuals for the unheated (upper plot) and heated (lower plot) Trans. SST $k-\omega$ simulations.

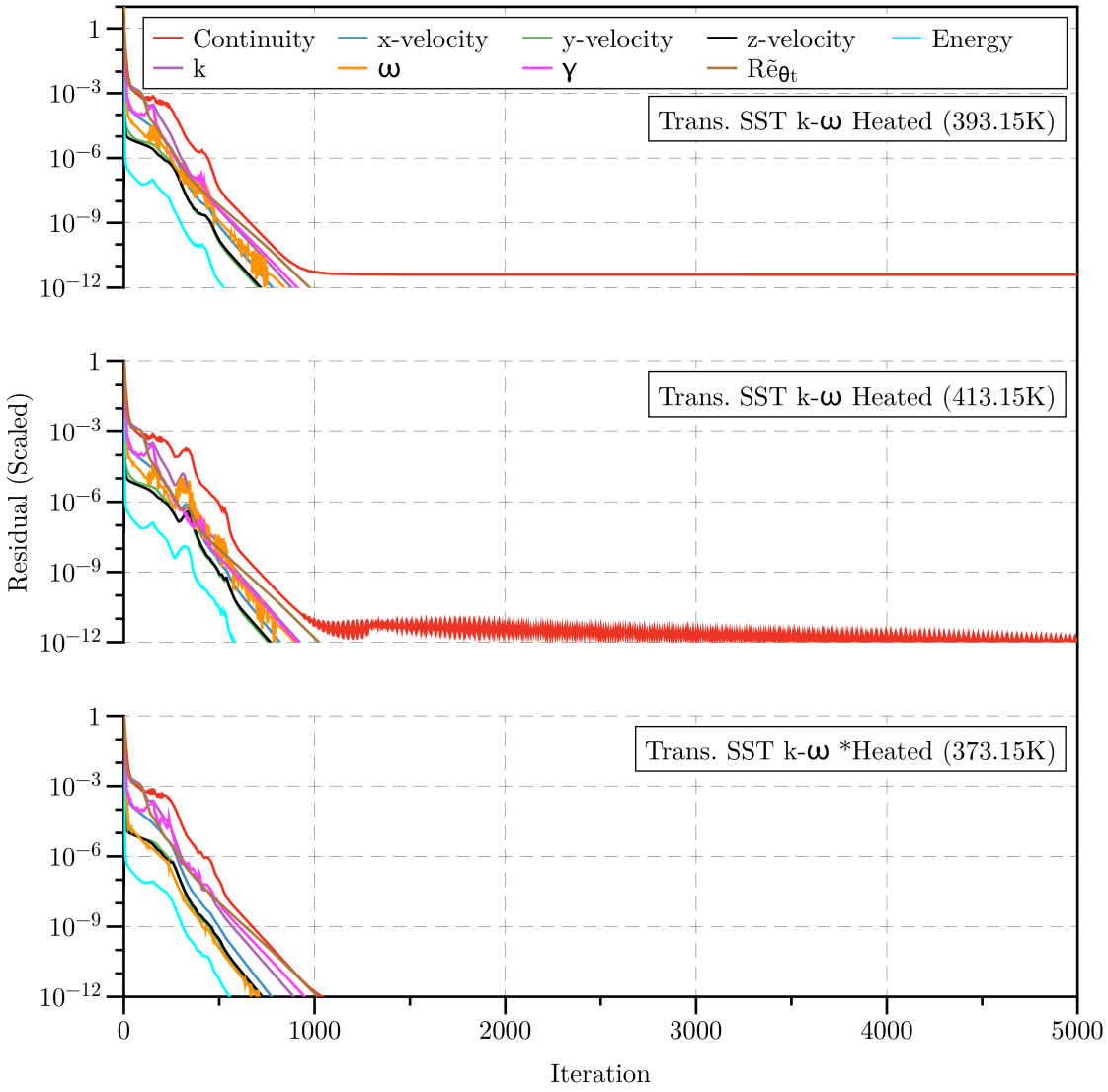

Figure F.16 Scaled residuals for the heated (393.15 K, upper plot), heated (413.15 K, middle plot) and *heated (373.15 K on all four walls of the channel, lower plot) Trans. SST $k-\omega$ simulations.

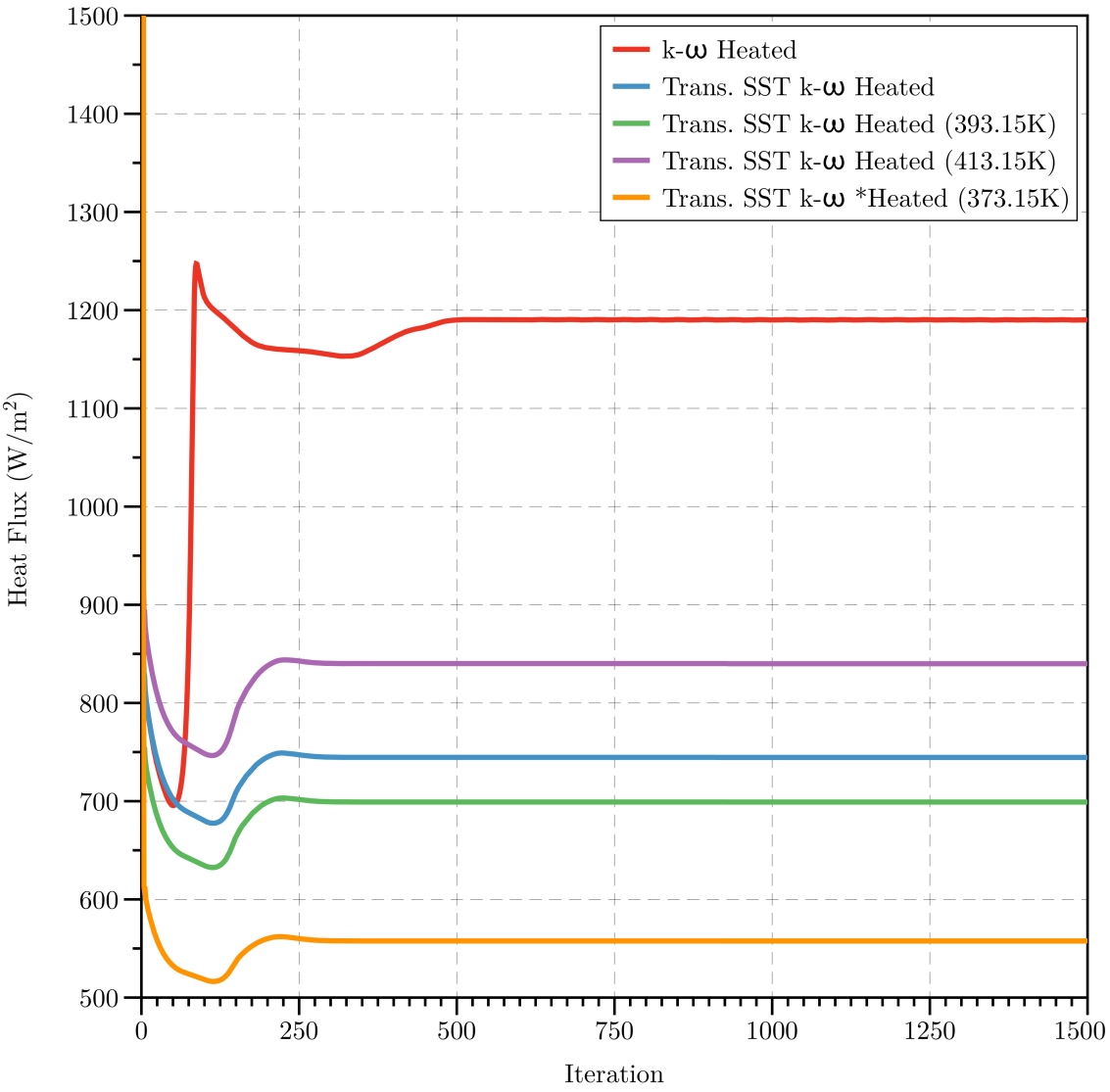

Figure F.17 Heat flux convergence for the heated channel simulations. *heated on all four walls of the channel.

This page intentionally left blank.

This page intentionally left blank.